Influence of random surface rougness on friction in elastohydrodynamic, mixed and boundary lubrication

Julien Bonaventure

Julien Bonaventure. Influence of random surface rougness on friction in elastohydrodynamic, mixed and boundary lubrication. Physics [physics]. École Centrale de Lyon, 2017. English. NNT : 2017LYSEC038 . tel-04917911

HAL Id: tel-04917911
https://theses.hal.science/tel-04917911v1

Submitted on 28 Jan 2025

THÈSE DE DOCTORAT

École doctorale n° 162 : Mécanique - Energétique - Génie civil - Acoustique (MEGA)

Laboratoire :
Laboratoire de Tribologie et Dynamique des Systèmes (LTDS)

présentée par
Julien BONAVENTURE

pour obtenir le grade de
Docteur en Mécanique

Influence of random surface roughness on friction in elastohydrodynamic, mixed and boundary lubrication.

Devant le jury composé de :

BIGERELLE, M.	Professeur	Laboratoire LAMIH, Valenciennes	Examinateur
BRUNETIÈRE, N.	CR CNRS, HDR	Université de Poitiers	Rapporteur
LUBRECHT, T.	Professeur	LAMCOS, INSA de Lyon, Villeurbanne	Examinateur
SCHIPPER, D.J.	Professeur	Université de Twente	Rapporteur
CAYER-BARRIOZ, J.	DR CNRS	LTDS	Directrice de thèse
MAZUYER, D.	Professeur	LTDS	Directeur de thèse

A Marie et à ma famille.

Remerciements

Je remercie Juliette et Denis pour leur enseignement dans le domaine de la tribologie, pour la confiance et la liberté qu'ils m'ont accordées pour mener ce travail à bien, ainsi que pour les agréables moments socio-culino-scientifiques passés en leur compagnie.

Je remercie Messieurs Bigerelle, Brunetière, Lubrecht et Schipper pour l'intérêt qu'ils ont porté à mon travail et pour le sérieux de leur relecture.

Je souhaite exprimer ma reconnaissance à Hélène Schoch, Sandrine Bec et Françoise Leynaud pour leur professionnalisme et leur disponibilité de tout temps, ainsi qu'à Simon Fédry, Sophie Pavan, Frank Dahlem, Jean-Michel Vernet, Bernard Beaugiraud, Michelle Salvia, Nazario Morgado, Serge Zara et Mickaël Sylvestre pour l'aide qu'ils m'ont fournie sur diverses questions techniques. Merci également à Anthony Chavanne pour m'avoir fourni la majorité des surfaces rugueuses utilisées dans les expériences.

Merci à toutes les personnes qui ont égayé ces années, notamment à Jocelyn, Paul, Malik, Thomas, Eloi, Gilles, Médard, Riad, Sylvain, André, Pierre, Mohamadou, Manuel, Fadlallah, Yann, Cédric, Johann, Alexia, Adalberto, Mehdi, Annabelle, Simon, Marième, James, Brandon, Thibaut, Thibaut, Nicolas, Estelle, Nicolas, Camille, Christian, Andrea, Irene, Coralie et Alex.

Enfin je remercie mes parents pour leur éducation et leur soutien, et bien-sûr Marie pour sa présence et la patience dont elle a fait preuve.

Contents

Nomenclature

ACF : autocorrelation function $ACF = ACV/\sigma^2$(-)
ACV : autocovariance (m^2)
a_{eff} : effective contact radius (m)
A_d : dimensionless roughness amplitude deformation $\frac{1}{2}(\underset{t}{max} H(X=0,t) - \underset{t}{min} H(X=0,t))$ (-)
a_H : Hertz radius $\left(\frac{3F_n R^*}{E'}\right)^{1/3}$ (m)
A_i : dimensionless roughness amplitude $a_i R^*/a_H^2$
A_{nom} : nominal contact area πa_H^2 (m^2)
A_{real} : contact area borne by the asperities within a Greenwood-Williamson contact modelling (m^2)
$a.u.$: abritrary units.
BL : boundary lubrication
c_l, c_s : lubricant and surface specific heat (J.kg^{-1}.K^{-1})
COF_a : asperity friction coefficient (-)
COF_{BL} : friction coefficient in the boundary regime (-)
COF_r : reduced traction coefficient $\frac{F_{f\ Couette}}{\tau_{max}}$ (-)
d : distance between two rough surfaces mean planes (m)
d_e : distance from the mean asperity height to the ideally smooth counter surface (m)
D_e : Deborah number $\frac{\eta_E\, u_e}{G_e\, a_H}$ (-)
D_l, D_s : lubricant and surface thermal diffusivity $\frac{K}{\rho c}$ (m^2.s)
DLC : Diamond-Like-Carbon
dx, dy : sampling interval in the x and the y directions (m)
E' : reduced elastic modulus $\left[\frac{1}{2}\left(\frac{1-\nu_1^2}{E_1} + \frac{1-\nu_2^2}{E_2}\right)\right]^{-1}$ (Pa)
EHL : elastohydrodynamic lubrication
EHD : elastohydrodynamic
E_i : Young modulus of body i (Pa)
F_f : friction force (N)
$F_{f\ Couette}$: Couette (or traction) friction force (N)
$F_{f\ Poiseuille}$: Poiseuille (or rolling) friction force (N)
F_n : load (N)
$F_{n\ a}$: load borne by the asperities (N)
$F_{n\ H}$: load borne by hydrodynamic action (N)
G_e : shear modulus of a viscoelastic fluid (Pa)
h : lubricant film thickness (generic notation) (m)
h_c : central nominal film thickness (m)
h_c^{ML-EHL} : nominal central film thickness at the ML-EHL transition (m)
h_0 : nominal film thickness (generic notation) (m)
H_v : Vickers hardness (Pa)
K_l, K_s : lubricant and surface thermal conductivity (W.m^{-1}.K^{-1})
L_w : cut-off length (m)

L_h : dimensionless number $\eta_0 u_e^2 \beta_l / K_l$ characteristic of the rolling heating
L' : Schipper lubrication number $2\eta_0 u_e/(p_m\ R_{a\,c})$
m : slope in the x direction : $\partial_x z$ (-)
ML : mixed lubrication
$Mode(X)$: most probable value taken by X ([X])
n_a : asperity density (m^{-2})
n_{p1D} : peak density per unit length (m^{-1})
n_s : summit density (m^{-2})
N_{samp} : number of lines times number of columns of survey (-)
$N_x,\ N_y$: number of columns and rows in a survey (-)
$N_w = L_w/dx$ (-)
$N_{samp} = N_x \times N_y$: number of height samples in a given image (-)
n_0 : number of zero-crossing points per unit profile length (m^{-1})
p : pressure (Pa)
PAO : poly-α olefin
$< p_{asp} >$: mean pressure over an asperity within the Greenwood-Williamson model (Pa)
p_{atm} : atmospheric pressure (Pa)
p_f : $\frac{F_{n\,H}}{A_{nom}}$ (Pa)
p_m : mean Hertz pressure (Pa)
$p_{m\,1D}$: mean Hertz pressure in a line contact (Pa)
pdf : probability density function
PSD : power spectral density
Q : dissipated heat $F_f \times u_s$ (W)
q_i : fluid lineic flow in the direction $\int_0^h dz\ u_i\ i,\ i \in \{x; y\}$ (m^2/s)
q_s : dissipated heat per unit surface $\frac{F_f}{A_{nom}} u_s$ (W/m^2)
q_v : dissipated heat per unit volume $\tau \cdot \dot{\gamma}$ (W/m^3)
R^* : reduced radius of curvature $(1/R_1 + 1/R_2)^{-1}$, where R_1 and R_2 are the surfaces curvature radii.
$R_{a\,c}$ composite centre line average roughness $\sqrt{R_{a\,1}^2 + R_{a\,2}^2}$ (m)
R_b : ball radius (m)
R_{jx} : curvature radius of surface $j,\ j \in \{1; 2\}$ in the x direction (m)
RMS : root mean square
$R_x,\ R_y$: contact reduced curvature radii inthe x and y directions : $R_x \equiv \left[\frac{1}{R_{1x}} + \frac{1}{R_{2x}}\right]^{-1}$ (m)
std : standard deviation
$S_{al\,x}$: autocorrelation length corresponding to a correlation of x (m)
S_{qB} : ball RMS roughness (m)
S_{qD} : disc RMS roughness (m)
$S_{q\,c}$: composite RMS roughness measured in 2D (m)
SRR : slide to roll ration defined by u_s/u_e
T_{amb} : room temperature (°C)
T_l : lubricant temperature (°C)
T_s : surface temperature (°C)
$t_{\mathrm{l\,cond\,z}} = \frac{h^2}{D_l}$: characteristic time for the heat diffusion across the film thickness (s)
$t_{\mathrm{\ transit}} = \frac{u_e}{2a_H}$: fluid transit time across the contact area (s)
$\vec{U}_1$, $\vec{U}_2$: surfaces velocities (m/s)
$\vec{u}_e$: entrainment speed defined as the mean surfaces velocity $\frac{1}{2}(\vec{U}_1 + \vec{U}_2)$ (m/s)
u_e : $|\vec{u}_e|$ (m/s)
$\vec{u}_s$: sliding speed $\vec{U}_1 - \vec{U}_2$ (m/s)
u_s : $|\vec{u}_s|$ (m/s)

u_i : fluid velocity field component along the direction i, $i \in \{x; y; z\}$ (m/s)
W_{eiss} : Weissenberg number $\frac{\eta \dot{\gamma}}{G_e}$ (-)
Y : yield strength (Pa)
z : roughness height signal (m)
z_{LP} : low-pass filtered surface heights (m)
α : piezoviscosity (1/Pa)
β_l : lubricant viscosity-temperature coefficient $\left(-\frac{\partial \, ln \, \eta_0}{\partial T}\right)$ (K^{-1})
β : asperity curvature radius (m)
β^* : reduced asperity curvature radius $\frac{\beta}{2}$(m)
$\dot{\gamma}$: shear rate (1/s)
ΔX : absolute uncertainty over quantity X ([[X]X])
ΔT_{inlet} : fluid temperature rise in the inlet (°C)
$\Delta T_{flash\,max}$: maximum flash temperature rise (°C)
$\Delta T_{l\,av}$: lubricant temperature rise spatially averaged over the contact area (°C)
$\Delta T_{l\,max}$: lubricant maximum temperature rise in the contact area (°C)
η : lubricant viscosity (Pa.s)
η_0 : lubricant inlet viscosity (Pa.s)
η_E : Eyring viscosity (Pa.s)
ϕ : probability density for the surface asperities (m^{-1})
λ : topographical wavelength (m)
λ_c : cut-off wavelength for a Fourier low-pass filter (m)
Λ : lambda ratio $\frac{h_c}{\sigma_c}$ (-)
Λ_{fluid} : ratio of the fluid shear strength with the mean pressure $\frac{\tau_{max}}{p_m}$ (-)
κ : curvature in the x direction : $\partial^2_{xx} z$ (m^{-1})
κ_m : mean curvature : $-\frac{1}{2}(\partial_{xx})^2 z + \partial_{yy})^2 z)$ (m^{-1})
ν_i : Poisson coefficient of body i (-)
ρ_1 : autocorrelation between two neighbours on a profile (m)
ρ_l, ρ_s : lubricant and surface gravity (kg.m^{-3})
σ^2_m : slope variance in the x direction (-)
$\sigma^2_{\kappa x}$: curvature variance in the x direction (m^{-2}) σ_c : composite RMS roughness (generic notation) (m)
σ_a : standard deviation of the asperity heights (m)
σ_X : fluctuations of the quantity X ($[X]$)
τ : shear stress (generic) (Pa)
τ_0 : Eyring stress (or Newtonian limiting shear stress) (Pa)
τ_m : Couette shear stress $\frac{F_{f\ Couette}}{A_{nom}}$ (Pa)
τ_{max} : lubricant shear strength at the operating pressure (Pa)
∇ : parameter defined as $\frac{\lambda M^{1/2}}{a_H L^{1/2}}$
$\tilde{\nabla}$: parameter defined as $\nabla \sqrt{2U_2/(U_1 + U_2)}$
$< >$: expectation operator, ensemble average
$\equiv$: is defined by

Chapter 1

Introduction

Lubricated contacts are present in numerous industrial applications. In the automobile industry, the internal combustion engine involves several components in which about 80% of the injected energy (fuel) is lost by exhausting (33%), engine cooling (29%), air viscous drag (5%) and friction losses (33%). Setting the tire rolling friction and the braking losses aside, the transmission and the internal engine dissipate 17 % of the injected energy[1] (67, fig. 4). Vehicle industry has continuously adapted to consumer's increasing demands to improve the vehicles comfort, durability and safety, which heightens the required injected energy (37% increase between 1995 and 2010 (2)). Nowadays, vehicles transport emit about 125 g/km CO_2 and is responsible for more than 75% of CO_2 emissions (2). Environmental policies aim at reducing vehicles CO_2 emission to 95 g/km for 2020 (38), (2). This goal requires the improvement of vehicles energetical efficiency, and by extension, the reduction of internal frictional losses in lubricated contacts.

Working in fully lubricated conditions is beneficial in terms of friction because it avoids direct contacts between the solids. In addition, separating completely the surfaces with a lubricant film prevents the occurence of wear and the costly workpieces replacement. To reach such conditions, the generation of a hydrodynamic lift is necessary. The influence of the surface speeds and of the load on this hydrodynamic bearing are well-known, at least, for ideally smooth surfaces. Unfortunately, the film thickness is importantly affected by the presence of roughness, such that a rough contact that was nominally intended to work in fully lubricated conditions may indeed experience solid contacts, which raises the energetic losses.

Most contacts are submitted to transient kinematics and loads (see e.g. fig. 1.1 for a cam-follower contact) and given the variety of workpiece geometries, loads and lubricants, reaching fully lubricated conditions is not permitted by all engine contacts. Different contacts, like the piston-ring, the skirt-cylinder or the cam-follower contacts, oscillate between different operating regimes (see fig. 2.1) according to their geometries and the lubricant viscosity. Furthermore, these systems experience numerous starts and stops during their lifetime. During these cycles, the film thickness vanishes, which increases the probability of surface damaging.

This has led tribologists to use additives that adsorb chemically on the surfaces to form solid-like protective layers. Alternately, the surfaces may be coated with a solid protective layer that increases the solid strength.

The present work was funded by the Région Auvergne Rhône-Alpes and by the DGCIS via the GMP-DLC[2] project (IREIS, LTDS, RSA, PSA, Thales, LPSC, MTS). This project aims at improving the engine contact performance by coating the steel operating workpieces with Diamond-Like-Carbon (DLC)[2]. The DLC having strong mechanical properties ($H_v \in [1000\ ;\ 3000]$), it is expected to increase workpiece lifespan. When a contact is intended to work in fully lubricated conditions, it is generally

---

[1] With variations of a few percents according to the specifics of the engine of interest.

[2] Using an a-C:H DLC coating, commercial name : Certess DDT by HEF.

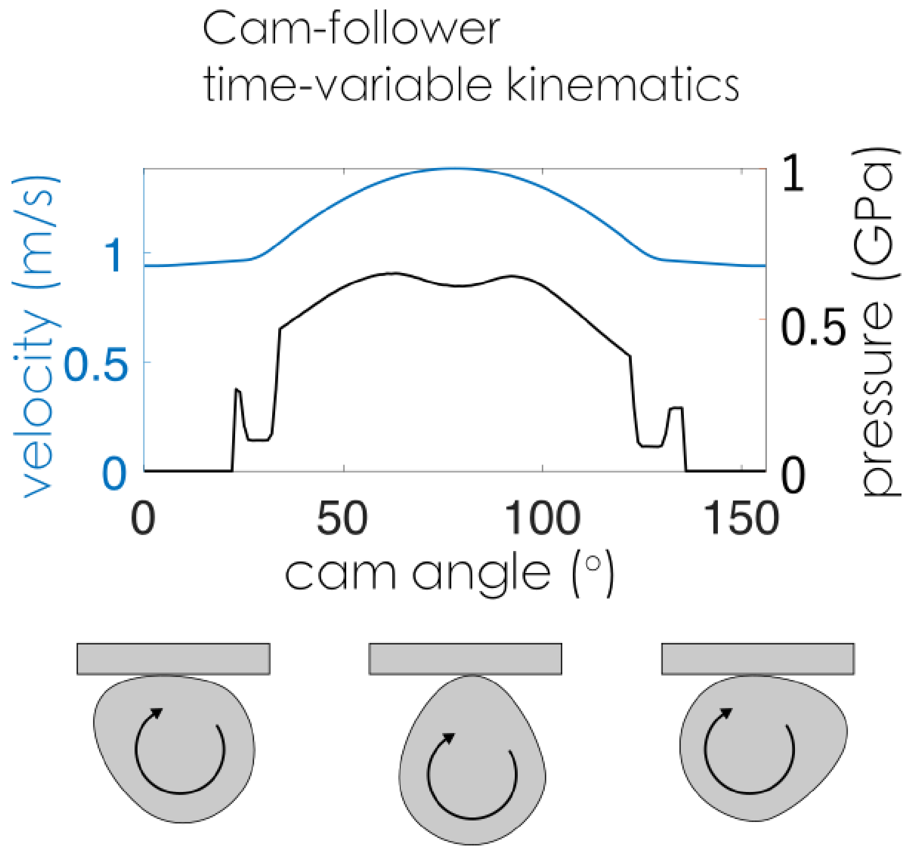

Figure 1.1: Real-life kinematics exemplified with a cam-follower contact operating at 1000 revolutions per minute. The variable cam curvature leads to variable pressures and speeds during a single cam cycle.

beneficial to polish the surfaces as much as possible. The DLC being hard, its surface finition is a costly step that must be optimized. If the surfaces are initially smooth enough, they may become even smoother during the workpiece running-in phase, thanks to scarce abrasive removal of the highest asperities. On the opposite, if the surface finition is insufficient, important asperity interactions may rapidly increase the roughness and even cause the removal of the coating (DLC-DLC contacts) or may plough the counter surface (DLC-steel contacts). From an industrial viewpoint, it is thus important to know the optimal roughness degree that should be aimed at during the finishing process to prevent wear and to get a friction as low as possible.

Goals The main object of the present work is to understand the interactions between two rough surfaces in a lubricated contact. Such a study would permit a priori the prediction of the friction force for a given surface and its corresponding set of operating conditions. Since most workpieces are made of steel, the majority of the study will be conducted with bulk steel surfaces, with and without DLC coating. The lacking knowledge about the effect of roughness on the film thickness and on the friction mechanisms is closely related to the problems in describing it. A first goal of this work is thus to describe different surfaces with as least as possible parameters to compare their contribution in friction tests. Secondly, it is required to measure these surfaces tribological response to different kinematics and loads for the purpose of predicting the conditions that lead a rough contact to operate in different lubrication regimes that are the elastohydrodynamic, mixed and boundary regimes, where the friction force is respectively low, moderate and high. Fully formulated lubricants contain chemicals that interact with the surfaces, and the importance of these interactions may differ according to the surface texture. In order to focus on the influence of roughness, only

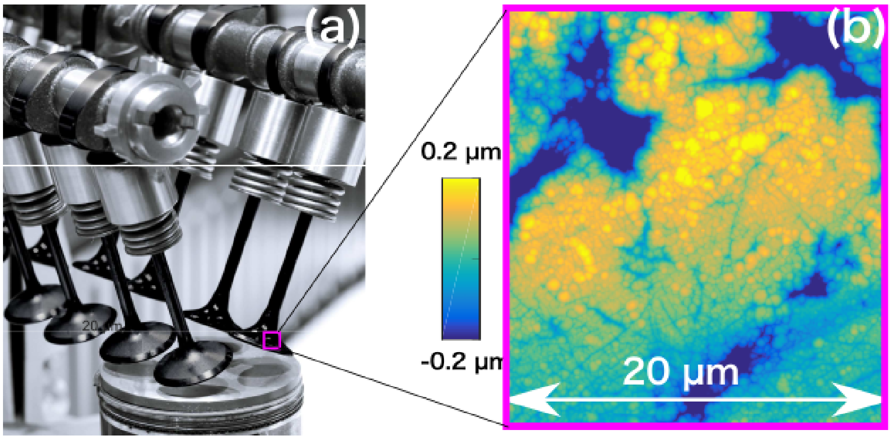

Figure 1.2: (a) : DLC-coated intake valves from HEF group. (b) : AFM survey of a DLC coated steel disc.

base oils are used in the present experiments.

Outline This work is decomposed in six chapters : in the first chapter, the basics of elasthydrodynamics and the lubrication regimes are introduced, with an attention towards the control parameters that affect the film thickness. Then, the theoretical and experimental advances regarding the influence of surface roughness on the film thickness are reviewed, before introducing the experimental issues raised by surface metrologists regarding the description of random surface roughness. The experimental tools used to conduct tribological tests and topographical measurements are presented in the second chapter. The third chapter focuses on prediction of the friction force in a lubricated contact for various kinematic and loading conditions discussing the fluid rheology, the pressure and thermal effects. The fourth chapter describes the surface roughness parameters used to describe rough surfaces, with a specific care regarding the stationarity of these parameters. In the fifth chapter, the transitions between the lubrication regimes are studied using Stribeck procedures and these transitions are correlated to the surface parameters to provide quantitative predictions for the onset of mixed and boundary lubrication. Finally, the friction mechanisms in the boundary and mixed regimes are discussed versus the materials and the surface roughness in the sixth chapter. This chapter is concluded with the calculation of complete predictive Stribeck curves for various contacts with only experimentally measured parameters.

Chapter 2

Lubrication of rough surfaces : state of the art

The lubrication of rough surfaces involves several fields of physics. In these contacts, a lubricant film thickness determines the lubrication and the friction mechanism. It is hence important to understand the role played by the operating parameters, such as the load and the velocity, and those governed by pressure-dependent properties of the fluids. Since the friction process is energy-dissipating, the influence of temperature on the film thickness must also be examined. The basics of the elastohydrodynamic (EHD) theory are presented in this chapter.

Most advances in EHD are based on the assumption that surfaces are perfectly smooth. The roughness, always present on real surfaces, has complicated the theoretical approaches to predict its impact on the hydrodynamic bearing mechanism. Theoretical advances in this domain are reviewed and are compared to previous experimental studies. Finally, the issues raised by surface metrologist, with regard to the proper description of random surfaces are reviewed.

2.1 Lubrication regimes from fully separated to boundary lubrication

2.1.1 What is a lubricated contact ?

A lubricated contact consists in two moving solids loaded against each other and nominally separated by a viscous fluid layer. Denoting $\vec{u}_1$ and $\vec{u}_2$ the surface speeds, the entrainment speed is defined as the average surfaces speed.

$$\vec{u}_e = \frac{1}{2}(\vec{u}_1 + \vec{u}_2) \tag{2.1}$$

$\vec{u_e}/|\vec{u}_e|$ defines the rolling direction. When the rolling direction is constant, u_e is defined as the modulus of $\vec{u}_e$. The product viscosity times entrainment speed $\eta_0 \times u_e$ determines importantly the film thickness h that separates the bodies as h increases with u_e :

- if u_e is large enough, the bodies are separated by a film thickness generated by hydrodynamic pressure
- below a critical speed, the film thickness is too small to separate the bodies and their roughnesses make contact

These two extreme cases define respectively the hydrodynamic lubrication (HL) and the boundary lubrication (BL). In HL, a pressure field is generated in the fluid and it withstands the loaded surfaces.

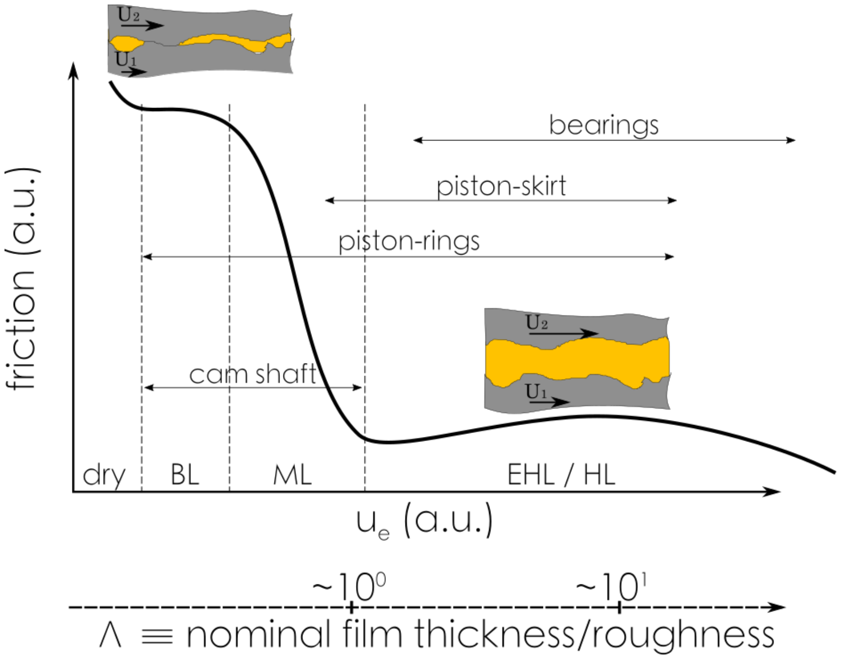

Figure 2.1: Scheme of a Stribeck experiment covering all lubrication regimes. The load and the sliding-rolling ratio are kept constant during the procedure. Moreover, these conditions are variable in time, such that most contacts operate in several lubrication regimes

If the fluid pressure is significant, the surfaces may be elastically deformed : these conditions define the elastohydrodynamic lubrication (EHL) regime.

The bodies shape plays a major role in the contact pressure field. If they have conforming geometries (e.g. journal bearings), then the load is distributed over a large apparent area determined by the bodies curvature (63). If they present non-conforming geometries (e.g. cam-follower contacts) then the contact area is determined by the body elastic flattening over an area determined by their elastic moduli, their curvature and the load according to the Hertz theory.

2.1.2 Introduction to lubrication regimes : Stribeck procedure

A Stribeck experiment consists in applying a constant load F_n between the bodies and varying the entrainment speed between these bodies while introducing sliding. More precisely, a constant ratio between the sliding speed $u_s \equiv ||\vec{u}_s|| = ||\vec{u}_1 - \vec{u}_2||$ and $u_e \equiv ||\vec{u}_e||$, called the sliding-rolling ratio $SRR \equiv \frac{u_s}{u_e}$, is applied. If the range of $\eta_0 \times u_e$ covered during the experiment is large enough, the experiment may allow to scan BL and EHL.

The friction mechanisms in EHL and BL respectively are fundamentally different. In the first case, the sliding results in shearing the fluid that separates the bodies. In the second case, the friction mechanism is caused by the shearing of a nanometric layer of lubricant adsorbed on the bodies along with facing asperities. BL results in a friction force significantly higher than in EHL and possible wear according to the materials and their roughness.

Figure 2.1 shows a typical Stribeck experiment illustrating the large friction drop from BL to EHL. The region in between these regimes is appropriately called the mixed lubrication (ML) as it corresponds to a transitional state between BL and EHL. The lift and friction mechanisms in ML are usually considered as a combination of BL and EHL, although this still constitutes a research topic (119).

2.2 Introduction to Elastohydrodynamic Lubrication

2.2.1 Thin-film lubrication : the Reynolds equation

The central equation in EHL is the Reynolds lubrication equation. On the one hand, the fluid is carried by the bodies motion because of the no-slip condition at the fluid-solid boundaries, always verified[1]. On the other hand, the high pressure present in the contact area tends to prevent the fluid from entering the contact area. The Reynolds equation balances these two counter effects and expresses the conservation of the fluid flow from the inlet to the outlet. The incompressible version of the Reynolds equation[2] reads :

$$\boxed{\vec{\nabla}_{x\,y} \cdot \left(-\frac{h^3}{12\eta} \vec{\nabla}_{x\,y} p + \vec{u}_{e\,x\,y} h \right) + \frac{\partial h}{\partial t} = 0 \quad ,} \tag{2.2}$$

with $\vec{\nabla}_{xy} \equiv \begin{pmatrix} \partial_x \\ \partial_y \end{pmatrix}$, $\vec{u}_e \equiv \begin{pmatrix} u_{e\,x} \\ u_{e\,y} \end{pmatrix}$, $p(x,y)$ the pressure field and $\eta(x,y)$ the fluid viscosity. Assuming the bodies are separated with a constant h_0 film thickness, h is determined by the bodies elastic deformation through :

$$h(x,y) = \underbrace{h_0}_{\text{hydrodynamicconstant}} + \underbrace{\frac{x^2}{2\,R_x} + \frac{y^2}{2\,R_y}}_{\substack{\text{bodies}\\ \text{undeformed}\\ \text{geometries}}} + \underbrace{\frac{2}{\pi E'} \int_{-\infty}^{\infty} du \int_{-\infty}^{\infty} dv \, \frac{p(u,v)}{\sqrt{(x-u)^2 + (y-v)^2}}}_{\substack{\text{bodies}\\ \text{elastic}\\ \text{deformation}}} \tag{2.3}$$

,where $R_x^{-1} \equiv (R_{1x}^{-1} + R_{2x}^{-1})$ and $R_y^{-1} \equiv (R_{1y}^{-1} + R_{2y}^{-1})$ are the bodies reduced curvatures. No general analytical solution exists for eq. (2.2) because the film thickness and the pressure field have to be solved at once. Moreover, the lubricant viscosity is generally not the same between the contact entrance and the contact zone. The Roelands isothermal relationship has been successful in describing the pressure-viscosity relationship :

$$\eta = \eta_0 \, \exp\left[(\ln \eta_0 + 9.67) \left(-1 + \cdot (1 + \mathrm{p}/\mathrm{p}_{\mathrm{ref}})^{\mathrm{Z}} \right) \right] \tag{2.4}$$

$$\text{with } \mathrm{Z} \equiv \frac{\alpha \, \mathrm{p}_{\mathrm{ref}}}{\ln(\eta_0) + 9.67} \tag{2.5}$$

α is the lubricant pressure-viscosity coefficient and is the order of 10^{-8} Pa^{-1} for commonly-used piezoviscous lubricants such as oils. p_{ref} is a reference pressure equal to 196.8 MPa (109). The viscosity increases almost exponentially with pressure.

2.2.2 EHD contact

2.2.2.1 Hertz contact approximation

EHD pressure fields are close to the Hertz pressure profile for a dry circular contact between curved surfaces, which is, in polar coordinates :

$$p_{Hertz}(r) = \frac{3\,p_m}{2} \cdot \sqrt{1 - \left(\frac{r}{a_H} \right)^2} \quad , \tag{2.6}$$

---

[1] Except in peculiar cases where the surfaces are atomically smooth (29), or when they present a chemically repulsive interaction with the fluid.

[2] See annex 9.3 for the derivation.

where a_H is the Hertz radius. Thanks to this likeness, the mean pressure in EHD is well approximated considering the load per unit Hertz area. The bearing area is then calculated with :

$$A_{nom} = \pi a_H^2 = \pi \left(\frac{3F_n\, R_b}{2E'} \right)^{2/3} \quad , \tag{2.7}$$

where E' is the reduced elastic modulus, defined as :

$$E' \equiv \frac{2}{\frac{1-\nu_b^2}{E_b} + \frac{1-\nu_d^2}{E_d}} \tag{2.8}$$

The mean Hertz pressure will be used to characterize the overall pressure field :

$$\boxed{p_m \equiv \frac{F_n}{A_{nom}} = \left(\frac{4F_n}{9\,\pi^3} \frac{E'^2}{R_b^2} \right)^{1/3}} \tag{2.9}$$

2.2.2.2 Isothermal film thickness formula

Assuming an isothermal Newtonian fluid and smooth surfaces, several authors solved numerically the Reynolds equation (2.2). They fitted their solutions using dimensionless grouping to provide ready-to-use formulas for the evolution of central film thicknesses in various conditions of load and speed (see for instance Hamrock and Dowson (62), Nijenbanning et al. (98)). In the case of an isothermal piezoviscous elastic point contact (62), i.e. a situation where the pressure is high enough to increase the lubricant viscosity and to deform the bodies, the most widely used isothermal Newtonian equation for the central film thickness reads :

$$\frac{h_c}{R_x} = 2.69\, U^{0.67}\, G^{0.53}\, W^{-0.067}\, (1 - 0.61 e^{-0.73\, k}) \tag{2.10}$$

$$\text{with the following dimensionless grouping : } U = \frac{\eta_0\, u_e}{E'\, R_x} \tag{2.11}$$

$$G = \alpha\, E' \tag{2.12}$$

$$W = \frac{F_n}{E'\, R_x^2} \tag{2.13}$$

$$k = 1.03 \left(\frac{R_y}{R_x} \right)^{0.64} \tag{2.14}$$

Expressed in physical units, the central film thickness formula reads :

$$\boxed{h_c = K_2 \cdot R_x^{0.33} \cdot (\eta_0\, u_e)^{0.67} \cdot \alpha^{0.53} \cdot E'^{0.061} \cdot p_m^{-0.201}} \tag{2.15}$$

With $K_2 = 2.69 \cdot (1 - 0.61 e^{-0.73 \times 1.03}) \cdot \left(\frac{4}{9\pi^3}\right)^{0.067}$.

Nijenbanning et al. (98), used a different dimensionless grouping and provided formulas not only applicable to elastic-piezoviscous contacts but also to rigid-piezoviscous, rigid-isoviscous and elastic-isoviscous ones. In terms of central film thickness, their results only show small differences with the solutions of Hamrock-Dowson and Higginson for elastic piezoviscous contacts. This work does not aim at answering which one is the truest, but it remains that the Hamrock-Dowson formulas are the most widely used and constitute a reference in most of the literature in EHL. Their use will thus be preferred in the present work, and also because the input variables appear separately through power products, which eases calculations.

2.2.2.3 Qualitative features of EHD contacts

Athough their precise boundaries are not mathematically established, it is convenient to distinguish three important zones of the EHD contact : the inlet, the central area and the outlet. The one-dimensional EHD contact is represented figs. 2.2.a , 2.2.b and a typical EHD pressure profile is shown fig. 2.2.c, in solid line. The inlet (left side of graphs 2.2) is the area where the fluid is being confined by the surfaces and where the pressure increases importantly from p_{atm} to typically 10^8 Pa and where the shear rates sometimes reach 10^6 s^{-1} (53). The film thickness is mainly governed by the events in this area, in particular through the bodies curvature and the fluid inlet viscosity η_0.

A magnification of the central area is represented figure 2.2.b : the pressure in this area is high, which causes the lubricant viscosity to be significantly higher than elsewhere. The tangential force hence mainly arises from the fluid shearing in that specific area, in contrast with the contact inlet and outlet.

The outlet is located downstream the contact area, where the pressure collapses (right side of graphs 2.2). The separation narrowing near the outlet is called the constriction zone and roughly coincides with the so-called Petrusevich pressure spike. Even though this constriction corresponds to a small film thickness reduction, it is crucial to generate a load bearing mechanism. Downstream this pressure spike, the pressure decreases rapidly and the fluid is somehow stretched, causing cavitation. The stretching rate depends upon the fluid average speed such that below a given entrainment speed, the fluid cavitation may not be observed.

The fluid velocity field (see eq. (9.17)) is schematically represented figure 2.2.b in one dimension along the rolling direction. According to the location in the contact, the pressure gradient sign is different. Between the inlet and the contact center ($x \in [-a_H\ ;0]$), the positive pressure gradient tends to prevent the fluid from entering the contact. Between the center and the outlet ($x \in [0\ ;a_H]$) the negative pressure gradient tends to expel the fluid towards the outlet. On the one side of the contact, the fluid flows inside the contact ($x < 0$) and on the other side, it flows outward ($x > 0$) : this pressure-induced component of the flow is referred to as the Poiseuille flow. The small asymmetry found on EHD pressure profiles causes the two opposite Poiseuille components to — almost — cancel each other. The fluid flow is mainly determined by the entrainment speed u_e.

EHD pressure profiles may be well approximated with the symmetric static Hertz pressure profile (black dashed line fig. 2.2.c) obtained in a dry contact with the same load, curvature and materials. In the present work, the pressure profile is considered uniform in the Hertz area ($p = constant = p_m$, see green line 2.2.c). Similarly, the film thickness in the high-pressure area is quite homogeneous and can be assimilated to the central film thickness h_c. This assumption holds as long as h/a_H does not overcome 1/100.

The film thickness formula presented eq. (2.15) was experimentally validated ((45) (p.3), (121)) down to a few nanometers (23) using smooth contacts. The evaluation of the film thickness is a key point in lubrication. Although direct measurements remain the safest and the most accurate method, they are not always possible, whence the usefulness of equation (2.15). Three major effects are likely to lower or modify the film thickness :

- Inlet thinning.
- Inlet heating.
- Surface roughness.

In the following, the importance of these aspects are discussed through some of the published contributions.

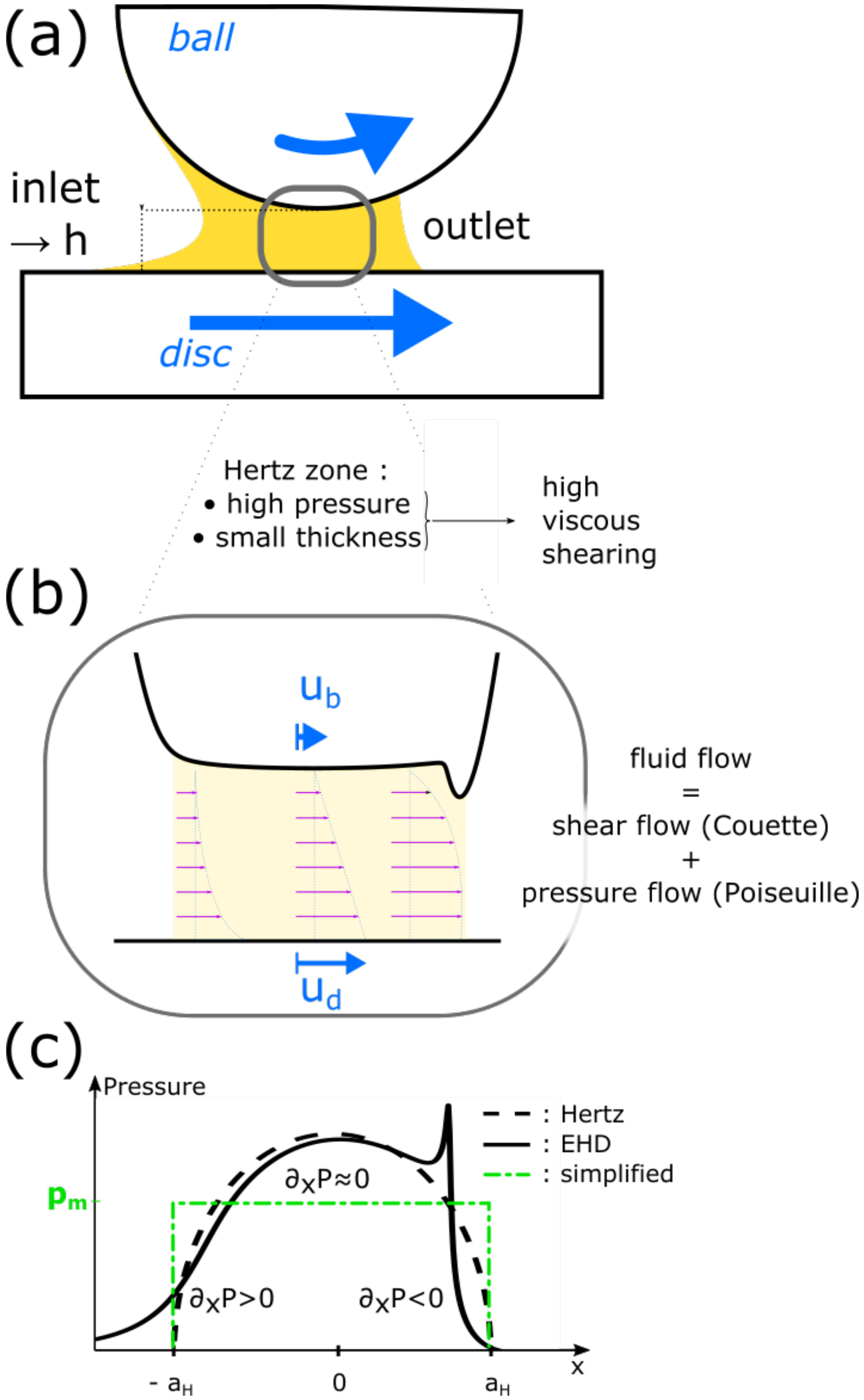

Figure 2.2: (a) : Schematic of a ball-plane contact. (b) Lubricant flow in the contact area (c). Pressure fields for a dry contact (Hertz), for an EHD contact and simplified pressure field.

2.2.3 Inlet shear-thinning

Oils and hydrocarbon derivatives generally exhibit a shear-thinning behaviour at shear rates over $10^6 - 10^7$ s^{-1} for the usual pressures in EHD contacts. The apparent inlet viscosity becomes lower than its low-shear (or Newtonian) value η_0.

In 1962, Bell (18) investigated theoretically the lubrication of an Eyring-like fluid described with a shear-thinning rheology[1]. Only considering pure rolling, he showed that shear-thinning in the inlet zone tends indeed to reduce the film thickness in comparison with the Newtonian case. Bell (18) also showed that including shear-thinning leads to a weaker influence of rolling speed and a more important one from the load than in Grubin's isothermal analysis of 1949.

In 1990 Peiran and Shizhu (103) numerically solved the modified Reynolds equation for a line contact with different rheological models : Newtonian, Eyring and viscoelastic from (71). The energy equation was solved in parallel and the Roelands thermal relationship (109) was used for the low-shear viscosity[2]. Their results showed that the film thickness and pressure distribution were little affected by the fluid shear-thinning behaviour. Furthermore, the difference with the isothermal film thickness, even combined with an Eyring rheology was negligible.

Bair (14) used a simplified (Grubin-style) approach to estimate the impact of inlet thinning on h for a viscoelastic Maxwell-like fluid. The fluid shear-thinning was described with a Carreau-like law : inlet thinning leads to a reduction of about 10 percent at SRR=0.6. Later, Bair (8) established a correction factor $\frac{h_{Non-Newtonian}}{h_{Newtonian}}$ based on 99 similar simulations at 1 GPa assuming that the shear-thinning was linked to the fluid elasticity. It was concluded that inlet shear-thinning slightly lowered the exponent of u_e in the expression of h.

Sliding-rolling experiments at $p_m = 0.5$ GPa were performed by Habchi et al. (60) with one fluid supposed to shear-thin in the inlet (squalane 15% + isoprene), and another one that presumably does not (glycerol). It was concluded that when the SRR is increased, the film thickness decrease is more importantly due to inlet heating than to inlet thinning.

The actual influence of inlet thinning remains unclear. The quantitative use of the abovementionned thickness corrective factors are demotivated by the lacking knowledge (121) of the inlet pressures and on the complex rheological properties of the fluids. Furthermore, little is known about the reverse flow in the inlet, and hence about the actual shear rates. This leads us to keep on viewing the inlet lubricant as a Newtonian fluid.

2.2.4 Lubricant film thickness vs temperature

Several studies are hereby reviewed among the literature dealing with film thickness reduction and thermal effects. Their conditions are summarized on table 2.1.

2.2.4.1 Compressive cooling-heating

Cheng (28), in 1965 solved the 1D Reynolds equation coupled with the energy equation, which reads :

$$\underbrace{\rho_l c_l\left(u_x\frac{\partial T}{\partial x}+u_z\frac{\partial T}{\partial z}\right)}_{\text{heat advection}} = \underbrace{\kappa\frac{\partial^2 T}{\partial z^2}}_{\text{conduction - z}} + \eta\underbrace{\left(\frac{\partial u_x}{\partial z}\right)^2}_{\text{shear heating}} - \underbrace{u_x\frac{T}{\rho_l}\frac{\partial \rho_l}{\partial T}\frac{\partial p}{\partial x}}_{\substack{\text{compressive}\\ \text{heating}-\text{cooling}}} \tag{2.16}$$

---

[1] see eq. (4.9).

[2] The following parameters were used : $\tau_0 = 18$ MPa, $G_e = 2 \times 10^2$ MPa, steel surfaces($E' = 230$ GPa), $\eta_0 = 0.08$ Pa.s., $\alpha \approx 21.8$ 1/GPa, $R_x = 0.05$ m, $\bar{p}_{m\,1D} \approx 400$ and 570 MPa, $u_e \approx 1.4$ m/s, SRR $\in [0\,;\,2]$.

Eq. (2.16) includes different terms. From left to right, they correspond to the temperature advection by the heated fluid in motion, the heat conduction inside the lubricant and towards the bodies, the (viscous) shear heating and finally, a compressive term. This last term refers to the local compression of the fluid as the pressure gradient is positive, in the inlet zone and at the pressure spike. After the pressure maximum, the lubricant is cooled down as its volume relaxes at the outlet sharp pressure drop. In Eq. (2.16), the first two terms correspond to heat transport while the two last correspond to heat sources.

Cheng performed numerical simulations with a Newtonian fluid at rather low pressures. His paper stresses the importance of two terms regarding temperature rise : the shear heating due to the large Poiseuille flow and the compressive heating-cooling, especially near the contact center where the pressure gradient is high (see equation 2.16). These two terms are important heat sources of the contact but barely reduce the film thickness, compared to the isothermal thickness. The friction force, however, is reduced. This means the temperature is increased in the center, where the shear stress is the most important, but that this increase may not reach the inlet.

Sadeghi and McClung (110) also investigated the effect of compressibility with a pressure-temperature law to describe the fluid density ρ_l. The material properties were those of steel and the operating mean Hertz pressures[1] lied from 0.5 GPa to 2.75 GPa. It was observed that the maximum temperature rise increases with the rolling parameter U and that the minimal film thicknesses is more sensitive to temperature rise than the mean film thickness. Results from (110) showed a small (0-10%) difference between their thermal solutions and the isothermal thicknesses formula of (40).

Pure rolling experiments were performed by Habchi et al. (60) with a mixture of squalane 15% and isoprene and with glycerol. The film thickness was thinner than those obtained for isothermal predictions and the difference, up to $\sim$ 10%, was more pronounced at large rolling speed $u_e = 5$ m/s. It was concluded that in pure rolling, the isothermal thickness can be relied on up to $u_e = 2$ m/s. In the same paper, Habchi et al. (60) measured the film thickness during traction experiments at $u_e = 0.38$ m/s and $u_e = 1.47$ m/s. For $SRR \in [0.5\ ;\ 2]$, a decrease of h of maximum 30% was observed as sliding increased. In parallel, a computational solving of the energy equation and the generalized Reynolds equation of (103) were obtained. The computed film thicknesses are compatible with such a decrease. Compressive heating-cooling affects the temperature near the Petrusevich pressure spike, in the outlet, whereas shear heating remains the dominant heating mechanism on the whole contact, including the inlet. This explains the slightly thinner film.

Reddyhoff et al. (107) measured in situ the contact temperature in pure rolling contacts with five fluids, including a PAO (see fig. 2.3.a) and solved the energy equation to calculate heat flux maps (fig. 2.3.b). The contact temperature rises at the inlet and decreases at the outlet, which agrees qualitatively with the fluid compression and relaxation in these areas. Yet, the temperature rises do not exceed 1°C and the heat generated by compression is small compared to that in sliding contacts. In addition, experiments at $SRR = 0.5$ showed no influence of sliding on the film thickness.

Recently, Habchi and Vergne (59) also concluded that shear heating is the dominant source of heating, except in pure rolling where the generated heat by compression and by shear heating may become comparable, depending on the lubricant high-pressure bulk modulus.

2.2.4.2 Viscous heating

Rolling shear heating In 1973, Greenwood and Kauzlarich (53) analyzed the stationary heat conduction through the lubricant, neglecting heat advection. The maximum temperature rise is assumed to occur at mid-height in the film and only pure rolling was considered. The Barus equation was used to evaluate the low-shear viscosity, compressibility and thermal expansion being neglected.

---

[1] $p_{m\ 1D} = \sqrt{\frac{pi\, W_{1D}}{32}}\,\frac{G}{\alpha}$

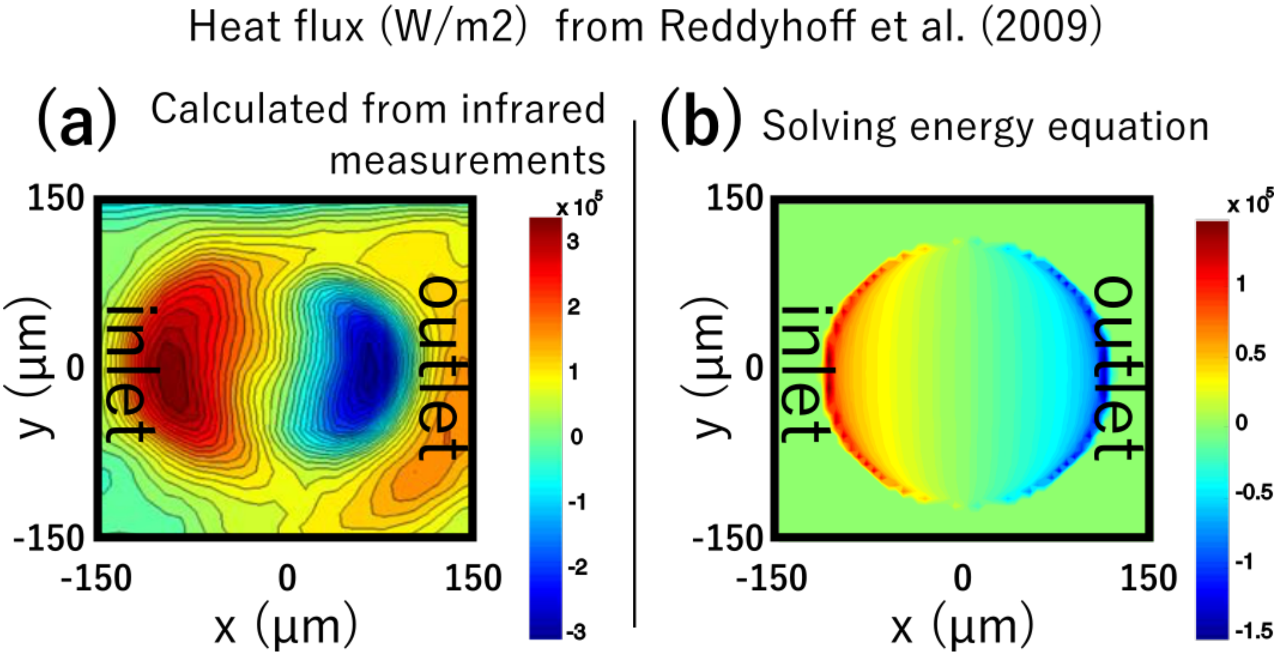

Figure 2.3: Heat flux maps from Reddyhoff et al. (107) calculated from infrared temperature measurements in pure rolling, in a sapphire/steel contact at 0.5 GPa with a PAO (a) and calculated from the energy equation using a Hertz pressure distribution (b).

In the case of a small temperature rise, their Grubin-like analysis raises the following film thickness reduction factor :

$$\frac{h_{thermal}}{h_{isothermal}} = (1 - 0.24L_h)^{3/4} \text{ for pure rolling (53)} \tag{2.17}$$

where L_h is a dimensionless parameter defined as :

$$L_h \equiv \frac{\eta_0 u_e^2}{K_{oil}} \underbrace{\left(-\frac{\partial \ln \eta_0}{\partial T} \right)}_{\equiv \beta_l} = \begin{cases} \frac{\eta_0\, u_e^2}{K_{oil}} \frac{n_{Sl}}{T+B_{Sl}} & \text{for a Slotte fluid} \\ \frac{\eta_0\, u_e^2}{K_l} \frac{B}{(T-C)^2} & \text{for a Vogel fluid} \end{cases} \tag{2.18}$$

The results of (53) confronted to experimental thickness measurements showed that rolling heating stops being negligible around a rolling speed of a meter per second :

Influence of sliding and load Recently, Guilbault (57) extended the Grubin 1D analysis led by Greenwood and Kauzlarich to add the contribution of sliding to shear heating with $\dot{\gamma} = \frac{z\,\partial_x p}{\eta} + \frac{u_s}{h}$. A quadratic temperature distribution $T(z)$ was assumed and the average temperature rise along the film thickness in the inlet was calculated :

$$\Delta T_{inlet} = \frac{L_h}{\beta_l} \left(\frac{1}{2.55} + \frac{51}{48} SRR^2 \right) \tag{2.19}$$

Wilson and Wong (138), Murch and Wilson (95) derivated a thermal Reynolds equation, assuming an exponential viscosity-temperature dependence. They transformed this differential equation into a functional one with dimensionless parameters, including in particular L_h from eq. (2.18). Following the same approach, a semi empirical correction factor was provided by Wilson and Sheu (137), including the effect of sliding. This approach was extended by Gupta et al. (58) at very high rolling speed ($u_e = 80$ m/s) and high pressure (1.2 GPa) to account for the effect of the load on the film thickness reduction, using a shear-thinning and viscoelastic rheology.

$$\frac{h_{thermal}}{h_{isoth}} = \frac{1 - 13.2 \, \frac{p_{m\,1D}}{E'} L_h^{0.42}}{1 + 0.213(1 + 2.23 \, SRR^{0.83}) L_h^{0.640}} \qquad \text{from (58)} \qquad (2.20)$$

Conry et al. (32) performed line-contact simulations with an Eyring fluid as a lubricant while solving the energy equation at high[1] pressure ($\sim 1-2$ GPa). Only shear heating and z conduction in the film thickness were considered. Their results were summarized with a thermal reduction factor[2] for the film thickness, where L_h (eq. (2.18)) plays a similar role as in eqs. (2.17) and (2.20).

Confrontation to experimental works Smeeth and Spikes (117) performed traction experiments with smooth steel balls against glass discs and measured film thicknesses within [30 ; 120] nm using interferometry (see conditions on table 2.1). During traction experiments at $u_e > 0.5$ m/s and $SRR > 1$, a film thickness decrease reaching 45% was observed. The film thickness reduction differed according to the sign of the sliding speed : this asymmetry was explained with the difference of conductivity between the two materials ($K_{glass} = 1.3$ W/(m.K), $K_{steel} = 50$ W/(m.K)). According to these experimental film thickness measurements, the inlet thermal analysis of (137) overestimates the effect of sliding on the film thickness reduction. Other measurements were made by LaFountain et al. (76), using a PAO. A reduction of only 0.001% was observed whilst the Gupta et al. factor predicted a 5% reduction.

Some experimental film thickness measurements in the range [100 ; 650] nm were also confronted to the Hamrock-Dowson solutions by Lord and Larsson (84) for 3 fluids (see table 2.1), at 3 different SRR : the isothermal thicknesses held true for SRR ≤ 0.6. The agreement between the isothermal film thickness and their measurements was roughly good (less than 25 % error) and only slightly improved using the corrective factor of (58). For higher $SRR = 1.2$, the film thickness reduced of typically 25% (w.r.t. h_{isoth}) at speeds close to 1 m/s. In that case, the (58) factors underestimated the film thickness reduction.

2.2.4.3 Literature summary on the inlet heating

In a contact, viscous heating is the dominant heating mechanism and compressive cooling-heating seems only a second order heat source. Viscous heating is always present regardless of the presence of sliding between the bodies. For moderate shear rates ($SRR < 1$), the rolling speed has a large impact on film temperatures because increasing u_e directly means increasing h, and hence increasing the heated volume. Isothermal conditions are reached when the film is thin enough to conduct all the generated heat to the bodies. When h is large, heat conduction is too slow and part of the heat is kept by the lubricant, rising its overall temperature.

From this short review, the parameter $L_h \propto \eta_0 u_e^2$ defined in eq. (2.18) seems central regarding the occurrence of inlet heating. The isothermal film thicknesses may be reliably used up to $L_h \approx 0.1$. For a given set of load and surface speeds, a significant temperature rise is more likely to occur inside the Hertz area before the temperature rise spreads towards the inlet. This explains why most lubricants can be considered Newtonian and isothermal in the inlet zone (121), even when the friction force exhibits heating in the high pressure zone.

---

[1] $20 < \alpha \times p_{Hertz\,max} < 30$.

[2] (32) calculations were validated for $20 < \alpha p_{Hertz\,max} < 30$.

Author	lubricant $\{\eta_0;\alpha\}$ (Pa.s), (1/GPa)	materials	speeds - h	p_m (GPa)	results and miscellaneous
Cheng (28)	{0.124; 40}, {0.04; 16}	E′ =133, 232 GPa	$u_e \in [2 ; 20]$ m/s, SRR $\in [0.005 ; 0.4]$	0.018, 0.040	h ≈ h_{isoth}, $\Delta T_{inlet} \in [0 ; 10]^{\circ}$C
Sadeghi and McClung (108)	{0.040 ; 15.9}	$3\times10^3 < G < 5\times10^3$	$U \in [3 ; 11] \times 10^{-11}$, SRR ≤ 0.2	[0.5 ; 2.75]	small reduction (0-10%) in hmin
Gupta et al. (58)	MIL-L-7808	ø	u_e = 80 m/s	1.2	simulations, thermal reduction factor h/h_{isoth}
Smeeth and Spikes (117)	{0.025; 15}, {0.032; 28}	steel / glass	$u_e \in [10^{-2} ; 3]$ m/s, SRR$\in$[0; 2]	0.52	decrease in h : ≤ 20% - Reduction in h overestimated by (24) factor.
LaFountain et al. (76)	{ [10−3; 10] ; [13.5 ; 23.5] }	steel / glass	$u_e \in [10^{-3} ; 100]$ m/s	[0.3 ; 0.9]	6 PAOs tested, small reduction in h, overestimated by (24) results
Lord and Larsson (84)	{0.056, 19} ; {0.05, 16} {0.154 , 31 }	ø	h $\in$ [100 ; 650] nm, SRR=0, 0.6 and 1.2	0.46	SRR ≤ 0.6: h ≈ h_{isoth} ; SRR=1.2: h < (24) h_{isoth} factor.
Habchi et al. (60)	squalane 15% + isoprene and glycerol	steel / glass	{SRR ; u_e} : { 0 ; 5 m/s}, {[0.5; 2];0.38, 1.47 m/s}	0.5	h/h_{isoth} down to 10% and 30%
Reddyhoff et al. (107)	{0.027; 30} ; {0.33 ; 52} ; {0.026 ; 25} ; {0.016 ; 19} ; {0.025 ; 18}	steel / sapphire	$u_e \in [10^{-2} ; 3]$, SRR = 0 and 0.5	0.5	SRR = 0 : $\Delta T(x,y)$ small, agrees with fluid compression-relaxation. $h(SRR=0.5) \approx h(SRR=0)$

Table 2.1: Operating conditions in the computational and experimental works reviewed in this work.

2.3 Theoretical approaches to determine the role played by roughness

To account for the effect of roughness on a contact film-forming capability, the Λ ratio is classically defined as :

$$\Lambda \equiv \frac{h_0}{\sigma_c} \tag{2.21}$$

, where $\sigma_c \equiv \sqrt{\sigma_1^2 + \sigma_2^2}$ is the two-solid composite roughness and h_0 is the nominal film thickness, i.e. the thickness that would be allowed if surfaces were perfectly smooth. At $\Lambda >> 1$, the roughness does not affect the film thickness. It is generally accepted that when Λ becomes close to 1, the real film thickness becomes significantly affected by roughness and metal-metal contacts start occurring, leading to ML and eventually to BL (see fig. 2.1). The common trend is to consider that the first asperity contacts occur at $\Lambda = 3$ (119). However, the friction rise associated with the onset of ML is not systematically associated to any well-defined value for Λ. For instance, (10) observed a friction mechnism only due to the lubricant shear properties down to $\Lambda \approx 2$, (23) reported that pure EHD conditions may hold down to $\Lambda = 0.5$ and (47) measured that the surface roughness start interacting at $\Lambda < 6$. The lambda ratio does not provide a sufficient understanding of what really happens in the contact when the surfaces start interacting because rough surfaces generally perturbate intrinsically the film thickness (23). Moreover, the roughness amplitude may differ inside the contact area (119) compared to the ex situ roughness because of elastic deformation of solids or local wear.

Several theoretical studies proposed ways to incorporate the presence of roughness on the solids in order to predict its effect on the film thickness and friction. Some focused on the role of roughness with respect to the fluid flow. Others considered the way asperities perturbate the pressure field and deform once they reached the central area.

2.3.1 Approaches including the effect of roughness on the lubricant flow

In 1969, a stochastic modelling of surface roughness was proposed by Christensen (30) :

$$h \equiv h_0 + r \tag{2.22}$$

, where r is a random variable descriptive of the surface roughness height and h_0 is the film thickness obtained with smooth surfaces. Taking the expectation value (denoted by $< \cdot >$) of the Reynolds equation (eq. (2.2)) and assuming longitudinal roughnesses, he obtained :

$$\frac{\partial}{\partial x}\left(< h^3 > \frac{\partial < p >}{\partial x}\right) + \frac{\partial}{\partial y}\left(\frac{1}{\frac{1}{<h^3>}} \frac{\partial < p >}{\partial y}\right) = 12\, u_e\, \eta\, \frac{\partial < h >}{\partial x} \tag{2.23}$$

Results were obtained using a polynomial bell-shaped probability density for r and assuming a constant viscosity and the independence of h with the pressure gradients. Longitudinal roughness[1] reduces the film thickness while transverse one increases the film thickness. The conclusions of this model have to be cautiously considered because of the numerous hypotheses made by the author.

Another stochastic approach was made by Patir and Cheng (102), who introduced the concept of flow factors to quantify the effect of roughness on the fluid flow. It consisted in generating a given roughness and balancing the fluid flow between two solids inside a small control volume. A given pressure gradient (or a given shear rate) was then imposed on this volume and the local flow was numerically averaged over the control volume. The averaged flow forms were imposed as:

---

[1] Relative to the lubricant flow direction

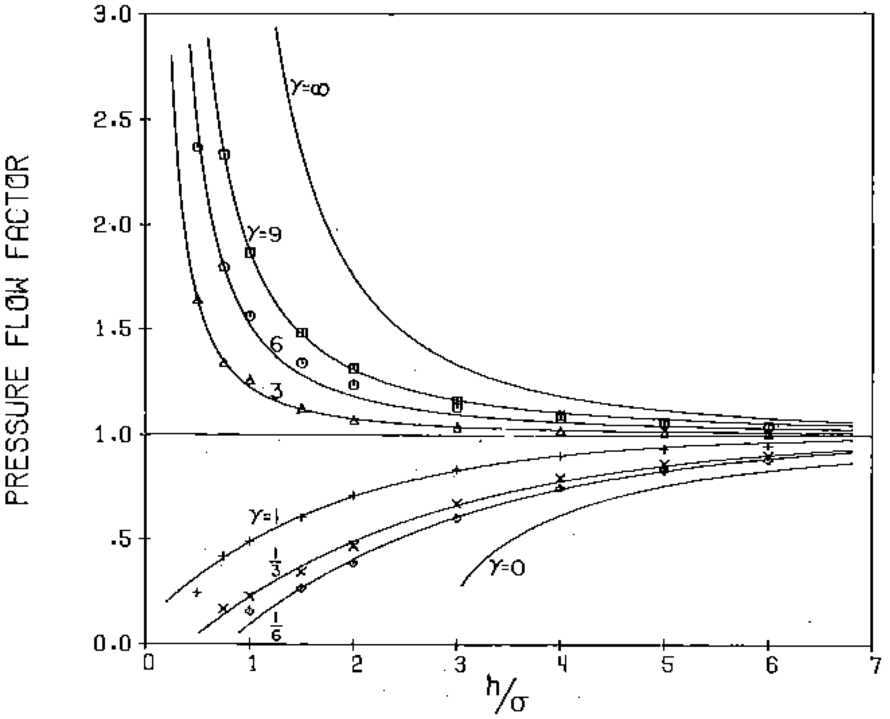

Figure 2.4: From (102) : Pressure flow factors Φ_x plotted versus the lambda ratio $\frac{h}{\sigma}$ for different surface anisotropies $\gamma \equiv \frac{S_{al\,0.5\,x}}{S_{al\,0.5\,y}}$.

$$< q_x > = -\frac{h_0^3 \partial_x < p >}{12\eta}\Phi_x + \frac{u_1 + u_2}{2} < h > + \frac{u_1 - u_2}{2}\sigma_c \cdot \Phi_s \tag{2.24}$$

$$< q_y > = -\frac{h_0^3 \partial_y < p >}{12\eta}\Phi_y \tag{2.25}$$

, where Φ_x, Φ_y are the so-called pressure flow factors, Φ_s is the shear-flow factor and σ_c is the surface composite roughness. This form was chosen to impose the homogeneity with the flow calculated without the presence of roughness (i.e. with $\Phi_x = \Phi_y = 1$ and $\Phi_s = 0$). The flow factors contain the effect of the input roughness on the lubricant flow. They change the weight of lubricant flow in the Reynolds equation, which turns into :

$$\partial_x \left(\Phi_x \frac{h_0^3 \partial_x < P >}{12\eta} \right) + \partial_y \left(\Phi_y \frac{h_0^3 \partial_y < P >}{12\eta} \right) = \frac{(U_1 + U_2)\partial_x < h >}{2} + \frac{U_1 - U_2}{2}\sigma_c \cdot \partial_x \Phi_s + \partial_t < h > \tag{2.26}$$

Eq. (2.26) was then solved to evaluate the effect of roughness on the film thickness. Patir and Cheng tested isotropic and anisotropic roughness. The surface anisotropy was accounted for with $\gamma = \frac{S_{al\,0.5\,x}}{S_{al\,0.5\,y}}$, where x is the rolling direction and $S_{al\,0.5\,x}$ is the rough surface autocorrelation length along the rolling direction. The results showed that transverse roughness ($\gamma < 1$) weakens the Poiseuille term while longitudinal one ($\gamma > 1$) increases the film thickness compared to the smooth case (see figure 2.4).

The flow factor approach was extensively applied in computational studies under various conditions. It was successful in quantifying local inertial (35) or micro-cavitation (64) effects. However, this approach does not account for the roughness in situ deformation, which makes it more suited for large lambda ratios. Furthermore, this approach requires considerable computational efforts (calculation of pressure factors and solving the averaged Reynolds equation) and showed sensitivity to the chosen boundary conditions (132) in the numerical scheme.

2.3.2 Roughness deformation into the contact

Lubrecht et al. ((87), (130), (86), (131), (27), (133)) performed multi-grid simulations involving an ideally smooth surface against another textured with sine waves of wavelength λ, either transverse or longitudinal (Lubrecht et al. (87), Venner and Lubrecht (130)) and with two-dimensional ones ((131), anisotropic, (27), isotropic). The authors accounted for the lubricant pressure-dependent density, through a relationship $p \mapsto \rho_l(p)$ presented in (42) and solved the Reynolds equation. The amplitude relative deformation[1] is proportional to the texture wavelength λ and falls within a master curve of the form :

$$\frac{A_d}{A_i} = \frac{1}{1 + a\,\nabla + b\,\nabla^2}, \tag{2.27}$$

In pure rolling, $a = 0.15$, $b = 0.015$ and $\nabla \equiv \frac{\lambda M^{1/2}}{a_H L^{1/2}}$ according to Venner and Lubrecht (130), where $M \equiv \frac{F_n}{E'\,R_x^2}\left(\frac{E'\,R_x}{2\,\eta_0\,u_e}\right)^{3/4}$ and $L \equiv \alpha\,E'\left(\frac{2\,\eta_0\,u_e}{E'\,R_x}\right)^{1/4}$ are the load and material parameters used in Nijenbanning et al. (98). The influence of sliding was introduced through a modified nabla parameter $\nabla \to \widetilde{\nabla} \equiv \nabla\sqrt{2u_2/(u_1 + u_2)}$, which resulted in $a = 0.125$, $b = 0.04$. Chapkov et al. (27) performed a similar study and showed that surface deformation is greater in sliding-rolling than in pure-rolling. Taking a shear-thinning rheology (Eyring type) lowers the influence of sliding on the roughness deformation. If a surface is considered as a finite sum of sine waves, the *in-situ* surface deformation might be calculated using eq. (2.27) provided wave deformations are independent. To the best of our knowledge, no experimental work has applied these calculations to real-life random roughness.

2.3.3 Mixed bearing models for rough surfaces

Greenwood and Williamson dry contact model In 1966, Greenwood and J.B.P. (55) introduced a dry-contact model for rough surfaces based on the concept of asperity (i.e. local surface maxima). The authors considered a perfectly smooth surface against a rough one as represented fig. 2.5.a. The asperities of this surface were assumed to be uniformly distributed with a surface density n_a, with the same curvature radius β. Their heights were governed by a given probability density function $z_a \mapsto \phi(z_a)$. At a given nominal distance d_e between the smooth surface and the asperity mean height, only the asperities having a height $z_a > d_e$ were in contact with the counter surface. It was considered that such an asperity will deform elastically of $z_a - d_e$ according to the Hertz theory, forming a local contact spot of area $\pi(z_a - d_e)\beta$. The real contact area can then be calculated according to the ensemble-averaged occurence of asperity contacts :

$$A_{real} = A_{nom} \times \pi\beta\,n_a \int_{d_e}^{\infty} dz_a\;\phi(z_a)\,(z_a - d_e) \tag{2.28}$$

, where A_{nom} is the nominal contact area. The real load borne by the asperities at a separation d_e can also be calculated by taking the expectation value of the Hertz load-deformation relationship :

---

[1] Defined as $A_d \equiv \frac{1}{2}(\underset{t}{max} H(X=0,t) - \underset{t}{min} H(X=0,t))$.

$$F_{n\,a}(d_e) = A_{nom} \times \frac{2}{3}\, n_a\, E'\, \beta^{1/2} \int_{d_e}^{\infty} dz_a\; \phi(z_a)\, (z_a - d_e)^{3/2} \tag{2.29}$$

$$\frac{F_{n\,a}}{A_{nom}} = \frac{2}{3}\, n_a\, E'\, \beta^{1/2} \int_{d_e}^{\infty} dz_a\;\, (z_a - d_e)^{3/2}\, \phi(z_a) \tag{2.30}$$

From an experimental viewpoint, the asperities are defined as peaks, i.e. ordinates higher than their two closest neighbours on a profile. According to the peak probability density ϕ, the real contact area and the real mean pressure on the asperities may be calculated versus the nominal distance d_e between the surfaces. Using an exponential and a Gaussian asperity height distribution (in eq. (2.30)), the authors found respectively perfect and almost exact proportionality between the load and the real contact area. As it could explain the proportionality between the load and the friction force, stated by Amontons' law, the Greenwood-Williamson model benefitted from numerous refinements to account for the ellipticity of asperities (20), plasticity (55), (88) or the inclusion of interaction between the deformed asperities (31).

Mixed lubrication model Johnson et al. (72) modelled the mixed lubrication in 1D between a smooth and a rough surface. At film thicknesses h larger than the roughness σ, the load is fully borne by hydrodynamic action. As h is reduced, there comes a time where the highest asperities contact the smooth surface and part of the load becomes borne by theses asperities according to the Greenwood-Williamson model. The load thens splits into a hydrodynamic and an asperity components :

$$F_n = F_{n\,a} + F_{n\,H} \tag{2.31}$$

These two types of bearing were considered as two —non-linear— springs in parallel, where the spring extent was analogous to the surface separation. Denoting $p \equiv \frac{F_n}{A_{nom}}$ the total pressure, responsible for the bodies deformation, and $p_f \equiv \frac{F_{n\,H}}{A_{nom}}$ the pressure generated by the hydrodynamic bearing, a situation where $p_f = \frac{p}{k}$ was considered, where k is a constant superior to 1, defined as $k \equiv \frac{F_n}{F_{n\,H}}$.

The authors first used the modelling of (30) with transverse and longitudinal roughness assuming $\sigma_c << h$ and showed that the effect of roughness in the inlet can be neglected. They argued that the asperities only affect the pressure field once they reach the high pressure area, while the EHD pressure field is mostly determined in the inlet. To calculate the film thickness, the authors wrote the classical bodies elastic deformation for a line contact :

$$h(x) = h_0 + \frac{x^2}{2R} - \frac{2\,k}{\pi E'} \int_{-\infty}^{\infty} du\, p_f(u)\, ln\left[\left(\frac{x-u}{u}\right)^2\right] \tag{2.32}$$

To calculate the fluid pressure field, it is necessary to solve at once eq. (2.32) and the load balance equation :

$$F_n = \int_{-\infty}^{\infty} dx\, p(x) \Leftrightarrow \frac{F_n}{k} = \int_{-\infty}^{\infty} dx\, p_f(x) \tag{2.33}$$

Equations (2.32) and (2.33) are the classical EHD equations where the load and the reduced elastic modulus were replaced with $\frac{F_n}{k}$ and $\frac{E'}{k}$ respectively. To obtain the real film thickness h, it is thus sufficient to use the smooth film thickness solutions given by Dowson et al. (41) with these two replacements. This yields :

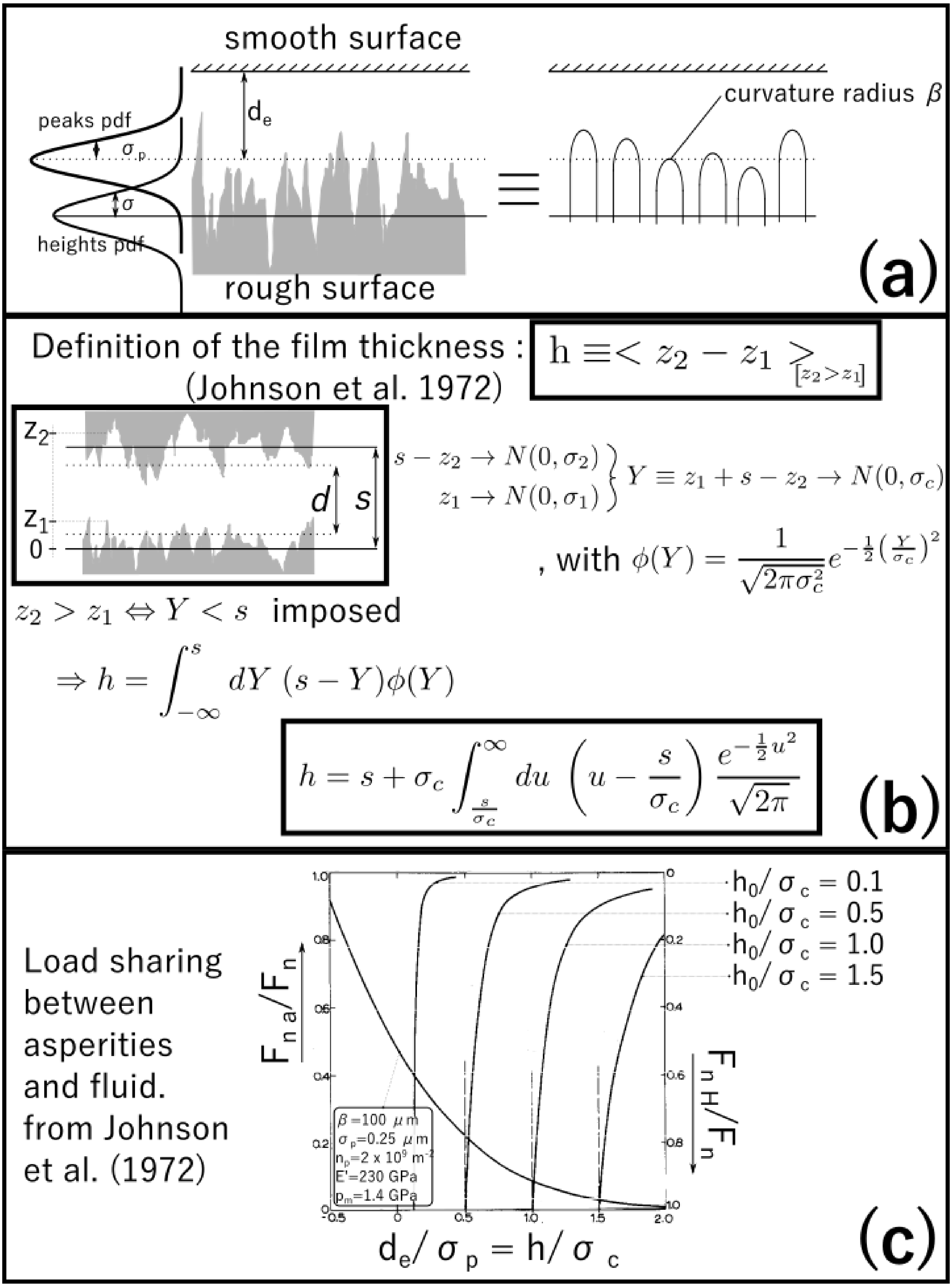

Figure 2.5: (a) Greenwood-Williamson rough surface modelling. (b) Definition of the film thickness by (72). $X \rightarrow N(\mu, \sigma)$ means that the random variable X follows a normal distribution with mean μ and standard deviation σ.

$$h = h_0 \times k^{0.16} \tag{2.34}$$

$$\text{i.e. } \frac{p_f}{p} = \left(\frac{h_0}{h}\right)^{6.3} = \left(\frac{\sigma_c}{h} \times \frac{h_0}{\sigma_c}\right)^{6.3} \tag{2.35}$$

, where h_0 is the nominally smooth film thickness, evaluated using F_n and E'.

To calculate a priori the fraction of the load borne by the fluid, it is necessary to know the film thickness h. The authors define it as the separation between the two surfaces, weighted by both surface height statistics, assumed Gaussian (see details on fig. 2.5.b). This allows to relate h to the ratio of the distance s between the surfaces' reference planes over the surfaces composite RMS roughness :

$$\frac{h}{\sigma_c} = \frac{s}{\sigma_c} + \int_{s/\sigma_c}^{\infty} du \left(u - \frac{s}{\sigma_c}\right) \frac{e^{-\frac{1}{2}u^2}}{\sqrt{2\pi}} \tag{2.36}$$

In order to express the asperity and the hydrodynamic "pressures" (equations (2.30) and (2.35) respectively) with the same parameter, the authors use several approximations and obtain a relationship[1] between $\frac{d_e}{\sigma_p}$ and $\frac{s}{\sigma_c}$. Inverting the function $\frac{s}{\sigma_c} \mapsto \frac{h}{\sigma_c}$ (eq. (2.36)) would allow to express $\frac{d_e}{\sigma_p}$ directly as a function of $\frac{h}{\sigma_c}$. Instead, the authors simplified this relationship taking :

$$\frac{d_e}{\sigma_p} \approx \frac{h}{\sigma_c} \tag{2.37}$$

Finally, the equilibrium film thickness is the value of h satisfying the load sharing equation (eq. (2.31)), i.e. at the intersection between the asperity pressure curve and one of the fluid pressure curves reproduced figure 2.5.c from (72), for different lambda ratios.

Equation (2.34) shows that h is only slightly increased compared to the nominal film thickness. The fluid bearing stiffness increases as h is reduced : $\partial_h p_f \propto h^{-7.3}$ (see eq. 2.35), which makes the film thickness quite insensitive to a small increase in asperity loading. The authors stress the importance of the parameter $\frac{h}{\sigma_c}$ with regard to the amount of load borne by asperities (eq. (2.37) and eq. (2.30)). This parameter is close to the lambda ratio since $h \approx h_0$.

Once the asperity and hydrodynamic pressures are known, the same approach may be applied to calculate the friction force in a mixed lubricated contact. Gelinck and Schipper (51), Liu (82), Faraon and Schipper (49) thus obtained Stribeck curve calculations from EHL to BL, in the case of a line contact. To do so, the asperity friction was described with a dry Coulomb law (solid-solid friction coefficient COF_a) and the hydrodynamic friction was introduced with a shear and pressure-dependent rheological law[2], namely :

$$F_f = COF_a \times F_{n\,a} + \int\int_{A_{nom}} dx\, dy\, \tau_{fluid}(p_f(x,y), \dot{\gamma}(x,y)) \tag{2.38}$$

In 2015, (91) extended the approach led by Patir and Cheng, using the flow-factors obtained in the case of a Gaussian height probability density :

$$\Phi_x = \Phi_y = 1 - 0.9 \times e^{-0.56\frac{h}{\sigma}} \tag{2.39}$$

---

[1] $\frac{d_e}{\sigma_p} = 1.4\frac{s}{\sigma_c} - 0.9$

[2] With an Eyring rheology

For the simulations of an elliptical contact, the load was also separated into a hydrodynamic bearing and an asperity bearing. An asperity contact model, referred to as the ZMC model (88) was used to compute the load borne by the asperities : the asperity interaction were alike that proposed by G-W, though plastic deformation were allowed. In particular, this micro-contact model yielded larger micro-contact areas than the GW model. (91) performed simulations with a rough surface for lambda ratios in the range $\frac{h_0}{\sigma_c} \in [0.5\ ;\ 1.3]$. Defining the film thickness as the separation between the two surface mean summit planes, the authors obtained the following equation :

$$\frac{h}{h_0} = 1 + 0.025\,\sigma_c^{1.248}\,(\eta_0 u_e)^{-0.884}\,\alpha^{-0.977}\,H_v^{0.119}\,R_x^{-0.098}\,E'^{-0.079} \tag{2.40}$$

, where H_v is the Vickers hardness, to be expressed in Pa. The authors found that asperties start bearing the load when $\frac{h}{\sigma} < 1.7$.

2.3.4 Experimental works conducted with random roughness

Bair and Winer (10) performed sliding-rolling experiments at high pressure ($p_m > 1$ GPa) using different fluids, a sapphire disc and a steel roller. Two RMS composite roughnesses were used : $\sigma_c = 0.05\ \mu$m and $\sigma_c = 0.12\ \mu$m. These experiments were plotted using the *reduced traction coefficient*, COF_r, versus the lambda ratio $\frac{h_0}{\sigma_c}$, where h_0 is the calculated, smooth-film thickness (see fig. 2.6). COF_r is the Couette shear stress divided by the lubricant limiting strength at the same pressure and temperature. For lambda ratios roughly inferior to 1, COF_r diverges. This was interpreted as the onset of mixed lubrication, with the load being increasingly borne by the asperities instead of the lubricant film. The observed friction rise was attributed to asperity friction. At lambda ratios superior to 20, COF_r decreases below 1. This was attributed to the pressure spreading beyond the Hertz area, as it was observed by (39) in Reynolds equation solutions for large film thickness.

In 1987, Evans and Johnson (47) studied the traction behaviour of several lubricants comparing the results with rather smooth contacts ($R_q = 0.018\ \mu$m) and with rougher contacts ($R_q = 0.57,\ 0.7,\ 1.27,\ 1.34\ \mu$m). The results obtained with smooth contacts lead to the phenomenological building of four sub-regimes of EHL governed by the lubricant bulk pressure: Newtonian, non linear viscous (Eyring-type), viscoelastic and elastic plastic. Rough surface tractions were operated at lambda ratios between 1 and 6 (against 33 for smooth traction experiments). As lambda is decreased, the traction behaviour is progressively shifted from a low-pressure behaviour to a high-pressure one (see fig. 2.7). Due to the lubricant piezoviscous behaviour HVI 650 presented here, the traction is dominated by the locally over-pressurized asperity contact areas.

This interpretation was consistent with asperity pressures calculated for a very rough surface ($R_q = 1.27\ \mu$m) according to a Greenwood-Williamson-like approach, based on a Hertz modelling of peak deformation. However, the input peak curvatures were calculated from profilometer samples, digitized using a method due to Greenwood (not found in the literature). It was stated that the estimation of peaks properties is not self-evident. Indeed, the mean peak curvature β and their standard height deviation $\sqrt{<(z_p - <z_p>)^2>}$ depend on the profile filtering, its cut-off length, the sampling interval and other subtleties of the software used (45, p.107).

A consequent experimental work regarding the effect of surface roughness in EHL was provided by Schipper (113). The author performed Stribeck experiments covering BL, ML and EHL and plotted the friction coefficient versus the so-called Lubrication number (114) $L' \equiv \frac{2\,\eta_0\,u_e}{p_m\,R_{a\,c}}$, with $R_{a\,c} \equiv \sqrt{R_{a1}^2 + R_{a2}^2}$ being the composite centre line average roughness, obtained on profilometer measurements with a cut-off length equal to 0.8 mm.

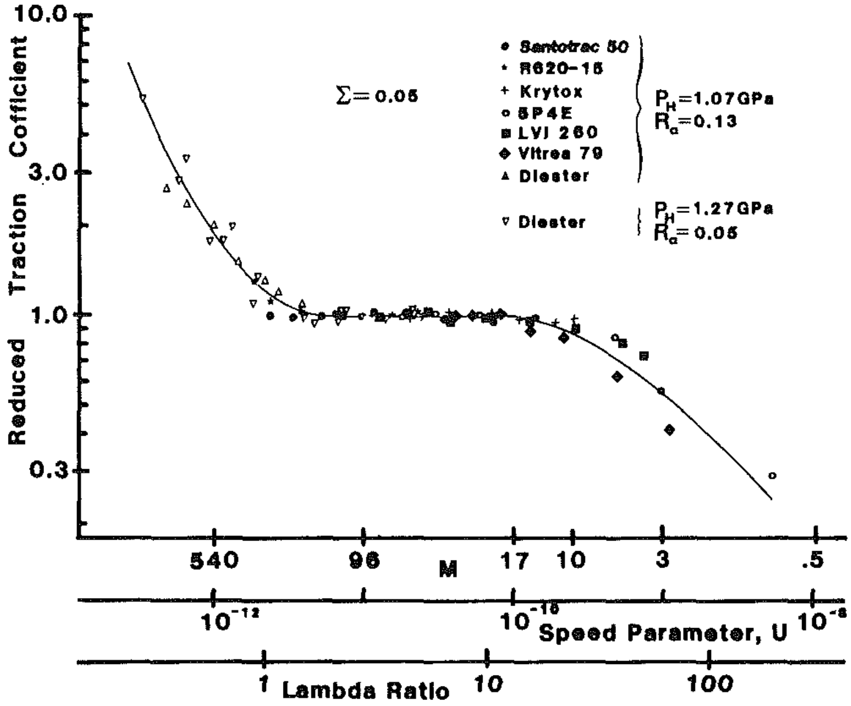

Figure 2.6: Reduced traction coefficient from Bair and Winer (10) corresponding to sliding-rolling experiments with two types of rough contacts : R_q = 0.13 μm and 0.05 μm using a cut-off length equal to the Hertz diameter.

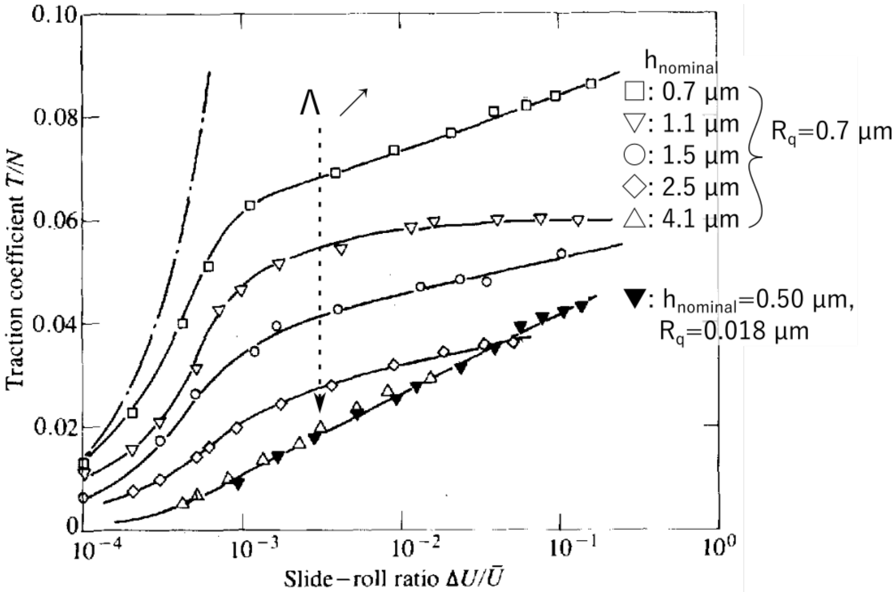

Figure 2.7: Traction experiments from Evans and Johnson (46) (fig. 5 in original reference) obtained at different rolling speeds for HVI 650 with a smooth steel-steel contact at Λ = 33 (filled triangles), and a rougher one at different rolling speeds (empty symbols) corresponding to Λ = 5.8, 3.6, 2.2, 1.6, 1.0 from bottom to top.

The determination of the entrainment speed at the ML-EHL transition and at the BL-ML transition as well, was based on the slope rupture between these regimes as shown fig. 2.8.a. The entrainment speed required to reach EHL increases with the surface roughness. Quantitatively, Schipper showed that the transition between ML and EHL responds to : $\eta_0\, u_e^{ML-EHL} = 1.55 \times 10^4\, p_m^{0.5}\, R_{a\,c}^{1.5}$ for roughness between 0.01 μm and 1 μm (see fig. 2.8.b). This result was obtained thanks to Stribeck experiments at mean Hertz pressures around 0.7-0.8 GPa and 0.1-0.2 GPa.

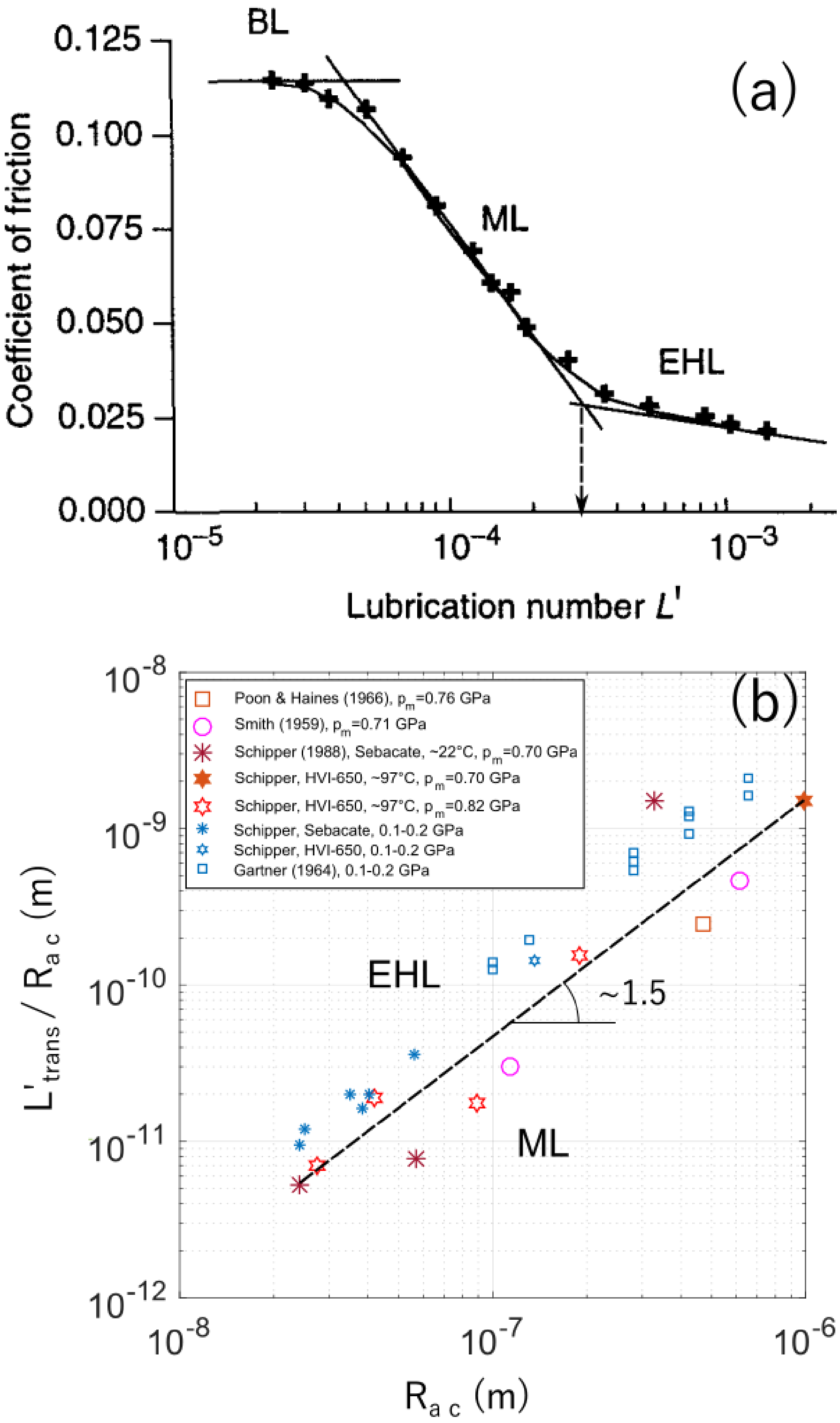

Figure 2.8: Phenomenological determination of the lubrication regimes on a Stribeck curve reproduced from Schipper and De Gee (114). L'≡ $\frac{\eta_0\, u_e}{p_m\, R_{at}}$. (b) : ML-EHL transition versus the composite center line average roughness from Schipper (113).

As stated earlier, the common description of the roughness influence on the transition from EHL to ML consists in a threshold lambda ratio Λ^{ML-EHL} under which the asperities start interacting (122).

$$\Lambda \leq \Lambda^{ML-EHL} \equiv \frac{h_c^{ML-EHL}}{\sigma_c} \Rightarrow \text{ML-onset} \tag{2.41}$$

with $h_c^{ML-EHL} \propto \left((\eta_0\, u_e)^{ML-EHL}\right)^{0.67} p_m^{-0.201}$. During a Stribeck procedure, when the entrainment product $(\eta_0\, u_e)$ is smaller than $(\eta_0\, u_e)^{ML-EHL}$, ML is reached. If the threshold Λ_{ML-EHL} does not depend upon the surfaces RMS roughness σ_c, then :

$$\begin{aligned}
&\Lambda \leq \Lambda^{ML-EHL} \\
&\Leftrightarrow \frac{C \cdot (\eta_0 u_e)^{2/3} p_m^{-1/5}}{\sigma_c} \leq \Lambda^{ML-EHL} \\
&\Leftrightarrow \eta_0 u_e \leq \left(\frac{\Lambda^{ML-EHL} p_m^{+1/5} \sigma_c}{C}\right)^{3/2} \\
&\Leftrightarrow \eta_0 u_e \leq \left(\frac{\Lambda^{ML-EHL}}{C}\right)^{1.5} p_m^{0.3}\, \sigma_c^{1.5} \propto \sigma_c^{1.5}
\end{aligned} \tag{2.42}$$

, with $C = K_2 \cdot R_x^{0.33} \alpha^{0.53} E'^{0.061}$. This transition entrainment speed scaling w.r.t. composite surface roughness and pressure is close to that obtained by Schipper.

2.4 Issues in describing realistic roughness

The above-mentioned rough contact models allow to account for the presence of roughness in lubricated contacts with the following set of roughness inputs :

- the height standard deviation R_q, S_q and the height centre-line average R_a, S_a
- the surface autocorrelation length S_{al}
- the number of asperities per unit area n_a
- the surface height and asperity height mean levels $< z >$, $< z_a >$
- the summit height standard deviation σ_s
- their local curvature β

Real surfaces have widely different textures and the evaluation of these parameters on a sampled topographical survey may not be straightforward. In particular the definition of an asperity and the influence of the sampling interval on these parameters are problematic.

2.4.1 Probabilistic descriptions and their input quantities

The noisy texture of real-life surfaces has led theoreticians and surface metrologists to consider roughness as a random noise described with a probability density function $z \mapsto pdf(z)$. The spatial statistics of a random variable are contained in its power spectrum, or equivalently, in its autocorrelation function (ACF). The ACF equals 1 in $x = 0$ and decreases to 0 when $x >> S_{al}$. Its specific definition may vary according to the ACF mathematical form (exponential, rational function, ...) and to other specifics[1] but it generally describes the distance over which the signal has lost its spatial

---

[1] The definition of S_{al} has to be chosen for a given rate memory loss $s \in [0\ ;\ 1]$ such that $ACF(S_{al\ s}) = s$.

memory : height bins separated by a distance $x < S_{al}$ are correlated whereas they become decorrelated when $x >> S_{al}$, which means the probability for these bins to be equally high is close to zero.

Since surfaces are always measured with a finite sampling interval dx, there may exist a certain correlation degree between two successive neighbours if $dx < S_{al}$. The random field theory was applied to surface roughness and the influence of the sampling interval on surface height properties was investigated through the informations contained in the autocorrelation function.

Whitehouse and Archard (136) considered the case of an isotropic surface having a Gaussian height distribution $z \mapsto \frac{1}{\sigma\sqrt{2\pi}} e^{-\frac{1}{2}\left(\frac{z}{\sigma}\right)^2}$ and an exponential autocorrelation function $x \mapsto e^{-\frac{x}{S_{al}e^{-1}}}$. For the experimenter, a peak was defined on a profile as a bin higher than its two surrounding neighbours. Based on the joint probability function of three successive bins on a profile, the number of peaks per unit length and probability density functions were derived from the peak heights, their slope and their curvature defined using finite difference estimators :

$$m(x) \equiv \frac{\partial z}{\partial x}(x) \approx \frac{z(x+dx) - z(x)}{dx} \tag{2.43}$$

$$\kappa(x) \equiv \frac{\partial^2 z}{\partial x^2}(x) \approx \frac{2z(x) - z(x+dx) - z(x-dx)}{dx^2} \tag{2.44}$$

These quantities depend on the sampling interval dx through the correlation $\rho_1 \equiv ACF(dx)$ between two successive height bins : for dx between 0.5 μm and 15 μm, ρ_1 goes from 0.96 to 0.1, according to profile measurements performed with different sampling intervals. The following results were derived by (136), where $z(x_0)$ denotes a peak and σ denotes the height standard deviation :

$$n_{p1D} \equiv \frac{\text{number of peaks}}{\text{profile length}} = \frac{1}{\pi\, dx} atan\left(\sqrt{\frac{3-\rho_1}{1+\rho_1}}\right) \tag{2.45}$$

$$z_p \equiv \left\langle z(x_0) \right\rangle = \frac{\sigma}{2\, dx\, n_{p1D}} \left(\frac{1-\rho_1}{\pi}\right) \tag{2.46}$$

$$\sigma_p^2 \equiv < (z(x_0) - z_p)^2 > = \sigma^2 \left(1 - \frac{\sqrt{1+\rho_1}}{2\, dx\, n_{p1D}\, \pi\, tan^2(\pi\, dx\, n_{p1D})} - \frac{1-\rho_1}{4\,\pi\,(dx\, n_{p1D})^2}\right) \tag{2.47}$$

$$\kappa_p \equiv \left\langle \frac{2z(x_0) - z(x_0 - dx) - z(x_0 + dx)}{dx^2} \right\rangle = \frac{\sigma(3-\rho_1)\sqrt{1-\rho_1}}{2\, dx^3\, n_{p1D}\, \sqrt{\pi}} \tag{2.48}$$

Those quantities were confronted to a series of profilometer measurements (referred to as "Aachen 64-13") and showed good agreement down to $dx = 2$ μm. At smaller sampling intervals, these predictions failed especially for the number of peaks per unit length n_{p1D} ($n_{p1D} \approx 0.3/dx$ yielded by the theory whereas experiments yielded about $0.1/dx$ for $dx = 0.5$ μm). Part of this may be explained by the implicit low-pass filter imposed with a profilometer tip radius of the same order of magnitude as dx.

Nayak (97) and later Greenwood (52) and Greenwood and Wu (56), stressed the necessity not to confuse local maxima on a profile and on a 3-D survey, arguing that *a profile will more often than not pass over the shoulder of an asperity on a surface instead of its summit.* He considered the following surface properties : z, $\partial_x z$, $\partial_y z$, $\partial_x^2 z$, $\partial_y^2 z$, $\partial_x \partial_y z$, assuming that they arose from cumulative and independent events. This allowed him to calculate joint probability densities for these properties according to the central limit theorem. Summits were then defined as 3D-local maxima (9-point definition) and their statistical properties were derivated. This work showed that only three parameters allow to describe all surface properties :

$$\text{the profile variance : } \sigma^2 =< (z- < z >)^2 > \tag{2.49}$$
$$\text{the profile slope variance : } \sigma_{mx}^2 =< (m- < m >)^2 > \tag{2.50}$$
$$\text{the profile curvature variance : } \sigma_{\kappa x}^2 =< (\kappa- < \kappa >)^2 > \tag{2.51}$$

, where the brackets mean ensemble averaging over all ordinates, and the surface is assumed isotropic. These parameters have to be estimated experimentally to apply Nayak's theory. With these, the following results were derived :

$$n_{p1D} = \frac{1}{2\pi}\frac{\sigma_{\kappa x}}{\sigma_{mx}} \tag{2.52}$$
$$n_s \equiv \frac{\text{number of summits}}{\text{sampling area}} = \frac{1}{6\pi\sqrt{3}}\frac{\sigma_{\kappa x}^2}{\sigma_{mx}^2} \approx 1.2 n_{p1D}^2 \tag{2.53}$$
$$z_s \equiv< z(x_0, y_0) >= \frac{4}{\sqrt{\pi}}\frac{\sigma_{mx}^2}{\sigma_{\kappa x}} \tag{2.54}$$
$$\sigma_s^2 \equiv< (z(x_0, y_0) - z_s)^2 >= \sigma^2 \left(1 - 0.8468\frac{\sigma_{mx}^4}{\sigma^2\sigma_{\kappa x}^2}\right) \tag{2.55}$$
$$\kappa_m \equiv \Big\langle -\frac{1}{2}\left(\frac{\partial^2 z}{\partial x^2}(x_0, y_0) + \frac{\partial^2 z}{\partial y^2}(x_0, y_0)\right)\Big\rangle = \frac{8\sigma_{\kappa x}}{3\sqrt{\pi}} \tag{2.56}$$

, where the brackets denote ensemble averaging over the summits.

Later, Greenwood (52) proposed another approach, again based on the assumption that the height pdf was Gaussian, without presuming the general form of the autocorrelation function. Instead of relying on the correlation between height neighbours, he introduced the cross-correlations between the profile heights z, slopes m and curvatures κ, estimated using eqs. (2.43) and (2.44). (52)'s results were compatible with a series of profilometer data for a sandblasted steel. The theory requires values of the autocovariance close to its maximum : $R_0 \equiv \sigma^2$, $R_1 \equiv ACV(dx)$, $R_{\sqrt{2}} \equiv ACV(\sqrt{2}dx)$, $R_2 \equiv ACV(2dx)$ and allows to write Nayak's input parameters (eqs. (2.49), (2.50), (2.51)) as :

$$\sigma^2 = R_0 \tag{2.57}$$
$$\sigma_{mx}^2 = \frac{2}{dx^2}(R_0 - R_1) \tag{2.58}$$
$$\sigma_{\kappa x}^2 = \frac{2}{dx^4}(3R_0 - 4R_1 + R_2) \tag{2.59}$$

The results of (52) predict that $\frac{\kappa_m}{\sigma_{\kappa x}}$ stays close to 1 whatever the sampling interval. His results lead to the same peak linear density as (136) (eq. (2.45)). For the summits, he used a five-point definition and obtained a summit density $(2 - \sqrt{6}/\pi) \approx 1.2$ higher than that given with a nine-point definition. (52)'s prediction showed good agreement with summit height and curvature data of a rough steel surface ($\sigma = 14.8$ μm) for different sampling intervals. For this surface, the measurement of summit and peak number respectively per unit surface and length yield $n_s/n_p^2 \approx 1.9$, which is closer to the (52) prediction ($n_s/n_p^2 \approx 1.5$) than the 1.2 factor predicted by Nayak.(eq. (2.53)).

(97) and (136) theories appear as a particular case of Greenwood's theory, in the limiting case of a sampling interval that tends to zero, assuming σ_{mx} and $\sigma_{\kappa x}$ remain finite. Experimental data of (52) contradict this, showing that σ_κ increases continuously of two orders of magnitude when lowering dx from 50 to 2 μm. When the sampling interval is large enough so the ordinates become independent, the slopes and curvatures no longer represent the shape of physical asperities. The problem of choosing a sampling interval small enough to measure in particular σ_{mx}, σ_κ still remains.

2.4.2 Roughness parameters variability

The parameters σ_m^2, σ_κ^2 may be obtained according to several different methods among which :

- using direct finite difference estimators (eqs. (2.43) and (2.44))
- calculating the power spectrum moments (eqs. (2.60) and (2.61))
- using values of the autocovariance function (eqs. (2.62) and (2.63))
- counting the number of peaks n_{p1D} and zero-crossing points n_0 per unit length (83) (eqs. (2.64) and (2.65))

$$\sigma_m^2 = \int_0^\infty dk\, k^2\, PSD_{1D}(k) \tag{2.60}$$

$$\sigma_\kappa^2 = \int_0^\infty dk\, k^4\, PSD_{1D}(k) \tag{2.61}$$

$$\sigma_m^2 = 2\frac{ACV(0) - ACV(dx)}{dx^2} \tag{2.62}$$

$$\sigma_\kappa^2 = \frac{2}{dx^4}(3ACV(0) - 4ACV(dx) + ACV(dx)) \tag{2.63}$$

$$\sigma_m^2 = \pi^2\sigma^2 n_0^2 \tag{2.64}$$

$$\sigma_\kappa^2 = \pi^2\sigma^2 n_0^2 n_{p1D}^2 \tag{2.65}$$

Moalic et al. (92) compared these estimators and showed that the use of finite difference estimators leads to bias errors that increase with the spatial frequency. Using the power spectrum moments also leads to a bias, but smaller than other methods. The same quantities σ_m^2 and σ_κ^2 may vary from 30 to 180 % according to the chosen method and the sampling interval $dx \in [3\ ;\ 8]$ μm.

All the previous studies assimilated surface roughness to its autocovariance and its probability density without referring to the cut-off length that should be used to access these quantities. Yet, in 1974, Leaver et al. (80) measured height standard deviations and autocorrelation functions, reproduced fig. 2.9 and 2.10 for two surfaces (worn and unworn). σ and the initial slope of the ACF both vary with the cut-off length, i.e. the profile length.

In 1978, Sayles and Thomas (111) argued that surface height bins usually arise from a cumulated material removing that occurs in a discrete manner over the surface. Under these circumstances, the central limit theorem hypotheses are fulfilled, and the height probability density is a Gaussian, with a standard deviation σ. However, surface roughness is always measured on samples having a finite extent $L = N \times dx$ and σ may thus depend on this sample size L. A simple functional analysis coupled with the properties of the normal distribution allowed to conclude that the surface variance is proportional to the sample size. This implies that for a given surface, there exists a constant T such that $\sigma(L) = T \times L^{1/2}$. T, named topothesy by the authors, describes the energy contained in large wavelengths, responsible for most of the spectral energy, which usually decreases in a power law fashion.

Thomas and Charlton (127) performed profilometer measurements on numerous surfaces shaped with different processes. For each surface, 10 profiles were measured and 14 roughness parameters were computed on each separate profile (see figure 2.11), without any further filter that the mean line detrending. For all parameters, only the ratio of their standard deviation over their mean is displayed, for three cut-off lengths (i.e. profile lengths) and for two orthogonal directions on the surface (left vs

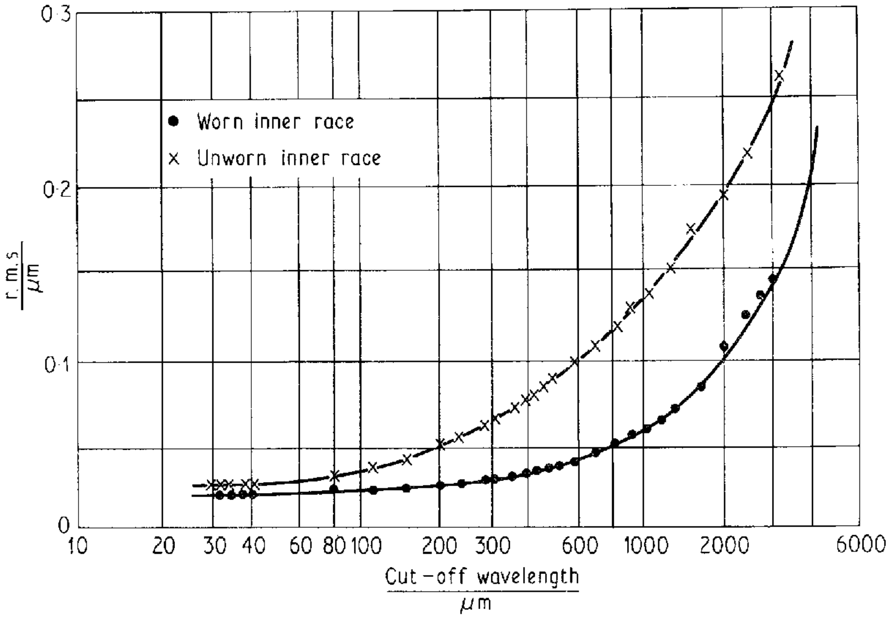

Figure 2.9: From Leaver et al. (80) : standard height deviations plotted versus the cut-off length

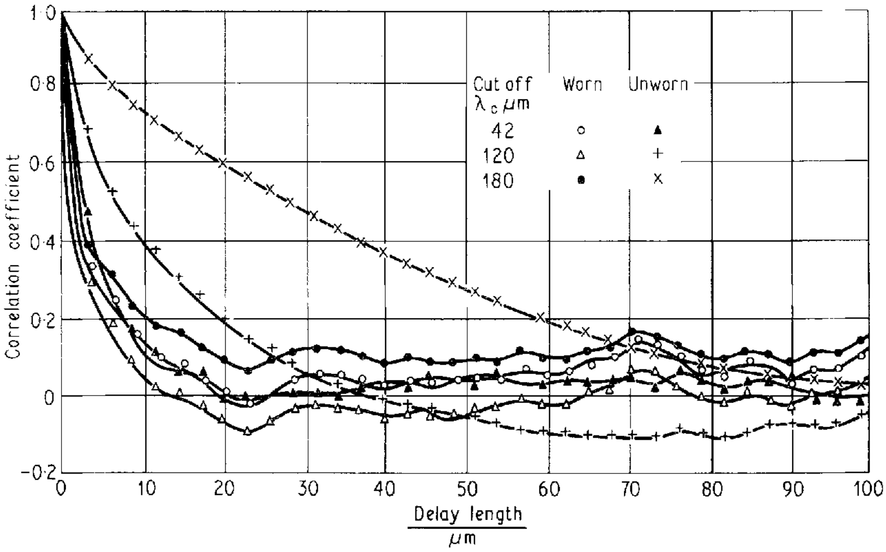

Figure 2.10: From Leaver et al. (80) : autocorrelation function calculated on profiles detrended with different cut-off lengths.

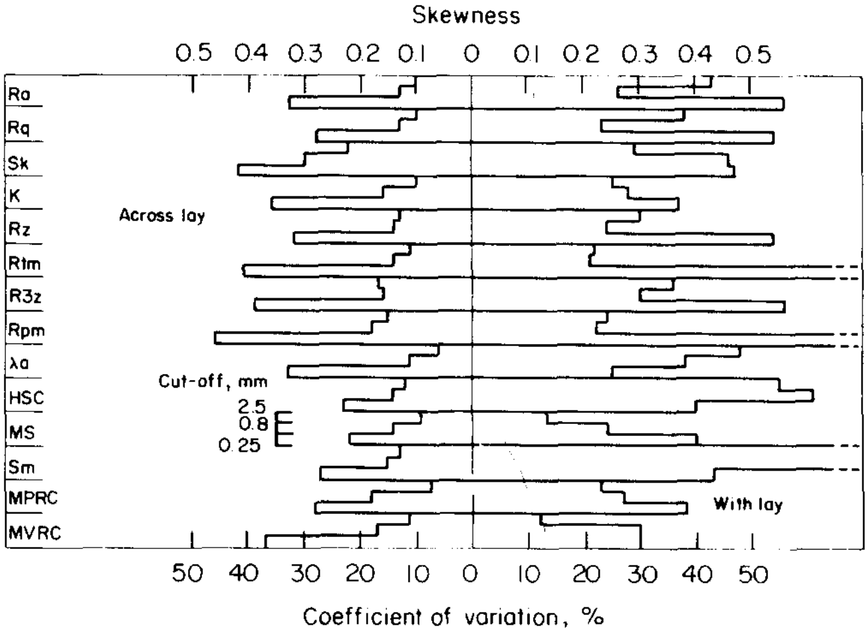

Figure 2.11: From Thomas and Charlton (127) : standard deviation divided by mean for different roughness parameters. Ra : centre line average roughness, Rq:rms roughness, Sk:skewness, K:kurtosis, Rz:10-point height, Rtm:mean peak-to-valley height, R3z:average roughness depth, Rpm:mean peak height, λa:average wavelength, HSC:high spot count, MS:mean slope, sm:mean high-spot spacing, MPRC:mean peak radius of curvature, MVRC:mean valley radius of curvature. For each surface, 10 profiles were measured. Here, the measured surface is a ground surface measured across (left) and with (right side) the lay for cut-off lengths of 0.25, 0.8 and 2.5 mm.

right on fig. 2.11). The typical dispersions between different profiles are between 15 and 50 %. The dispersion also depends on the cut-off length, and it is generally higher using small cut-off lengths. The effect of the sampling interval was also investigated on a ground surface measured with a cut-off length of 0.25 mm (see fig. 2.12) : height parameters (R_a, R_q) are almost unchanged while spatial parameters, that involve profile derivatives (λ_a, MS, $MPRC$, $MVRC$) differ from several hundreds percents according to the sampling interval used.

The advances in random field theory were derivated assuming Gaussian surfaces. This hypothesis is not general and the summit-related quantities, used in the GW model may thus only be applied to a restricted class of surfaces. Beyond the non-Gaussianity, the direct use of the above-mentioned rough contact models is limited by some experimentally-observed features about real surface roughness :

- Its dependence towards the cut-off length.
- Its dependence towards the sampling interval.
- At even sampling interval and cut-off length, roughness parameters vary routinely from 10 to 50% when probed on different areas of the same surface. (125)

These remarks limit the direct application of the abovementionned GW-like contact models which are based on summit-related quantities[1] and lead first to deal with the surface texture variability according to the probing zone. Then, its dependence towards sampling conditions may be examined and a suitable surface roughness description may arise from the observations instead of an idealized conception, suitable to calculations. Getting around the surface roughness variability is required before discussing the effects of roughness on friction tests.

---

[1] but also other models such as the contact model of (104), based on the surface slopes.

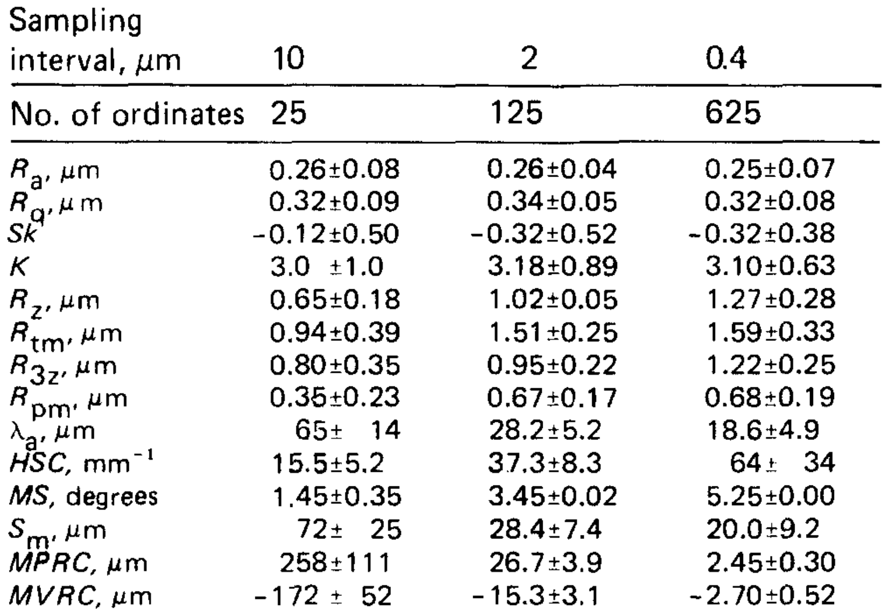

Sampling interval, μm	10	2	0.4
No. of ordinates	25	125	625
R_a, μm	0.26±0.08	0.26±0.04	0.25±0.07
R_q, μm	0.32±0.09	0.34±0.05	0.32±0.08
Sk	-0.12±0.50	-0.32±0.52	-0.32±0.38
K	3.0 ±1.0	3.18±0.89	3.10±0.63
R_z, μm	0.65±0.18	1.02±0.05	1.27±0.28
R_{tm}, μm	0.94±0.39	1.51±0.25	1.59±0.33
R_{3z}, μm	0.80±0.35	0.95±0.22	1.22±0.25
R_{pm}, μm	0.35±0.23	0.67±0.17	0.68±0.19
λ_a, μm	65± 14	28.2±5.2	18.6±4.9
HSC, mm^{-1}	15.5±5.2	37.3±8.3	64± 34
MS, degrees	1.45±0.35	3.45±0.02	5.25±0.00
S_m, μm	72± 25	28.4±7.4	20.0±9.2
$MPRC$, μm	258±111	26.7±3.9	2.45±0.30
$MVRC$, μm	-172 ± 52	-15.3±3.1	-2.70±0.52

Figure 2.12: Roughness parameters of a ground surface measured across the lay : effect of the sampling interval for a cut-off length of 0.25 mm, from Thomas and Charlton (127)

Chapter 3

Materials and methods

3.1 Introduction

In this chapter, we list and describe the materials and tools used in the experiments. The materials are the lubricants and the surfaces used in the tribological experiments. The fluid viscosity, and especially the fluid viscosity in the contact inlet zone, is a first-order key parameter that governs the film formation. We describe here the nature of the fluid and the method to access the inlet viscosity regarding the temperature. The surfaces are presented in terms of material and geometry. However, the surface roughness is not detailed in this section because the processing tools used for their description are too complex for the present introductive chapter. The surface roughness and its metrology are the main topic of the chapter 5. The two sections on tools present the topographical and friction measurements as well as the procedures developed accordingly.

Metrological considerations are specifically detailed regarding the measurements for :

- The inlet viscosity.
- The surface topography.
- The surface speeds.
- The normal and tangential forces.

Some preliminary remarks are required for the evaluation of the uncertainties, i.e. the degree of confidence that can be attributed to an estimated value $\tilde{Y}$, for a variable Y. The variable Y can always be written as a function f of one or several measurable variables $\{X_i\}_{i=1\ldots N_p}$:

$$Y \equiv f(X_1, ..., X_{N_p}) \tag{3.1}$$

The absolute error is the maximum possible difference between $\tilde{Y}$ and the real value of Y, such that the real value of Y cannot differ from $\tilde{Y}$ by more than $\frac{\Delta Y}{2}$. When Y is directly measured with an apparatus specifically designed for it, the absolute error ΔY is basically the apparatus nominal resolution. In cases where Y can only be accessed through equation (3.1), assuming that f is differentiable and denoting ΔX_i the resolutions associated to the X_i ($i = 1...N_p$), the absolute error on Y is calculated with :

$$\Delta Y = \sum_{i=1}^{N_p} \left| \left(\frac{\partial f}{\partial X_i}\right) (\tilde{X}_1, ..., \tilde{X}_{N_p}) \right| \cdot \Delta X_i \tag{3.2}$$

Using equation (3.2) only makes sense if each one of the N_p individual functions $X_1 \mapsto f(X_1, \tilde{X}_2, ..., \tilde{X}_{N_p})$, ..., $X_{N_p} \mapsto f(\tilde{X}_1, ..., \tilde{X}_{N_p-1}, X_{N_p})$ does not present fast variations around

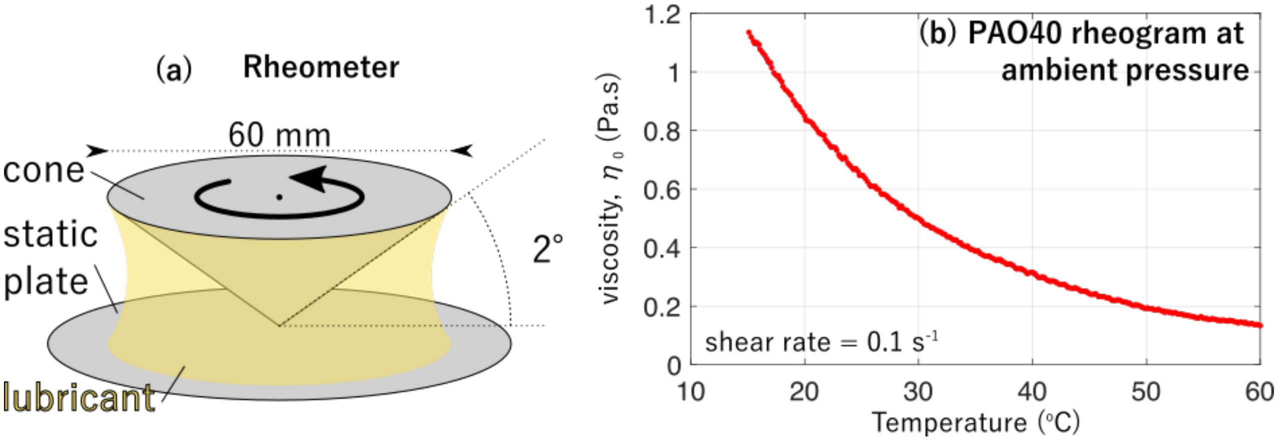

Figure 3.1: (a) : Schematic of the TA Instrument AR 2000 rheometer in a cone plate geometry. (b) : Evolution of the PAO40 viscosity with temperature obtained from the shearing at $\dot{\gamma} = 0.1\ s^{-1}$ of the lubricant put into a plane-cone viscometer.

the working point[1]. The summands in equation (3.2) are taken in absolute values. This represents the most pessimistic case where all the errors made on each X_i are maximal and that in addition, where these errors would collectively add up either to overestimate or to underestimate Y (in the oppposite optimistic case, they could compensate each other). For this reason, the absolute uncertainties usually underestimate the confidence that can be put into a measurement. For time-averaged variables, it is common to observe fluctuations σ_Y around the average that are considerably weaker than the absolute uncertainty ΔY. In these cases, σ_Y provides a more reliable information for the confidence over the estimated value $\tilde{Y}$. On the opposite, some time-averaged variables may fluctuate more than what is predicted by ΔY. In such cases, a physical phenomenon is to be invoked to explain these large fluctuations.

In the present chapter, we thus estimate both the absolute uncertainties ΔY and the standard deviation σ_Y for the inlet viscosity, the surface velocities, the normal and tangential forces, when the apparatuses documentation allows it.

3.2 Lubricants

3.2.1 Choice of lubricants

In order to prevent the experimental results from being pertubated with physico-chemical issues, such as additive adsorption on surfaces, the lubricants used in this study are pure base oils. The Poly-α Olefins (PAO) were chosen as they constitute the base oil of most of formulated lubricants.

3.2.2 Viscosity vs temperature

A cone-plane TA Instrument AR 2000 rheometer was used to measure the Newtonian fluid ambient-pressure viscosity η_0 of all the lubricants while varying the temperature from 15°C to 60°C. The rheometer has a cone plate geometry with a cone diameter and angle of 60 mm and 2° (see schematic fig. 3.1.a). During experiments, the shear rate is kept constant : $\dot{\gamma} = 0.1$ s^{-1} (except for the PAO2 that was sheared at 10 s^{-1} due to the low value of its viscosity). An example is displayed on figure 3.1, for the PAO 40.

---

[1] For instance, let us assume that $X_1 \mapsto f(X_1, \tilde{X}_2, ..., \tilde{X}_{N_p})$ presents an abrupt change of slope, or becomes highly oscillating within the interval $[\tilde{X}_1 - \Delta X_1/2\ ;\ \tilde{X}_1 + \Delta X_1/2]$, where ΔX_1 is the resolution to measure the input parameter X_1. It becomes impossible to reliably estimate the local slope $\frac{\partial f}{\partial X_1}$ around the working point $(\tilde{X}_1, ..., \tilde{X}_{N_p})$

lubricant	$\eta_0(20°C$ (Pa.s)	A (Pa.s)	B (°C)	C (°C)	$\frac{\Delta\eta_0}{\eta_0}(T=20°C)$
PAO 2	0.006	37×10^{-6}	863	-148	3%
PAO 4	0.030	48×10^{-6}	970	-131	4%
PAO 8	0.085	13×10^{-9}	5222	-314	5%
PAO 40	0.85	47×10^{-6}	1686	-152	6%
PAO 100	3.94	33×10^{-6}	1963	-148	7%
330NS	0.185	368×10^{-9}	2942	-204	6%

Table 3.1: Lubricants and their ambient-pressure viscosity at 20°C. A, B, C are the Vogel parameters obtained from an interpolation according to equation (3.3). The viscosity relative uncertainties are calculated according to equation (3.4) for an uncertainty $\Delta T = 1°C$ over the temperature.

The PAOs viscosity evolution with temperature can be described with the empirical Vogel law :

$$\boxed{\eta_0(T) = Ae^{\frac{B}{T-C}}} \tag{3.3}$$

This allows us to know the inlet viscosity during the tribological experiments irrespective of the operating temperature. For the whole set of lubricants tested in this work, the viscosity at ambient conditions is displayed on table 3.1, as well as their corresponding Vogel parameters A, B, C.

3.2.3 Temperature

The tribological experiments were performed using two tribometers - see section 3.5.1 of this chapter - for which the temperature is measured differently. During the friction tests performed with the IRIS tribometer (see section 3.5.1), the temperature was measured either using a thermocouple at a distance ~50 cm of the contact, or with a temperature probe located into an aluminium reservoir located closer to the ball as shown on figure 3.8.a. For experiments using the MTM (see section 3.5.1), the temperature was measured using an incorporated temperature probe located inside the lubricant reservoir. The three thermocouples have a nominal resolution of $\Delta T = 0.1$°C. However, the temperature fluctuations during the Stribeck experiments were usually slighlty higher than this. The friction experiments lasted between 10 minutes and 1 hour. During that period, although none systematic study of the temperature variations was conducted, the temperature variation was usually positive and did not exceed $\Delta T \sim 0.5 - 1$°C.

3.2.4 Error made on $\eta_0(T)$

The inlet viscosity η_0 is calculated according to a Vogel law (cf eq. (3.3)). At $T = 20$°C assuming an uncertainty $\Delta T = 1$°C over the inlet temperature and using the Vogel values B and C in table 3.1 leads to the relative uncertainties over η_0 that are listed in table 3.1 and calculated according to :

$$\frac{\Delta\eta_0}{\eta_0} = \frac{-B\Delta T}{(T-C)^2} \tag{3.4}$$

3.3 Surface materials

3.3.1 Balls

The balls of radius $R_b = 9.525$ mm are made of AISI 52100 steel. They were polished using a solution of 10 μm diamond particles. Some of the balls used on the IRIS tribometer were coated with

designation	details	material
dRP80MTM	rough ($R_a < 0.1$ μm, PCS) + roughening P80	AISI M2
dAR	rectified steel	AISI 52100
dARTEb	finished steel + roughening ($R_a \approx 0.1$ μm, IREIS)	AISI 52100
dR0MTM	rough ($R_a < 0.1$ μm, PCS)	AISI M2
dRP800	MTM rough + smoothing	AISI M2
dART	finished steel	AISI 52100
d1RTdeccl	classical pickling (IREIS)	AISI 52100
d2RTdecdou	soft pickling (IREIS)	AISI 52100
dAP	polished-by-hand P4000	AISI 52100
dAPMTM	polished-by-hand P4000	AISI M2
d2AP	polished-by-hand P4000	hardened steel
dAsabz3	polished-by-hand P4000 + light sandblasting	hardened steel
dAsabz4	polished-by-hand P4000 + sandblasting	hardened steel
dSaph	polished	sapphire
dSi	polished	silica
dSiDLC	polished + 90 nm DLC	silica DLC
dRDLC	Rectified + DLC (IREIS)	steel
d1RTDLC	pickled steel + 3 μm DLC (IREIS)	steel
d3RTDLC	pickled steel + 3 μm DLC (IREIS)	AISI 52100
d4RTDLC	pickled steel + 3 μm DLC + polishing (IREIS)	AISI 52100

Table 3.2: Discs materials used in the friction experiments.

3 μm-thick layer of a:C-H Diamond-Like Carbon (Certess DDT coating provided by IREIS, HEF Group). In that case, a further polishing with another solution of diamond particles was performed on the coated balls.

3.3.2 Discs

All the non-transparent discs used in this study were made of steel with an elastic modulus E=210 GPa. The discs having a diameter of 60 mm and a thickness of 8 mm (see the two last rows of photographs shown figure 3.2) are in AISI 52100 steel and were designed to be used for several experiments on the IRIS tribometer (see section 3.5.1) using several rubbing tracks. Other steel discs (second row on fig. 3.2) were used for a single experiment per disc on the PCS Mini Traction Machine (see section 3.5.1) : these are made of M2 steel. Some discs tested on the IRIS tribometer were coated with a 3 μm-thick layer of the same DLC as for the balls. In order to obtain "intermediate" roughnesses, some discs were either polished or roughened using a polisher and different sandpapers. These sandpapers are designated with the nomenclature ISO/FEPA in table 3.2. Regarding the transparent smooth surfaces, two kinds of discs were used : silica (Spectrasil quartz) discs (E=70 GPa) with a diameter of 60 mm and a thickness of 10 mm, and sapphire discs (E=420 GPa) with a diameter of 90 mm and a thickness of 5 mm. The disc materials as well as the roughening processes, are summarized in table 3.2, with their designation.

Figure 3.2: Surfaces used in friction tests.

3.4 Topographical measurements

3.4.1 Interferometry

The large marjority of topographical measurements were performed using a Bruker interferometer. As depicted on figure 3.3.a, a source emits light in the direction of the sample, which acts as a mirror. A semi-reflective light beam separator is put in-between the source and the sample. This results in two reflected light beams : one due to the light separator, the other coming from the sample (beams 1 and 2 respectively on figure 3.3.a). If the difference path between the two beams is less than the source coherence length[1], then the interaction between the two beams produces interferometric fringes, as shown on figure 3.3.b and c. Each light intensity variation is characteristic of a given distance between the light separator and the sample. The interferometer used in this work has 3 modes that correspond to different image processing techniques to relate theses light intensity variations to the surface heights. These modes are the Phase Shifting Interferometry (PSI), the Vertical Shifting Interferometry (VSI) and a modified VSI mode called VXI. The PSI mode uses monochromatic light and its processing is based upon the intensity variations over the constructive fringes. The VSI and

---

[1] This coherence length l is related to the coherence time τ through $l \sim c \times \tau$, where c is the light speed and τ is a time characteristic of the source that is inversely proportional to its bandwidth $\Delta\nu$. τ is a measure of the time over which the phase of the light emitted by the source changes randomly. Two beams emitted at time intervals larger than τ will not be able to produce constructive interference. For a white source emitting in the visible light, $l \sim 6 \times 10^{-7}$ m whereas for a monochromatic source, l may be between a few millimeters and a few meters according to its spectral bandwidth.

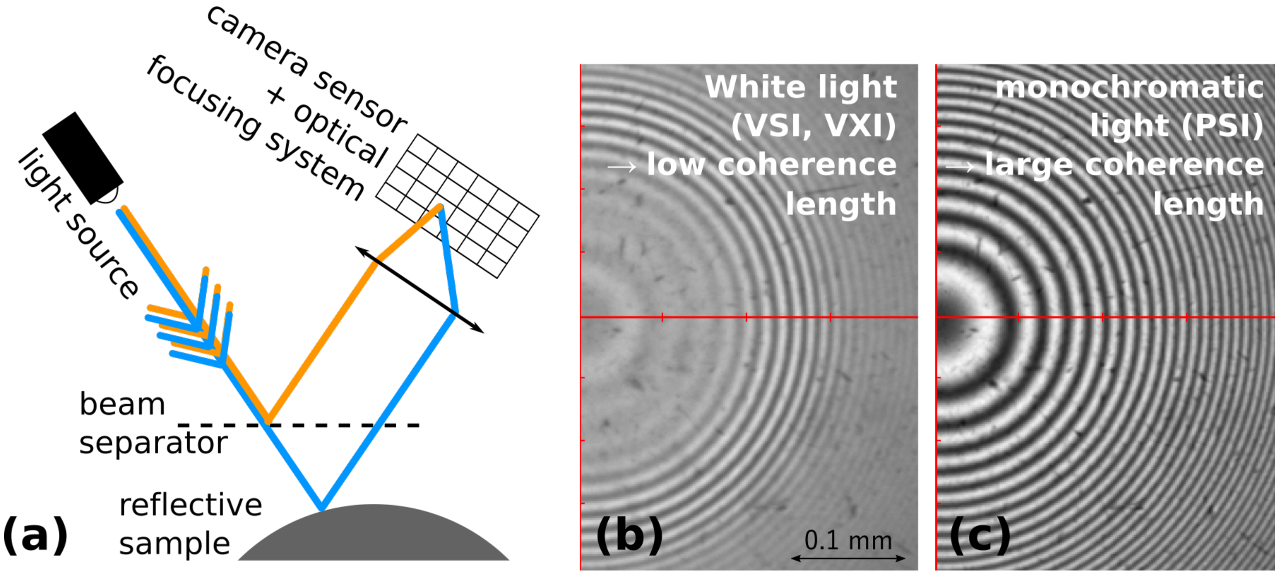

Figure 3.3: Principle of interferometry-based topographical measurements. (a) : Schematic illustrating the source beam split and their successive reflexions. Fringes resulting from constructive monochromatic interferences on a steel ball with a white source (b) and a monochromatic source (c).

VXI modes use white light, hence with a lower coherence length that cannot produce fringes over the same vertical distance as a monochromatic source would do (see, for comparison, figures 3.3.b and c). These modes thus require a recording of the different interferometric fringes obtained as the optical system is vertically translated to the measured sample. This allows the fringes in VSI (and VXI) to cover even higher vertical distances than those obtained with a static monochromatic source.

The PSI is announced with a vertical resolution $\Delta Z \leq 1$ nm and is known as the most precise mode (115). To confirm its reliability, topographical measurements using non-contact Atomic Force Microscopy (AFM) and interferometry were compared. As an example, the same area of a DLC-coated steel ball is displayed on figure 3.4. The hole depth difference between the PSI and the AFM measurement is of the order 30 nm while it is of the order of 170 nm between the AFM and the VSI measurement. This confirms the greater reliability of the PSI mode. The difference observed between PSI and AFM measurements lies in the range of uncertainties of the AFM, which presents some thermal drift-induced artifacts of the same order of magnitude.

However the PSI mode could not be used to measure the topography of the discs : most of them[1] present steep steps that can be mistaken for $2\pi k$-phase shifts, $k \in \mathbb{Z}$. This limitation is not present in VSI and VXI(115), which makes them better candidates than PSI to measure the discs' topography. Although its inner functioning is poorly documented, the VXI clearly proved to be more reliable than the VSI in terms of repeatability. Moreover, measurements using VSI always led to overestimated height deviations —positive and negative— and to a non negligible background noise that might be related to the optical system translation during the measurement. This noise is obviously filtered out in the VXI processing. As it is shown on figure 3.5, the measurements perfomed using VXI were in perfect agreement with those performed in PSI on a relatively smooth surface. All discs topography were thus measured using the VXI mode.

3.4.2 Balls topographical measurement protocol

Before each friction experiment, the ball topography was measured using PSI on 6 randomly chosen zones with a magnification ×5 that implied a sampling interval of 1.975 μm along the two

---

[1] Except for the sapphire, silica and polished-by-hand discs.

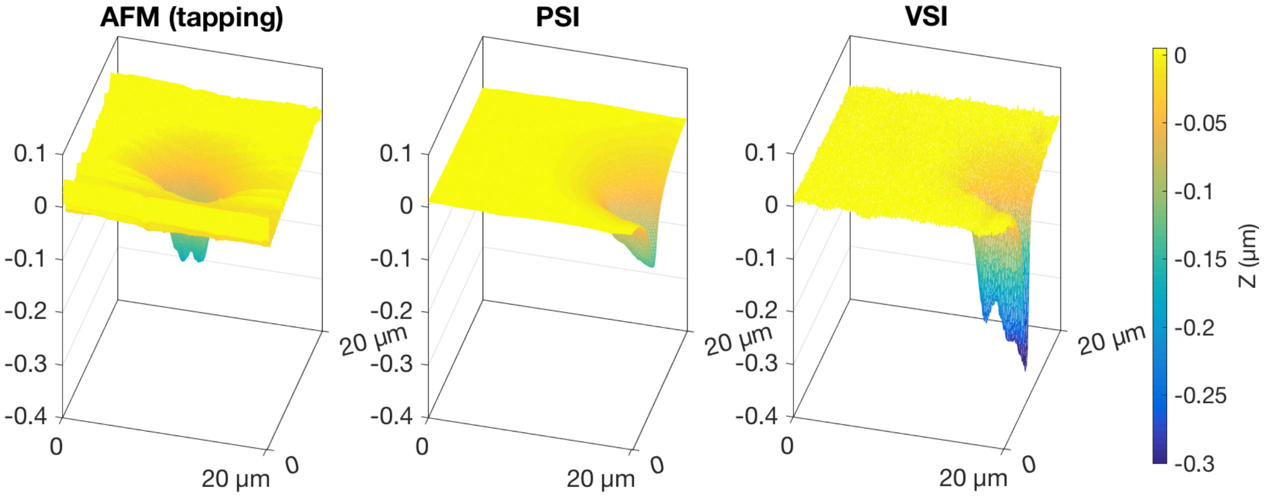

Figure 3.4: Comparison of AFM measurement against the PSI and VSI interferometric modes on the same hole, on a DLC-coated ball. The AFM and the PSI mode give the same hole depth, which confirms the reliability of the PSI mode.

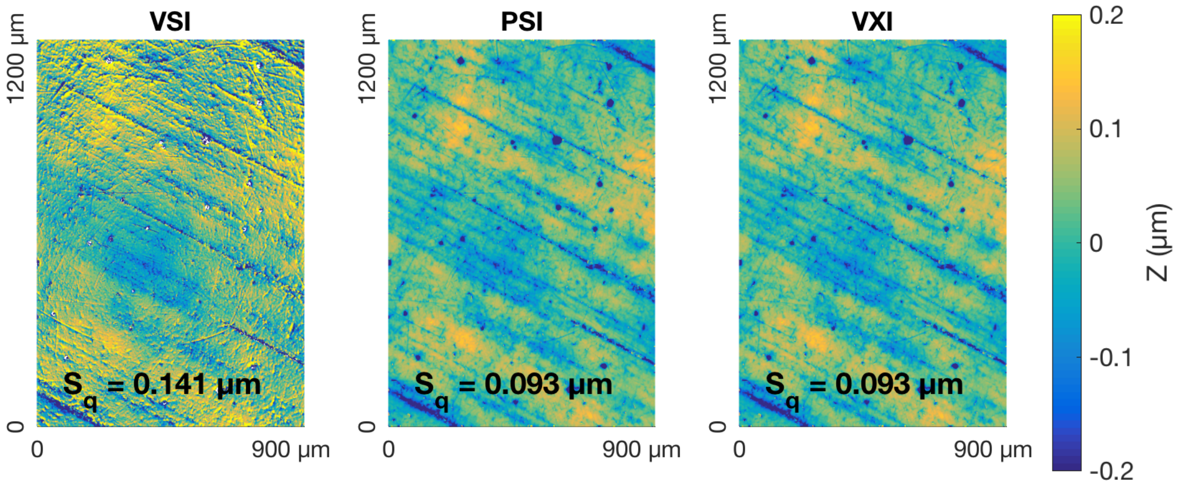

Figure 3.5: Comparison of the different interferometric modes on the same zone of a finished and DLC-coated disc, smooth enough to perfom a measurement in the PSI mode. The VXI gives the same resultas as the PSI mode while the VSI overestimates the height deviations.

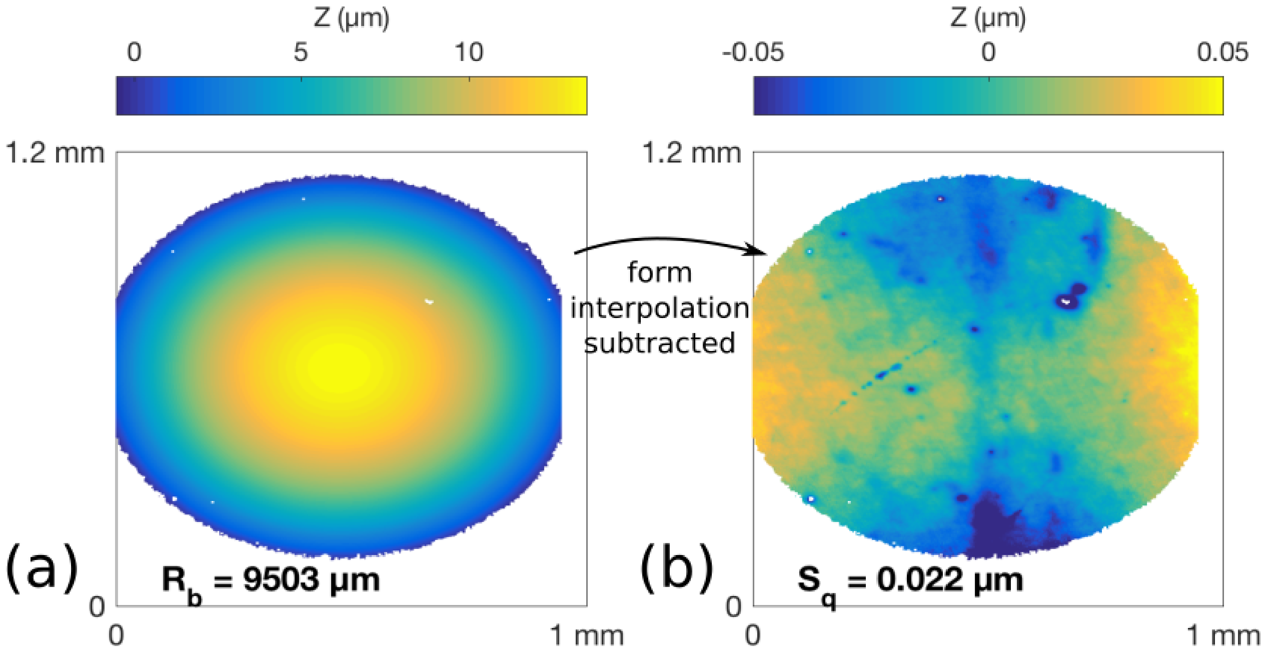

Figure 3.6: Typical smooth steel ball topography obtained using PSI (a) : Raw measurement. (b) : Resulting topography after subtraction of the interpolated sphere of radius R_b=9.503 mm.

Tribometer	Surface speeds	Loads	specificities
IRIS	$[1 \times 10^{-3}$; 1] m/s	[0.5 ; 15] N	In situ film thickness measurements ($h \in$[1 nm ; 1 μm])
MTM	$[1 \times 10^{-3}$; 4] m/s	[0.5 ; 75] N	Lubricant temperature control, high loads

Table 3.3: Tribometers characteristics.

main axes of each 1264 μm × 948 μm image. This allows to observe approximately one eighth of the ball rubbing track. As it is illustrated on figure 3.6, the balls topography is then interpolated according to a sphere. The interpolated radii of curvature on these images scarcely differed by more than $\Delta R_b = 0.5$ mm from the balls nominal radius 9.525 mm.

3.4.3 Discs topographical measurement protocol

Except for the sapphire, silica and polished-by-hand steel, all the discs listed in table 3.2 were rougher than the balls and their various textures were more complex than the textures from a ball to another. For these reasons, more attention was paid to the discs topography. As those presented on figure 3.5, the discs topography was measured in VXI with individual interferometric images (640 × 480 pixels). Moreover, large images with different sampling intervals (dx=0.099, 0.988, 1.975, 3.653 μm) were obtained from these surfaces. Their analysis is detailed in chapter 5.

3.5 Friction experiments

3.5.1 Ball-on-disc tribometers

The friction experiments were performed on two ball-on-disc tribometers with controlled applied load and speeds : the IRIS tribometer and the Mini Traction Machine (MTM). The balls described previously with a radius of 9.525 mm are used on both tribometers. The range of respective operating conditions is summarized on table 3.3.

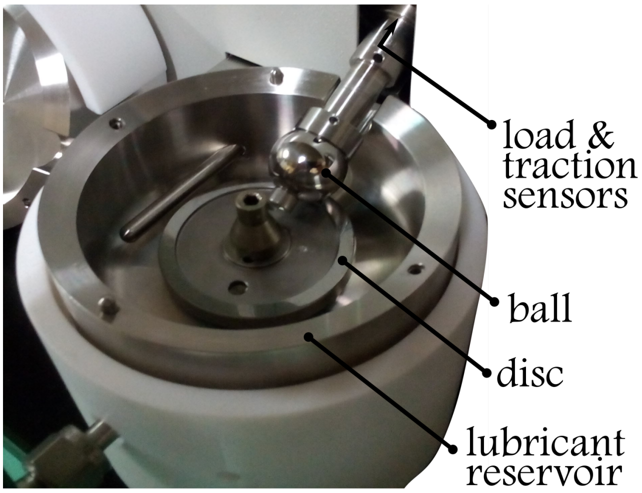

Figure 3.7: Mini traction machine (PCS) with steel samples.

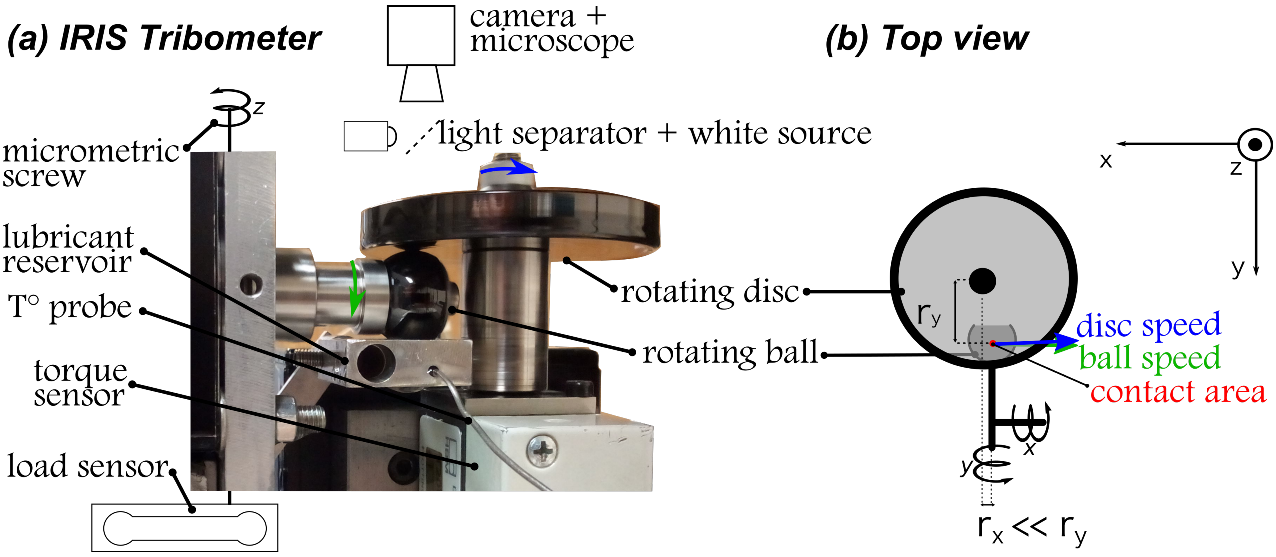

Figure 3.8: IRIS tribometer with moving DLC-coated steel samples. The normal force sensor is attached to the ball motor, not visible here.

Mini traction machine

The MTM (fig. 3.7) is a commercial tribometer (*PCS Instrument*) able to operate at loads up to 75 N. The ball and disc speeds, the load and the lubricant temperature are controlled and measured separately.

IRIS tribometer

The IRIS tribometer (fig. 3.8) is a home-made apparatus developed at the LTDS. Its specificity consists in controlled contact kinematics with a simultaneous observation of the contact - inlet, high-pressure zone and outlet - when using a transparent disc. It is equipped with a white light source and a camera connected to a computer. Using a transparent disc (sapphire or silica) against a ball allows lubricant film thickness measurements by interferometry during the friction test. For such experiments, a static white source emits light that is reflected onto the ball and a 6 nm-thick semi-reflective layer of chromium that is deposited beforehand on the transparent disc. Most of the friction

procedure	*entrainment speed* $\mathrm{u_e}$	*sliding speed* $\mathrm{u_s}$	*load* $\mathrm{F_n}$
Traction	constant	variable $\in$ [0 ; $u_{s\,max}$] m/s	constant
Stribeck	variable $\in$ [0 ; $u_{e\,max}$]	variable such that $\frac{u_s}{u_e} = SRR$=constant	constant

Table 3.4: Kinematic procedures for traction and Stribeck experiments.

experiments used in this work were performed on the IRIS tribometer with steel, hence opaque, discs.

3.5.2 Friction procedures

Before each test, both surfaces were put into an ultrasonic cleaner during 10 minutes in heptane, then 10 minutes in propanol. They were finally dried with nitrogen before the friction test that started less than 5 minutes after the cleaning. Two friction procedures were used in this work : traction experiments and Stribeck experiments. The input parameters for such experiments are the entrainment speed u_e and the sliding speed u_s, defined as :

$$u_e \equiv \frac{1}{2}(u_b + u_d) \tag{3.5}$$

$$u_s \equiv u_b - u_d \tag{3.6}$$

, where u_b and u_d denote the ball and disc velocities. The kinematic conditions for a traction and a Stribeck procedure are summarized on table 3.4. During a traction experiment, u_e is kept constant and u_s is varied from zero to its maximum value, usually until a maximal sliding-rolling ratio of $SRR = \frac{u_s}{u_e}$ equal to 100%. During the Stribeck experiments, the entrainment speed was always varied from its maximum value (0.7 m/s on IRIS, 1 m/s on the MTM) to its minimum value (1 mm/s), while keeping SRR equal to 5, 15, 25, 50 or 100% depending on the experiment.

On both tribometers, we performed both speed steps experiments and linear ramps. Linear ramps consist in measuring the forces and speeds signals while varying the speeds linerarly in time. An example of Stribeck procedure on the MTM at SRR=25% with speed ramps is displayed on figure 3.9.a. The duration of the ramps lied from 2 to 5 minutes according to the experiment. This corresponds to a surface speed acceleration between 3×10^{-3} and 8×10^{-3} m/s^2, which is slow enough to let the average friction force reach its equilibrium.

During speed steps, the speed is kept constant during a certain duration (30 seconds on the IRIS tribometer and 6 seconds on the MTM) after which it is varied to another value. On the IRIS tribometer, the first 5 seconds of the measured signals were put aside for each step in order to diminish the sensitivity to the unavoidable speed overshoots that occur at the transition between two speeds, as shown on figure 3.9.b, for a Stribeck procedure at SRR=25%.

3.5.3 Surface speeds uncertainties and fluctuations

3.5.3.1 IRIS speeds

On the IRIS tribometer, the ball and the disc rotations are produced thanks to two independent brushless synchronous motors from Kol Morgen DBL. The distances r_x and r_y between the disc axis and the contact area (see figure 3.8.b) are measured using two micromectric screws. r_y ranges from 19 to 30 mm depending on the experiment, and $r_x = 0$ is chosen to align the solid speeds with the x axis. Then, the speeds are calculated according to :

$$u_b = R_b\,\omega_b \tag{3.7}$$

$$u_d = r_y\,\omega_d \tag{3.8}$$

The motors are driven at $f_m = 32$ kHz and are announced with an uncertatinty of 1% on the rotational speed. Assuming an error $\Delta R_b = 1$ mm, which is reasonable to account both for a possible error of perpendicularity between the ball axis and the vertical axis z and for an error of alignement between the ball — and disc — revolution axis and the motor axis.

$$\Delta u_{b\ \mathrm{IRIS}} = R_b\,\Delta\omega_b + \omega_b\,\Delta R_b \leq \begin{cases} 0.12 \text{ m/s for } u_b\text{= 1 m/s} \\ 1.0 \times 10^{-4} \text{ m/s for } u_b\text{= 1 mm/s} \end{cases} \tag{3.9}$$

$$\tag{3.10}$$

The uncertainties on the location of the contact with the micrometric screws are less than 0.5 mm. It might be worth noting that the use of equation (3.8) implicitely raises an error on u_d due to the fact that R_x may not be exactly zero. The corresponding disc speed component error on the disc speed modulus writes $||\vec{u}_d|| - r_y\,\omega_d = r_y\,\omega_d\sqrt{1+(r_x/r_y)^2} - r_y\,\omega_d \approx \frac{r_x^2}{2r_y}\omega_d$. Summing these errors with $\Delta r_y = 0.5$ mm and $r_x = 0.5$ mm leads to the following absolute uncertainties on the disc speed :

$$\Delta u_{d\ \mathrm{IRIS}} = r_y\,\Delta\omega_d + \omega_d\,\Delta r_y + \frac{r_x^2}{2r_y}\omega_d \leq \begin{cases} 0.03 \text{ m/s for } u_d\text{= 1 m/s} \\ 3 \times 10^{-5} \text{ m/s for } u_d\text{= 1 mm/s} \end{cases} \tag{3.11}$$

$$\tag{3.12}$$

The surface speed fluctuations can be compared to these absolute uncertainties while performing 30 second-long time-steps on the IRIS tribometer, as shown on figure 3.9.b.

$$\sigma_{u_b\ \mathrm{IRIS}} \sim \begin{cases} 10^{-2} \text{ m/s for } u_b \text{ from 1 to 0.1 m/s} \\ 10^{-3} \text{ m/s for } u_b \text{ from 0.1 to 0.03 m/s} \\ 10^{-4} \text{ m/s for } u_b \text{ from 30 to 1 mm/s} \end{cases} \tag{3.13}$$

$$\tag{3.14}$$

$$\sigma_{u_d\ \mathrm{IRIS}} \sim \begin{cases} 10^{-3} \text{ m/s for } u_d \text{ from 1 to 0.03 m/s} \\ 10^{-4} \text{ m/s for } u_d \text{ from 30 to 1 mm/s} \end{cases} \tag{3.15}$$

$$\tag{3.16}$$

3.5.3.2 MTM speeds

The surfaces speed resolution of the MTM are announced[1] at :

$$\Delta u_{b\,MTM} = \Delta u_{d\,MTM} = 1 \text{ mm/s} \tag{3.17}$$

The MTM output measurements are given by a commercial software such that the speed and force signals are only accessible through their values averaged during a period Δt, presumably larger than the real sampling time of the apparatus. For speed steps, only one average value per speed step is displayed, which makes the estimation of fluctuations impossible. For linear ramps $\Delta t = 1$ s. In that case, the fluctuations of the average surface speeds $< u >_{\Delta t}$ around the motor control (abbreviated M.C.) can be calculated with the standard deviation of $(< u >_{\Delta t} (t) - M.C.(t))$, where $M.C.(t)$ are straight lines (dashed lines on figure 3.9.a.2). Depending on the experiment, we find :

$$\sigma_{<u_d>\ \mathrm{MTM}} \sim \sigma_{<u_b>\ \mathrm{MTM}} \sim 10^{-3} \text{ m/s} \tag{3.18}$$

---

[1] 0.025 % of the maximum speed, according to the MTM user guide.

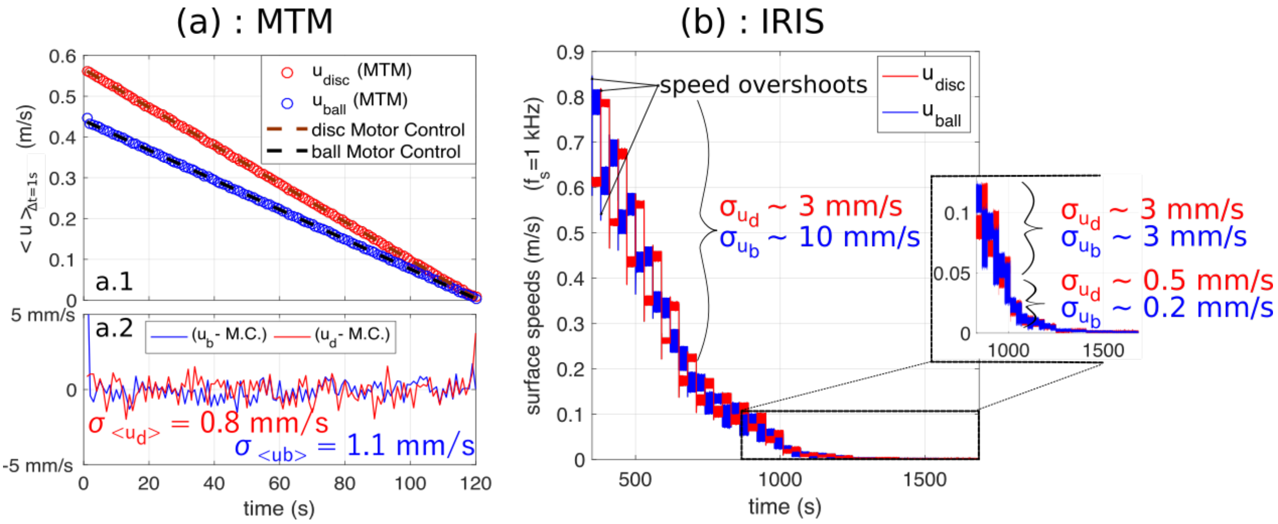

Figure 3.9: Surfaces speeds evolution during a Stribeck procedure. The speeds are decreased according to a Stribeck procedure at SRR=25% while imposing : (a) speed linear ramps on the MTM, (b) speed steps on the IRIS tribometer.

3.5.4 Normal and tangential force measurements

3.5.4.1 IRIS force signals

On the IRIS tribometer, the normal force F_n is measured using a strain gauge [Utilcell-100 N, full bridge 2mV/V nominal gain] located under the ball holder, with a nominal resolution of $\Delta F_{n\text{ raw}} = 0.002$ N and a maximal load of 15N. Before the surfaces are in contact, the load offset F_{n0} is averaged during 20 seconds at the beginning of each experiment, then the load is applied by moving the ball with a micrometric screw parallel to the z axis. The load is simply calculated according to :

$$F_n = F_{n\text{ raw}} - F_{n0} \tag{3.19}$$

The absolute error on F_n is thus :

$$\Delta F_n = 2\Delta F_{n\text{ raw}} = 0.004 \text{ N} \tag{3.20}$$

The tangential force F_f is measured using a torque transducer T20WN on the disc axis, with a nominal resolution of ΔC=0.2 mN.m. The mean torque offset C_0 is averaged during 20 seconds at the beginning of each experiment while the solids move without contact. The friction force is then calculated according to :

$$F_f = \frac{C - C_0}{r_y} \tag{3.21}$$

Knowing the maximum tangential force in our lubricated contacts has never exceeded 3 N, the absolute error made on F_f can be calculated :

$$\Delta F_f = 2\frac{\Delta C}{r_y} + \frac{\Delta r_y}{r_y} \cdot F_f \leq 0.12 \text{ N} \tag{3.22}$$

During a tribological experiment, the load signal fluctuates differently depending on the operating surface speeds because of the electrical noise associated to the speed control loop and also because of the out-of-roundness due to the misalignment[1] between the ball and its motor axis, as it is shown

---

[1] This misalignement was measured at 0.02 mm with a lever arm test indicator.

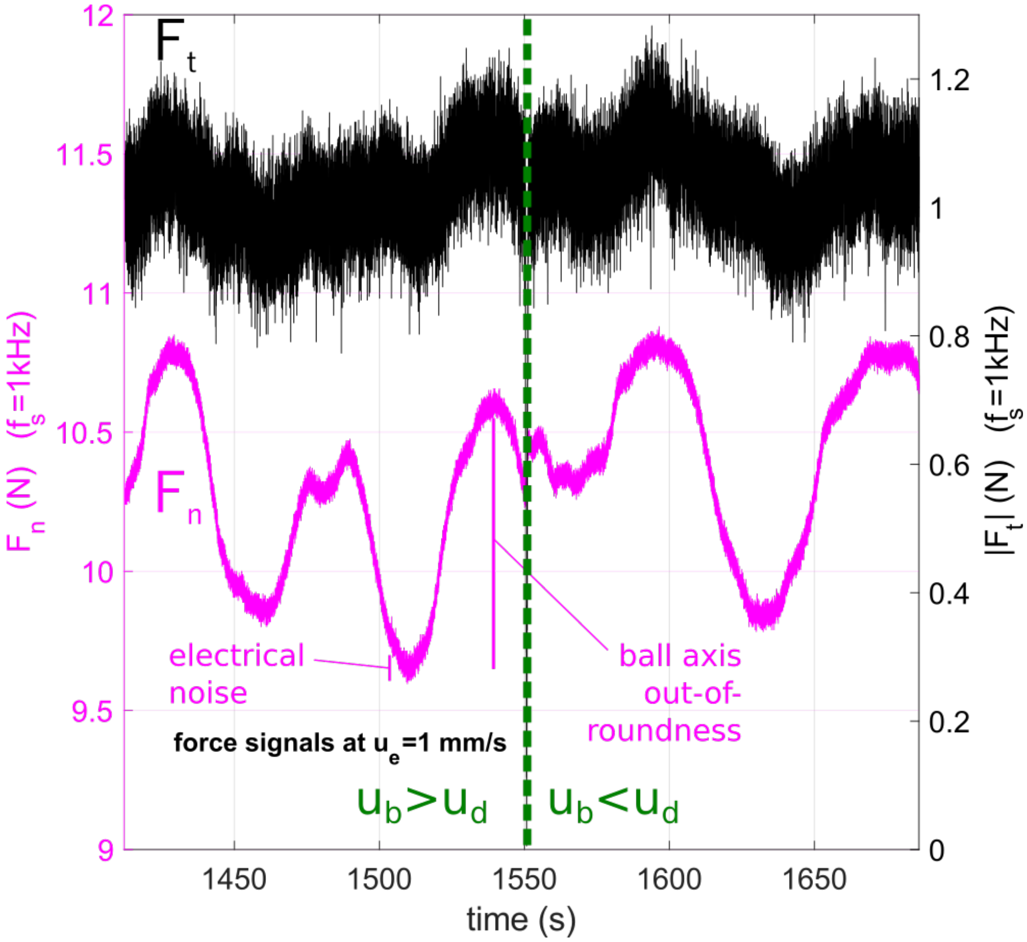

Figure 3.10: Normal and tangential force signals during two speeds steps (SRR = 25% and SRR = −25%) at u_e=0.001 m/s. The surfaces used here are a rectified steel disc against a DLC-coated steel ball, lubricated with PAO40 at 20°C.

on figure 3.10.b. Finally, for all speeds, the load fluctuates around its preset value with a standard deviation of :

$$\sigma_{F_n\ \text{IRIS}} = 0.3 \text{ N} \tag{3.23}$$

During a speed step, the friction force F_f reaches a stationary average value in a few milliseconds, as it is shown on figure 3.10.

Unlike the speeds and load that are imposed during the experiments, the friction force fluctuations do not only result from the torque sensor but also from the different physical phenomena occuring inside the lubricated contact. Estimating the fluctuations of F_f during a speed step would thus make little sense. It would require a detailed description of the surface roughness, the lubricant and other parameters, which constitute the core of this work.

Still, in response to the rather large maximum uncertainty ΔF_f, given by equation (3.22), the standard deviation of F_f can be estimated by taking its standard deviation during tests with a constant sliding speed (speed steps) :

$$\sigma_{F_f\ \text{IRIS}} = \begin{cases} 0.1 \text{ N at } u_e = 700 \text{ mm/s} \\ 0.05 \text{ N at } u_e = 1 \text{ mm/s} \end{cases} \tag{3.24}$$

3.5.4.2 MTM force signals

On the MTM, the resolutions ΔF_n and ΔF_t are not given by the documentation and the raw force signals are not more accessible than those of speeds. The time-averged signals automatically given by the MTM software do not allow the estimation of tangential force fluctuations in a stationary regime, i.e. at constant speed and load. During a speed ramp procedure, an indicator of the load fluctuations can be obtained based on the load signal averaged every second :

$$\sigma_{<F_n>\text{MTM}} \sim 2 \times 10^{-2} \text{ N} \tag{3.25}$$

3.5.5 Uncertainties over calculated quantities

3.5.5.1 Hertz area and pressure

The uncertainty over A_{nom} follows from those on F_n, R_b and E'. According to eq. (2.7), with $\frac{\Delta F_n}{F_n} = 4\%$, $\frac{\Delta R_b}{R_b} = 5\%$:

$$\frac{\Delta A_{nom}}{A_{nom}} = \frac{2}{3}\left(\frac{\Delta F_n}{F_n} + \frac{\Delta R_b}{R_b}\right) = 6\% \tag{3.26}$$

In terms of Hertz radius a_H, the corresponding absolute uncertainty is of a few microns. The uncertainty over p_m can equally be calculated using eq. (2.9) :

$$\frac{\Delta p_m}{p_m} = \frac{\Delta F_n}{F_n} + \frac{\Delta A_{nom}}{A_{nom}} = 10\% \tag{3.27}$$

3.5.5.2 Film thicknesses

According to eq. (2.15), the film thickness depends on many parameters. Its relative uncertainties with respect to each physical parameter are displayed on table 3.5 :

input parameters X →	p_m	α	E'	R_x	u_e	T_{inlet}
relative uncertainty $\frac{\Delta X}{X}$	10%	5%	1%	5%	10%	5%
$\frac{\Delta X}{h}\frac{\partial h}{\partial X}$	2 %	3 %	$< 1\%$	2%	7%	4%

Table 3.5: Film thickness relative uncertainty $\frac{\partial_X h\,\Delta X}{h}$ w.r.t. each parameter it depends on according to eq. (2.15)

3.5.5.3 Inlet temperature rise and film thicknesses

Section 2.2.4 showed that the inlet temperature might overcome the ambient temperature. The expected inlet temperature rise increases with the rolling speed, but also with the sliding-rolling ratio and with the pressure. The results of (53)(eq. (2.17)), (58) are inverted in terms on effective inlet temperature rise (see annex 9.2) and plotted versus the nominal film thickness on fig. 3.11 along with the temperature rise formula given by (57) (eq. (2.19)). The experimental inputs correspond to a Stribeck procedure with the most dissipative conditions reached in the present work ($p_m = 860$ MPa, $SRR = 1$) with a thick lubricant film formed with PAO40. The rolling heating yields a maximum inlet temperature rise of 1°C (dashed line, fig. 3.11). Accounting for the influence of sliding and load yields a maximum inlet temperature rise of 8°C when $h_c = 2\,\mu$m. For $h < 1\,\mu$m, this temperature rise does not exceed 2°C. Except in this extreme case, the reduction factors of (58), (53) and the inlet temperataure rise formula of (57) predict an inlet temperature rise that does not overcome $1°C$ in our conditions. This leads us to prefer the use of (62)'s classical isothermal film thickness formula which is based in particular on the ambient temperature viscosity.

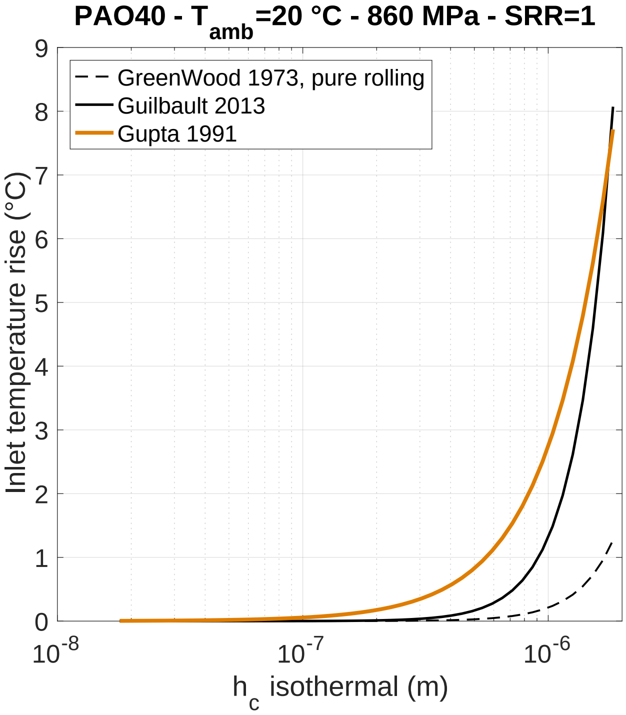

Figure 3.11:

Predictions of inlet temperature rise acording in the most dissipative conditions for a Stribeck procedure:$p_m = 860$ MPa, $SRR = 1$, with $10^{-3} \leq u_e \leq 1$ acording to our speeds range. Since inlet heating increases with $L_h = \frac{\eta_0 u_e^2 \beta_l}{K_l}$, the PAO40 parameters ($\eta_0 = 0.85$ Pa.s, $\alpha = 20$ GPa^{-1}) were used for its large viscosity that allows to cover micrometric film thicknesses at the highest speeds.

Chapter 4

EHD friction for smooth surfaces

4.1 Introduction

4.1.1 Goals

The goal of this chapter is to predict the friction force arising between two smooth surfaces in sliding-rolling experiments in the EHL regime. Before dealing with roughness, the friction force first depends on the loading conditions, the speeds, the temperature and the thermal environment. Even though it is necessary to know those operating conditions, it is also required to know a priori the fluid rheological behaviour as viscous friction is the main source of dissipation in EHL.

4.1.2 Viscous drag decomposition

In EHD contacts, the Reynolds number $Re \equiv \frac{u_e\, h\, \rho}{\eta}$ is always inferior to 10^{-3}. The fluid flow is thus completely laminar and since the lubricant film thickness is at most a hundredth of the contact extension in the x and y directions, the lubrication hypothesis $\partial_x, \partial_y \;<<\; \partial_z$ is satisfied. Assuming in addition a no-slip boundary condition between the fluid and the surfaces, the fluid flow in the rolling direction x is :

$$u_x = \underbrace{\frac{\partial_x P}{2\eta} \cdot \left(z^2 - z \cdot h\right)}_{\substack{\text{Poiseuille flow} \\ \text{(parabolic)}}} - \underbrace{z \cdot \frac{u_s}{h}}_{\substack{\text{Couette flow} \\ \text{(triangular)}}} + u_b \tag{4.1}$$

, with the sliding speed defined as $u_s \equiv (\vec{u}_b - \vec{u}_d) \cdot \vec{e}_x$. The tangential force F_f exerted on the disc $(z = h)$ can then be derivated :

$$F_f = -\vec{F}_{disc/fluid} \cdot \vec{e}_x = -\int\!\!\int dx\; dy\; \underbrace{\tau_{xz}(x, y, z = h)}_{\approx \eta \cdot \frac{\partial u_x}{\partial z}}$$

$$\text{i.e. } F_f = \underbrace{-\int\!\!\int dx\; dy\; \frac{\partial P}{\partial x} \cdot \frac{h}{2}}_{\substack{\text{Poiseuille force} \\ \to f(u_e)}} + \underbrace{\int\!\!\int dx\; dy\; \eta \cdot \frac{u_s}{h}}_{\substack{\text{Couette force} \\ \to f(\eta(P, T, \dot{\gamma}), u_s)}} \tag{4.2}$$

Poiseuille force : On the right-hand side of equation 4.2, the first term is usually referred to as the rolling resistance, or the Poiseuille force. The fluid entering between the inlet meniscus and the contact center $(-a_H < x < 0)$ is submitted to a large positive pressure gradient $\frac{\partial \mathrm{p}}{\partial \mathrm{x}}$ that tends to repel it towards the inlet. On the other side, the outgoing fluid between the center and the outlet meniscus ($0 < x < a_H$) is repelled towards the outlet because of the negative pressure difference between the contact outlet and the center. If the overall pressure gradient $\frac{\partial \mathrm{p}}{\partial \mathrm{x}}$ were perfectly balanced over the contact (i.e. $\int\int \mathrm{dx}\ \mathrm{dy}\ \partial_{\mathrm{x}}\mathrm{P} = 0$), the same global amount of fluid would be expelled towards the inlet as towards the outlet. Real EHD pressure profiles are not symmetrical. The overall pressure gradient acts in opposite to the surfaces motion (i.e. $\int\int \mathrm{dx}\ \mathrm{dy}\ \partial_{\mathrm{x}}\mathrm{P} > 0$) regardless of the sliding speed sign. This results in a global tangential force acting in the direction opposite to $\vec{u_e}$ on both surfaces.

Couette force : The second r.h.s. term of equation 4.2 is the Couette force, or traction force. It is the viscous drag force resulting from imposing a non-zero sliding speed between the surfaces. This integral involves the lubricant viscosity η and the shear rate $\dot{\gamma} = \frac{u_s}{h}$ inside the contact. Assuming the Poiseuille force (see eq. (4.2)) is independent of u_s, equation 4.2 yields :

$$\boxed{F_{f\,Couette}(u_e, |u_s|) = \frac{F_f(u_e, u_s) - F_f(u_e, -u_s)}{2}} \tag{4.3}$$

$$F_{f\,Poiseuille}(u_e, |u_s|) = \frac{F_f(u_e, u_s) + F_f(u_e, -u_s)}{2} \tag{4.4}$$

The Couette force, defined with equation (4.3), may simply be regarded as the average [absolute] friction between positive and negative sliding for equal load and rolling speed.

Poiseuille and Couette forces respective contributions to the friction In figure 4.1.a, two traction experiments are shown with the Couette force (or traction force) in solid line and the direct friction measurements at $u_s > 0$ (□) and $u_s < 0$ (×). At low entrainment speed, ($u_e = 0.02$ m/s), the film is thin and the pressure field presents a small asymmetry, as it is shown in black on fig. 4.1.b. This results in a small Poiseuille force. At higher entrainment speed ($u_e = 0.6$ m/s), the film is thicker (see interferograms fig. 4.1.c) and the EHD pressure profile spreads differently as in thin-film conditions (red line on fig. 4.1.b). It results in a more asymmetric pressure field and in a more pronounced Poiseuille force, as it is visible fig. 4.1.a. In EHL, there exists an intrinsic link between the surface separation and the pressure field such that a large film thickness always induces a larger Poiseuille force. Yet, for all experiments in EHD, the Poiseuille force is always lower than the Couette force ((45), (113)) : typically $\frac{\mathrm{F_{f\,Poiseuille}}}{\mathrm{F_{f\,Couette}}} < \frac{1}{10}$. For this reason, we focused our study on the Couette force measurements. The Couette tangential shear stress is defined as :

$$\boxed{\tau_m \equiv \frac{F_{\mathrm{f\ Couette}}}{\pi\, a_H^2}} \tag{4.5}$$

The shear rate that contributes to the Couette force corresponds to the second r.h.s. term of equation (4.1). It is calculated according to :

$$\boxed{\dot{\gamma} = \frac{u_s}{h_c}} \tag{4.6}$$

, where h_c is calculated using eq. (2.15).

4.1.3 Shear-thinning rheological models

At low shear rates, τ_m increases linearly with $\dot{\gamma}$: this corresponds to the Newtonian shear regime. The slope of the τ_m vs $\dot{\gamma}$ curve , referred to as the low-shear viscosity, is only determined by the pressure and the temperature. The Roelands law (eq. (2.4)) is the most widely used pressure-viscosity relationship allowing a quite good estimate of the low-shear viscosity in isothermal contacts.

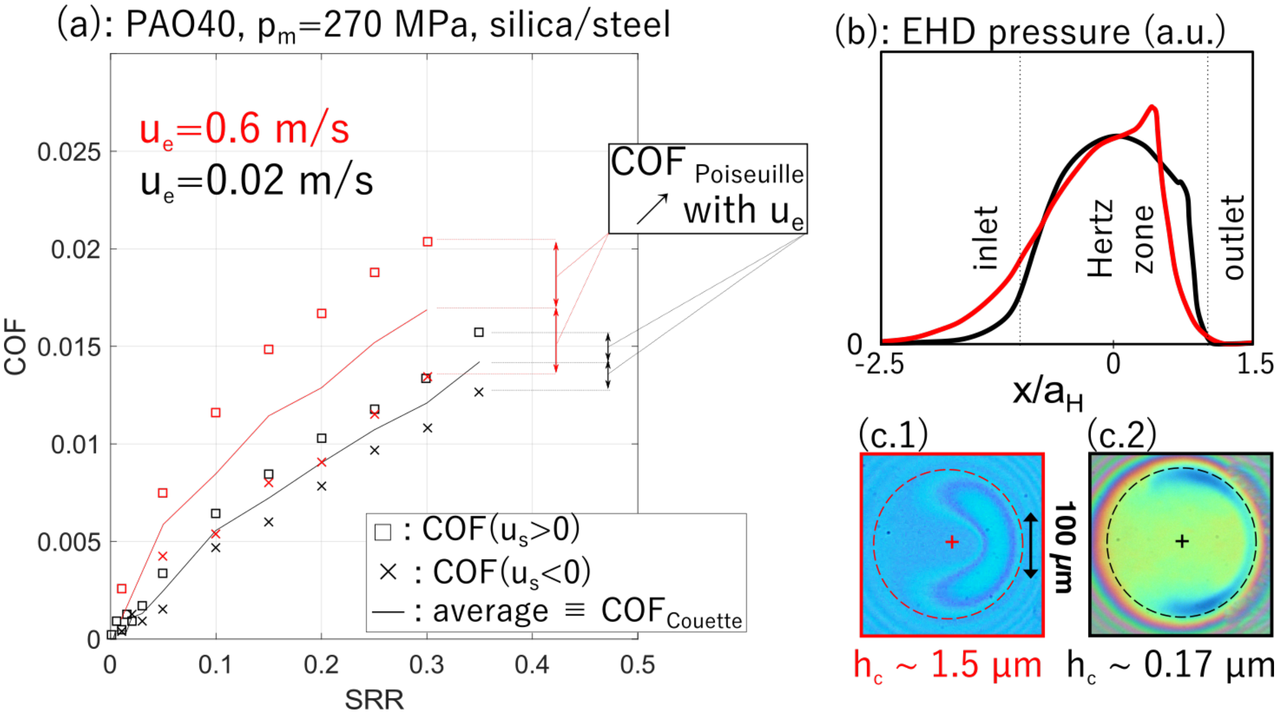

Figure 4.1: (a) : Evolution of the Couette and the Poiseuille forces during traction experiments with two lubricants at $p_m = 270$ MPa with smooth surfaces and PAO40 at two entrainment speeds. The symbols correspond are the time-averaged absolute force according to the sign of the sliding speed. The solid lines correspond to the average between positive and negative sliding, referred to as the traction, or Couette friction coefficient. (b) : one-dimensional EHD pressure profiles corresponding to the two entrainement speeds. (c) : In situ interferograms captured during the traction experiments.

However, the thin films obtained in EHL cause shear rates typically in the range $10^5 - 10^7$ s^{-1} (121). At such high shear rates, a decrease of the τ_m vs $\dot{\gamma}$ slope is observed, i.e. the lubricant shear-thins. This is reflected in a yielding of the traction force versus the slide-to-roll ratio as illustrated fig. 4.1. Some rheological models commonly used in the litterature are shortly reviewed in the following parts.

4.1.3.1 Lubricant shear strength

Bair and Winer (9) introduced a viscous-plastic model where the shear stress is separated into an elastic part and a non-linear viscous one. In the limiting case where the elastic stress becomes negligible, the shear stress-shear rate relationship takes the form :

$$\tau = \tau_{max} \left(1 - e^{-\frac{\eta\dot{\gamma}}{\tau_{max}}}\right) \tag{4.7}$$

At sufficiently high shear rates, the viscous shear stress reaches a plateau, referred to as the lubricant strength τ_{max}. At this point, increasing the shear rates lets the viscous stress unchanged : the fluid speed gradients become heterogeneous and the shearing only occurs between two fluid layers (7).

The reasons invoked for this plastic behaviour are generally related to the appearance of shear bands in the film (13). These may be caused by temperature rises localized on a small fluid layer which viscosity becomes significantly reduced (26). Shear bands may also appear in isothermal conditions considering the pressurized fluid as a solid material having a given coefficient of internal friction. Tensile failure appears when there exist a plane in which the ratio of tangential to normal stress overcomes this internal friction coefficient. (6), (16) thus measured failure angles in lubricant films showing shear banding. Within a Mohr-Coulomb failure criterion formulation, they calculated internal friction coefficients $\sim 10^{-1}$ for several fluids. Even though the physical origin of fluids internal friction coefficient is still under research (16), many fluids exhibit a limiting shear stress (120) that is roughly proportional to the pressure (9), (124), (113), (11), (7). Furthermore, fluids shear strength was recognized to be little dependent on temperature (11)[1], (113).

$$\tau_{max} = \Lambda_{lubricant} \times p_m \qquad \text{with } \Lambda_{lubricant} \approx \ 0.05 - 0.1 \tag{4.8}$$

4.1.3.2 Non-linear viscous models

Eyring model In 1936, Eyring (48) proposed a theoretical model relating the shear stress and the shear rate in a viscous fluid. The fluid layers motion is considered as a kinetic thermal activated process between periodically organized molecules. Denoting the fluid low-shear viscosity with η_E, the tangential stress and the shear rate become related with :

$$\tau = \tau_0 \ \text{asinh}\left(\frac{\eta_{\text{E}}\,\dot{\gamma}}{\tau_0}\right) \tag{4.9}$$

In spite of its simplifying assumptions, the Eyring model has the advantage of correctly describing the rheological behaviour of many fluids (121) with only two parameters. The Eyring model was used to fit fluids rheograms by several authors. The Eyring[2] stress, τ_0, determines the characteristic stress above which the lubricant shear thins. For many fluids, it was observed that τ_0 is generally the order a few MPa (68), (17, p.12). τ_0 generally increases linearly with pressure, with a slope close to 0.01. (45), (71), (96).

---

[1] Bair and Winer (11) proposed $\Lambda_{5P4E} = 0.095 - 0.00035 \times T$ for the 5P4E.

[2] Also called the Newtonian limiting shear stress

Cross model Cross (34) developped a model for the fluid viscosity based on links kinetics between linear chains. He derivated a shear stress- shear rate relationship depending on 4 parameters relating the viscous shear stress to the shear rate :

$$\tau = \dot{\gamma}\left(\eta_\infty + \frac{\eta_\mathrm{C} - \eta_\infty}{1 + \left(\frac{\dot{\gamma}}{\dot{\gamma}_\mathrm{c}}\right)^{\mathrm{n_c}}}\right) \tag{4.10}$$

In this model, two Newtonian regimes exist respectively when $\dot{\gamma} \to 0$ and $\dot{\gamma} \to \infty$. η_C is the low-shear viscosity, η_∞ is the infinite shearing viscosity, $\dot{\gamma}_c$ is a critical shear rate separating the two regimes and n_C is an exponent or the order 1. There exist numerous similar rheological models allowing a shear-thinning response, most of them are presented in (17).

4.1.3.3 Viscoelasticity

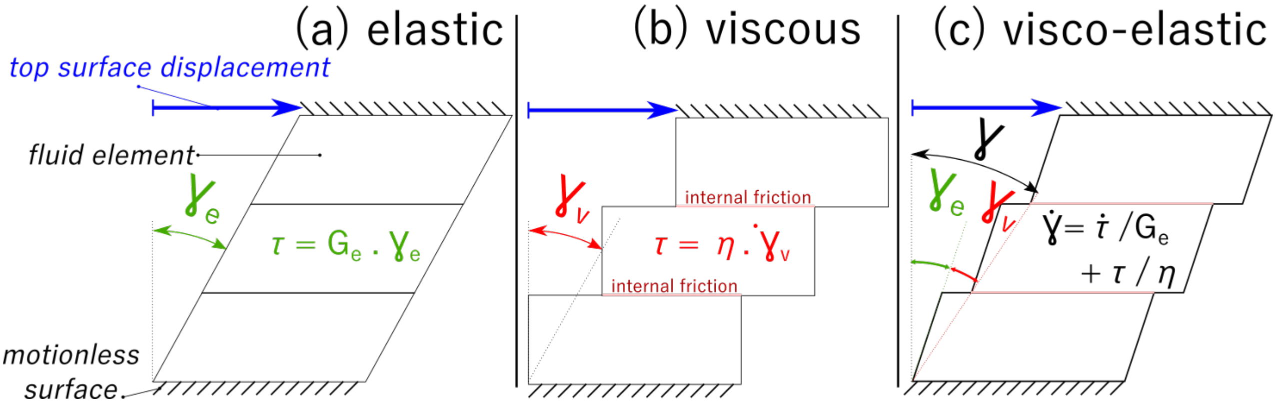

Figure 4.2: Schematic of fluid layers under shear showing from left to right a purely elastic (a), purely — Newtonian— viscous (b) and a viscoelastic (c) behaviour.

Lubricants are polymeric fluids and have at least one relaxation time. Johnson and Tevaarwerk (71) indicate that depending on the rate at which the fluid crosses the high pressure area, it may be put out of equilibrium and behave partially as an elastic solid. (71) modelled the fluid response using a Maxwell damper and a spring in series representing respectively the fluid viscous dissipation and its tangential elastic response, accounted for with a shear modulus G_e. Figure 4.2.a, 4.2.b and 4.2.c depict purely elastic, purely viscous and viscoelastic behaviours respectively. Applying this decomposition to a given fluid element as those represented figure 4.2.c yields :

$$\dot{\gamma}_v = f_v(\tau) \tag{4.11}$$

$$\gamma_e = \frac{\tau}{G_e} \tag{4.12}$$

$$\dot{\gamma} = \dot{\gamma}_v + \dot{\gamma}_e \tag{4.13}$$

For a Newtonian fluid, $f_v(\tau) = \frac{\tau}{\eta(P)}$. Johnson and Tevaarwerk (71) assumed an Eyring relationship : $f_v(\tau) = \frac{\tau_0}{\eta_E}\, sinh\left(\frac{\tau}{\tau_0}\right)$. The latter equations were derived considering a given fluid element in motion in the fluid flow, the time derivatives are hence convective ones : $\dot{\tau} = \partial_t \tau(x,t) + u_e \partial_x \tau(x,t)$. If we consider a stationary flow ($\partial_t \tau = 0$), eq. (4.13) takes the dimensionless form (58) :

$$\underbrace{\frac{\dot{\gamma} a_H G_e}{u_e \tau_0}}_{\text{dimensionless total shear rate}} = \underbrace{\frac{sinh(\tau/\tau_0)}{D_e}}_{\text{viscous shear rate}} + \underbrace{\frac{d(\tau/\tau_0)}{d(x/a_H)}}_{\text{elastic strain rate}} \tag{4.14}$$

where D_e is the Deborah number :

$$D_e \equiv \frac{\eta_E \, u_e}{G_e \, a_H} \tag{4.15}$$

Equation (4.14) shows that the elastic strain is important when $D_e >> 1$ whereas the fluid response becomes viscous when $D_e << 1$. Piezoviscous fluids have a large viscosity and therefore usually raise Deborah number superior to one. For such fluids, Johnson and Tevaarwerk report that even at small shear rates, friction can not be purely viscous, which makes difficult the measurement of the low-shear viscosity with sliding rolling experiments.

It may be noticed that the Deborah number definition does not include any shear-related quantity such that a large Deborah number can be obtained even when no sliding is introduced between the surfaces. An other dimensionless number is often found in the rheology literature, called the Weissenberg number :

$$W_{eiss} \equiv \frac{\eta \, \dot{\gamma}}{G_e} = D_e \times SRR \times \underbrace{\frac{a_H}{h}}_{>>1} \tag{4.16}$$

Bair (8) thus used the Weissenberg number in the inlet to evaluate the importance of inlet shear thinning. Habchi et al. (61) considered that shear thinning in the contact area becomes important when $W_{eiss} > 1$. However, in the lubrication hypotheses, $\frac{h}{a_H}$ is very inferior to unity, such that for even operating conditions, the Weissenberg number is typically 100 times higher than the Deborah number. Comparing W_{eiss} or D_e to 1 therefore leads to different conclusions towards the importance of elastic to viscous forces, which discredits the practical use of at least one of these two dimensionless numbers.

According to Poole (105), D_e is the ratio between the fluid relaxation time and an observation time — here, the fluid transit time $\frac{a_H}{u_e}$, across half the contact area — during which it is implicitely assumed that the fluid experiences a deformation in the Lagrangian sense. The Deborah number is a measure of flow unsteadiness (105). Stationary EHD flows where the shear rate is steady should thus yield a zero Deborah number. However, the fluid flow steadiness is not directly related to a constant stretch history for fluid particles according to Marrucci and Astarita (90).

Under certain assumptions, the Weissenberg number equals the ratio of elastic to viscous forces applied to a fluid element (105) and may be interpreted as the rate of recoverable strain (105), (43). Dealy (36) wrote that the Weissenberg number compares the fluid relaxation time to a time characteristic of the fluid deformation rate, $\frac{1}{\dot{\gamma}}$, whether pure shear or pure elastic deformation be considered. According to the way D_e and W_{eiss} are interpreted in the literature, Dealy (36), (43), (90), (105), which of both is the most appropriate to account for the occurence of viscoelasticity remains unclear.

An other major pitfall to evaluate the importance of elastic forces is the lack of knowledge for lubricants shear moduli G_e which dependence towards temperature and pressure is not well-known (113), (45). An estimation of G_e was proposed by Tabor (124) :

$$G_e(P) \approx 30 \cdot \tau_{max} \tag{4.17}$$

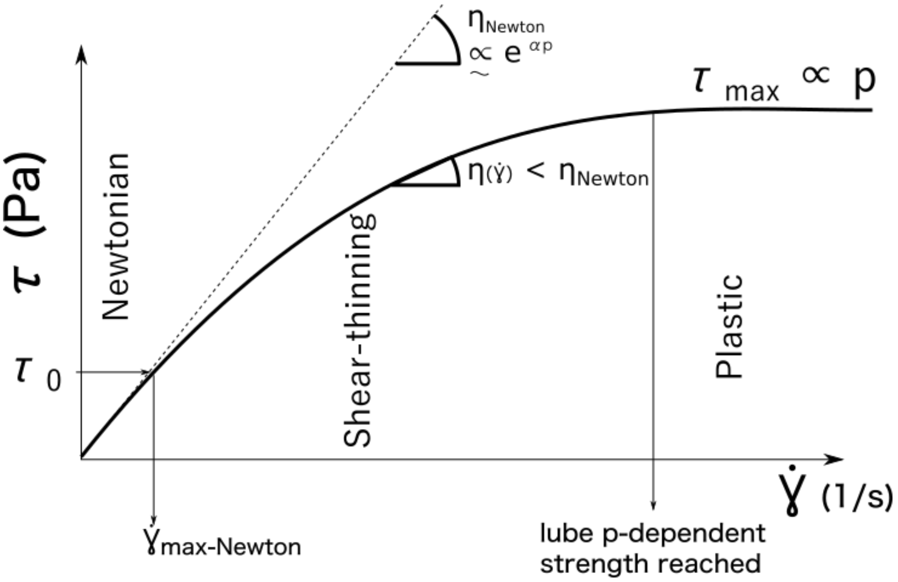

Figure 4.3: Typical features of a the shear stress-shear rate relationship during a traction experiment corresponding to different shearing regimes : a linear evolution at low sliding (Newtonian), then the rheograms becomes concave (shear thinning) and saturates at a given plateau (plastic).

Even though this relationship is consistent with the shear strength of crystalline theories and with some oscillatory shear measurements, this can only provide a rough estimation of a fluid shear modulus. These remarks discourage the consideration of viscoelasticity in the rheological description of the present lubricants.

4.1.3.4 Summary

For the present experiments, three features must be captured to correctly reproduce the apparent evolution of the lubricant shear stress with pressure, temperature and shear rates :

- A linear evolution at low shear rates.
- At higher shear rates, the yielding of the shear stress-shear rate curve.
- At infinite shear rates, the lubricant stress presents a plateau towards $\dot{\gamma}$.

These features are represented fig. 4.3.

Given the unknown values for PAOs' shear moduli under pressure and the abovementionned physical issues about the occurrence of visco-elasticity, a time-independent non linear viscous description was chosen.

Even though a rheological equation such as the Cross model is likely to provide better fits for it contains 4 ajustable parameters, the Eyring asinh law seems more robust precisely because it involves fewer parameters : the Newtonian limiting shear stress τ_0 and the low-shear viscosity η_E. Contrary to the four-parameter Cross law, the two-parameter Eyring law does not allow to reproduce the stress plateau. Yet, the lubricant rheology can be described in the manner proposed by (15) with the hybrid expression (4.18) where both τ_0 and η_E depend on pressure and temperature a priori :

$$\tau_{\mathrm{m}} = \min \left\{ \quad \Lambda_{\mathrm{lubricant}} \cdot \mathrm{p_m} \quad ; \quad \tau_0(\mathrm{p_m}, \mathrm{T}) \ \mathrm{asinh} \left(\frac{\eta_{\mathrm{E}}(\mathrm{p_m}, \mathrm{T}) \ \dot{\gamma}}{\tau_0(\mathrm{p_m}, \mathrm{T})} \right) \quad \right\} \tag{4.18}$$

, where τ_m is defined by eq. (4.5).

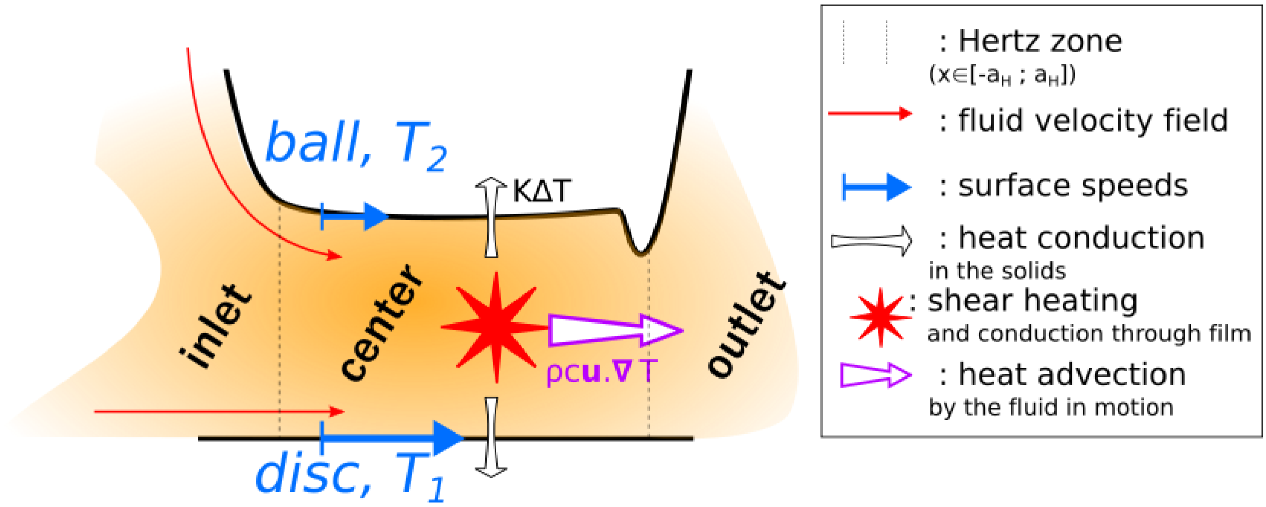

Figure 4.4: Schematic representation of different heat flows in the contact. The heat $q_v = \tau\,\dot{\gamma}$ is almost completely generated in the Hertz area because of the combined high shear stress and shear rates.

4.1.4 Contact temperature rise

Crook (33) considered a Newtonian fluid and showed that apparent thinning can occur only because of fluid being increasingly warmed as the sliding is increased. The advances in thermal EHD have permitted to identify three important notions about temperature rises :

- *lubricant temperature rise :*

  [◇] In the inlet, which affects the film thickness by thinning the lubricant before it enters the high-pressure area (see section 2.2.4.2).

  [◇] In the high-pressure zone due to viscous shear heating $q_v = \tau \cdot \dot{\gamma}$ per unit fluid volume.

- *Surface temperature rise :* depending on the time spent inside the contact, a given element of surface will receive a different amount of heat dissipated in the contact. These surface temperature rises are called *flash temperature rises.*

4.1.4.1 Lubricant temperature rise inside the high-pressure area

For a line contact at a few hundreds MPa, Crook (33) considered separately heat conduction in the solids and heat advection by the fluid constantly renewed in the contact (see fig. 4.4). He concluded that the heat evacuation out of the contact is dominated by conduction. Because the film is thin compared to its lateral extent[1], the heat flow in the pressurized lubricant is almost completely due to conduction in the z direction, which simplifies the energy equation. Denoting D_l and K_l the fluid thermal diffusivity and conductivity[2], heating is produced at a rate per unit volume $q_v = \tau\,\dot{\gamma} = q_s/h$, where q_s is the heat rate per unit contact area. The temperature is governed by the one-dimensional heat equation :

$$\frac{1}{D_l}\frac{\partial T}{\partial t}(z,t) - \frac{\partial^2 T}{\partial z^2}(z,t) = \frac{q_v}{K_l} \tag{4.19}$$

---

[1] Under the lubrication hypotheses.

[2] For oils, $D_l \sim 10^{-4} - 10^{-6}$ m^2/s, $K_l \sim 10^{-1}$ W/(m.K) and $c_l \sim 10^3$ J/(kg.K) (122, p.34) : heat capacity of mineral oils $\sim$ 1600 J/(kg.K).

The surface temperatures (at $z = 0$ and $z = h$) are assumed constant and are denoted T_s. The lubricant initial temperature is assumed equal to T_s. If q_v is constant, turned on from $t = 0$ homogeneously over the contact area, the solution was provided by Carslaw and Jaeger (24, p.130) :

$$\Delta T_l(z,t) \equiv T_l(z,t) - T_l(z,0) = \frac{q_v}{2K_l}\left(zh - z^2 - \sum_{n=0}^{\infty} \frac{sin(\frac{(2n+1)z\,\pi}{h})}{(2n+1)^3} e^{-\frac{t\,D_l \pi^2}{h^2}(2n+1^2)} \right) \tag{4.20}$$

The maximum temperature rise at mid-height ($z = h/2$) in the lubricant film can be deduced from eq. (4.20) :

$$\boxed{\Delta T_{l\;max} = \frac{q_v\,h^2}{8K_l} = \frac{q_s\,h}{8\,K_l}} \tag{4.21}$$

and the average temperature rise across the film thickness is :

$$\Delta T_{l\;av} \equiv \frac{1}{h}\int_0^h dz\,\Delta T_{(z,\,t\to\infty)} = \frac{q_v\,h}{12\,K_l} \tag{4.22}$$

Equations (4.21) (4.22) apply only if enough time elapsed so the heat transfer between the contact and the isothermal bodies is established. From eq. (4.20), the steady conduction characteristic time is :

$$t_{\text{l cond z}} \equiv \frac{h^2}{D_l} \tag{4.23}$$

This time may be compared to the lubricant transit time through the contact :

$$\frac{t_{\text{l cond z}}}{t_{\text{ transit}}} = \frac{h^2/D_l}{2a_H/u_e} = \begin{cases} \sim 10^{-1} & \text{in the thickest (1 } \mu\text{m) films} \\ \sim 10^{-10} & \text{in the thinnest (1 nm) films} \end{cases} \tag{4.24}$$

According to Archard (5), it can be shown that the lubricant reaches 95% of its maximum value when the latter ratio becomes 0.3. The lubricant temperature thus follows almost instantly the surface temperature variations. Finally, Archard discussed the hypothesis made by (24) to obtain eq. (4.21), according which the heat generation is homogeneous across the film thickness. The opposite case would be that of heat generation only occuring in the plane at mid-height in the film thickness, like when thermal shear banding occurs. This results (5) in twice the maximum temperature rise of eq. (4.21). Similarly, the average and maximum temperature rises (equations (4.21) and (4.22)) only differ from a factor 1.5. Equation (4.21) will thus be used to estimate the lubricant temperature in the contact area.

For symmetrical surfaces, as long as the surface temperature variations occur on time scales large to $t_{\text{l cond z}}$, the lubricant temperature may be obtained according to :

$$T_l = \underbrace{T_s}_{\text{surface temperature}} + \underbrace{\Delta T_{l\;max}}_{\text{eq. (4.21)}} \tag{4.25}$$

In order to correctly estimate the lubricant temperature, it is now necessary to examine the transient heat transfer between the contact area and the moving solid bodies.

material	D_s ($m^2.s^{-1}$)	K (W.m^{-1}K^{-1})	c_s (J.kg^{-1}K^{-1})	ρ_s (kg.m^{-3})
Steel AISI 52100	1.2×10^{-5}	46.6	477	7850
Steel M2	7.0×10^{-6}	24	420	8160
Fused silica (Spectrasil 2000)	8×10^{-7}	1.3	733	2203
Sapphire	7.6×10^{-6}	23.1	760	3980
DLC Certess DDT	4×10^{-7}	0.6 from (19)	700 from (19)	2×10^3

Table 4.1: Thermal properties of the materials used in the present study. D, K, c_m, ρ are the diffusivity, the thermal conductivity, the specific heat capacity per unit mass and the density.

4.1.4.2 Flash temperatures : transient conduction in bodies

During a friction test at constant surface speeds, heat is dissipated in the high-pressure area at a rate $Q = F_f \times u_s$. If the shear rates are homogeneous over the contact area, the sheared lubricant may be assimilated to a homogenous heat source per unit area $q_s = \frac{F_f}{A_{nom}} u_s$. Figures 4.5.a and 4.5.b represent a solid body in contact with a motionless heat source and with a heat source moving at speed U. The following dimensionless number was introduced by Jaeger (70) :

$$J \equiv \frac{a\,U}{D_s} \tag{4.26}$$

For the materials and speeds used in our experiments, J lies within $[10^{-2}\,;\,10^0]$ (see table 4.1).Jaeger (70) solved this thermal problem (see annex 9.1) and provided average and maximum surface temperature rise formulas in the two opposite cases where the heat source moves slowly and fast, that correspond respectively to $J << 1$ and $J >> 1$. The spatially-averaged temperature rise formulas only differ with the maximum temperature formulas by numerical factors of the order 10^0 and similar results are obtained for square and circular sources. Later, Greenwood (54) proposed a rule of thumbs to interpolate Jaeger (70)'s results for the intermediate speeds. On figure 4.6, the flash temperature rises corresponding to eq. (4.27) are plotted for different values of dissipated heat (on a contact of radius $a = 100$ μm), for speeds up to 100 m/s and for different heating rates $Q \in [10^{-3}\,;\,1]$ W typical of EHD experiments. The slower the surface, the warmer it gets. These results may be extended to the case of two surfaces crossing a circular heated area of radius a, assuming the heat Q is evenly shared between the two bodies :

$$\Delta T_{flash\,max} = \frac{1}{2}\frac{Q}{a\,K_s} \times \begin{cases} 1/\pi & \text{for } J < 0.1 \\ 0.508/\sqrt{J + 2.546} & \text{for } 0.1 < J < 10 \\ \sqrt{8/(\pi^3\,J)} & \text{for } 10 < J \end{cases} \tag{4.27}$$

The previous flash temperature formula (eq. (4.27)) applies once the heat transfer between the contact and the bodies reached a stationary state. Furthermore, these flash temperature rises do not account for the air convection that tends to cool the surfaces down. In experiments, the flash temperature formulas must hence be considered as upper boundaries for the surfaces temperature.

4.1.5 Choice of experimental conditions to measure fluids isothermal rheology

The purpose of the previous thermal considerations is to choose optimal experimental conditions to measure the lubricant rheology in isothermal conditions. The only thermal parameter that must be used for the lubricant temperature rise is the oil thermal conductivity K_l. According to hot-wire measurements under pressure (77), (78), the thermal conductivity of several lubricants increases slowly with pressure according to :

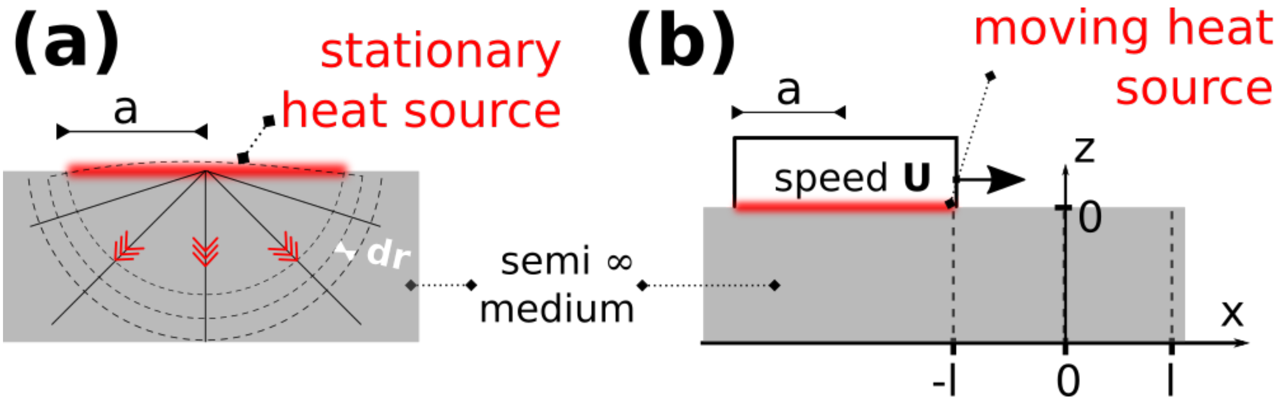

Figure 4.5: Rectangular heat source in motion on a semi infinite solid. (a) : For a slowly moving surface in contact with a constant heat source, an analogy with the Ohm law can be drawn using the concept of constriction resistance. The contact surface and the body medium at infinity play the role of equipotential surfaces. When the surface is stationary, heat conduction is only limited by the smallness of the contact area between the source and the body and the material thermal resistivity. The heat flow in the bulk material, of conductivity K_s, can be modelled as a series of infinitesimal hemispheres of width dr that constitute thermal resistances in series. (b) : When the surface motion is sufficiently fast, the body heating becomes also limited by the time spent in contact with the warm source. This transient problem was solved in various geometries by (70).

$$K_l = K_0 \left(1 + \frac{c_1\, p}{1 + c_2\, p}\right) \tag{4.28}$$

As an example, a fully formulated PAO yields the values $K_0 = 0.154$ W/(K.m), $c_1 = 1.72 \times 10^{-9}$ W/K/m/Pa, $c_2 = 0.54 \times 10^{-9}$ 1/Pa (77). Using these values between $p = 1$ MPa and $p = 1$ GPa, this yields an increase of about 1.8 in K_l. Since the present lubricants are not exactly the same as those studied by (78), we use for all PAOs $K_l = 0.154$ W/(m.K) and neglect the increase due to pressure. During experiments, the dissipated heat takes values superior to 10^{-3} W and sometimes overcomes 0.1 W in fully lubricated conditions at the largest pressures. Figure 4.7.a shows the surface maximum flash temperature rise assuming AISI 52100 steel surfaces and figure 4.7.b shows the lubricant maximum temperature rise versus the film thickness and the heat for the present conditions, using the largest contact diameter $a_H = 167$ μm.

On the one hand, a large entrainment speed reduces the surface temperature rise as $T_s - T_{amb} \underset{\sim}{\propto} \frac{Q}{\sqrt{u_e}}$. On the other hand, when u_e is large, a thick film is generated, which increases the fluid temperature as $\Delta T_l - T_s \propto Q \times h$.

The lubricant temperature rise is reached in a few microseconds to a few milliseconds whereas the applicability of flash temperature rise calculations requires that the surface motion has run during a time long enough so the heat flux field reached a stationary state in the solid bodies. It would be illusory (or cumbersome) to reliably calculate this duration as it depends on many parameters such as the bodies tridimensional geometries, air convection and the amount of fluid in the reservoir. The experiments indicate that this duration must be superior to a few minutes since the only cases where body warming was noticed were for experiments lasting more than 30 minutes.

The heat flux steady state is thus more rapidly reached in the lubricant film than in the surfaces, which makes the condition on the film thickness more restrictive than that over the surface speed. Furthermore, figure 4.6 and 4.7.a show that the reduction in flash temperature rise obtained by increasing the surface speed is a second-order effect compared to the influence of the heat $Q = \tau_m \times \pi a_H^2 \times u_s$, which can not be estimated without the lubricant friction properties. Assuming

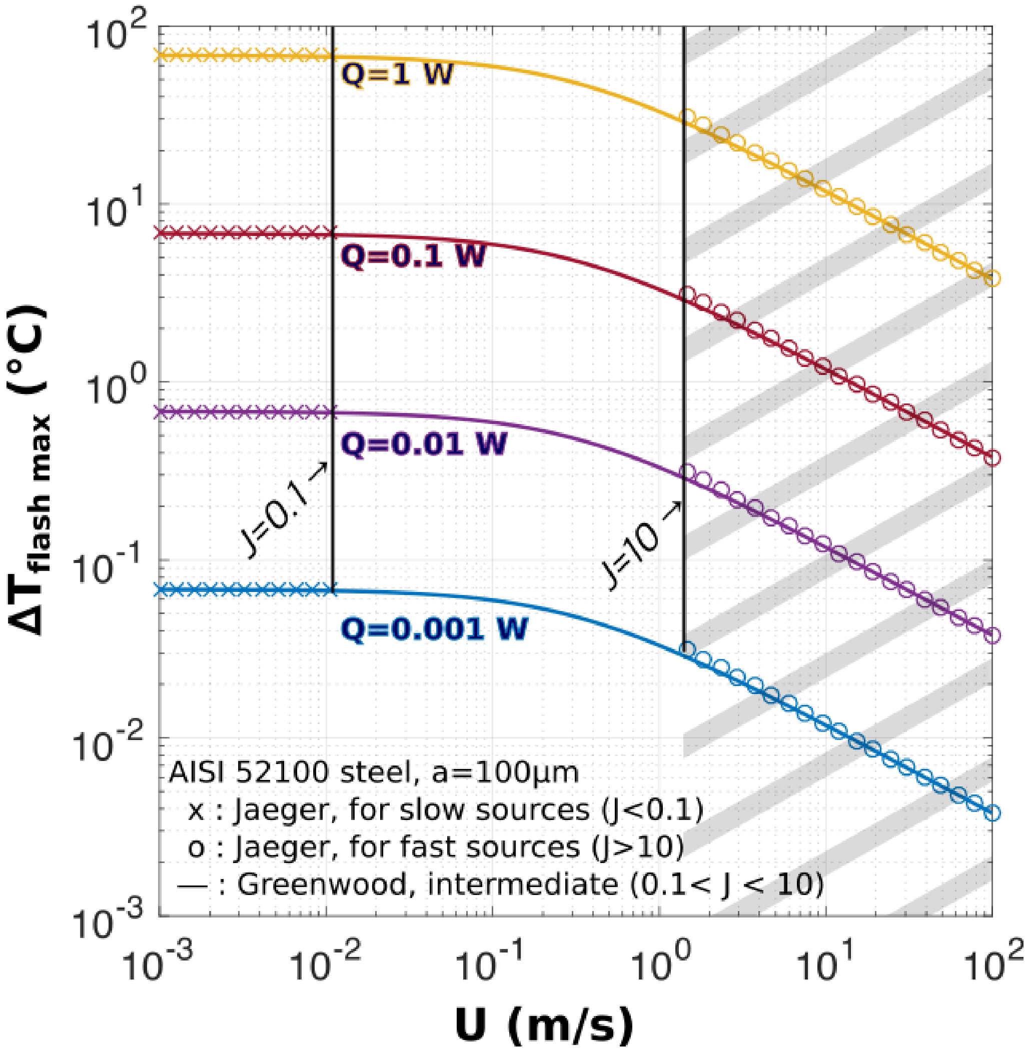

Figure 4.6: Illustration of the impact of the dissipated heat Q on a circular contact of radius $a = 100\ \mu$m using the properties of AISI 52100 steel. The maximum flash temperature rise for a slow source (70) ((x) : eq. (9.5)), for a fast source ((o) : eq. (9.8)), and the interpolation for the intermediate conditions $0.1 < J < 10$ proposed by (54) ((-): (9.10)). For each color, the heat source Q is assumed constant. The slower the source, the warmer it gets because the time spent by each surface element is increased as the body speed U is decreased.

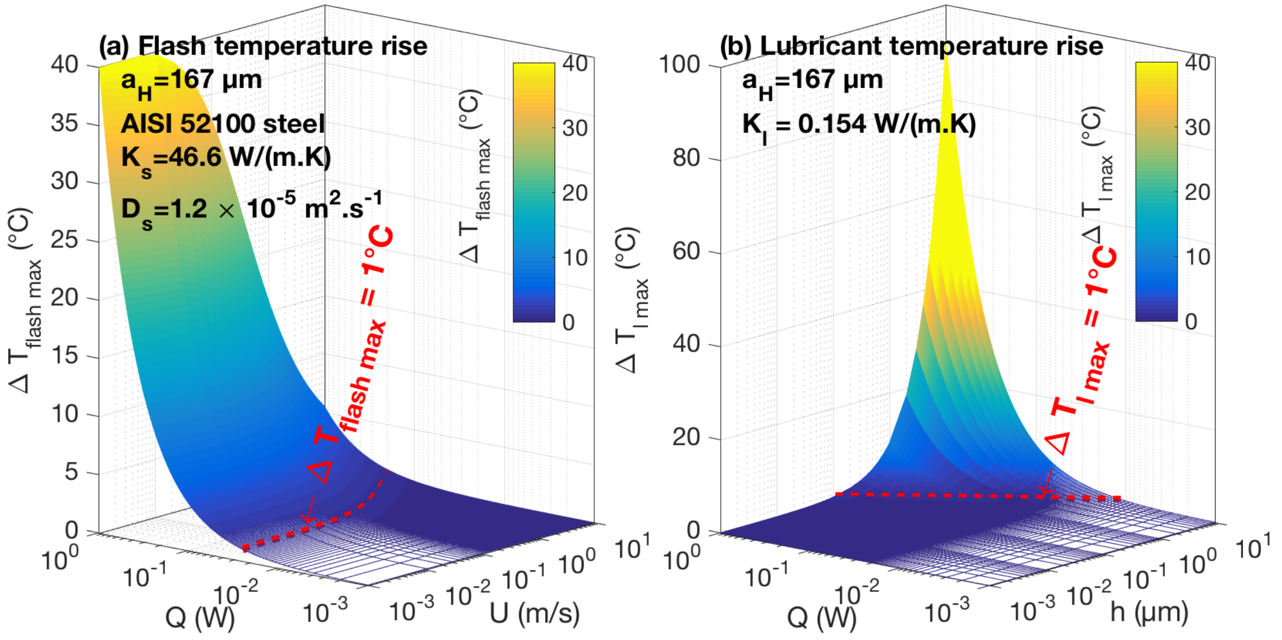

Figure 4.7: (a) : Maximum flash temperature rise versus the surface speed and the dissipated heat. (b) : Maximum lubricant temperature rise (eq. (4.21)) versus the film thickness and the dissipated heat. Red dotted curves correspond to a temperature rise of 1°C.

$Q = 1$ W implies a film thickness inferior to 0.1 μm. The entrainment speed for the traction tests on PAO4 and PAO40 are chosen to generate films about 0.1 μm-thick.

4.2 Building the fluid theoretical rheological law

4.2.1 Traction experiments at different pressures

To investigate the influence of pressure on fluids rheology, thin-film tractions with PAO40 (respectively, PAO4) were performed with an entrainment speed equal to 0.02 m/s (resp. 0.2 m/s), for $p_m = 310$, 440, 500, 750 and 860 MPa and a temperature of 22 °C (resp. 22 °C). The film thicknesses lied in the range 0.130-0.160 μm (respectively 0.06-0.07 μm). Again, this allows to ensure that the lubricant temperature does not increase by more than 1°C compared to the surfaces temperatures.

Using these entrainment speeds, the maximum flash temperature rise at $SRR = 2$ reaches values of 5°C and 34°C using respectively $u_e = 0.02$ m/s and $u_e = 0.2$ m/s at the highest pressure ($p_m =$ 860 MPa) and calculating the heat as $Q = p_m \times \pi a_H^2 \times COF \times\ SRR \cdot u_e$ with an overestimated friction coefficient of 0.08. These temperature rises are small but not negligible. In order not to reach the steady conduction state assumed for the derivation of the flash temperature rise formulas, short-time experiments are performed using speed ramps instead of speed steps. The traction total duration was 5 minutes for the most lengthy and 2 minutes for the shortest ones. Moreover, to get a better resolution in the range of shear rates where the friction increases the most, i.e. at low shear rates, the speed ramps were two or three times longer from $SRR = 0$ to $SRR = 0.1$ than from $SRR = 0.1$ to $SRR = 2$.

These thin-film tractions are displayed in figures 4.8.a and 4.8.b and will be used as a reference to measure lubricants rheology.

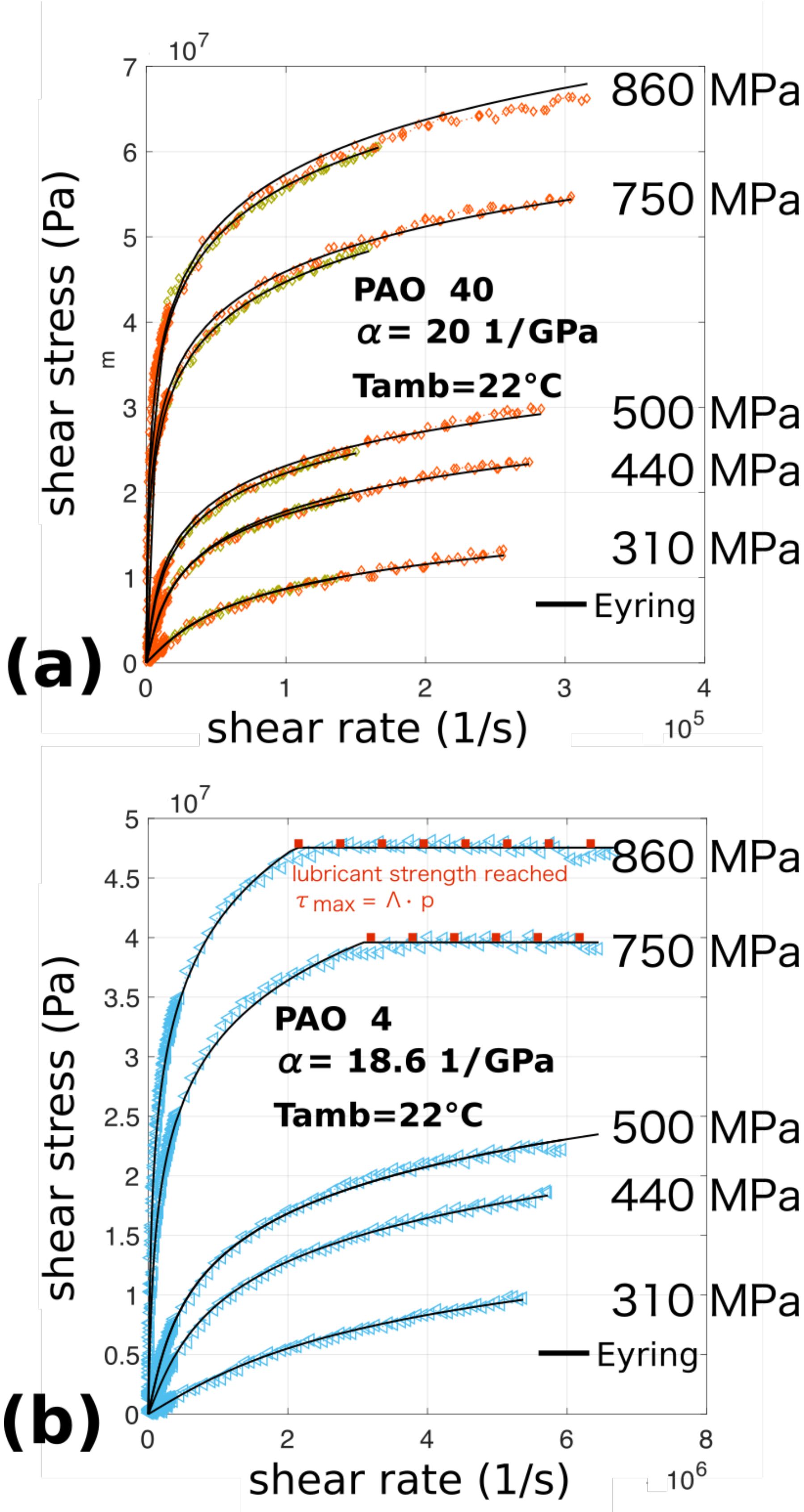

Figure 4.8: Traction experiments with polished steel surfaces with (a) PAO40 and (b) PAO4. Each traction curve is interpolated according to an Eyring (-) law. Tractions at 750 and 860 MPa with PAO4 exhibit the lubricant shear strength τ_{max}, the fitting domain was restricted for these tractions.

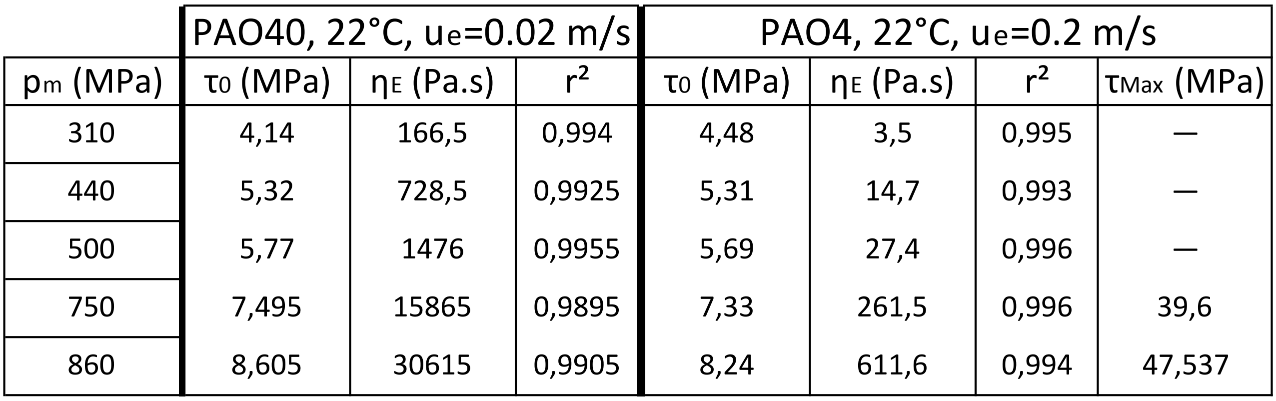

	PAO40, 22°C, u_e=0.02 m/s			PAO4, 22°C, u_e=0.2 m/s			
p_m (MPa)	τ_0 (MPa)	η_E (Pa.s)	r^2	τ_0 (MPa)	η_E (Pa.s)	r^2	τ_{Max} (MPa)
310	4,14	166,5	0,994	4,48	3,5	0,995	—
440	5,32	728,5	0,9925	5,31	14,7	0,993	—
500	5,77	1476	0,9955	5,69	27,4	0,996	—
750	7,495	15865	0,9895	7,33	261,5	0,996	39,6
860	8,605	30615	0,9905	8,24	611,6	0,994	47,537

Figure 4.9: Fitted Eyring parameters on smooth thin-film tractions with polished steel surfaces using the PAO40 (two experiments for each pressure) and the PAO4.

Fluid	τ_{00} (MPa)	$\mathbf{a}_{\tau_0}$ (·)	$\mathbf{a}_{\eta_E}$ (S.I.)	$\mathbf{b}_{\eta_E}$ (S.I.)
PAO 40	1.436	8.646×10^{-3}	$e^{-91.62}$	4.944
PAO 4	1.907	7.561×10^{-3}	$e^{-95.75}$	4.956

Table 4.2: Parameters for eq. (4.29), descriptive of the lubricant Eyring stress τ_0 and viscosity η_E according to eqs. (4.30), (4.29).

4.2.2 Pressure-dependent rheology

The traction experiments plotted fig. 4.8 exhibit a pronounced shear-thinning. They are interpolated with an Eyring model (eqs. (4.9)) and the fitted parameters are tabulated fig. 4.9.

PAO4 shear strength The PAO4 tractions at 750 MPa and 860 MPa exhibit the lubricant limiting shear strength $\tau_{max} = \Lambda_{PAO4}\, p_m$, reached around $\dot{\gamma} \gtrsim 2 \times 10^5$ 1/s. For these two traction curves, the corresponding shear stress plateau and its standard deviation are plotted on the top-right corner of fig. 4.10. According to these traction experiments on PAO4, an affine fit of τ_{max} versus p_m yields : $\tau_{max} = -16.2 \times 10^6 + 0.074 \times p_m$. Given the small pressure range where this shear strength was observed, a simple linear fit is more reliable : $\Lambda_{PAO4} \equiv \frac{\tau_{max}}{p_m} = 0.054 \pm 0.002$. Jacobson (69) indicates a shear strength versus pressure slope of 0.054 and 0.055 for PAOs at 20°C, which makes the present value of Λ_{PAO4} consistent with the literature.

Eyring stress versus pressure Figure 4.10 shows the Eyring stress τ_0 versus the pressure (circles). For the two lubricants, the evolution of τ_0 with p_m is close to linear with a slope approximately equal to 0.008. Table 4.2 gives the affine fit parameters τ_{00}, a_{τ_0}.

$$\tau_0(\mathrm{p_m}) = \tau_{00} + \mathrm{a}_{\tau_0} \cdot \mathrm{p_m} \tag{4.29}$$

In figure 4.11, the Eyring stress is compared to those obtained for different fluids from the litterature (71), (45), (76), (96). For these fluids, the τ_0 vs p_m slopes lie from 0.001 to 0.013, which is compatible with those obtained in the present study.

Low-shear viscosity parameters The low-shear viscosity parameters η_E, from the Eyring fits are plotted versus the pressure in fig. 4.12.

The Roelands viscosity (eq. (2.4)), calculated and added on graphs 4.12.a and 4.12.b is smaller than the Eyring viscosity. The difference could be attributed to the pressure-viscosity coefficients α

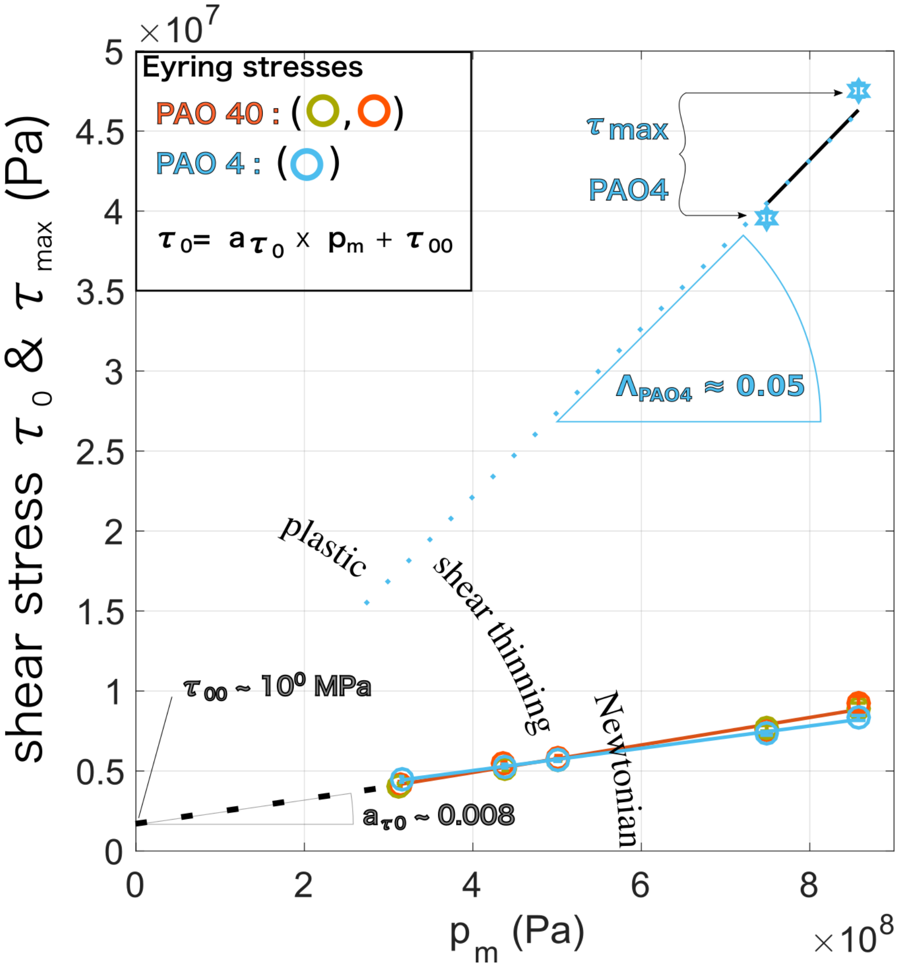

Figure 4.10: Lubricant shear stress properties extracted from traction experiments with smooth steels. The circles are the Eyring stress τ_0 versus the mean Hertz pressure for the PAO40 and the PAO 4. The errorbars (o) correspond to a confidence interval of 95 % for τ_0. On the top-right corner, the PAO 4 limiting shear strength τ_{max} is plotted with its standard deviation in errorbars std(τ_{max}) $\approx$ 0.4 MPa. For the two lubricants, the Eyring stress is interpolated with an affine law w.r.t. the contact pressure ($r^2 > 0.98$).

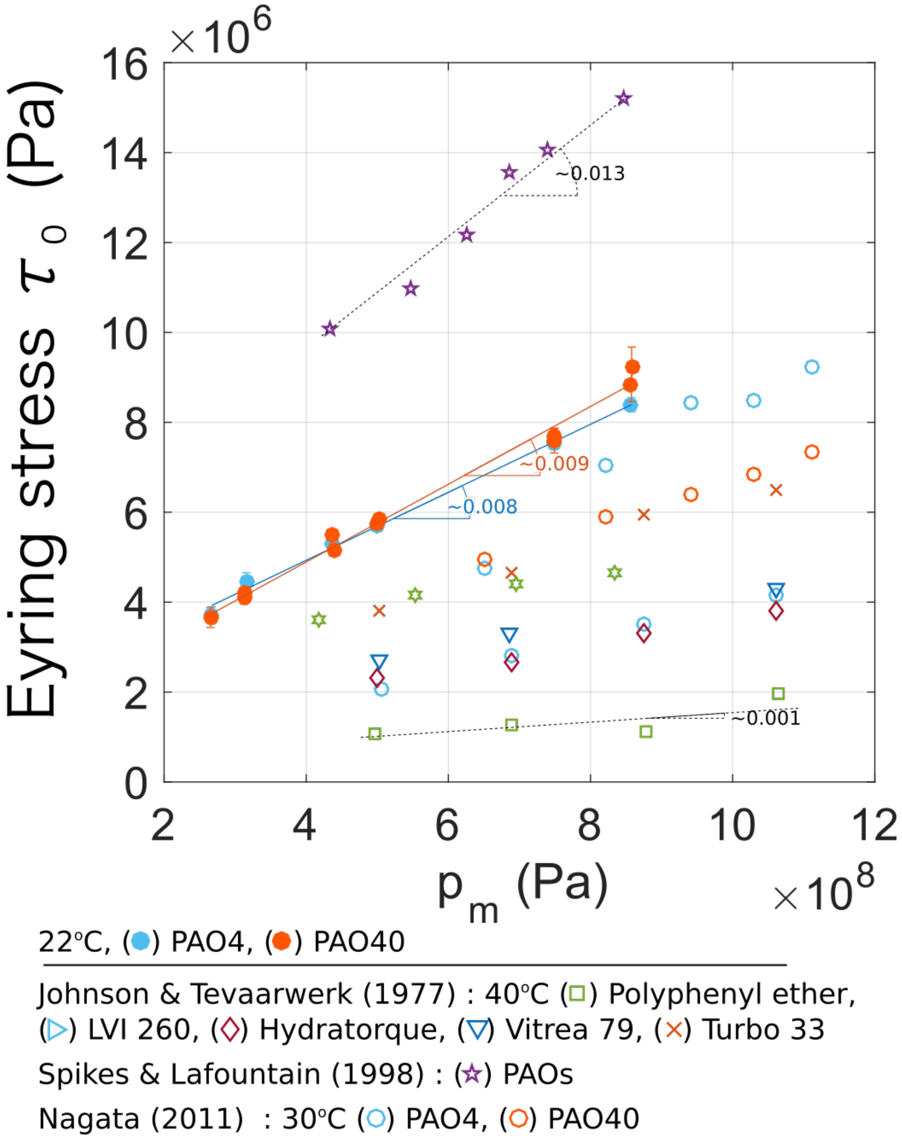

Figure 4.11: Comparison of the Eyring stress (filled symbols) with the the literature.

indeed higher than the values we used[1]. To represent the shape of the tractions of figures 4.12.a and b, it is required to consider pressure viscosity coefficients different from those given in the literature (12), (37).

The low-shear slope $\left.\frac{dF_{f\ Couette}}{du_s}\right|_{u_s \to 0}$ was measured on traction curves. Assuming that the fluid was Newtonian at the lowest sliding speeds, the α-dependent Roelands isothermal formula (eq. (2.4)) was considered valid to describe the low-shear behaviour of the PAO4 and of the PAO40. Using the Hamrock and Dowson relationship to calculate the shear rates (eq. (2.15)), pressure-viscosity coefficients were calculated for these two fluids by inverting the relationship $\left.\frac{dF_{f\ Couette}}{du_s}\right|_{u_s \to 0} = \pi a_H^2 \frac{\eta_{Roelands}(\eta_0, p_m, \alpha)}{h_c(\alpha, \eta_0, p_m, u_e, E', R_x)}$ towards α. Figure 9.18 shows these pressure-viscosity coefficients. For the two lubricants, this method yields values of α that decrease with the pressure and with the temperature. However, this approach is fragile given the lack of direct measurements (17) of α able to confirm these observations and because there does not seem to exist any general behaviour towards pressure and temperature for α (45). Furthermore, the measurement of the slope $\left.\frac{dF_{f\ Couette}}{du_s}\right|_{u_s \to 0}$ is not straightforward. Finally, when the low-shear parameter η_E is imposed equal to the low-shear slope $\frac{h_c}{\pi a_H^2} \left.\frac{dF_{f\ Couette}}{du_s}\right|_{u_s \to 0}$, the asinh fit does not follow the data correctly for the shear rates that correspond to the shear-thinning regime of the fluid ($\dot{\gamma} \gtrsim 10^5$ 1/s for the PAO40, $\dot{\gamma} \gtrsim 10^6$ 1/s for the PAO4). This is problematic because in EHD experiments, these shear rates are more often covered than the Newtonian regime. These complications led to discard both the Roelands formula and the account for the dependence of α with pressure.

For both lubricants, $p_m \mapsto \eta_E(p_m, 22°C)$ is fitted according to a power law according to eq. (4.30). The fitted parameters (a_{η_E} ; b_{η_E}) are given table 4.2.

$$\mathrm{\eta_E(p_m) = a_{\eta_E}\ p_m^{b_{\eta_E}}} \tag{4.30}$$

4.2.3 Influence of temperature on the fluid rheology

The effect of temperature on the fluid rheology is investigated through tractions with smooth steels over a temperature range : [19 ; 29] ° C for the PAO 40, [19 ; 39] ° C for the PAO 4, at 440 MPa (see fig. 4.13.a). Although these temperature ranges are restricted, they were chosen because they are close to the operating temperatures and because the temperature rises were expected small. From now, the lubricant properties are described only with the Eyring (asinh) law for its powerful ability to fit the tractions with only two adjustable parameters. The effect of temperature can only be included in the low-shear viscosity η_E : each traction experiment presented fig. 4.13.a is interpolated according to the Eyring law while letting only η_E temperature-dependent and τ_0 kept constant at 5.3 MPa. Then, $T \mapsto \eta_E(440\ \mathrm{MPa}, T)$ is interpolated with a Vogel law (black solid lines on fig. 4.13.b).

$$\eta_E(p_m, T) = A_{Vo}\ exp\left(\frac{B_{Vo}}{T - C_{Vo}}\right) \tag{4.31}$$

, with T in °C. The Vogel parameters corresponding to $p_m = 440$ MPa are given in table 4.3.

To recapitulate, the PAO4 and PA40 rheology were measured using tractions performed with smooth steel surfaces at $u_e = 0.02$ m/s for the PAO40, $u_e = 0.2$ m/s for the PAO4. The Eyring model was used to fit these rheograms : the temperature influence was only included in the low-shear

---

[1] $\alpha_{PAO40} = 20.0$ 1/GPa (12), α_{PAO4}=18.6 1/GPa (37).

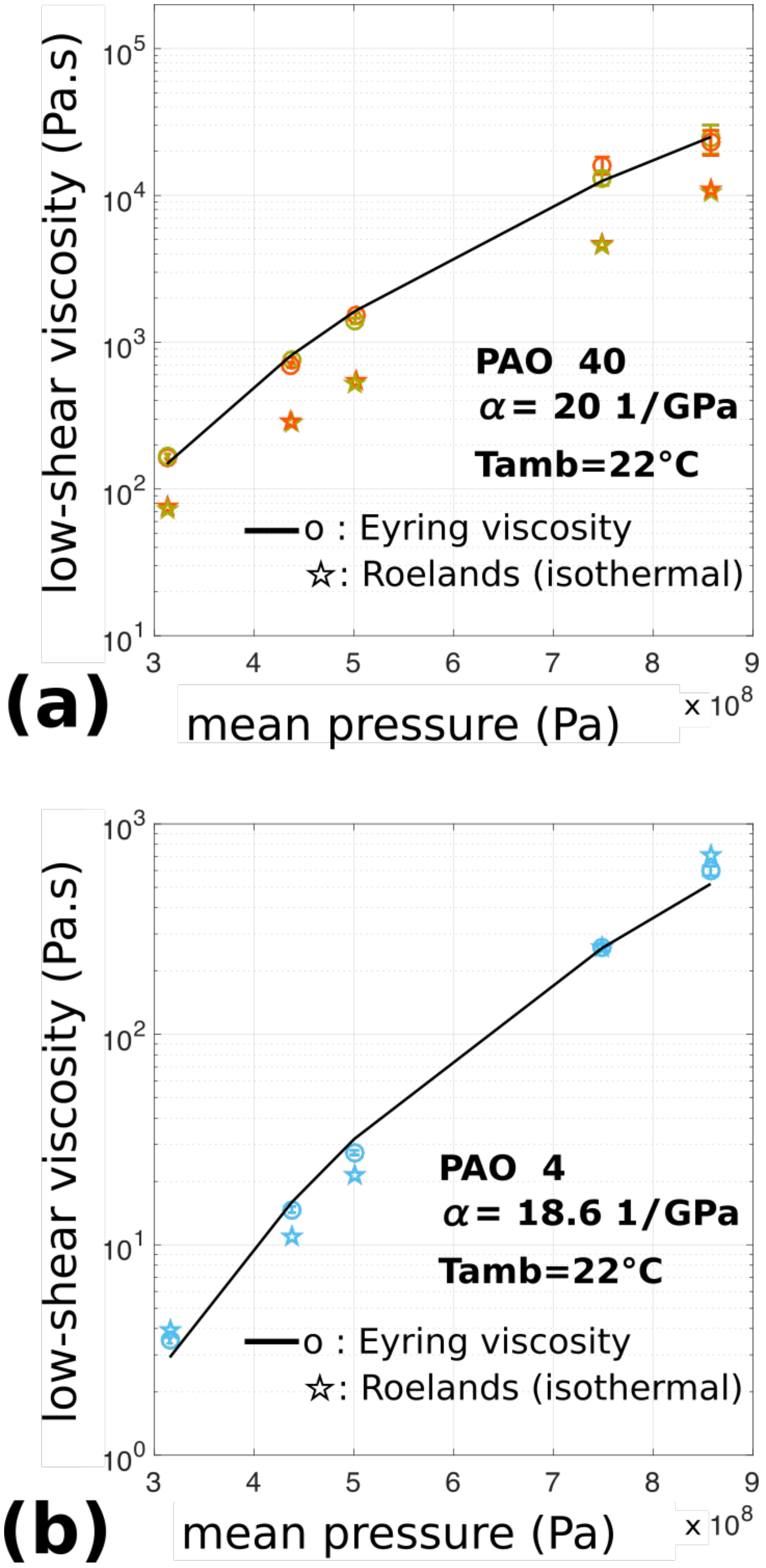

Figure 4.12: Low-shear viscosity parameters obtained with an Eyring law. The isothermal Roelands relationship is added for comparison and the Eyring viscosities are interpolated with power laws (Black solid lines), the uncertainties correspond to the 95% confidence intervals for the fitted coefficients.

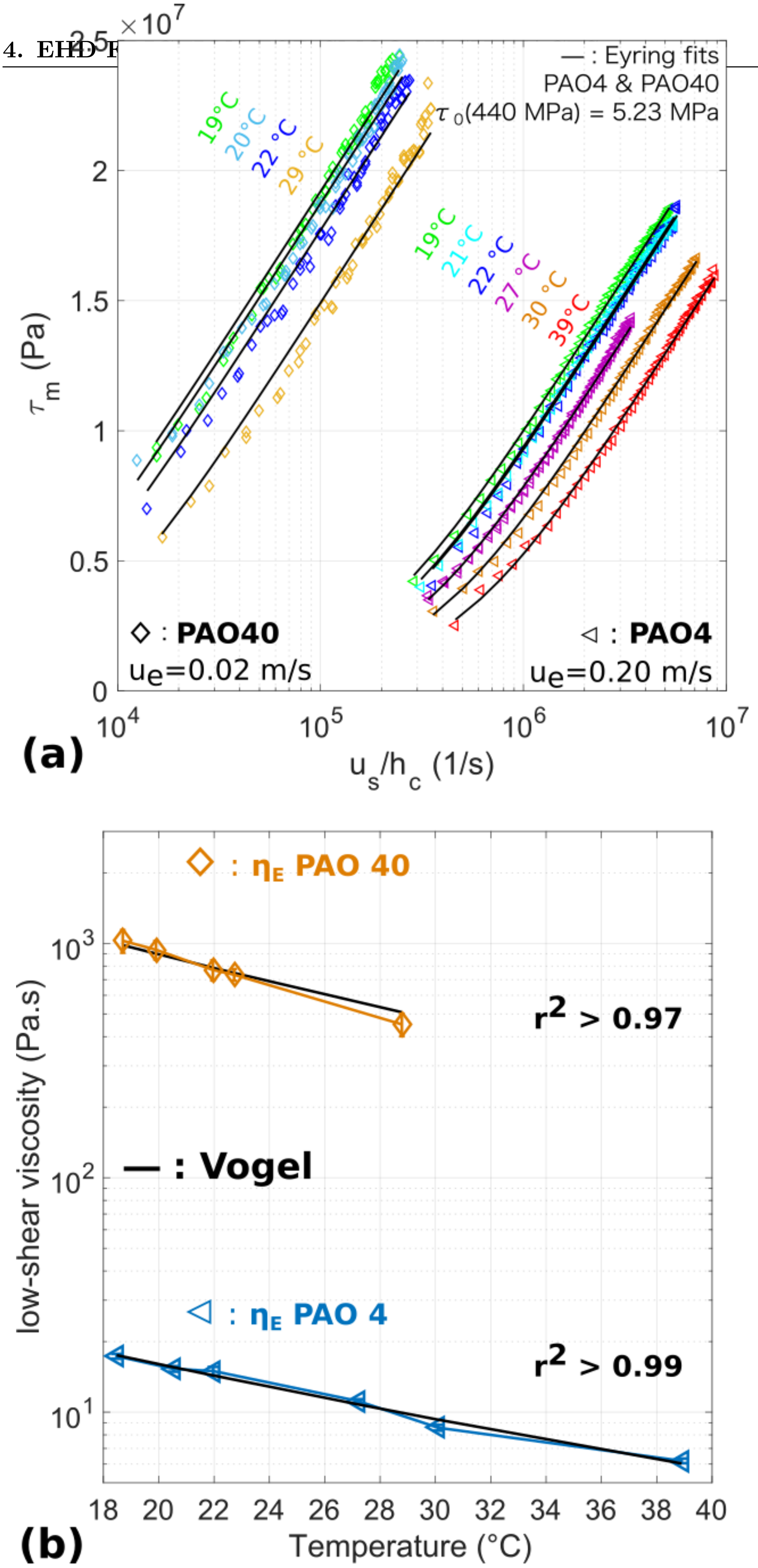

Figure 4.13: (a) : Traction experiments operated at various temperatures on the MTM using smooth polished steel surfaces, interpolated with the Eyring asinh law. (b) : Eyring viscosities η_E versus the lubricant temperature. For both lubricants at 440 MPa, $\tau_0 = 5.23 \times 10^6$ Pa. (b) : For both lubricants, η_E is interpolated with an affine law according to the displayed slopes and offsets, with their associated 95% confidence intervals.

Lubricant (p_m = 440 MPa)	$\mathbf{A_{Vo}}$ (Pa.s)	$\mathbf{B_{Vo}}$ (°C)	$\mathbf{C_{Vo}}$ (°C)
PAO 40	26.2×10^{-3}	1.592×10^{3}	-132.5
PAO 4	6.02×10^{-4}	1.818×10^{3}	-158.4

Table 4.3: Vogel coefficients (eq. (4.31)) of the Eyring viscosity η_E at $p_m = 440$ MPa versus the lubricant temperature.

viscosity η_E. The piezoviscous response was shared between τ_0 and η_E with an affine and a power law respectively. For a given set of pressure, temperature and shear rates, the Couette shear stress may thus be calculated using :

$$\boxed{\tau_\mathrm{m}(\mathrm{p_m}, \mathrm{T}) = \tau_0(\mathrm{p_m})\ \mathrm{asinh}\left[\frac{\mathrm{u_s}}{\mathrm{h_c}} \frac{\eta_\mathrm{E}(\mathrm{p_m}, \mathrm{T})}{\tau_0(\mathrm{p_m})}\right]} \tag{4.32}$$

$$\text{with } \tau_0(p) = \tau_{00} + a_{\tau_0}\ p \tag{4.33}$$

$$\eta_E(p_m, T_0) = a_{\eta_E}\ p^{b_{\eta_E}} \text{ with } T_0 = 22\ °\mathrm{C} \tag{4.34}$$

$$\eta_E(p_m, T_0 + \delta T) = \eta_E(p_m, T_0)\ e^{\frac{-B_{Vo}\delta T}{(C_{Vo}-T_0)(C_{Vo}-(T_0+\delta T))}} \tag{4.35}$$

$$\tag{4.36}$$

4.2.4 Experimental validation of the PAO4 and PAO40 rheological laws with different materials

In order to test the influence of the materials, in particular with respect to shear heating, traction experiments were operated on the PAO4 (fig. 4.14.a) and the PAO40 (fig. 4.14.b) with silica (tests at 270 MPa) and sapphire discs (tests at 440 and 450 MPa) at the same rolling speeds as previously : $u_e = 0.2$ m/s for the PAO4, $u_e = 0.02$ m/s for the PAO40. The agreement between the calculated isothermal tractions (black dashed lines on fig. 4.14) and these experiments is satisfactory. The error between experiments and viscous stress predictions, denoted $< err >$ on graphs is defined as the relative difference, averaged over the whole speed range covered in the experiments :

$$< err > \equiv \left\langle \left| \frac{\tau_{exp} - \tau_{calc}}{\tau_{exp}} \right| \right\rangle \tag{4.37}$$

The stress prediction error is higher at 270 MPa because the calculated tractions arise from the fitting of tractions operated at $p_m \geq 310$ MPa, which has imposed an extrapolation of the rheological parameters $\tau_0(p)$ and $\eta_E(p)$, obtained section 4.2.1. The first-order source of error is due to the low-shear viscosity η_E because this parameter is highly pressure-dependent. Nevertheless, the average error is less than 10% at 440 MPa and between 10 and 30% for experiments operated at 270 MPa. The flash temperature rises calculated with the silica properties raise about 15 to 40 times the temperature rises obtained with steel. Given the shear rates obtained with the PAO4 tractions, using the silica thermal properties raise a flash temperature rise superior to 100 $°C$ at $SRR = 2$, which should have decreased the fluid viscosity importantly. The fact that the isothermal stress prediction underestimates the experimental tractions performed with silica confirm that flash temperature rise could not reach a steady state during these tests. These tests validate the use of the rheological equations at least when films about 0.1 μm-thick separate the surfaces.

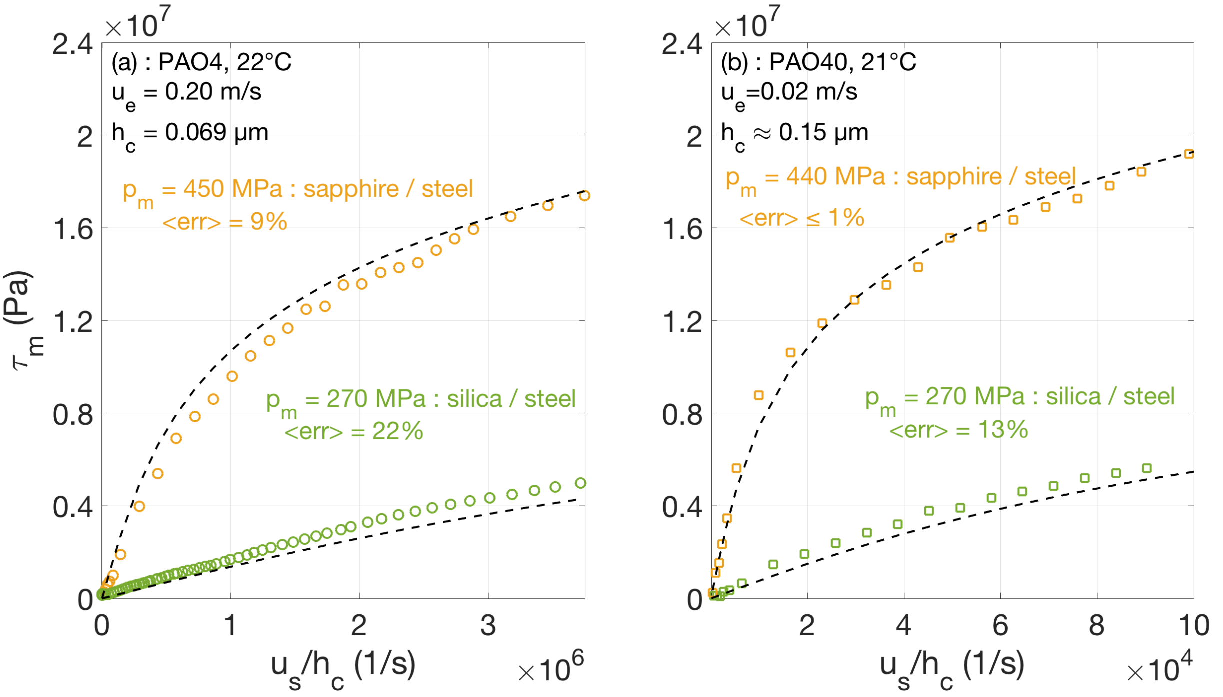

Figure 4.14: (a) : Traction tests on the PAO4 with a silica disc (270 MPa) and a sapphire disc (450 MPa). (b) : traction tests on the PAO40 with a silica disc (270 MPa) and a sapphire disc (440 MPa). The black dashed lines correspond to isothermal tractions calculated according to eqs. (4.32).

4.3 Friction mechanisms beyond the shear stress-shear rate approach

4.3.1 From thin-film EHL to mixed lubrication

Figures 4.15 displays a traction ($u_e = 0.350$ m/s, $h_c = 0.036$ μm) and a Stribeck test ($SRR = 0.25$, $h_c \in [0 \ ; \ 0.06]$ μm) on the PAO2, at $p_m = 445$ MPa. Plotting these experimental points in terms of shear stress versus shear rate show the same apparent rheology, as long as the film thickness overcomes 0.01 μm, which is the same order of magnitude as the composite surface roughness. At smaller film thickness, the EHD friction mechanism is progressively switched to a mixed one, yielding a higher friction.

On figure 4.16, traction experiments on PAO4 with sapphire discs are shown at different entrainment speeds : $u_e = 0.2, \ 0.1, \ 0.05, \ 0.02, \ 0.01, \ 0.005$ m/s, corresponding to nominal film thicknesses $h_c = 70$, 44, 28, 15, 10 and 6 nm. The tractions performed at $u_e > 0.02$ m/s show the same evolution of τ_m with $\dot{\gamma}$. They are well predicted by the isothermal Eyring equation (4.32) (black dashed line on fig. 4.16) based on the mean Hertz pressure p_m. The average error between these experiments and the friction predictions is less than 8%.

However, at smaller rolling speeds ($u_e \leq 0.02$ m/s) the experimental friction is 30 to 180 % higher than the thin-film prediction because the opposing roughnesses are no longer separated and interact mechanically. For the traction performed at the lowest entrainement speed ($u_e = 0.005$ m/s), the shear stress even reaches the PAO4 shear strength $\tau_{max} = \Lambda_{PAO4} \times p_m \approx 28$ MPa.

Interferometric measurements during the traction experiments (see fig. 4.16.b) show that for these smooth surfaces, the Hamrock-Dowson formula holds true even at the smallest rolling speeds $u_e = 0.005$ m/s, i.e. in the ML regime. At least for these smooth contacts, these thickness measurements confirm the assumption made by (72), according which the film thickness is mainly determined in the inlet even though the friction is partly due to interactions between the elastically deformed asperities.

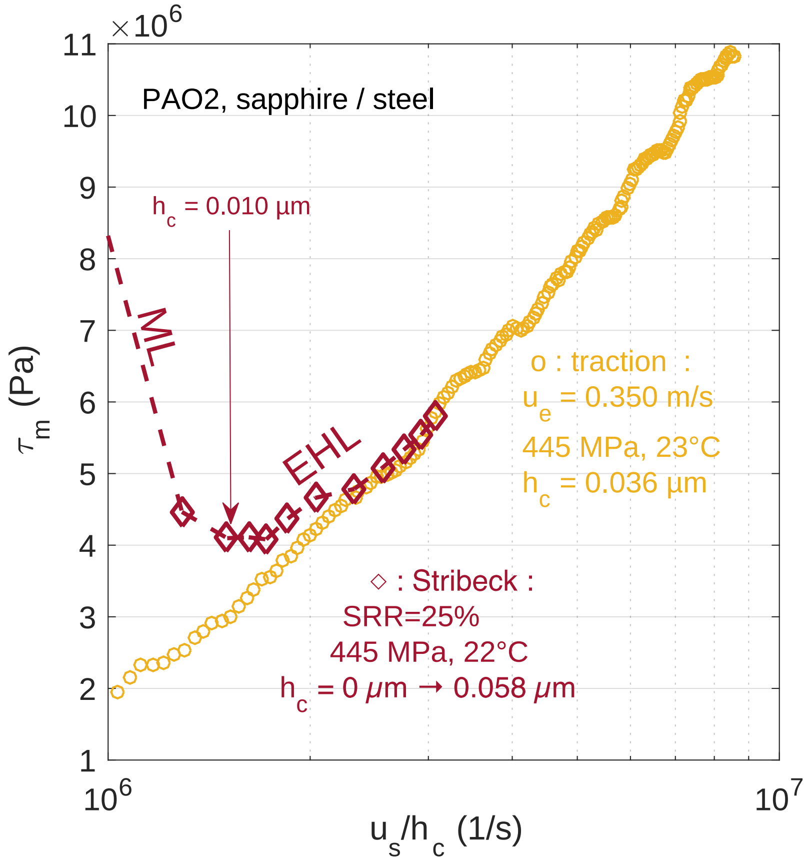

Figure 4.15: Traction and Stribeck experiments operated at 445 MPa on the PAO2.

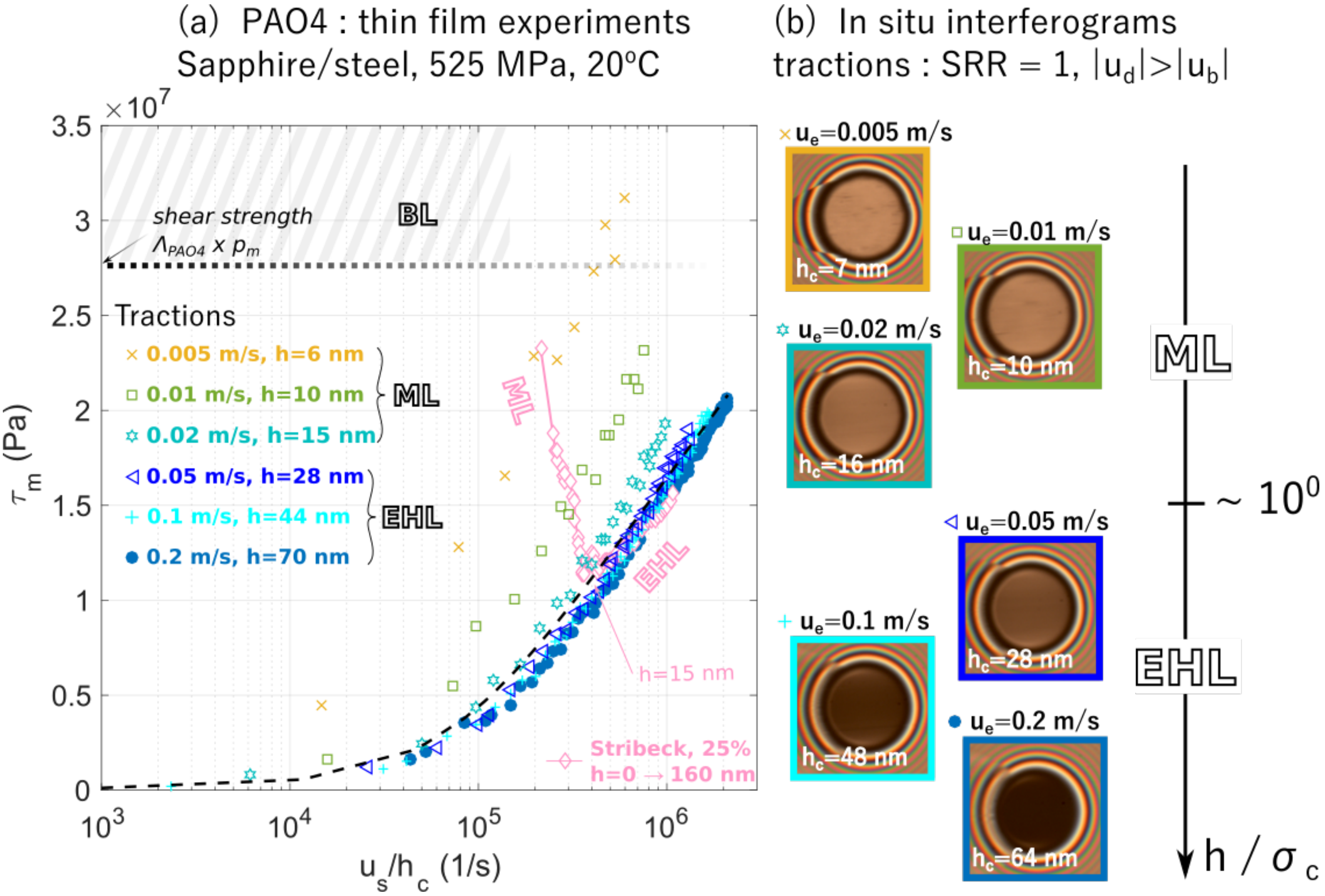

Figure 4.16: (a) : 6 Traction tests at 0.5 GPa on PAO4 with smooth surfaces at different rolling speeds from full-film ($u_e = 0.2,\ 0.1,\ 0.05$ m/s) to mixed lubrication ($u_e = 0.005$). A Stribeck experiment operated in the same conditions is shown in pink : the film thicknesses allow to cover EHL and ML. The grey area corresponds to the lubricant strength calculated at 525 MPa. The dashed black line corresponds to the predicted lubricant rheology interpolated from thin-film tractions (eq. (4.32)). (b) : In situ interferograms showing the experimental central film thickness for each traction test.

Some heterogeneities passing through the contact are visible on the interferograms and are responsible for barely visible and infrequent wear on the disc track. The scarcity of such heterogeneities leads us to believe that they contribute little to the mean shear stress τ_m. For these smooth contacts, if the ML friction mechanism were to involve solid/solid contacts, the fragile semi-reflective layer would have worn rapidly, as it was observed in some other cases. As it was suggested e.g. by (47), the most plausible reason for the friction being higher when $h_c \leq 0.015\ \mu$m remains a micro-EHD mechanism between the surface asperities : as the opposing asperities approach, the film thickness stiffens and still separates the asperities that deform elastically, raising locally the fluid pressure. Nevertheless, this assumption will be further discussed in chapter 7 (paragraph 7.3.1) since the experimental shear stress slightly overcomes the fluid shear strength on the traction at the smallest separation, fig. 4.16.a.

For surfaces having a composite RMS roughness inferior to 0.015 μm, the same shear stress versus shear rate relationship is observed for sliding-rolling experiments with film nominal thicknesses in the range [0.015 ; 0.2] μm. These correspond to lambda ratios in the range [0.5 ; 10]. Experiments with thicker films are now investigated.

4.3.2 Thick-film EHD friction

Given the tribometers limited speeds, the more viscous PAO40 allows to cover thicker films than the PAO2 and the PAO4 do. Tractions with PAO40 were performed at a lambda ratio roughly equal to 100 (see figure 4.17). The isothermal thin-film prediction shear stress is plotted with the dashed black line and is about 5 MPa higher than the experimental tractions.

4.3.2.1 Temperature explanation

In order to assess whether this could be explained with shear heating, the lubricant temperature may be overestimated by calculating the lubricant temperature rise (eq. (4.21)) and the maximum flash temperature rise (eq. (9.10)), where the whole heat is transmitted to the most insulating body (i.e. the sapphire disc, here). These temperature rises are shown fig. 4.17.b, and the corresponding thermal traction is displayed in red dashed line on fig. 4.17.a. Although the traction is slighlty lowered at the highest shear rates, this thermal correction does not explain the experimental friction being significantly diminished for the whole range of shear rates.

The same statement arises from thickness-variable sliding experiments, as it is shown figure 4.18 : a Stribeck experiment with h_c ranging from 0.03 to 1.5 μm is plotted along with the isothermal and the thermal predictions. When the nominal separation overcomes about 0.2 μm, both these predictions overestimate the experimental shear stress. At the highest film thickness ($h \approx 1.5$ μm), the experimental Couette shear stress is about a third of the thermal and isothermal predictions. An isothermal prediction is also plotted in orange on fig. 4.18, where the lubricant temperature was assumed 50°C higher than the ambient temperature. Explaining thermally the stress decrease at large rolling speeds would require roughly a 50°C temperature increase, i.e. about 7 times the maximum possible temperature rise according to eqs. (4.27) and (4.21). The thermal argument is thus rather unlikely to explain the decrease of τ_m at large separation.

4.3.2.2 Effective pressure explanation

Given the piezoviscous behaviour of lubricants, it may be interesting to question the representativeness of the mean Hertz pressure with respect to the mean shear stress in thick-film EHD contacts.

On fig. 4.19, the Stribeck experiment of fig. 4.18 is reproduced with two isothermal predictions at $T = T_{amb}$ (dashed lines) : the black line corresponds to the nominal mean Hertz pressure $p = p_m = 450$ MPa while the blue one corresponds to $p = 300$ MPa. The experimental stress decrease is compatible with a fluid bulk pressure decreasing as the film thickness increases. The reason why the fluid pressure should decrease, even though the load is kept contant, may be qualitatively understood by looking at the relationship between EHD pressure and film thickness distributions.

Spreading of the bearing area at large film thickness One-dimensional EHD pressure profiles[1] in pure rolling with smooth surfaces are plotted figure 4.20, for a mean Hertz pressure equal to 440 MPa, using the (98) equivalent point contact with the PAO 40 inlet viscosity at 20°C. In thin-film conditions, the pressure field stays confined within the Hertz area ($x \in [-a_H \; ; \; a_H]$). As the film thickness is increased, the pressure field spreads increasingly in the inlet ($x < -a_H$) such that part of the load becomes borne by the inlet. Thus, the contact area grows as the surface separation increases and consequently, the average pressure is reduced.

---

[1] Kindly provided by Thomas Touche, PhD Ecole Centrale de Lyon/ LTDS/Perth Tribology Laboratory 2016. The simulation uses Finite Volume Elements (F.V.E.) method to solve the Reynolds equation, with smooth surfaces under isothermal hypotheses, with a no-slip assumption between the fluid and the surfaces.

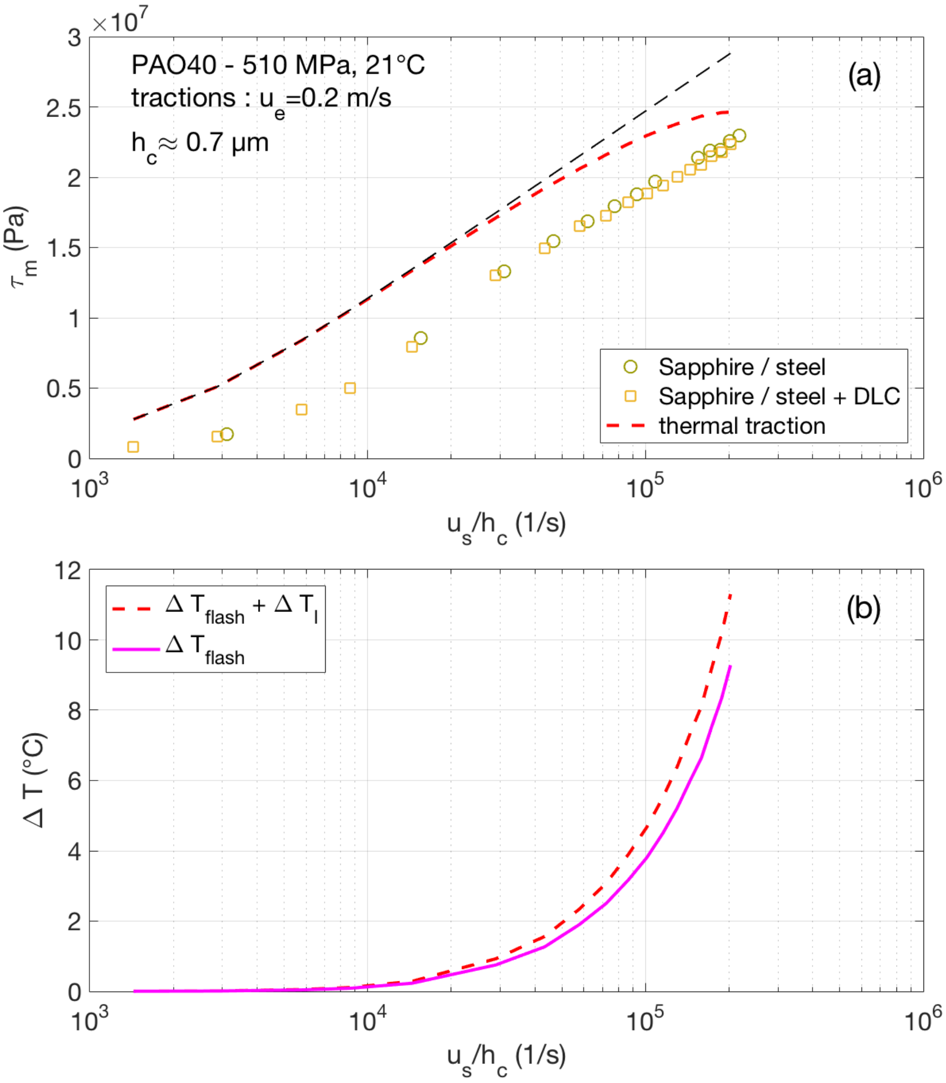

Figure 4.17: (a) : Two thick-film traction experiments with PAO40 with smooth surfaces at $p_m \approx$ 0.5 GPa at $u_e = 0.2$ m/s. (b) : The magenta line corresponds to the maximal flash temperature rise (eq. (9.10)) assuming all the heat is transmitted to the most insulating body. Adding the maximum lubricant temperature rise (4.21) gives the red curve. This total overestimated temperature rise is included in the calculated thermal traction displayed in red dashed line on (a).

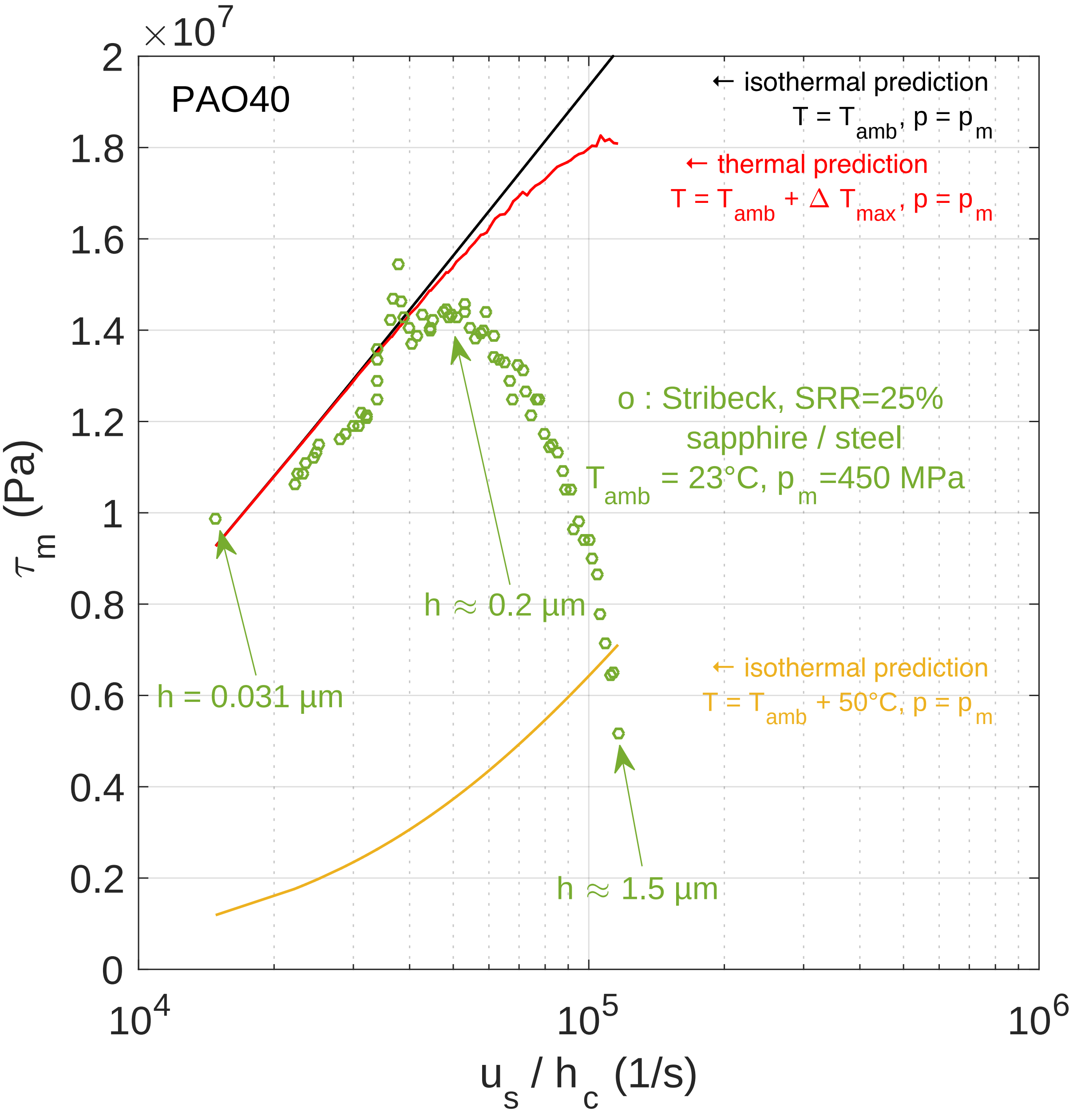

Figure 4.18: Stribeck experiment with PAO40 (circles) where the film thickness ranges from 0.03 to 1.5 μm. The black line is the isothermal prediction and the red line correspond to the thermal prediction, accounting the lubricant temperature rise and the maximum flash temperature, assuming the heat is conducted to the most insulating of the two bodies (the sapphire disc here). The maximum total temperature rise is 7 °C. The orange line corresponds to the isothermal shear stress calculated assuming a temperature rise $\Delta T = 50°$C, constant during the whole experiment.

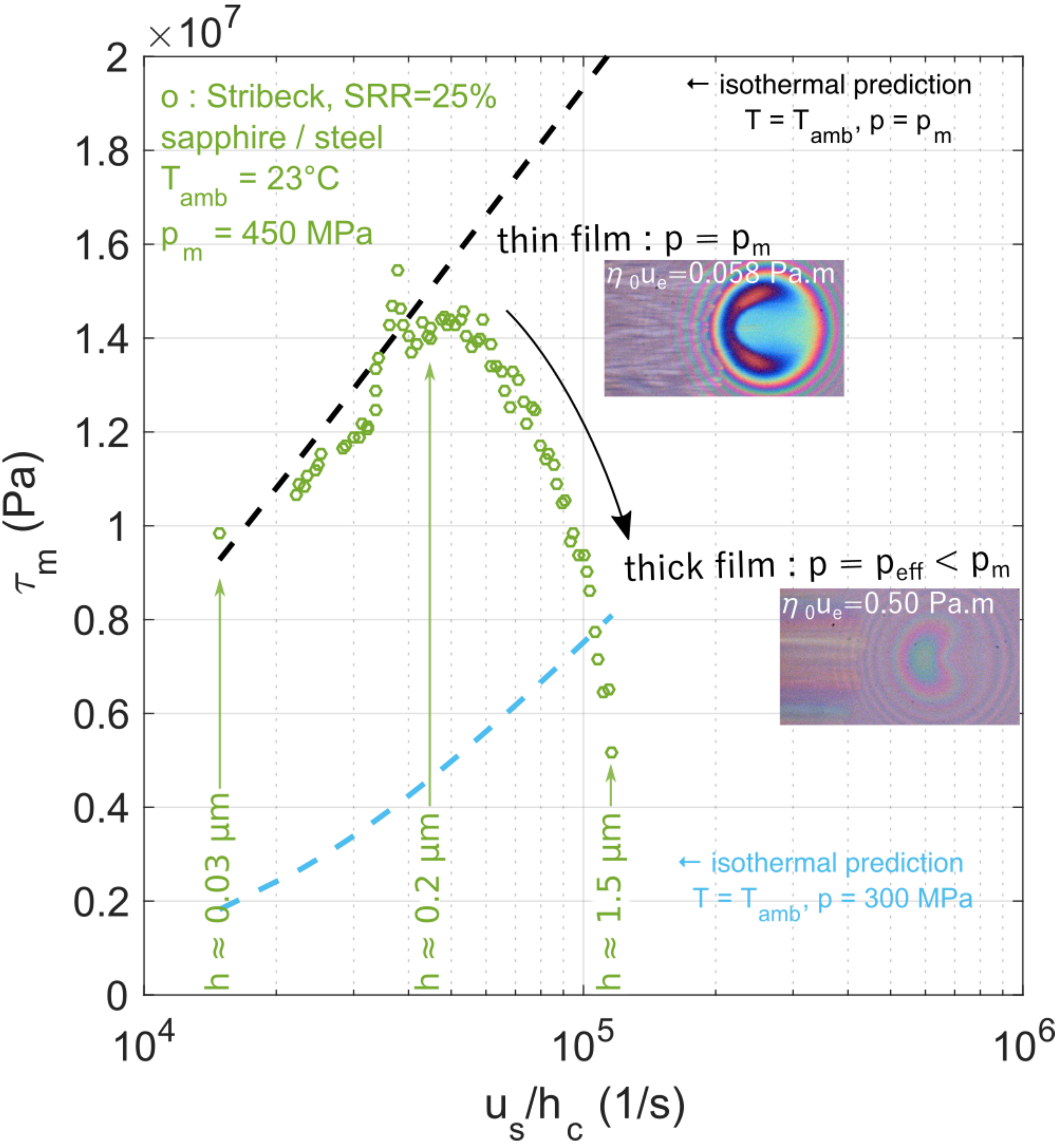

Figure 4.19: Same Stribeck experiments on PAO40, at SRR=25% than those plotted on fig. 4.17. The symbols are experiments, the dotted lines are the Eyring preciction assuming the lubricant is kept at room temperature T_{amb} and at mean Hertz pressure p_m. The dashed lines are calculated isothermal tractions at the pressures displayed.

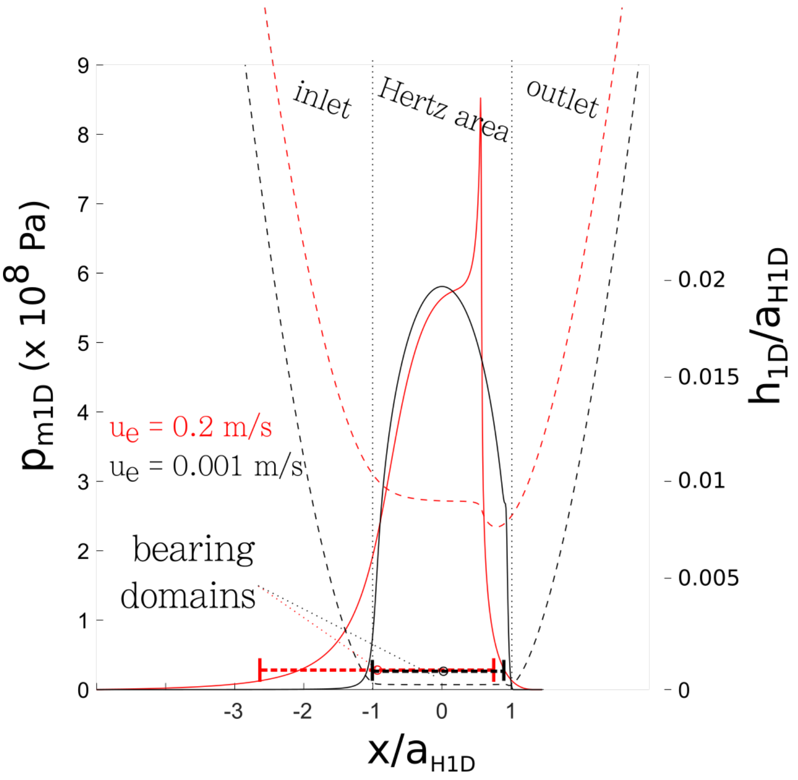

Figure 4.20:

Smooth EHD film thickness (dashed lines) and pressure fields (solid lines) in line contact conditions corresponding to our point contact conditions with p_m = 440 MPa, steel surfaces (E' = 231 GPa) and PAO40 (η_0 = 0.851 Pa.s) as a lubricant, using the equivalent point contact analogy of (98) that equates the maximum Hertz pressure and the reduced radius in a line and a point contact respectively. Two sets of EHD conditions : u_e = 0.2 (red lines) and 0.001 m/s (black lines).

Effective pressure from the average viscous stress viewpoint The fact that the contact area spreads towards the inlet must result in a lower mean pressure, hence a lower mean shear stress. Led by this idea, we introduced an effective pressure p_{eff}, seen from the lubricant shear response viewpoint in isothermal conditions (see procedure fig. 4.21). The effective pressure should change continuously with the thickness. The 0.2 μm thickness could be the thickness above which the effective pressure is relevant : significant enlargement of the contact area could perhaps be observed at this thickness. For a given sliding-rolling experiment, p_{eff} is calculated while equating the experimental shear stress τ_m with the lubricant rheology obtained with thin-film tractions section 4.2.1 :

$$\tau_m = \tau_0(\mathbf{p_{eff}})\ asinh\left[\frac{\eta_E(\mathbf{p_{eff}}, T_{amb})}{\tau_0(\mathbf{p_{eff}})}\ \frac{u_s}{h_c(p_m)}\right] \tag{4.38}$$

For each experimental point, $p_{eff} \mapsto \tau_m$ is then inverted to obtain the equivalent pressure p_{eff}. Alternatively to the concept of effective pressure, it is convenient to consider an effective contact area. In thin-film conditions, the pressure is only high within the Hertz area πa_H^2. Assuming the contact zone stays circular at larger film thicknesses, the effective contact radius a_{eff} may be defined according to eq. (4.39) :

$$p_{eff} \equiv \frac{F_n}{\pi\ a_{eff}^2} = \frac{p_m\ \pi\ a_H^2}{\pi\ a_{eff}^2}$$

$$\text{i.e.} \qquad a_{eff} \equiv a_H \sqrt{\frac{p_m}{p_{eff}}} \tag{4.39}$$

On figure 4.22.a, Stribeck experiments at SRR=25%, with smooth polished M2 steel against AISI 52100 steel and PAO40 are shown along with the isothermal Eyring prediction evaluated at the

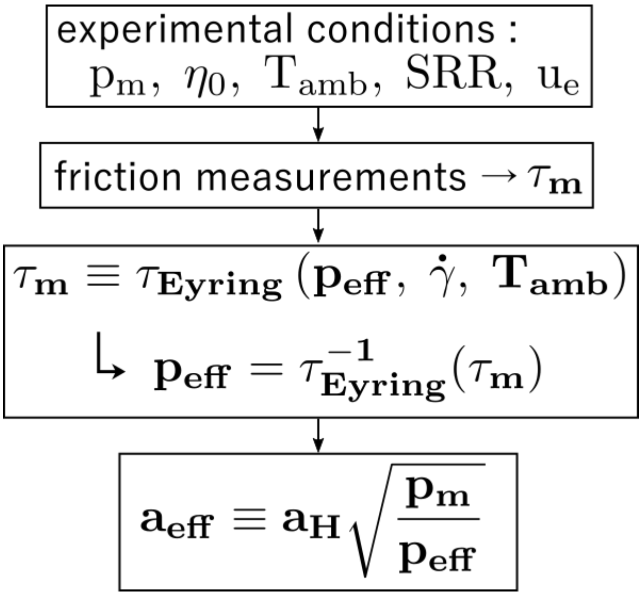

Figure 4.21: Procedure to calculate the effective contact radius (eq. (4.39)) allowing the experimental shear stress to equate the calculated isothermal viscous stress (eq. (4.32)).

operating mean pressures p_m = 440, 500 and 860 MPa. Alike all the experiments conducted with PAO40, the shear stress prediction using ($T = T_{amb}$; $p = p_m$) overestimates the measurements when the film thickness overcomes a few hundreds nanometers. The error increases with the rolling speed and is hence maximal at the highest shear rates on the Stribeck tests fig. 4.22.

For each experimental point, the effective radius, defined by eq. (4.39), is calculated and displayed fig. 4.22.b. In thin-film conditions, a_{eff} equals the Hertz radius a_H. As the surface separation increases, a_{eff} increases up to 10-20% w.r.t. the Hertz radius. On figure 4.23, the calculated effective radii are confronted to the central film thickness : it appears that a_{eff} increases linearly with h_c in the same manner regardless of the operating load :

$$a_{eff} \approx a_H \left(1 + 10\,\frac{h_c}{a_H}\right) \tag{4.40}$$

, with an uncertainty of 0.4 over the a_{eff} versus h_c slope. This correction is tested on fig. 4.24 for a traction operated on the PAO40 at u_e = 0.2 m/s (data previously exposed on fig. 4.17) : compared to the prediction at $p = p_m$, the average error is reduced from 38 % to 4 %. The correction is also tested over different Stribeck experiments with smooth surfaces (see fig. 4.25.a) operated with the PAO40. This reduces the error w.r.t. the experimental shear stress, especially at the highest film thickness as it is shown on table 4.25.b. Only at the lowest pressure p_m = 270 MPa (last row of table 4.25.b), the prediction is better without correcting the input pressure. Again, this might arise from the viscous stress calculated at this pressure being only an extrapolation of experiments performed at higher pressures. For all experiments performed at $p_m \geq 0.3$ GPa, the corrected pressure allows a more precise prediction for the shear stress.

4.3.3 Summary

In our operating conditions, we have demonstrated that heating is negligible, which permits the use of the Hamrock and Dowson isothermal film thickness formula to calculate the film thickness. Thin-film isothermal tractions at $22°C$, with smooth surfaces were used to measure the PAO40 and the PAO4 shear response in a point contact at mean Hertz pressures from 0.3 to 0.9 GPa. The

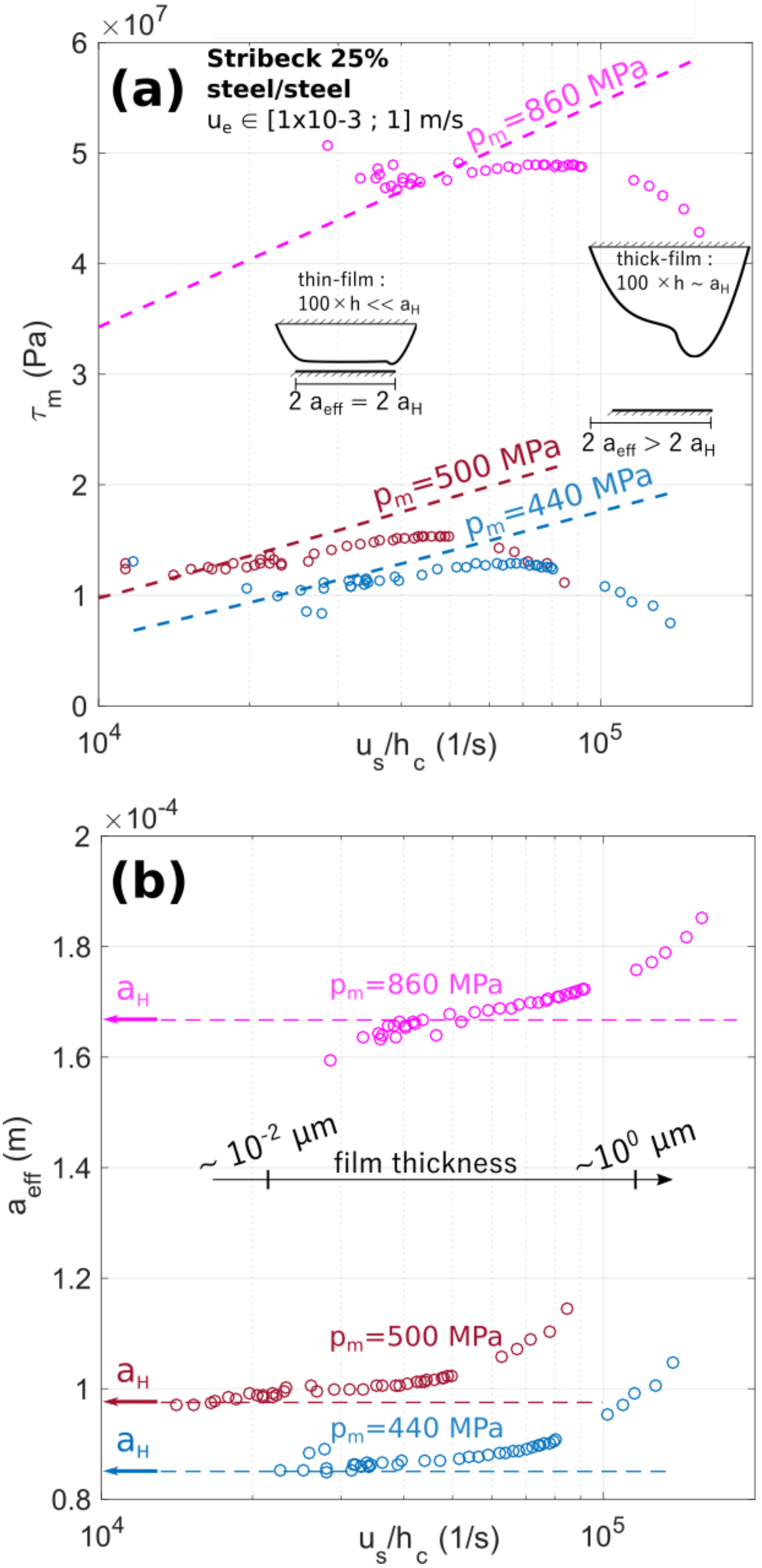

Figure 4.22: (a) Stribeck experiments with smooth steel surfaces (M2 agains AISI 52100) operated at three different loads (10N, 15N, 75N). The isothermal shear stress predictions (eq. (4.32)), evalutaed at the mean Hertz pressure p_m, are represented with dashed lines. (b) : Effective contact radii a_{eff} satisfying eq. (4.38).

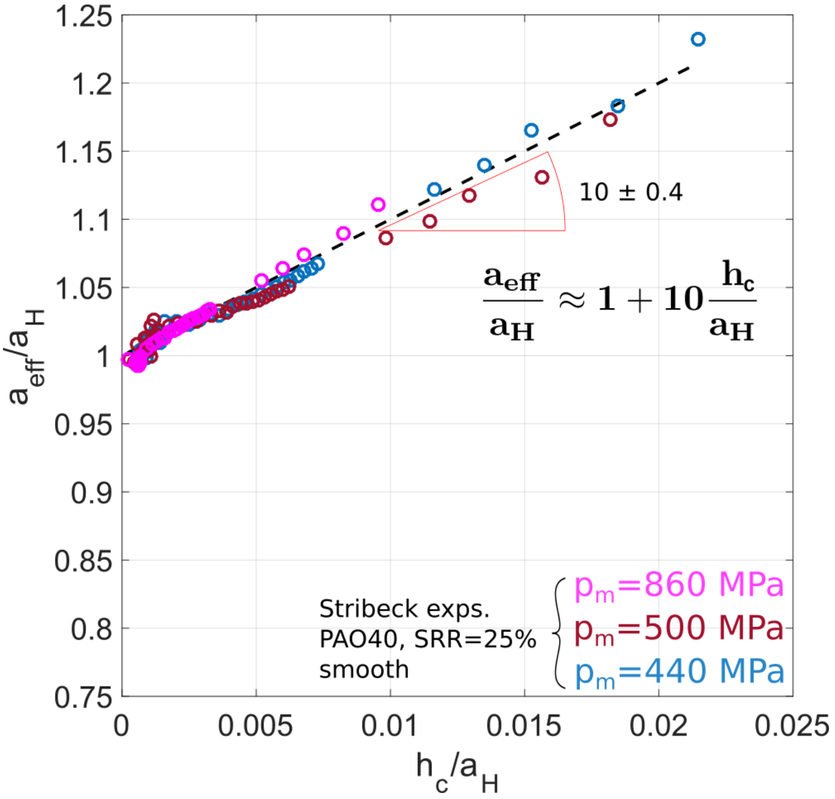

Figure 4.23:

Evolution of the effective radius defined by eq. (4.38)

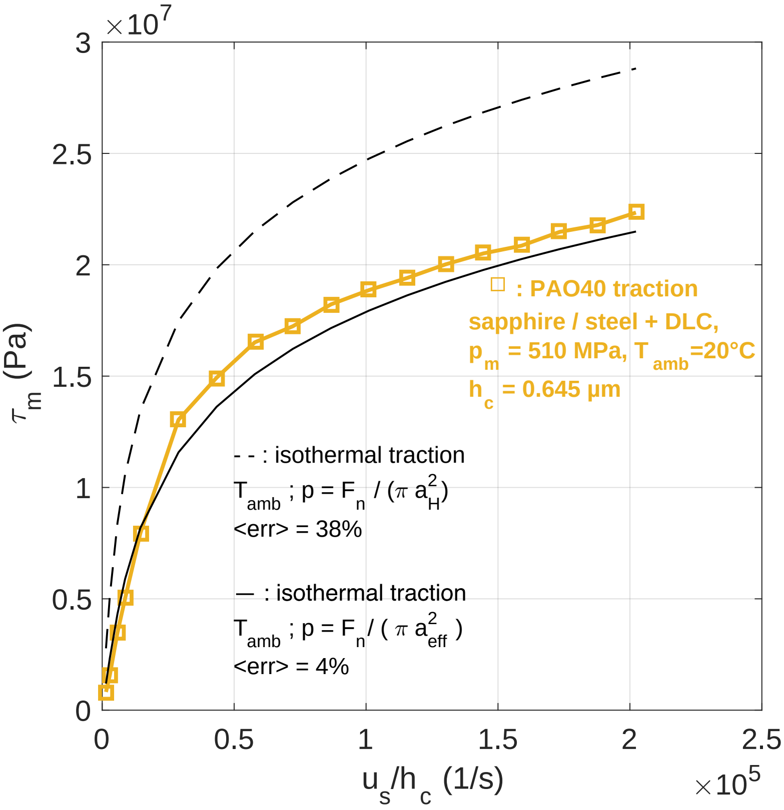

Figure 4.24:

Thick-film traction compared to isothermal predictions using the mean Hertz pressure (black dashed-line, eq. (4.32)) and using a corrected effective pressure (black solid line, eq. (4.39) and (4.40)) in the lubricant rheological formula.

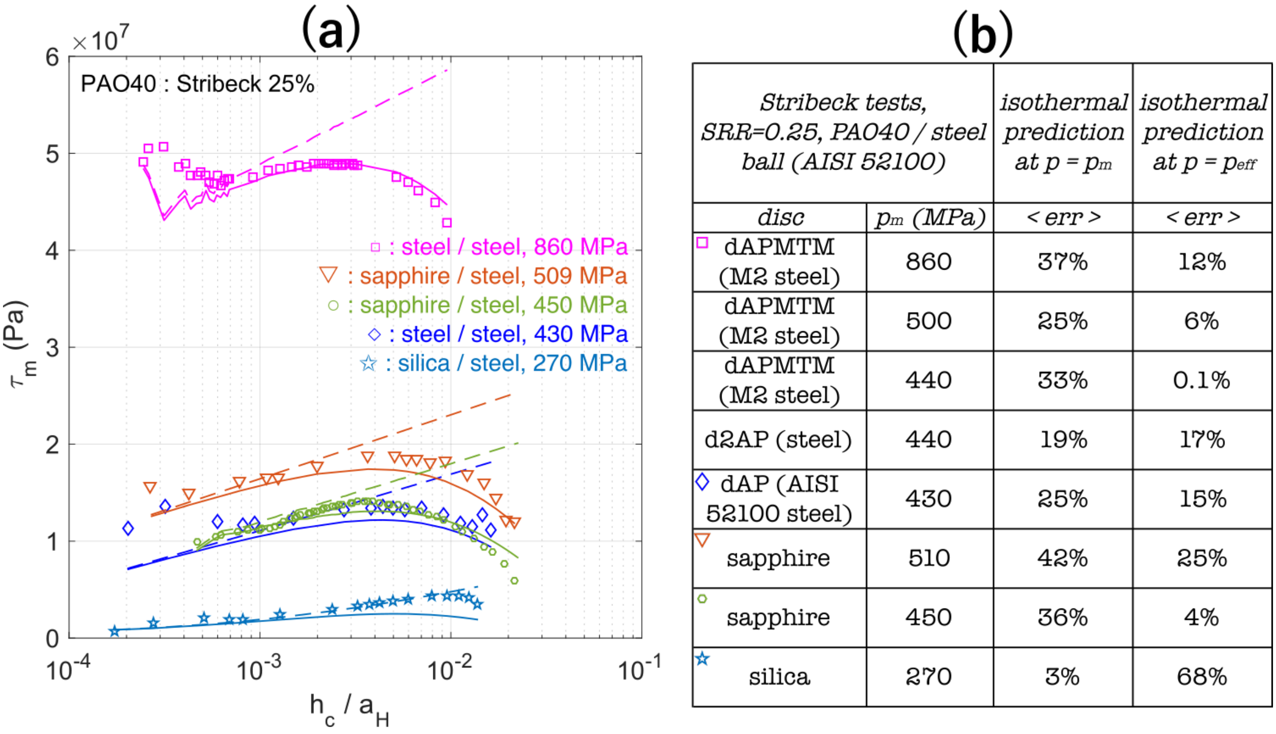

Stribeck tests, SRR=0.25, PAO40 / steel ball (AISI 52100)		isothermal prediction at $p = p_m$	isothermal prediction at $p = p_{eff}$
disc	p_m (MPa)	< err >	< err >
□ dAPMTM (M2 steel)	860	37%	12%
dAPMTM (M2 steel)	500	25%	6%
dAPMTM (M2 steel)	440	33%	0.1%
d2AP (steel)	440	19%	17%
◇ dAP (AISI 52100 steel)	430	25%	15%
▽ sapphire	510	42%	25%
○ sapphire	450	36%	4%
☆ silica	270	3%	68%

Figure 4.25: (a) : Four Stribeck experiments using PAO40 compared to the isothermal predictions at $p = p_m$ (dashed lines) and using the effective pressure : $p_{eff} = \frac{p_m}{(1+10\frac{h_c}{a_H})^2}$ (solid lines). (b) : Relative error on these shear stress predictions w.r.t. the experimental data. The error is averaged over the whole range of speeds for each experiment.

Eyring asinh law allows to capture accurately the rheograms with only two parameters : the lubricant Newtonian limiting shear stress $\tau_0(p)$, and the apparent low-shear viscosity $\eta_E(p)$. At pressure higher than 0.7 GPa, PAO4 tractions exhibit the fluid shear strength τ_{max}. The pressure dependence of the rheological parameters η_E, τ_0 and τ_{max} are in good agreement with the values found by other authors. The present approach considers the traction force as a purely viscous dissipation. Little is known about the present fluids shear modulus, viscoelastic effects were hence neglected. The effect of temperature on the rheograms was interpolated on a limited temperature range : $[19\ ;\ 29]\ ^\circ C$ for the PAO40 and $[19\ ;\ 39]^\circ C$ for the PAO4, which allows us to consider the effect of moderate heating on the viscous stress.

The rheological study leads to an accurate prediction of other sliding-rolling experiments with thin films and smooth surfaces with a composite RMS roughness of the order 10 nm. At nominal film thicknesses becoming comparable to the composite roughness, mixed lubrication is reached because of the interactions between the opposing roughness. Yet, even in ML, the experimental film thickness does not deviate from the smooth film thickness formula of Hamrock and Dowson. These low roughnesses hence barely modify the pressure building in the inlet and start perturbating the contact only once they reach the high pressure area. The negligible wear on fragile discs tends to refute the occurrence of direct asperity contacts in favor of a micro EHD mechanism between the low roughnesses. For these ML experiments, it is believed that the opposing roughnesses are always separated with a nanometric continuous fluid layer having a similar piezoviscous response as the bulk fluid. This hypothesis will be questioned in chapter 7 with more quantitative arguments.

Sliding-rolling experiments with film thicknesses higher than 0.2 μm exhibit a tangential stress that decreases as the film thickness is increased. Since the lubricant temperature is expected to increase with the surface separation, according to equation (4.21), it is generally accepted ((76), (121)) that the temperature rise is only responsible for such a decrease. Nevertheless, overestimating the fluid temperature with the flash temperature theory coupled with the lubricant temperature rise reveals insufficient to explain the observed decrease.

However, the contact mean pressure decreases with h because the pressurized area grows at increasing separations. Pressure being of primary importance on the lubricant viscosity, the shear stress should also decrease with the surface separation. The evolution of the shear stress can be predicted using the Eyring isothermal law considering an effective input pressure that decreases with increasing film thickness. The friction force in sliding-rolling experiments with thick film is well predicted using the following :

$$\mathrm{\tau_m} = \mathrm{\tau_0(p_{eff})\, asinh}\left[\frac{\mathrm{\eta_E(p_{eff}, T_{amb})}}{\mathrm{\tau_0(p_{eff})}}\,\frac{\mathrm{u_s}}{\mathrm{h_c(p_m)}}\right] \tag{4.41}$$

$$\mathrm{p_{eff}} = \frac{\mathrm{p_m}}{(1 + 10\frac{\mathrm{h}}{\mathrm{a_H}})^2} \tag{4.42}$$

$$\mathrm{\tau_0(p) = \tau_{00} + a_{\tau_0}\ p} \tag{4.43}$$

$$\mathrm{\eta_E(P, T) = a_{\eta_E}\ p^{a_{\eta_E}}} \tag{4.44}$$

In the latter equation, the shear rate is calculated classically with the Hertz pressure and the ambient temperature. The effective pressure is only implemented in the parameters $\tau_0(p)$ and $\eta_E(p)$ as they describe the fluid piezoviscous-shear response. This corrected input pressure for the fluid rheological law clearly improves the shear stress prediction for traction and Stribeck experiments with PAO40.

Chapter 5

Random surface metrology

5.1 Introduction

5.1.1 Generic definition of surface roughness

Any surface can be regarded locally as a shape deviating from a reference plane. The scales responsible for height deviations from this plane occur on different lateral extents. The term roughness generally refers to the small scales according to a decomposition between scales smaller and larger than a critical lateral extent, generally of a few hundreds microns though it can be larger in other topics of matter like tyre shaping, road industry or earth topography. Roughness is defined as the remainder after removing large scales according to :

$$z(x, y) = z_{raw}(x, y) - z_{LP}(x, y) \tag{5.1}$$

, where z_{raw} denotes the raw surface and z_{LP} is the low-pass filtered surface, where the scales inferior to a determined cut-off length were removed. Equation (5.1) thus defines a high pass-filtering operation.

Fluctuations used as a surface signature Contrary to many signals, the surface roughness z is less characteristic of its mean value than its fluctuations above and below the mean plane (or the mean line, for profilometer measurements). This arises from the fact that, whatever the filtering method, the average value is determined by the large scales contained in the low-pass filtered surface z_{LP}.

A survey of a rectified disc (dAR), originally measured using $dx = 3.653$ μm with 10^6 height bins (fig. 5.1.c), was also subsampled by steps of 4 pixels, dividing the sample size by 16 between each sub-survey : $N_{samp} = 65200$, 3844 (shown on fig. 5.1.d), 196 and 4. The corresponding height histograms are shown fig. 5.1.a.

The height standard deviation S_q is the most widely-used parameter to express the typical height fluctuations. After applying a high-pass filtering operation[1], S_q is calculated as :

$$\mathrm{S_q} \equiv \sqrt{< (\mathrm{z}- < \mathrm{z} >)^2 >} = \sqrt{\frac{1}{\mathrm{n}-1}\sum_{\mathrm{i}=1}^{\mathrm{n}}\left(\mathrm{z_i} - \frac{1}{\mathrm{n}}\sum_{\mathrm{j}=1}^{\mathrm{n}}\mathrm{z_j}\right)^2} \tag{5.2}$$

---

[1] The simple planar detrending operation was used for the surveys shown fig. 5.1. The cut-off length was taken equal to the extent of the survey:$L_c = 1000 \times 3.653 = 3.6$ mm.

, where $< \cdot >$ correspond to spatial averaging in the probing area. The centre-line average S_a is often preferred in industrial surface metrology, it is defined as :

$$\mathrm{S_a} \equiv < | \mathrm{z} - < \mathrm{z} > | > = \frac{1}{\mathrm{n}} \sum_{\mathrm{i}=1}^{\mathrm{n}} \left| \mathrm{z_i} - \frac{1}{\mathrm{n}} \sum_{\mathrm{j}=1}^{\mathrm{n}} \mathrm{z_j} \right| \tag{5.3}$$

Both parameters relate to the heights typical deviations from the mean plane. S_a is always smaller than S_q because of the square exponent to which height deviations are raised (see eq. (5.2)). In the present study, it was generally observed that $\frac{S_a}{S_q} \approx 0.7 \pm 0.1$.

The standard deviation varies from less than 1 % between subsampled surveys (see fig. 5.1.c), and the height histogram is little affected by the sample size, i.e. the total number of bins contained in the survey. Roughness may thus be seen as a background noise having a stationary amplitude, determined by the standard deviation. S_q thus can be used as characteristic of the height deviations in a given probing zone and can be reliably obtained from sub-sampled surveys containing at least 100 bins provided they cover the same probing zone, and that they were measured with the same sampling interval dx.

5.1.2 Cut-off length

The total area probed with a given survey $(N_x\, dx) \times (N_y\, dy)$ constitues an upper bound for the scales that can contribute to height deviations. This area is commonly called the cut-off area, or the sampling area (123) by analogy with the cut-off length (or sampling length) used for one-dimensional surface measurements. The surface nominal form (plane, cylinder, sphere, ..) has first to be interpolated to obtain a low-pass filtered image z_{LP}. Then, this image is subtracted to the original one according to eq. (5.1). These are the minimal steps, recommended by metrology standards (79), allowing the definition of a surface roughness, and the associated cut-off lengths are respectively $L_{w\,x} = N_x\, dx$ and $L_{w\,y} = N_y\, dy$ in the x and y directions. In some cases, a range of intermediate scales between the roughness and the form is introduced under the term of *waviness*, but since there is no consensus about the critical scales that separate roughness from waviness and form from waviness (126), this intermediate range of scales is not considered in the present surface description.

The main issue brought by this definition of surface roughness is that the cut-off lengths ($L_{w\,x} = N_x\, dx$ and $L_{w\,y} = N_y\, dy$) used to remove large scales can be freely chosen by the experimenter. For simplicity, the cut-off length are taken equal in the x and the y directions : $L_w \equiv L_{w\,x} = L_{w\,y}$. The metrology standards (ISO-4288, (89), (79)) recommend a wide range of cut-off lengths from 80 μm to 8 mm. These values were chosen empirically for convenience (135) and it is widely accepted that changing the cut-off length may define a different signal z and affect the extracted roughness parameters.

In addition of the form interpolation, several low-pass Fourier-based filters are proposed by the metrology standards (94), (79). Convolution in the real space corresponds to multiplication in the Fourier space, which explains partly their usefulness. The Gauss-filter is the most widely used (94) and may be used to illustrate the definition of a cut-off length for a Fourier filter. To implement that filter, the survey is convoluted with a weighing-function $S(x, y)$.

$$\mathrm{S(x,y)} \mapsto \frac{\sqrt{\pi}}{\lambda_{\mathrm{xc}}\sqrt{\ln 2}}\, \mathrm{e}^{-\left(\frac{\pi\,\mathrm{x}}{\lambda_{\mathrm{xc}}\sqrt{\ln 2}}\right)^2} \times \frac{\sqrt{\pi}}{\lambda_{\mathrm{yc}}\sqrt{\ln 2}}\, \mathrm{e}^{-\left(\frac{\pi\,\mathrm{y}}{\lambda_{\mathrm{yc}}\sqrt{\ln 2}}\right)^2} \tag{5.4}$$

The filter width in the real space is inversely proportionnal to its width in the frequency space, as it can be seen on the Fourier transform of eq. (5.4), which is also a gaussian :

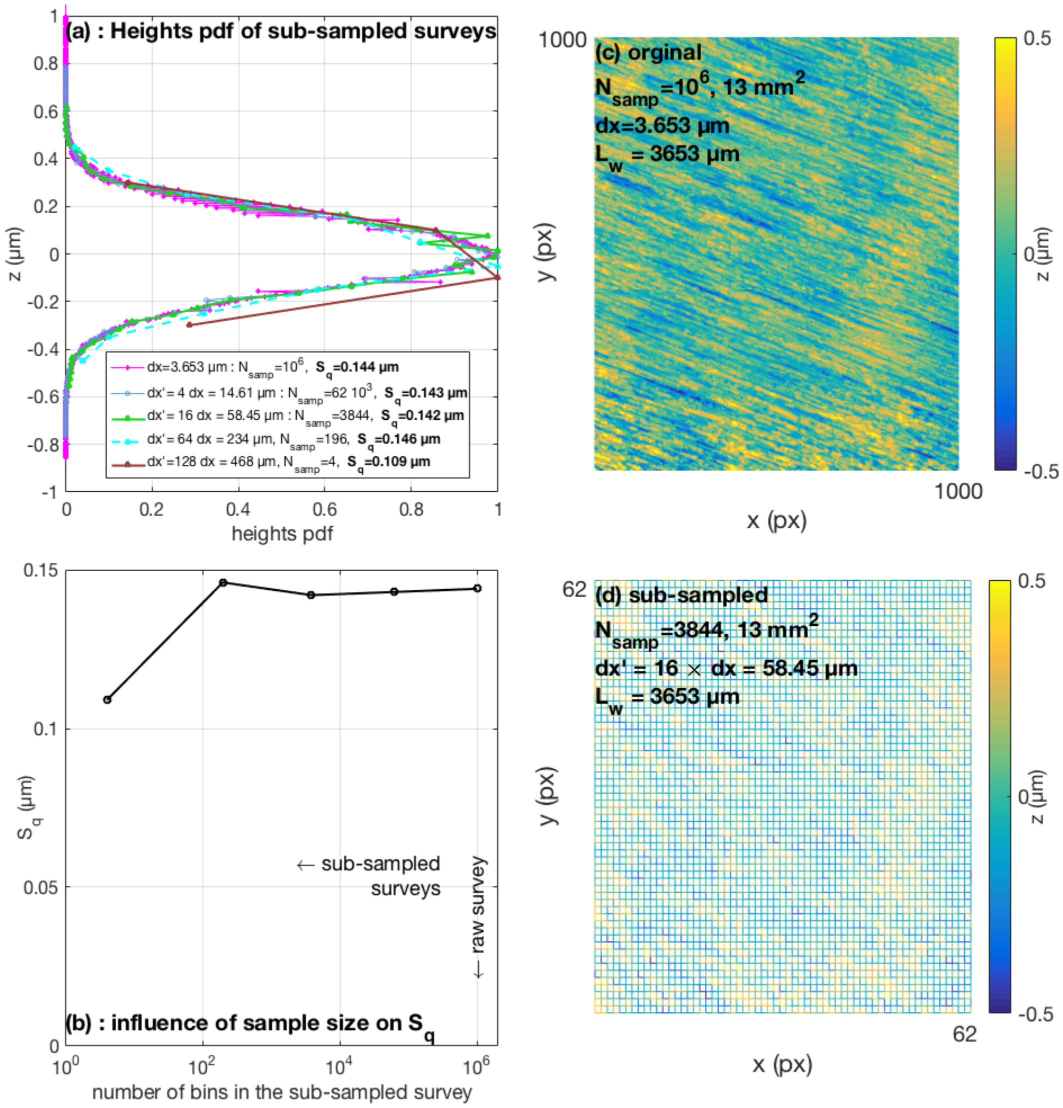

Figure 5.1: (a):Height histogram calculated on the same survey of a rectified steel disc beforehand detrending with a cut-off length equal to the image length : $L_w = 3653\ \mu$m. (b):Evolution of S_q with the sample size of the survey, in number of bins. (c):raw survey measured with a sampling interval $dx = 3.653\ \mu$m. The image is then subsampled by pixel steps of 4 and the heights histograms are calculated on the same area (in physical units). (d):image subsampled with $dx' = 16 \times 3.653 = 58.45\ \mu$m

$$\mathrm{TF}\,[\mathrm{S}]\,(\mathrm{k_x},\mathrm{k_y}) \equiv \int\limits_{\mathbb{R}^2} dx\,dy\; S(x,y)e^{i\,k_x\,x}e^{i\,k_y\,y} = e^{-\left(\frac{k_x\,\lambda_{xc}\,\sqrt{ln\,2}}{2\pi}\right)^2} e^{-\left(\frac{k_y\,\lambda_{yc}\,\sqrt{ln\,2}}{2\pi}\right)^2} \tag{5.5}$$

$$= e^{-ln\,2\left[\left(\frac{\lambda_{xc}}{\lambda_x}\right)^2+\left(\frac{\lambda_{yc}}{\lambda_y}\right)^2\right]} \text{ with } \lambda_{x,\,y} \equiv \frac{2\pi}{k_{x,\,y}} \tag{5.6}$$

For each direction x and y, the spectrum amplitude is divided by 2 when the wavelength equals λ_{xc}, which defines the cut-off length in the x direction. The convolution of the surface topography with a gaussian filter $e^{-\frac{x^2}{2\sigma^2}}$ thus corresponds to low-pass filtering the surface topography with the cut-off wavelength $\lambda_c = \sigma\,\frac{\pi\sqrt{2}}{\sqrt{ln\,2}} \approx 5\,\sigma$:

$$z_{LP_{\lambda_c}}(x,y) = \int\limits_{\mathbb{R}} dx' \int\limits_{\mathbb{R}} dy'\; S(x'-x,y'-y)\,z(x',y') \tag{5.7}$$

After this surface smoothing, the roughness (i.e. the high-pass filtered topography) can be defined according to eq. (5.1). Using another filter will a priori remove or smooth large scales differently because these filters have different Fourier tranforms. Their transfer function is thus different even while imposing the same cut-off length (79).

5.1.3 Goals and methodology

We are interested in describing the effective surface roughness in an EHD contact, with the purpose of correlating the surface roughness to tribological tests in rough lubricated contacts. The goals and requirements of the present chapter are :

1 The definition of a compact set of parameters characteristic of the surfaces topography.

2 The values taken by these parameters must not vary importantly with the specifics of the filtering method used to separate large and small scales.

The last requirement limits the amount of filters that can be imposed for the evaluation of a height standard deviation. It is implicitely required that the evaluation of the parameters be little dependent on the presence of outliers and scarce events in topographical measurements.

The first point requires that these parameters be stationary, i.e. their value must not depend on the choice of the probing zone. This is the most restrictive condition because surface roughness is generally non stationary (127). However, the friction tests reveal characteristic of the surfaces regardless of the topographical differences between different rubbing tracks of the same disc. The extracted set of parameters must permit to classify surfaces according to their likeness and to give a meaning to "smoothness" and "roughness" with respect to the current tribological conditions. The height standard deviation, being widely used in all tribology papers dealing with roughness, was used. Since parameters characteristic only of the height do not account for the x and y directions, they do not represent the whole texture of a surface. The autocorrelation function was thus chosen to study the transverse directions. The summit properties were measured because of the importance of asperities in rough contact models.

5.1.3.1 Isotropic description

Many industrial surfaces have an anisotropic texture. However, during friction tests, the contact area receives the disc orientated in all angles because of the tribometers configuration. An anisotropic surface description would require either to presume, for the present friction problem, one specific direction along which the surface properties would be more important than other directions or to retain as many parameters as number of directions judged important. The former yields a cumbersome surface description while the latter is tackled by the question of the most important direction. For the sake of simplicity, we conducted an isotropic description of surfaces height probability densities. Furthermore, no difference was observed between friction tests using speed ramps and speed steps procedures, where the friction force is always averaged on several discs turns:it can then be assumed that the average friction responds equally to all directions.

5.1.3.2 Choice of cut-off lengths

Since the EHD lubricated contact consists basically in two surfaces being flattened over an area equal to the Hertz area, 2 $\mathrm{a_H}$ forms an upper limit for the wavelengths contributing to friction. At the first order, the surface roughness of rubbing surfaces must then be compared on the basis of a cut-off length close to the contact diameter $L_w \approx 2\ a_H$ (80), (117). For the present experiments, $2 \times a_H \in [100\ ;\ 400]$ μm. Yet, the EHD film thickness is determined ahead of the Hertz circle, in the inlet where the pressure goes from 0.1 MPa to several hundreds MPa. In that region, the surfaces form lies in between their ex-situ nominal shape and the surface roughness. This also leads us to study surface roughness on scales larger than the Hertz area, up to the millimeter.

5.1.3.3 Processing method

The first drawback, raised by Thomas and Charlton (127), is the variability of surface texture from an area to another : a standard error of 50% is typically found on topographical parameters. It is hence important to probe surfaces on an area large enough to include all their variability. Surveys of 1 cm^2 were stitched for this reason. A sampling interval of $dx = dy = 3.653$ μm seemed a good compromise to capture enough details of surface textures while having files not too large (7.5 millions bins) and measurements that did not last more than 1 hour.

The surface variability and the presence of outliers limit the amount of mathematical transforms that should be applied on a raw topographical survey for reasons of computation time and because different processes should yield a priori different results. The more numerous the number of filtering operations applied on a topographical measurement, the more complex the task of weighing the relevance of the output topographical parameters with respect to outliers and the surface inner variability.

After the nominal form (sphere or tilted plane) be first interpolated and subtracted from the whole survey, a cut-off length $L_w = N_w\, dx$ was chosen and the following steps were performed.

- The survey is decomposed into a series of maximum 1000 windows of area $L_w \times L_w$.
- On each sub-window, the mean plane is interpolated and subtracted.
- The standard deviation (or any topographical quantity) is calculated over each sub-window.

These steps are represented fig. 5.2.a. Then, the collection of standard deviations can be regarded as a random variable and an S_q histogram was calculated for each cut-off length L_w, as it is represented figure 5.2.b. For each of the cut-off lengths, several key parameters were retained from the S_q histograms : the mean $< S_q >$, the mode $Mode(S_q)$, the standard deviation $std(S_q)$ and the upper and lower boundaries of S_q.

5.2 Capturing the surface variability through centimetric surveys

5.2.1 Surface statistics

An example is displayed figure 5.3.a for a polished ball with pitted areas. For a given cut-off length ($L_w = 110$ μm on fig. 5.3.b), these pits cause high values for $S_q(L_w)$, which correspond to large positive tails in the S_q histograms as it is shown fig. 5.3.c. The mean and standard deviation calculated including all the S_q values collected is plotted in grey : the histogram positive tails cause a dispersion of the same order of magnitude as the mean of S_q, which agrees with the large variability observed by (127). Ignoring the 5% least probable $S_q(L_w)$ values, $< S_q > \pm std(S_q)$ is calculated (black circles and errorbars on fig. 5.3.c) and seems to better represent the values typically taken by $S_q(L_w)$. It was observed that the relative dispersion of S_q decreases with the cut-off length as $-a \times ln(L_w)$, with $a \in [-5\ ;\ -20]$ (see figures 9.1.a.2, 9.1.b.2, 9.1.c.2 in annex 9.4.1). Alternately to this arbitrary thresholding, the most probable value — or mode, plotted in red on fig. 5.3.c — is not sensitive to the inclusion or the removal of extreme values. Generally, S_q histograms present a single maximum such that $Mode(S_q)$ is well-defined. Its existence is comforted by surfaces textures being recognizable with their overall texture on a given magnification, regardless of the location on the surface. Describing a surface with its most probable parameters ensures the representativeness of these parameters.

Figure 5.3.d compares the evolution of $Mode(S_q)$ and $< S_q > \pm std(S_q)$ versus the cut-off length L_w. As larger wavelengths are included in the sub-surveys, both $Mode(S_q)$ and $< S_q >$ increase with L_w and they follow the same trend. Yet, beyond a certain cut-off length ($L_w \geq 50$ μm on fig. 5.3.d), the dispersion in S_q becomes the same order of magnitude as $< S_q >$ and $< S_q >$ starts diverging from $Mode(S_q)$.

The mode of roughness parameters was investigated systematically in parallel with their mean and standard deviation as it is shown figure 5.4 for several discs. These curves correspond to surveys of 1 cm^2 using a sampling interval of $dx = 3.653$ μm. For all these discs, $< S_q >$ and $Mode(S_q)$ increase in a power-law fashion with L_w, for L_w between 30 μm and 1000 μm. Because S_q can only take positive values, the sub-surveys showing very low values of $S_q(L_w)$ do not balance significantly the very large values of $S_q(L_w)$ sometimes raised by outliers and pits. Consequently, $Mode(S_q)$ is generally inferior to $< S_q >$, from 1% to 40%.

5.2.2 Repeatability of the surface signature

In order to evaluate the representativeness of $Mode(S_q)$ and $< S_q >$, a second survey of 1 cm^2 ($dx = 3.653$ μm) was taken for 8 discs. The relative error of $< S_q >$ between the two surveys was averaged on all cut-off lengths in the range $L_w \in [30\ ;\ 1000]$ μm, and plotted on figure 5.5.a. The same procedure was done for the $Mode(S_q)$ on fig. 5.5.b. The error on $< S_q >$ is of the order 5% for smooth discs (polished, pickled and finished steels). However, this error is larger, between 10% and 26%, for rougher discs (*dARTEb*, *dAR* and *d1RDLC*). For the mode of S_q, an error of 15-20 % is found for the polished steel disc *dAP* and the DLC-coated disc *d4RTDLC*. This relative error being higher for mode than for the mean is also due to the fact that $Mode(S_q) \leq << S_q >$. For other surfaces, the $Mode(S_q)$ keeps the same value between these surveys within an error inferior to 10%, even for the roughest ones.

The better repeatability of $Mode(S_q)$, especially for the rougher surfaces, leads us to use it to describe the height deviations. An other advantage of the mode is that to calculate a relevant value of $< S_q >$, the least frequent values of S_q must be removed with an abritrary threshold (5% was used for the graphs 5.3.c and 5.5.b).

Sayles and Thomas (111) considered the height process as resulting from many random causes *without preference for any wavelength.* Using the central limit theorem and the properties of a

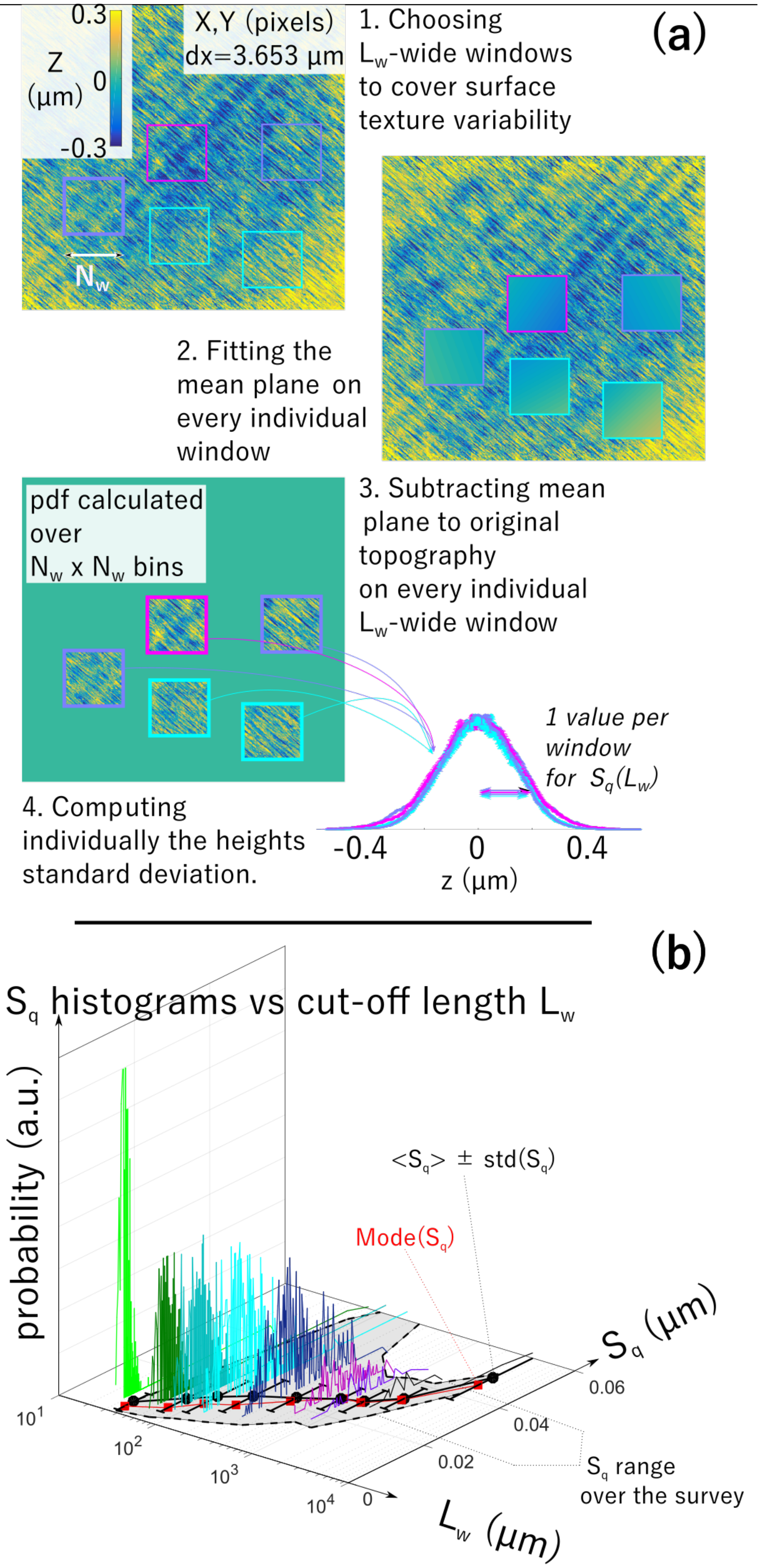

Figure 5.2: (a) : decomposition of a survey into several sub-surveys having an extent of L_w^2, from which the height histogram and the height standard deviation can be extracted individually. (b) : Histograms of the standard deviations $S_q(L_w)$, collected on the survey of a polished steel disc (dAP, measured using $dx = 3.653$ μm) with different cut-off lengths between $L_w = 40$ μm and $L_w = 3000$ μm.

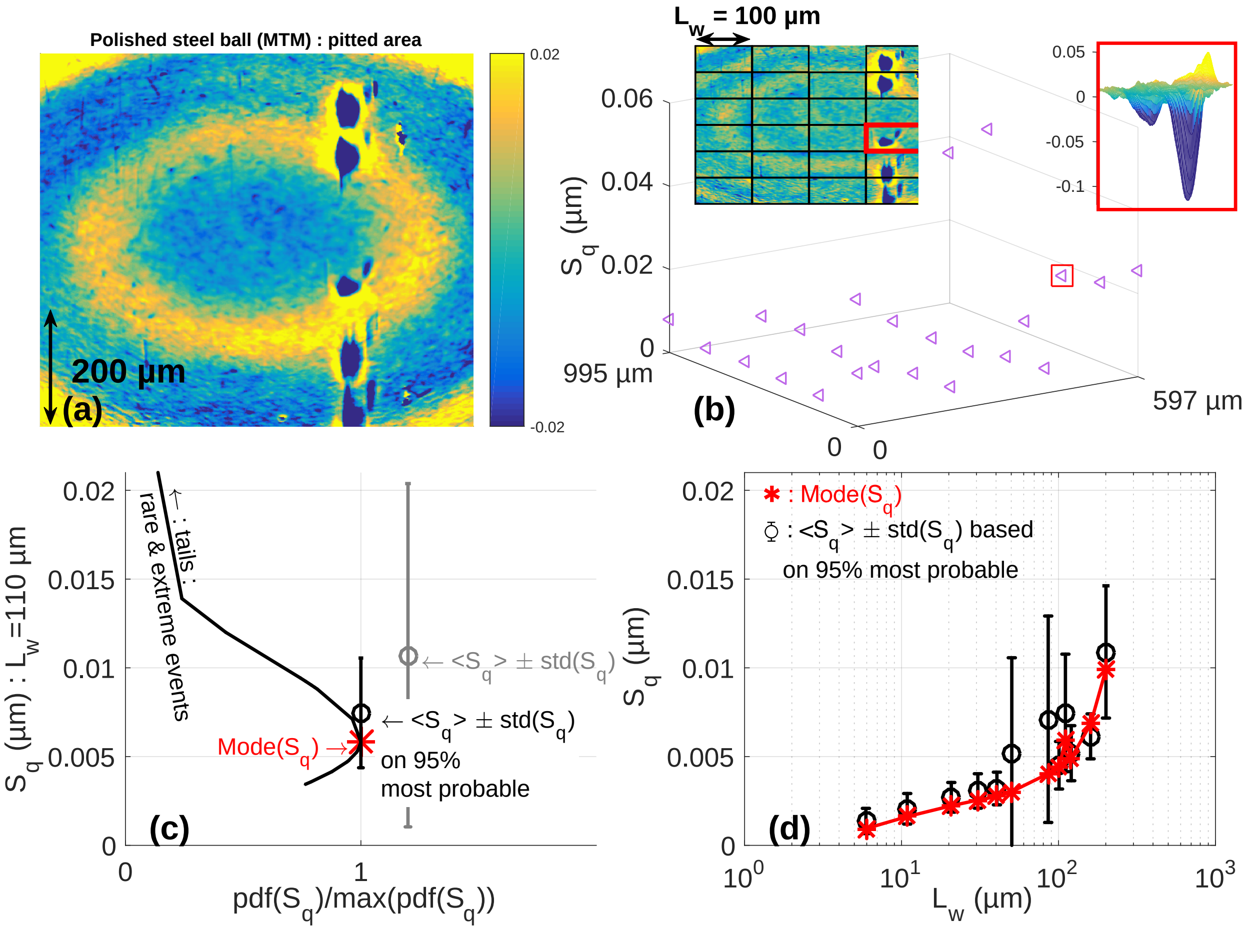

Figure 5.3: (a):Raw survey of a pitted steel ball with $dx = 0.988$ μm. (b):S_q values after local planar detrending with a cut-off length $L_w = 100$ μm. (c):S_q histogram for a cut-off length $L_w = 110$ μm. Circles with errorbars correspond to the $< S_q > \pm std(S_q)$ considering all (grey symbol) and the 95 percent most frequent values (black symbol) of S_q. The mode is plotted with red symbols. (d):Evolution of $Mode(S_q)$ (red symbols) and of $< S_q > \pm std(S_q)$ (based on the 95 most probable percents) with the cut-off length L_w.

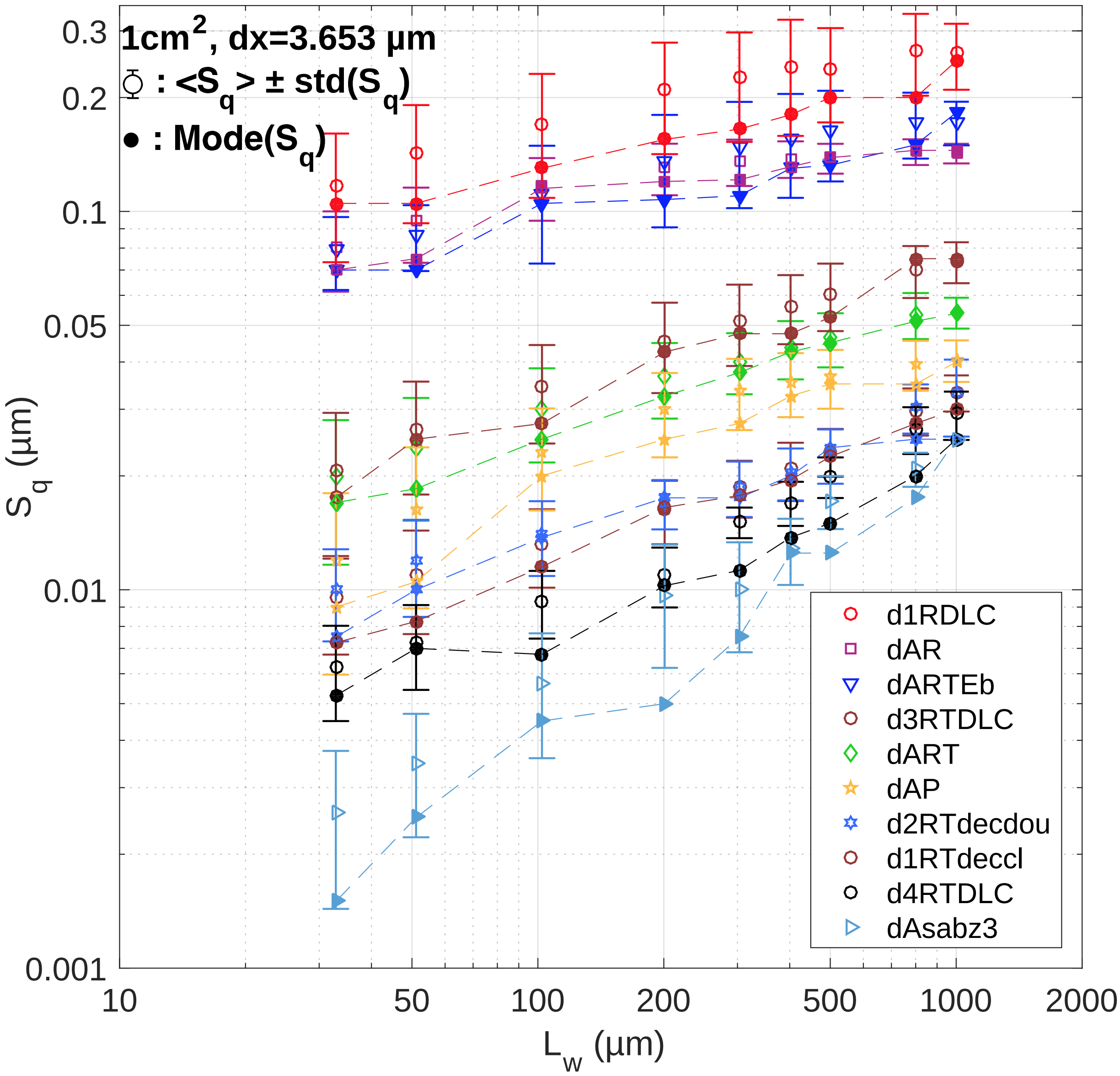

Figure 5.4: Statistical description of S_q collected using local planar detrending versus the window size, or cut-off length L_w. Filled symbols correspond to the mode of S_q, dashed lines with empty symbols and vertical errorbars correspond to $< S_q > \pm std(S_q)$.

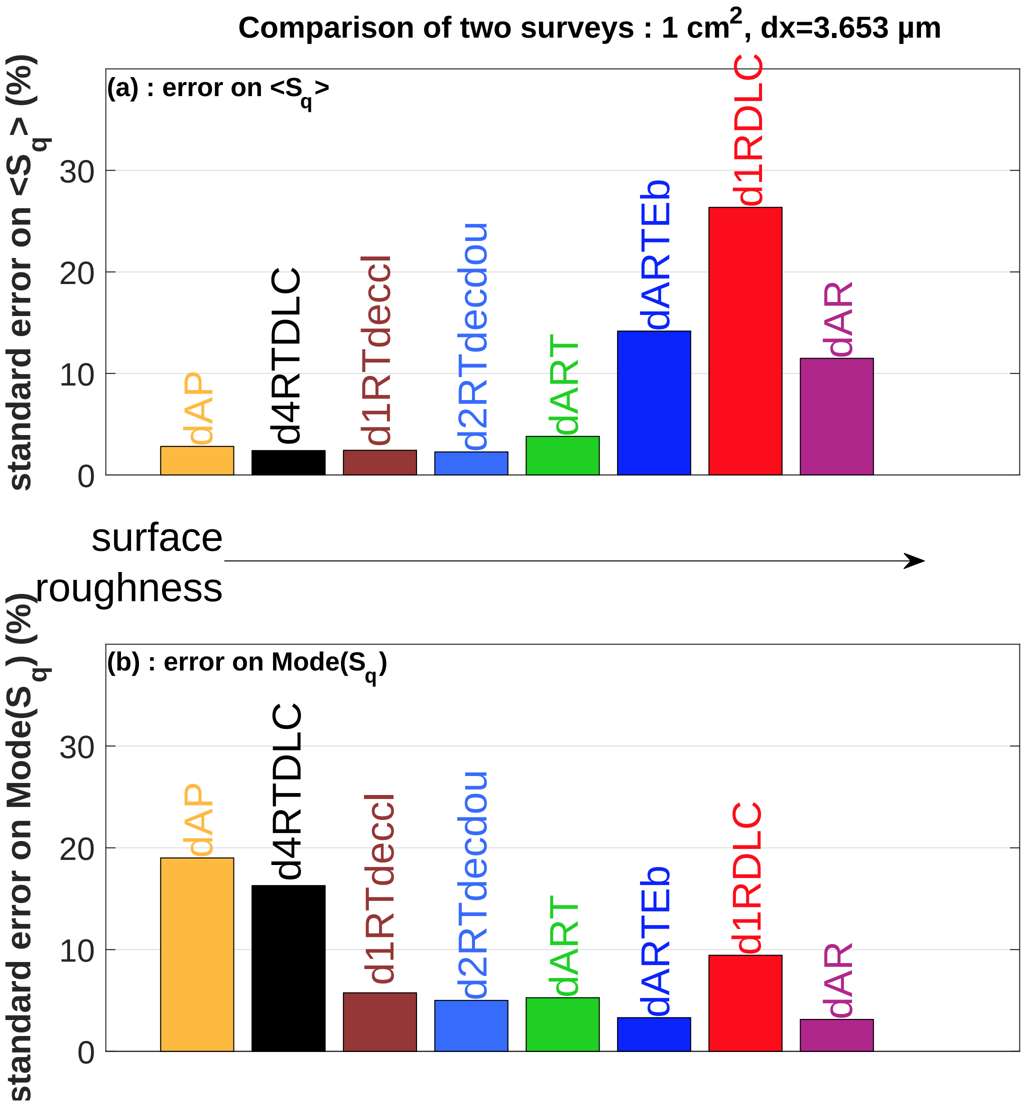

Figure 5.5: Relative error on $< S_q >$ (a) and $Mode(S_q)$ (b) between two centimetric surveys of the same disc, averaged for all cut-off lengths between $L_w = 30$ μm and $L_w = 1000$ μm for several surfaces. For the calculation of $< S_q >$, the 5% least frequent values of $< S_q >$ were removed.

(i)	Mode(Sq) = a x L_w^b (1cm^2, dx=3.653 µm) (S.I. units)									
	dAP	**d1RTdeccl**	**d4RTDLC**	**d2RTdecdou**	**dAsabz3**	**dART**	**d3RTDLC**	**dARTEb**	**d1RDLC**	**dAR**
a	9.30E-07	5.43E-07	3.95E-07	3.04E-07	4.34E-06	6.58E-07	1.27E-06	9.95E-07	1.26E-06	7.00E-07
b	0.439	0.42	0.424	0.347	0.766	0.356	0.409	0.26	0.246	0.216
<err> (%)	1.1	0.3	0.8	0.5	0.9	0.1	0.3	0.3	0.4	0.3

(ii)	<Sq> = a x L_w^b (1cm^2, dx=3.653 µm) (S.I. units)									
	dAP	**d1RTdeccl**	**d4RTDLC**	**d2RTdecdou**	**dAsabz3**	**dART**	**d3RTDLC**	**dARTEb**	**d1RDLC**	**dAR**
a	5.07E-07	3.57E-07	6.20E-07	2.96E-07	2.32E-06	4.33E-07	9.70E-07	1.01E-06	1.46E-06	4.76E-07
b	0.347	0.356	0.454	0.331	0.657	0.294	0.366	0.243	0.237	0.162
<err> (%)	0.5	0.2	0.1	0.3	0.3	0.3	<0.1 %	0.1	<0.1 %	0.3

(iii)	Gauss HP-filtered : <Sq> = a x λ_c^b (16.2 mm^2, dx=3.653 µm) (S.I. units)									
	dAP	**d1RTdeccl**	**d4RTDLC**	**d2RTdecdou**	**dAsabz3**	**dART**	**d3RTDLC**	**dARTEb**	**d1RDLC**	**dAR**
a	6.11E-06	1.23E-06	1.83E-05	1.70E-06	1.60E-06	2.54E-06	5.19E-06	6.28E-06	1.09E-05	2.96E-06
b	0.649	0.493	0.75	0.51	0.634	0.505	0.552	0.442	0.47	0.386
<err> (%)	2.5	2.5	2.9	3.5	0.6	2.3	2.2	1.6	2.5	1.1

(iv)	<Sq> = a x L_w^b (1 mm^2, dx=0.099 µm) (S.I. units)									
	dAP	**d1RTdeccl**	**d4RTDLC**	**d2RTdecdou**	**dAsabz3**	**dART**	**d3RTDLC**	**dARTEb**	**d1RDLC**	**dAR**
a	2.47E-05	3.00E-09	2.00E-09	4.00E-09	1.00E-09	5.00E-09	6.00E-09	1.16E-07	1.26E-07	5.60E-08
b	0.72	0.464	0.417	0.593	0.611	0.493	0.484	0.144	0.237	0.235
<err> (%)	0.1	8.4	4.1	5.2	1.9	4	5.1	0.3	1.8	0.4

Table 5.1: Power law fits of the RMS roughness with the cut-off length.

Gaussian process, they concluded that the surface RMS roughness should increase with a power $\frac{1}{2}$ with the cut-off length. The evolutions of $< S_q >$ and $Mode(S_q)$ of fig. 5.4 were fitted versus L_w using power laws $L_w \mapsto aL_w^b$. The coefficients a, b, and the relative error averaged on L_w are displayed on table 5.1. The fits follow generally the experimental trends with an error inferior to 1%. Most of the exponents lie between 0.1 and 0.4, which discredits the picture used by Sayles and Thomas to describe surfaces. Finally, a Kolmogorov-Smirnov (4, p. 430) (with a 5% confidence interval) test was applied to determine whether the surveys are Gaussian. The test rejects the Gaussian hypothesis for all surfaces and cut-off lengths between $L_w = 30$ μm and $L_w = 2000$ μm. The present surfaces are thus non Gaussian. Nevertheless, the height histograms can be quite well fitted with a Gaussian model (see example fig. 5.6.a), the non-Gaussianity is due to the tails of these histograms. These tails may be due to outliers but also to form residues that are not completely removed using planar detrending.

5.2.3 Comparison with Gaussian-filtered surfaces

The above statistical description uses planar detrending to filter large wavelengths out. However, form interpolation cannot be written as a convolution. This makes the use of the concept of filtered wavelengths improper as these refer to the Fourier transform. We hereby compare the latter planar-detrending description to the Gaussian high-pass filtering (using equations (5.1), (5.4) and (5.7)) in order to test the robustness of the surfaces standard deviation to a different method for removing the large scales. Convoluting two images corresponds to multiplying their Fourier transforms. The Gauss filter spectrum decreases at 50% of its maximum in $k_c = \frac{2\pi}{\lambda_c}$, where λ_c is related to the filter standard deviation σ through :

$$\lambda_c \equiv \pi \sqrt{\frac{2}{ln(2)}} \times \sigma \tag{5.8}$$

Figure 5.6.b shows the height histogram of the same survey as that used for fig. 5.6.a, but

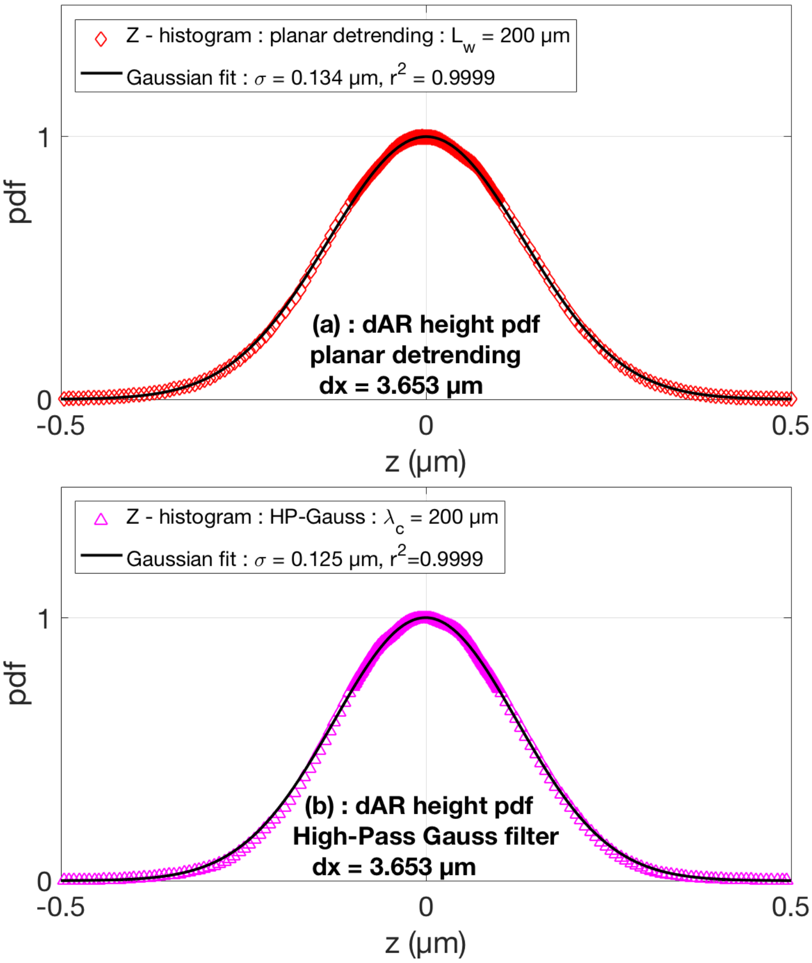

Figure 5.6: Height histograms of a rectified steel disc (dAR, $dx = 3.653$ μm).

high-pass filtered with a Gauss filter and a cut-off length $\lambda_c = 200$ μm. The way now large scales are removed using this filter does not change the result of the Kolmogorov-Smirnov test, which still rejects the Gaussian hypothesis within a 5% confidence interval. Nevertheless, the height pdf can still be quite well approximated with a Gaussian expression (black line on fig. 5.6.b).

For each surface, 6 surveys of 2.7 mm^2 were high-pass filtered using different cut-off wavelengths between $\lambda_c = 10$ μm and $\lambda_c = 400$ μm. S_q was then calculated and averaged between the 6 surveys to be plotted on fig. 5.7.a. To compare the effect of the Gaussian filter with the method based on planar detrending (fig. 5.2.a), the relative error between the $< S_q >$ values shown fig. 5.7.a and values calculated using planar detrending are shown fig. 5.7.b. This absolute error is generally inferior to 20%, though it may reach larger values for pickled discs (with and without a DLC coating). It can hence be concluded that, in terms of standard deviation S_q, the Gaussian filter gives a response very similar to that of the local planar detrending even though both methods proceed differently to remove large scales.

5.3 Surface roughness and sampling interval

5.3.1 Influence of the sampling interval on S_q

The previous study was based on surveys obtained using the same sampling interval $dx = 3.653$ μm. The sampling interval is known to have a large influence on topographical parameters

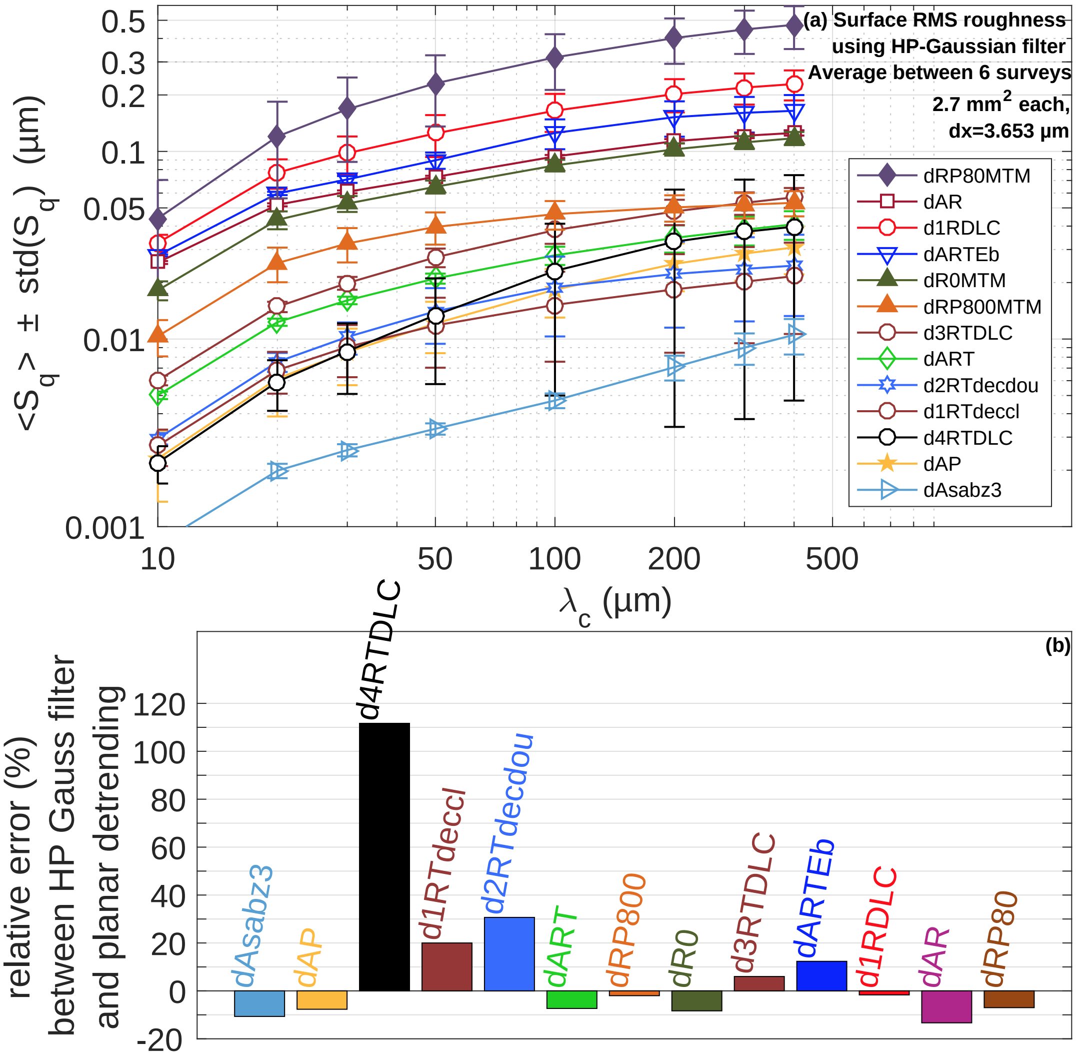

Figure 5.7: (a):Evolution of $< S_q >$ with the cut-off wavelength λ_c (defined with eq. (5.8)) using a high-pass Gaussian filter. S_q was averaged between 6 surveys measured using using $dx = 3.653$ μm on a total area of 16 mm^2. The standard deviation of S_q between the 6 surveys is represented with vertical errorbars. (b):Relative error on $< S_q >$ with respect to the use of local planar detrending ($\frac{<S_q>_{\text{Gaussian filter}} - <S_q>_{\text{planar detrending}}}{<S_q>_{\text{planar detrending}}}$).

(52). Figure 5.8.a represents in black the complete spectrum of a profile. Using a finite sampling interval dx and a cut-off length L_w imposes that the maximum and minimum accessible spatial frequencies be $\frac{1}{2dx}$ and $\frac{1}{L_w}$ respectively. The height variance is equal to the integrated profile spectrum on frequencies between 0 and $+\infty$:

$$\sigma^2 = \int_0^\infty dk\, PSD(k) \approx \int_{\frac{1}{L_w}}^{\frac{1}{2\,dx}} dk\, PSD(k) \tag{5.9}$$

, where PSD denotes the profile power spectral density. The finite sampling interval and cut-off length thus limit the integration domain, such that only a fraction of the variance can be estimated using a sampled topographical measurement. The estimated variance is represented with the area filled in green on figures 5.8.a, 5.8.b and 5.8.c. Figure 5.8.b shows that this area must grow using a larger cut-off length because larger wavelengths are included in the profile, and their spectral energy is generally high. This explains the previous dependence of S_q with L_w (or with λ_c, using a Gaussian filter). However, the term *rough* is generally used to refer to large height deviations occurring on small scales instead of large ones. Figure 5.8.c shows that reducing the sampling interval to dx' leads to increasing the variance of $\int_{\frac{1}{2dx}}^{\frac{1}{2dx'}} dk\, PSD(k)$, which corresponds to the area circled in red, fig. 5.8.c. Yet, if the profile (or the surface) does not contain significant height deviations on wavelengths between $2dx'$ and $2dx$, the increase in variance can be minute.

The power spectral densities of three discs are shown fig. 5.9.a, after azimutal averaging over all angles. There is more than one order of magnitude between the spectral energy of the rectified steel *dAR* and that of the finished steel *dART*, and about 3 orders of magnitude between the rectified and the polished disc *dAP*. This is because the rectified disc has larger height deviations — on all scales — than the two other discs.

Local planar detrending was applied on surveys of a rectified steel disc (dAR) measured at different sampling intervals (figure 5.9.b). The two solid lines correspond to surveys covering 1 cm^2 using $dx = 0.988$ μm (□) and $dx = 3.653$ μm (▽). It is indeed observed that for the *dAR* disc, S_q increases as dx is reduced whereas for the *dART* and *dAP* discs (figures 5.9.c and 5.9.d), the additional spectral energy contained at micrometric scales is too low to increase significantly $< S_q >$ between $dx = 3.653$ μm and $dx = 0.988$ μm.

The sampling theorem of Shannon and Nyquist states that the sampling interval for a given measurement must be chosen inferior to half the smallest wavelength contained in the signal under interest. If this is not realized, i.e. if the surface contains wavelengths inferior to $2dx$, then these small wavelengths become invisible (undersampling) and the sampling may create fictious patterns, with apparent wavelengths superior to $2dx$. This latter phenomenon is called *aliasing.* It can not be predicted a priori whether a surface contains scales inferior to the smallest sampling interval available on the measurement apparatus. Thankfully nature (and the machining processes) generally generates smaller height deviations on small scales than on large scales : even though it is very improbable that a surface becomes perfectly flat below a certain scale, the spectral energy in small scales is generally inferior to that contained in the form. The consequences of using a sampling interval superior to the smallest wavelength of a surface depend thus on the surface. For a smooth surface such as the *dAP* disc, the surface variance (i.e. the total spectral energy) remains almost unaffected by the use of a sampling interval inferior to $dx = 3.653$ μm (see fig. 5.9.d) because most of the spectral energy is contained in scales superior to a few tens microns. For the rough *dAR* disc though, there is enough spectral energy between 0.988 μm and 3.653 μm to cause an important error on the surface variance (see fig. 5.9.b) in this range of sampling intervals. For this reason, topographical parameters must be compared on the basis of surveys (or profiles) measured with the same sampling interval. The comparison of surveys at different sampling intervals allows to determine whether a surface standard

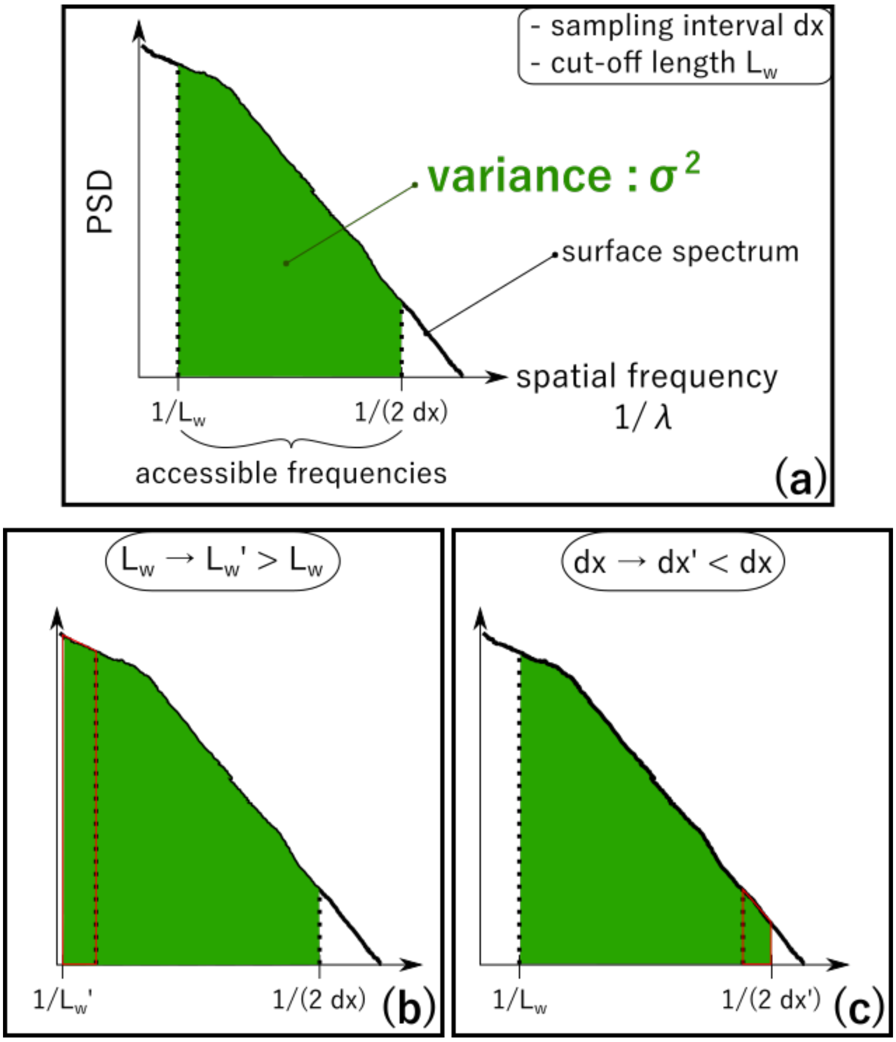

Figure 5.8: Effect of sampling interval and cut-off length on the variance (R_q^2 in 2D, S_q^2 in 3D). The area filled in green corresponds to the variance measured with (dx, L_w) (a), (dx, $L_w' > L_w$) (a), ($dx' < dx$, L_w) (c) which varies because these sampling conditions determine the lowest and highest spatial frequencies that are accessible on a profile (or on a survey).

deviation is due to large, wavy form remains (e.g. manually polished steel, *dAP* disc) or to small scales (e.g. rectified steel, *dAR*).

Local planar detrending was performed on millimetric surveys measured with a sampling interval[1] $dx = 0.099$ μm, for cut-off lengths between $L_w = 10$ μm and $L_w = 400$ μm. Using these magnified surveys, $< S_q >$ still evolves with L_w in a power-law fashion (see fitted parameters on table 5.1.(iv).) with exponents comparable to those obtained with a larger sampling interval. Table 5.2 lists the mean standard deviation using the same cut-off length ($L_w = 200$ μm) for several surfaces. The difference is generally smaller for rough surfaces, i.e. when for $< S_q > \geq 0.1$ μm, though it may reach very high values for smooth surfaces such as the *d2RTdecdou* disc, for which $< S_q >$ reaches 0.09 μm because pits having a depth of a few microns are present in the survey using $dx = 0.099$ μm. Such a small sampling interval limits the extent of topographical measurements to 1 mm^2, which makes them less representative of the surface variability than the centimetric surveys. The height RMS

---

[1] Using interferometry, the resolution is limited by the light diffraction, classically expressed by the Rayleigh criterion (135). This limit was pushed back by a technology, called *AcuityXR*, patented by Bruker (99) and available on the present interferometer.

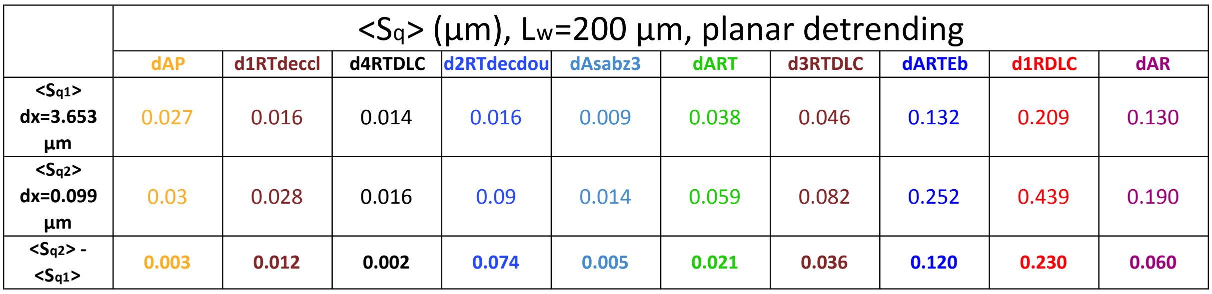

	<Sq> (µm), Lw=200 µm, planar detrending									
	dAP	d1RTdeccl	d4RTDLC	d2RTdecdou	dAsabz3	dART	d3RTDLC	dARTEb	d1RDLC	dAR
<Sq1> dx=3.653 µm	0.027	0.016	0.014	0.016	0.009	0.038	0.046	0.132	0.209	0.130
<Sq2> dx=0.099 µm	0.03	0.028	0.016	0.09	0.014	0.059	0.082	0.252	0.439	0.190
<Sq2> - <Sq1>	0.003	0.012	0.002	0.074	0.005	0.021	0.036	0.120	0.230	0.060

Table 5.2: Comparison of surface mean standard deviation between two sampling intervals.

roughness measured using centimetric surveys with a sampling interval $dx = 3.653$ μm will thus be prefered to characterize the surface height deviations. More magnified surveys are more likely to be helpful to characterize the properties of surface asperities.

5.3.2 Summits

Defining a summit as a height bin higher than its four closest neighbours, the summit density n_s and their mean curvature radius β were estimated. β is defined as :

$$\beta(x_0, y_0) = -\frac{1}{2}\left(\frac{(\partial_x z(x_0, y_0) + 1)^{3/2}}{\partial^2_{xx} z(x_0, y_0)} + \frac{(\partial_y z(x_0, y_0) + 1)^{3/2}}{\partial^2_{yy} z(x_0, y_0)}\right) \tag{5.10}$$

, where (x_0, y_0) denotes the location of a summit. The following finite difference estimators[1] were used for the slope and curvature :

$$\partial_x z(x, y) = \frac{z(x + dx, y) - z(x - dx, y)}{2dx} + o(dx) \tag{5.11}$$

$$\partial^2_{xx} z(x, y) = \frac{z(x + 2\,dx, y) - z(x - 2\,dx, y)}{4dx^2} + o(dx) \tag{5.12}$$

For a given survey, the curvature radii take highly dispersed values. Generally, the mean curvature radius $< \beta >$ has the same order of magnitude as its standard deviation : $std(\beta) \sim < \beta >$. As an example, the reader may appreciate the dispersion of these curvature radii considering the width of curvature radius histograms of the dAP disc shown on fig. 5.10. However, these histograms always contain a single maximum, corresponding to the most frequent value of β. As previously, the mode of β is thus considered to characterize the surfaces curvature radii. Using planar detrending lets the n_s and β histograms constant. However, they are highly dependent on the sampling interval, as it can be seen for instance from the curvature radius histograms of the dAP disc, shown figure 5.10.

These measurements can be compared to results of the random process theory. Assuming the surfaces isotropic, their autocorrelation function is a one-variable function $x \in [0\,; +\infty] \mapsto ACV(x)$. Using the finite difference scheme of eq. (5.12) for the curvature, and $m(x, y) = \frac{z(x+dx,y)-z(x,y)}{dx} = \partial_x z + o(1)$ for the slope, σ^2_{mx} and $\sigma^2_{\kappa x}$ are related respectively to the autocovariance (the convolution of the surface with itself, eq. (5.18)) and to the sampling interval through :

$$\sigma^2_{mx} = \frac{2}{dx^2}(\sigma^2 - ACV(dx)) \tag{5.13}$$

$$\sigma^2_{\kappa x} = \frac{2}{dx^4}(3\sigma^2 - 4ACV(dx) + ACV(2\,dx)) \tag{5.14}$$

---

[1] This is the default estimator using the Matlab *gradient* function.

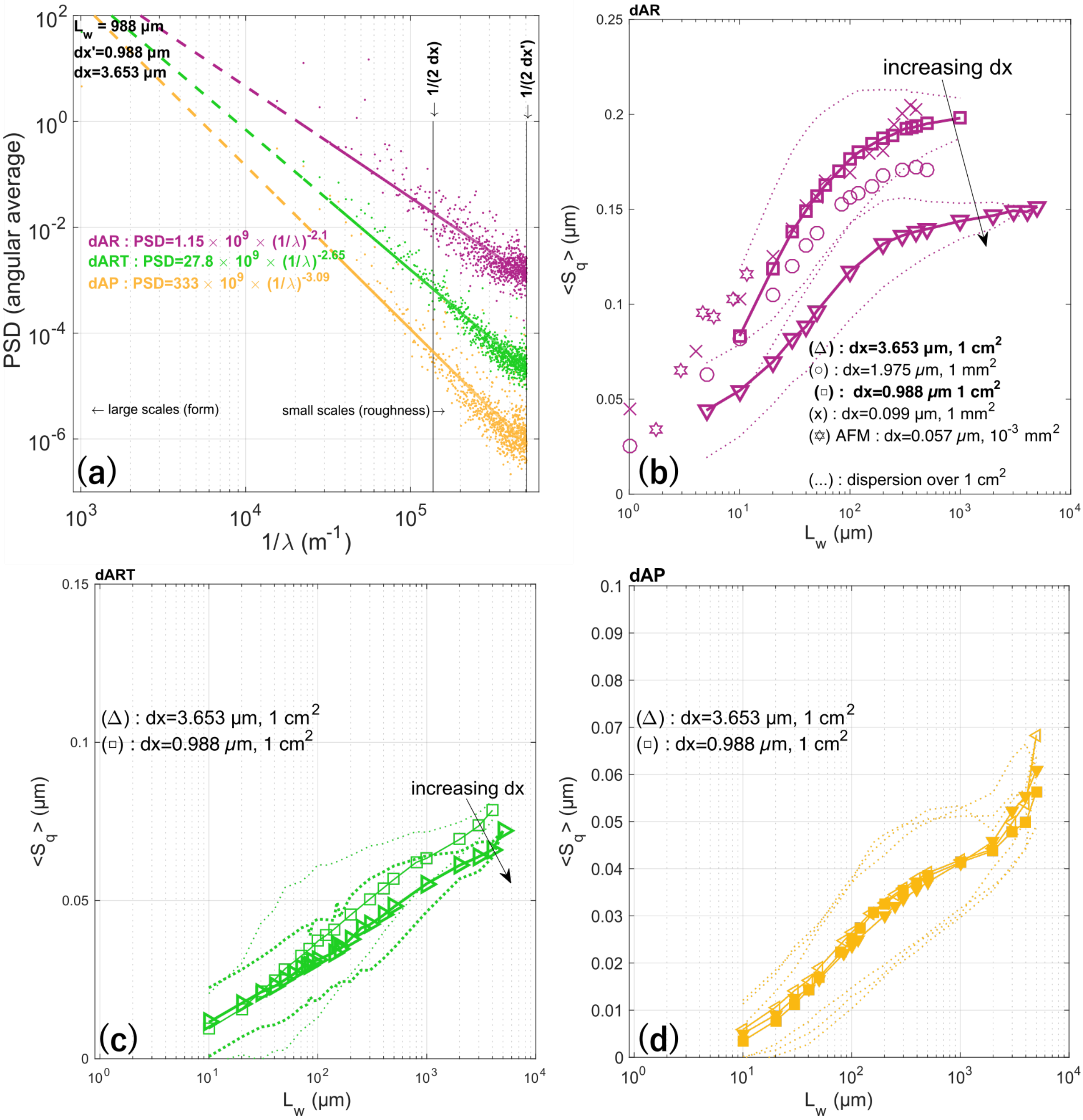

Figure 5.9: (a) : Angular average of the power spectral density versus the wavelength, calculated one three surveys sampled at $dx = 0.988\ \mu m$ with a cut-off length $L_w = 988\ \mu m$. (b,c,d) : evolution of the surface roughness with the cut-off length for different sampling intervals. Solid lines correspond to surveys of 1 cm^2, and the surrounding dotted lines correspond to the standard deviation of S_q over these surveys.

Combining the two last equations with the results of Nayak (equations (2.53) and (2.56)) gives :

$$n_s = \frac{1}{6\pi\sqrt{3}} \times \frac{1}{dx^2} \times \frac{3\sigma^2 - 4ACV(dx) + ACV(2dx)}{\sigma^2 - ACV(dx)} \tag{5.15}$$

$$\kappa_m = \frac{8\sqrt{2}}{\sqrt{3\,\pi}} \times \frac{\sigma}{dx^2} \times \sqrt{1 - \frac{4\,ACV(dx)}{3\,\sigma^2} + \frac{ACV(2dx)}{3\,\sigma^2}} \tag{5.16}$$

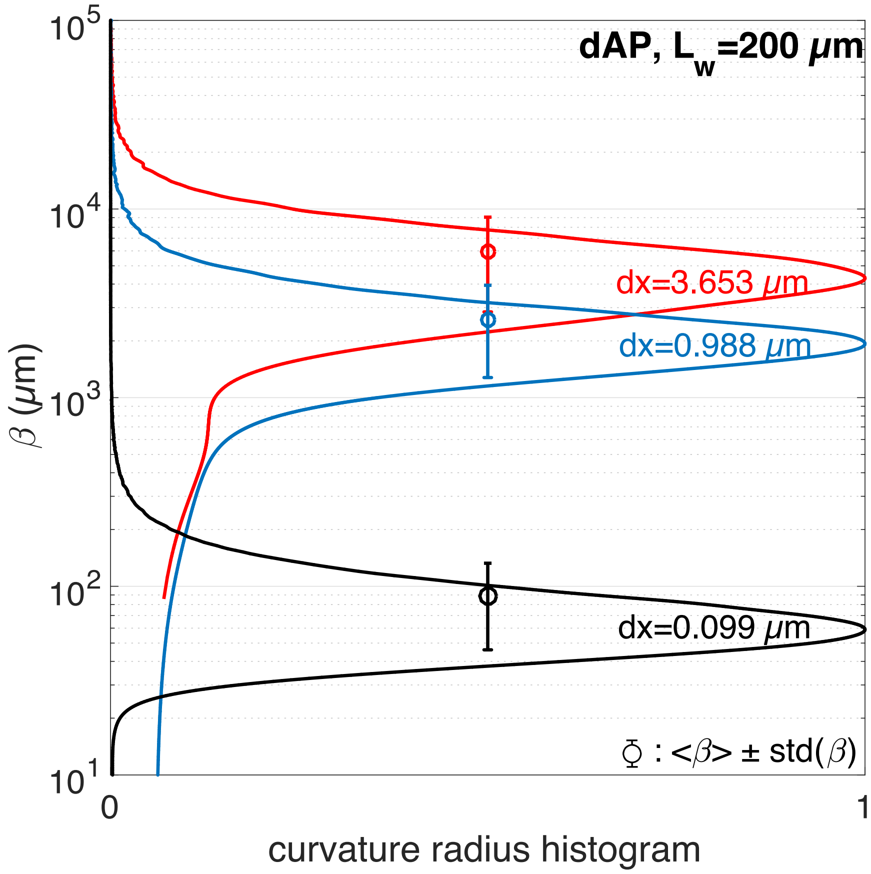

Figure 5.10: Histograms of the summit curvature radius of a polished steel disc (dAP) calculated on surveys measured with different sampling intervals : $dx = 3.653$ μm, $dx = 0.988$ μm, $dx = 0.099$ μm, respectively on areas of 1 cm^2, 1 cm^2 and 1 mm^2.

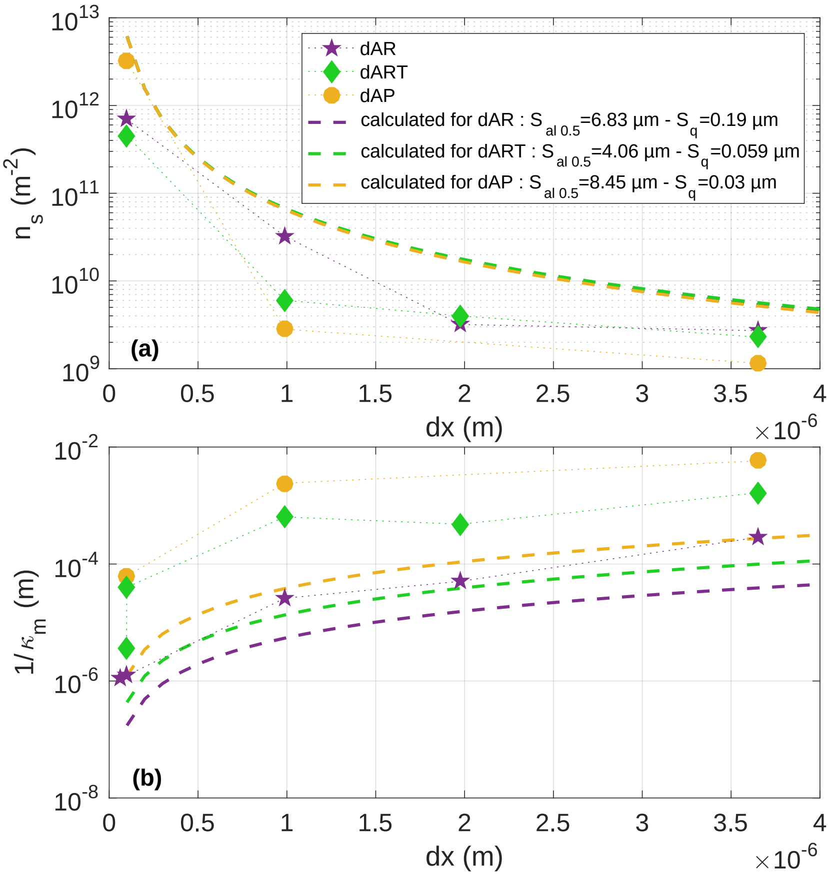

Figure 5.11: Summit density n_s (a) and asperity curvature radius β (b) of different discs measured (symbols) on surveys with different sampling intervals and calculated (dashed lines) using equations (5.15) and (5.16) on the basis of surface properties $S_{al\,0.5}$ and S_q measured using $dx = 0.099$ μm.

Figure 5.11.a and 5.11.b shows the evolution of n_s and $Mode(\beta)$ with the sampling interval for the dAR, $dART$ and dAP discs. The summit density was calculated with eq. (5.15). The mean curvature was calculated using eq. (5.16). Neglecting the slopes on the asperity tips combined with the isotropic[1] hypothesis yields $\beta = \frac{1}{\kappa_m}$. To calculate $ACV(dx)$ and $ACV(2dx)$, the autocovariance function was assumed exponential, i.e. :

$$ACV(x) = S_q^2 \, e^{-\frac{ln(2)*x}{S_{al\,0.5}}} \tag{5.17}$$

, where S_q and $S_{al\,0.5}$ were measured on millimetric surveys with a sampling interval $dx = 0.099$ μm. Even though the trend followed by the experimentally measured parameters is similar to that predicted by Nayak's theory, they do not agree quantitatively. (97) assumed that the surface heights, the first and the second spatial derivatives are independent events, and that the surface is isotropic. It is not possible to prove the independence between different events, but the surface anisotropy can be observed by calculating the three dimensional autocorrelation function. This was done in the next paragraph.

---

[1] $< \partial^2_{xx} z > = < \partial^2_{yy} z >$

5.3.3 Autocorrelation function

5.3.3.1 Anisotropy

The autocovariance is the convolution of the surface with itself :

$$ACV(x;y) \equiv \frac{1}{L_x \times L_y} \int \int dx'\, dy'\; z(x',y')\, z(x-x';y-y') \tag{5.18}$$

, with L_x, L_y denoting the survey extent. In particular, $ACV(0,0) = S_q^2$ and the autocorrelation function is defined as $ACF(x,y) \equiv \frac{ACV}{ACV(0;0)} \in [-1\ ;\ 1]$. The autocorrelation length is defined setting an arbitrary threshold $s \in [0\ ;\ 1]$ for the ACF. In 2D, $S_{al\,s}$ is the minimum distance such that :

$$\forall\theta,\ ACF(S_{al\,s}\, cos(\theta); S_{al\,s} sin(\theta)) \leq s \tag{5.19}$$

$S_{al\,s}$ describes the speed at which the memory, or likeness between bin heights, is lost at a threshold s. A short autocorrelation length reveals a short spatial memory.

Figure 5.12 shows the two-dimensional autocorrelation function contours of three surfaces, calculated using two sampling intervals over sub-surveys of extent 0.04 mm^2. The autocorrelation lengths $S_{al\,0.9}$, $S_{al\,0.5}$ $S_{al\,0.1}$ are plotted in black, they define the direction according which the memory decay is the fastest. $S_{al\,0.9}$ is barely visible because the contours corresponding to a memory decay level of $s = 0.9$ are very close to the origin. Red symbols correspond to the largest distance between the origin and the closest contour for memory decay levels of $s = 0.9$, $s = 0.5$ and $s = 0.1$. This distance is denoted $S_{max\,s}$ and it defines the direction of slowest memory decay. The texture aspect ratio, recommended to characterize the surface anisotropy (79), (123), is defined as :

$$S_{tr\,s} \equiv \frac{S_{al\,s}}{S_{max\,s}},\ \text{for } s \in [0\ ;\ 1] \tag{5.20}$$

$S_{tr\,0.1}$ and $S_{tr\,0.5}$ are repeatable within 30% between $dx = 0.099$ μm and $dx = 3.653$ μm. The values of $S_{tr\,0.1}$ between 0.1 and 0.5 show that the surfaces can not be considered as isotropic. This explains qualitatively the difference between calculated and measured summit density and curvature radius on figures 5.11.a and 5.11.b. It is possible, though cumbersome, to include this anisotropy in the random process theory. However, the 3D autocorrelation functions are non stationary:they present numerous shapes according to the probed area and to the cut-off length.

5.3.3.2 Autocorrelation length stationarity

Figure 5.13.a shows the histograms of these three lengths, probed on two 3 mm^2-wide surveys of the *d4RTDLC* disc using $dx = 3.653\mu$m. $S_{al\,0.9}$ was not retained as a descriptive surface parameter because depending on the steepness of the ACF, the resolution is rather poor close to its maximum. At 10 % of its maximum, almost all the process memory is lost, $S_{al\,0.1}$ should thus intuitively be the best estimate to measure the process memory. Unfortunately, large scales change importantly the tails of the ACF and it results in very dispersed values of $S_{al\,0.1}$ (see red histograms figure 5.13.a). For these reasons, $S_{al0.5}$ was prefered to characterize the autocorrelation decay. Using the method presented fig. 5.2.a, $S_{al0.5}$ was thus collected using different cut-off lengths between $L_w = 30$ μm and $L_w = 2$ mm, their histograms were calculated and their mean and standard deviation were retained and plotted figure 5.13.b for two 1 cm^2-wide surveys of the *d4RTDLC* disc. The difference at $L_w > 1$ mm is believed to be due to the lack of statistics available on these centimetric surveys

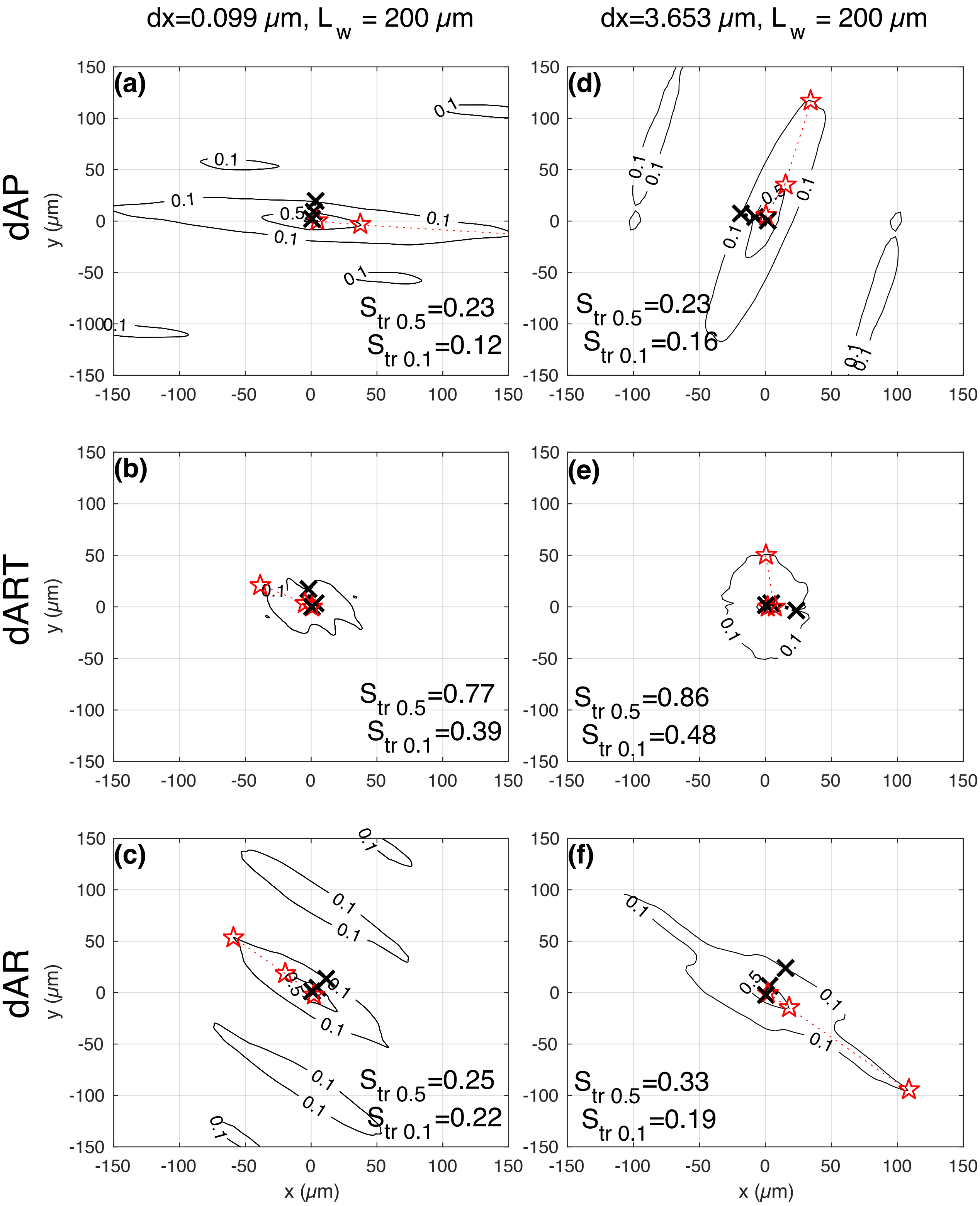

Figure 5.12: Autocorrelation lengths of different discs (dAP : (a), (d) ; $dART$: (b), (e) ; dAR : (c), (f)) measured with the same cut-off length $L_w = 200$ μm and with two sampling intervals : $dx = 0.099$ μm (a, b, c) and $dx = 3.653$ μm (d, e, f). For $s = 0.1,\ 0.5,\ 0.9$, the smallest (respectively largest) distance between the origin and the contour corresponding to $ACF = s$ are plotted in black (respectively in red) and designate the autocorrelation length $S_{al\ s}$ (respectively $S_{max\ s}$).

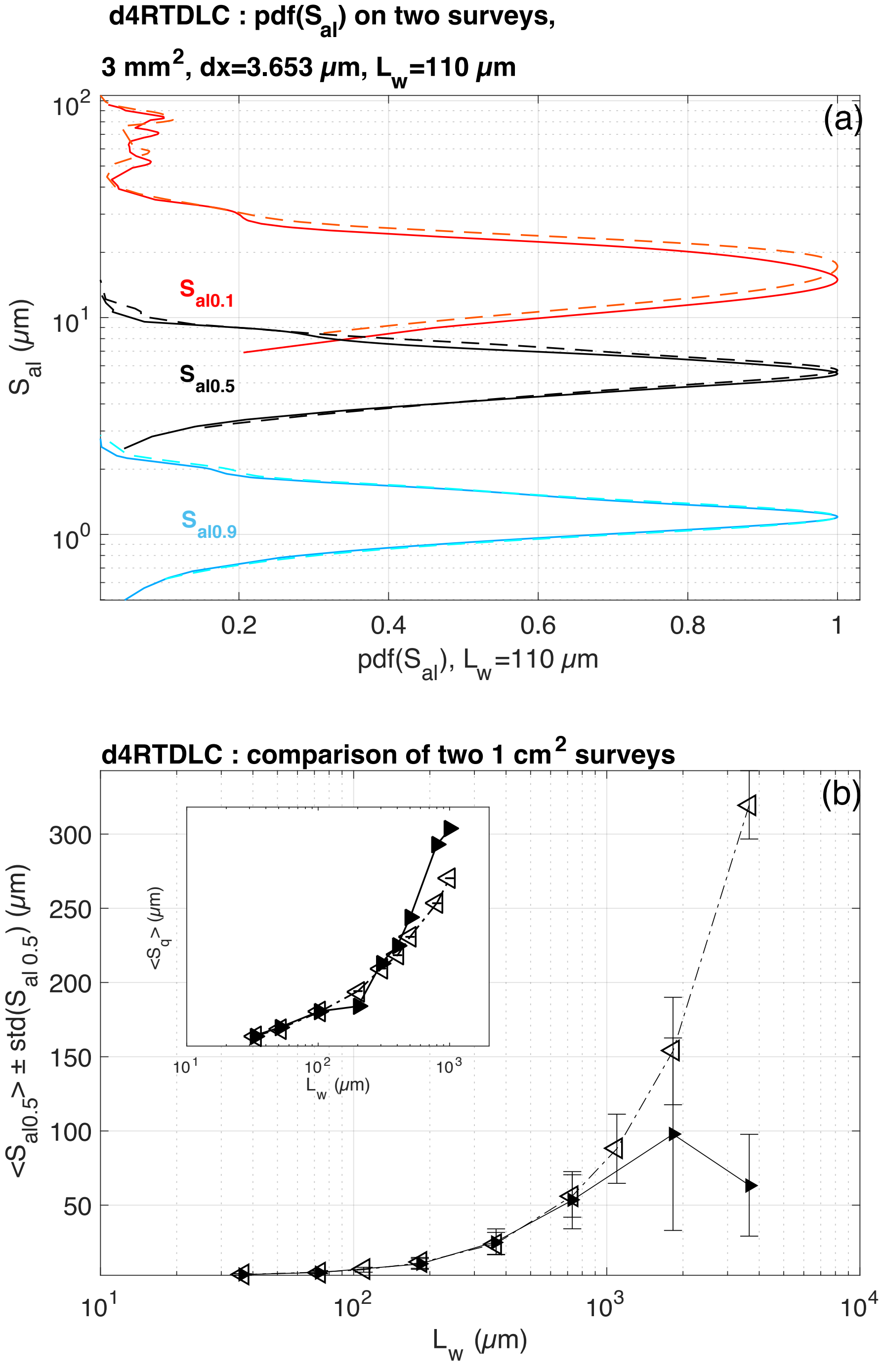

Figure 5.13: Autocorrelation length of a pickled DLC-coated steel. (a) : Comparison of the autocorrelation length collected on two on two small surveys (3 mm^2, dx=3.653 μm each). (b) :Comparison of the mean autocorrelation length collected on two large surveys (1 cm^2, dx=3.653 μm each). The corresponding evolution of $< S_q >$ is shown on the top-left insert.

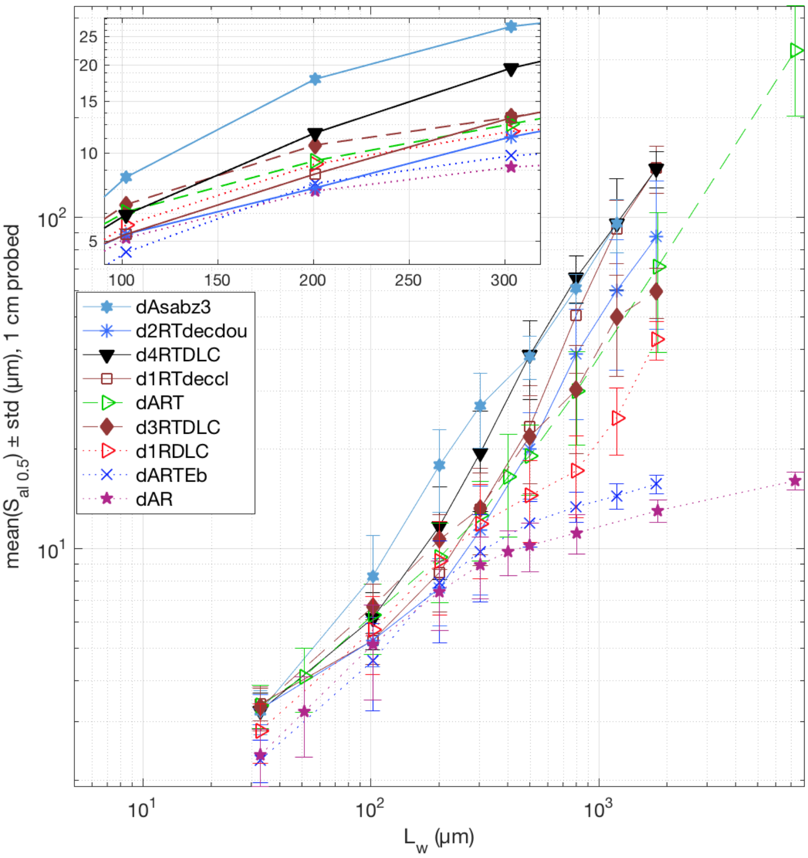

Figure 5.14: Autocorrelation length of different surfaces collected on surveys measured with a sampling interval dx=3.653 μm. The attached plot is a zoom on the cut-off lengths close to the present EHD contact Hertzian width. Dotted lines correspond to the roughest surfaces in terms of S_q.

because for such cut-off lengths, the sample size for $S_{al0.5}$ is inferior to 100 windows. For $L_w < 1$ mm, the mean and the standard deviation of $S_{al\ 0.5}$ sounds stationary.

Autocorrelation lengths were calculated on centimetric surveys with a sampling interval $dx = 3.653\ \mu$m using local planar detrendin (fig. 5.14). It is shown that rough surfaces (dotted lines) have generally a narrower autocorrelation function than smoother surfaces. Reminding that the Fourier transform of the autocorrelation function corresponds to its power spectral density[1], a surface autocorrelation function domain is inversely proportional to its extent in terms of spatial frequencies. For cut-off lengths superior to 100 μm, rough surfaces (dAR, d1RDLC, dARTEb) have a narrower autocorrelation function than smooth surfaces, i.e their spectrum contains more energy towards high spatial frequencies.

5.4 Conclusion

Roughness is defined as the remaining height deviations after the removal of scales larger than a certain cut-off length. The height standard deviation increases with the cut-off length because the height deviations are generally higher on large scales. If the cut-off length determines the largest scales that contribute to the RMS roughness, the small scale contribution is determined by the sampling interval. Comparing surveys with different sampling intervals allows one to estimate whether the

---

[1] From the Wiener-Kintchine theorem.

RMS roughness is of first order due to large scales (form) or to small scales (roughness).

The measurement of summit density and curvature radius do not agree with predictions from the random signal theory that considers surfaces as an isotropic noise with scale-independent autocorrelation function and height deviation. The picture of surface roughness as the result of a cumulated material removal without preferential scales seems to have been widely used to apply the central limit theorem, which allows the convenient use of Gaussian probability densities and other classical results from the random process theory. Yet, surfaces are generated with different manufacturing processes which do have preferential scales, governed by the size of the abrasive grain present on polishing paper, or the curvature of machining dents. It seems that any theoretical attempt to relate different roughness parameters will always be made difficult because of the important non-stationarity of these parameters.

Roughness is highly variable from an area to another. A statistical approach was thus conducted on centimetric surveys by cutting the surveys in sub-surveys of extent $L_w \times L_w$ and subtracting locally the mean plane. Topographical parameters such as S_q or S_{al} were considered as random variables that depend of the cut-off length L_w. Their histograms were calculated for each surface. These histograms are skewed both because of the surface inner variability (pits, for instance, were not homogenously distributed) and because of outliers that cause sometimes unrealistically large values. These extreme values weight the mean whereas the mode (i.e. the most often met values) is not affected by their presence. This has led us to prefer the use of the mode to characterize surface most typical features (height deviations, summit properties, autocorrelation length).

Chapter 6

Transition between lubrication regimes

6.1 Onset of mixed lubrication

6.1.1 What is mixed-lubrication ?

During a Stribeck experiment in EHL conditions, the surfaces are separated by a continuous lubricant film and the friction arises from the shearing of the lubricant pressurized at p_m. When the lubricant flow is progressively diminished, there comes a time where the friction force overcomes that of the single lubricant shearing in the equivalent smooth contact. Different scenarios can be responsible for this friction increase :

1 Dry friction between the solids.

2 Shearing of a nanometric boundary layer of fluid adsorbed on the surfaces.

3 Micro EHL : lubricant is confined between opposing asperities, which increases locally the pressure and hence the fluid viscosity.

The most direct way to assess whether a contact is operating in the ML regime is to measure in situ the film thickness distribution. This experimental task can be made either by resistive measurements (106) — which allow to detect the occurence of metal-metal contacts — or using interferometry (75). Electrical techniques require a calibration (100) between the electrical contact time and a degree of real contact area that depends on the surface topography. Interferometric techniques require that one of the two bodies be transparent and coated with a nanometric semi reflective layer. If it is possible to coat such a layer on nanometrically smooth surfaces such as silica, mica, sapphire plane surfaces, this task becomes trickier on randomly rough surfaces. Except for the experiments with silica and sapphire discs, no direct film thickness measurement could be made during the friction tests. A criterion to spot robustly the ML-EHL transition on experimental friction curves is thus required to allow any statement about this transition.

6.1.2 Phenomenological criteria to spot the ML-EHL transition

6.1.2.1 Minimum friction point

The Stribeck curve is often depicted (134), (21), (116), (63) with a minimum friction point separating ML from EHL. The existence of such a minimum presumes that EHD friction increases with u_e. According to the smooth EHD theory, $h_c \propto u_e^{2/3}$, which yields shear rates increasing with u_e as : $\dot{\gamma} = SRR \cdot u_e / h_c \propto u_e^{1/3}$. Since EHD contacts usually exhibit a shear-thinning behaviour of the lubricant, the shear stress is not exactly proportional to $\dot{\gamma}$ and an exponent slightly smaller than

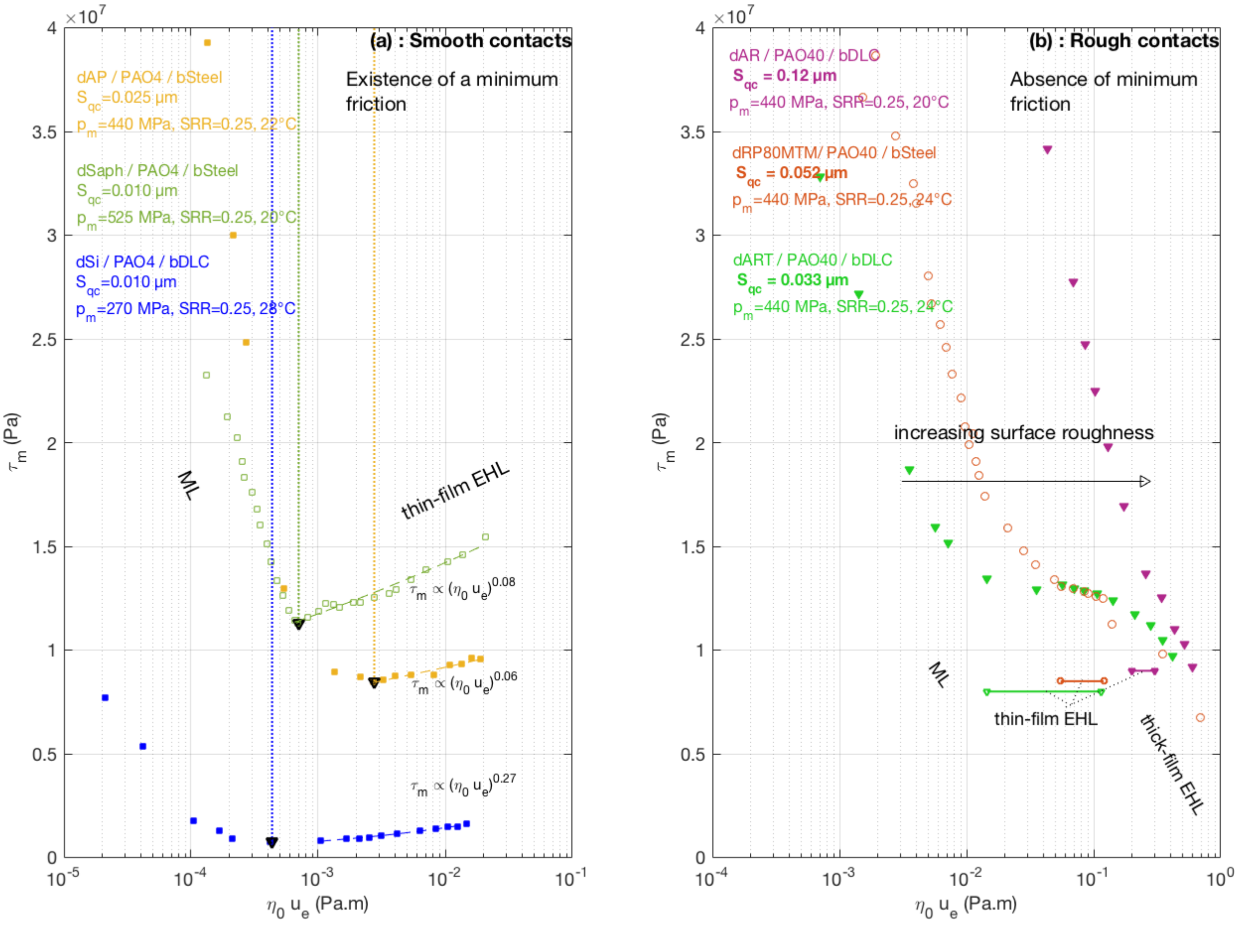

Figure 6.1: (a) : Stribeck curves performed with smooth surfaces showing an increasing friction in the thin-film EHD regime that leads to the existence of a minimum friction point between ML and EHL. (b) : Stribeck curves with rougher contacts do not exhibit such a minimum friction point. Furthermore, in terms of entrainment product, the extent of the presumed thin-film EHD regime shrinks as the composite roughness gets higher.

1/3 is generally found experimentally[1] — typically 0.2 — on the friction vs entrainment relationship. Figure 6.1.a shows indeed smooth contacts with transparent discs against polished balls (with or without a DLC coating) and with a polished steel disc (dAP) against a steel ball where such a minimum friction point exists.

Unfortunately, Stribeck curves with rougher surfaces do not present any increase of τ_m with $\eta_0 u_e$ in the thin-film EHD regime : from BL to thick-film EHL, τ_m may either remain constant until the thick-film EHD regime (see green symbols on fig. 6.1.b with a finished steel disc) or even decrease continuously with $\eta_0 u_e$ from ML to thick-film EHL (see orange and purple symbols on fig. 6.1.b for roughened steel dicsc $dRP80MTM$ and a rectified steel disc dAR respectively).

6.1.2.2 Classical criterion to spot the ML-EHL transition

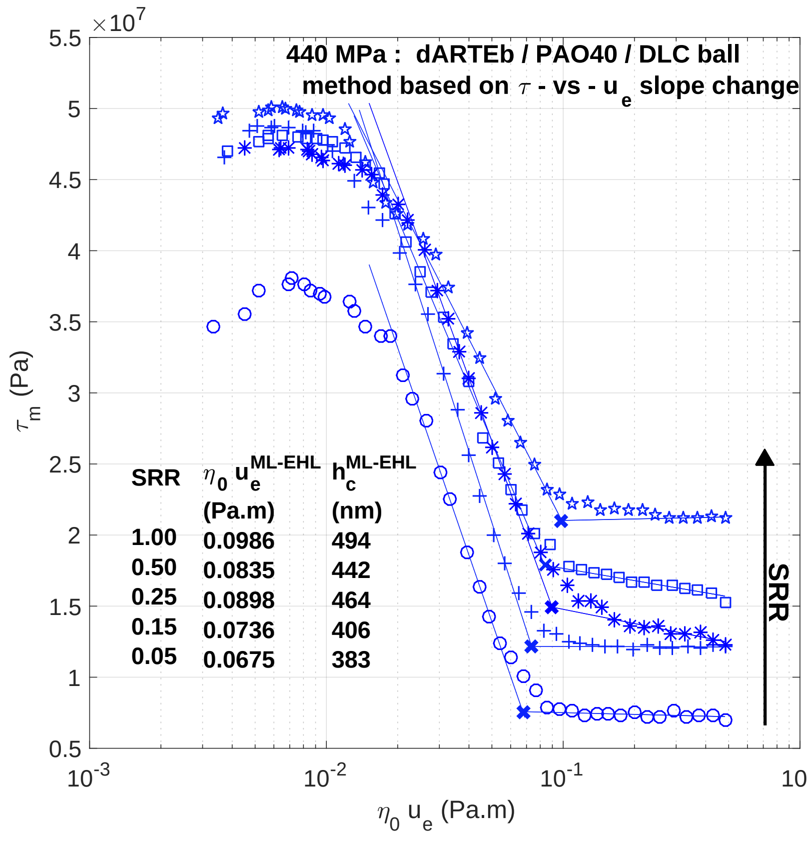

Figure 6.2:

ML-EHL transition defined using the slope rupture between ML and EHL on Stribeck curves performed at sliding-rolling ratios between 0.05 and 1.

Schipper (113) thus used a different criterion to spot ML-EHL transition, based on the linear evolution of friction with the logarithm of u_e that is generally observed in both ML and EHL. He plotted Stribeck curves using the friction coefficient versus the logarithm of the lubrication number $\frac{2\eta_0 u_e}{p_m}$ and defined the ML-EHL transition at the intersection between the two straight lines corresponding to ML and EHL respectively (see example on fig. 6.2). This method requires that the speed range covered in experiments lead the mixed and EHD regimes to allow a robust fit of τ_m against $ln(\eta_0 u_e)$ in both lubrication regimes. It is especially constraining when the motors speed range is restricted to working conditions such that only a small part of the EHD regime is covered.

Beyond this limitation, the boundary between thin-film EHL and the regime of thick-film EHL, where friction always decreases with $\eta_0 u_e$, is usually blurred in rough contacts, such that fitting the

---

[1] This exponent is zero when the fluid shear strength is reached, which occurs at sliding ratios higher than 1, according to the fluid pressure and temperature-dependent rheology.

EHD regime with a straight line can only be done through the eyes of faith (the Stribeck test with a rectified steel disc shown with purple symbols fig. 6.1.b illustrates particulary well this difficulty). Two separate effects due to the surface roughness explain this blurring.

Firstly, a large composite surface roughness lowers the contact film-forming capability compared to smooth contacts and reduces the $\eta_0 u_e$ range allowing thin-film EHL. This is the most important effect due to surface roughness. Figure 6.1.b shows that increasing the surface composite roughness leads to a ML-EHL transition shifted towards upper entrainment products or otherwise said, the contact film-forming capability is diminished by the effect of surface roughness. Figure 6.3.(i) represents the expected shape of the Stribeck curve for a smooth and a rough contact assuming the roughest contact generates smaller films than the smooth one for all entrainment products. The weaker film-forming capability leads to a shift of all lubrication regimes towards higher $\eta_0 u_e$ on the corresponding schematic Stribeck curve drawn with a dashed line fig. 6.3.b. A second-order consequence of the lower film-forming capability is a higher viscous shear stress in EHL. Higher shear rates are generated in the rougher contact because it requires a higher entrainment speed — kept proportional to the sliding speed in a Stribeck procedure — to generate films equally thick as in the smooth contact.

Secondly, sliding-rolling tests with rough surfaces in the thin-film EHD regime may induce asperity interactions (dry contacts and micro EHL) that increase the friction force compared to contacts with an even film-forming capability but with smaller or no asperities. On fig. 6.3.c, two surfaces were assumed to have the same film-forming capability for all entrainment products, which yields equal shear rates and thus equal viscous shear stress in both contacts. Yet, when the film thickness is inferior to the second surface asperities height, the asperities cause an additional contribution to friction, represented with red arrows on fig. 6.3.d. This effect is increasingly important as the film thickness is reduced.

Lubricated contacts with real rough surfaces involve these two contributions. Contrary to the picture 6.3.a, the loss of film forming capability due to surface roughness vanishes as the film thickness is large enough to screen the effect of roughness on the film-forming capability, generally in the thick-film EHD regime. A more realistic Stribeck curve combining the lower film-forming capability and the asperity contribution is shown in fig. 6.3.e with a dashed line.

6.1.2.3 Asperity wear during running-in

As the experiment is run, the asperities can be removed, reducing their contribution to friction in thin-film EHL. As an example, the experiment shown fig. 6.4.a was performed with a DLC coated ball against a sandblasted steel disc (*dAsabz4*). The friction curves showed a decrease of the mixed friction at the second run, each of which lasted 30 minutes. The friction decrease is of 6% at speeds close to the BL regime and is higher, close to the EHL regime with a maximum of 38% at $\eta_0 u_e = 0.1$ Pa.m. For this disc, the rubbing track could be identified (see interferogram 6.4.a and photograph fig 6.4.b). Using a sampling interval $dx = 1.975$ μm, a survey of the rubbing track shows lower height deviations (for the summits and the heights as well) and dulled asperities compared to the topography located outside the track. Yet, most of these disc asperities extend over scales inferior to 2 μm (see AFM image using $dx = 0.0977$ μm, showing the disc unworn topography) such the height parameters tabulated fig. 6.4.c — measured using $dx = 1.975$ μm — must be taken as qualitative hints of the disc smoothing. For other rough contacts such as those with the *dAR* and *dARTEb* discs, some asperities were certainly removed as the friction in ML is reduced at the second run , but these discs were so rough that no difference with the rest of the topography could be quantified. Even though the asperity contribution can be reduced in time by running-in, the asperity removal generally lets the surface texture — accounted for with the RMS composite roughness S_{qc} — unchanged. The contact film-forming capability is mainly governed by the heights standard deviation and not by the summits specifics. Running-in generally removes or smoothens the summit tops, but it does not improve importantly the contact film-forming capability. Consequently,

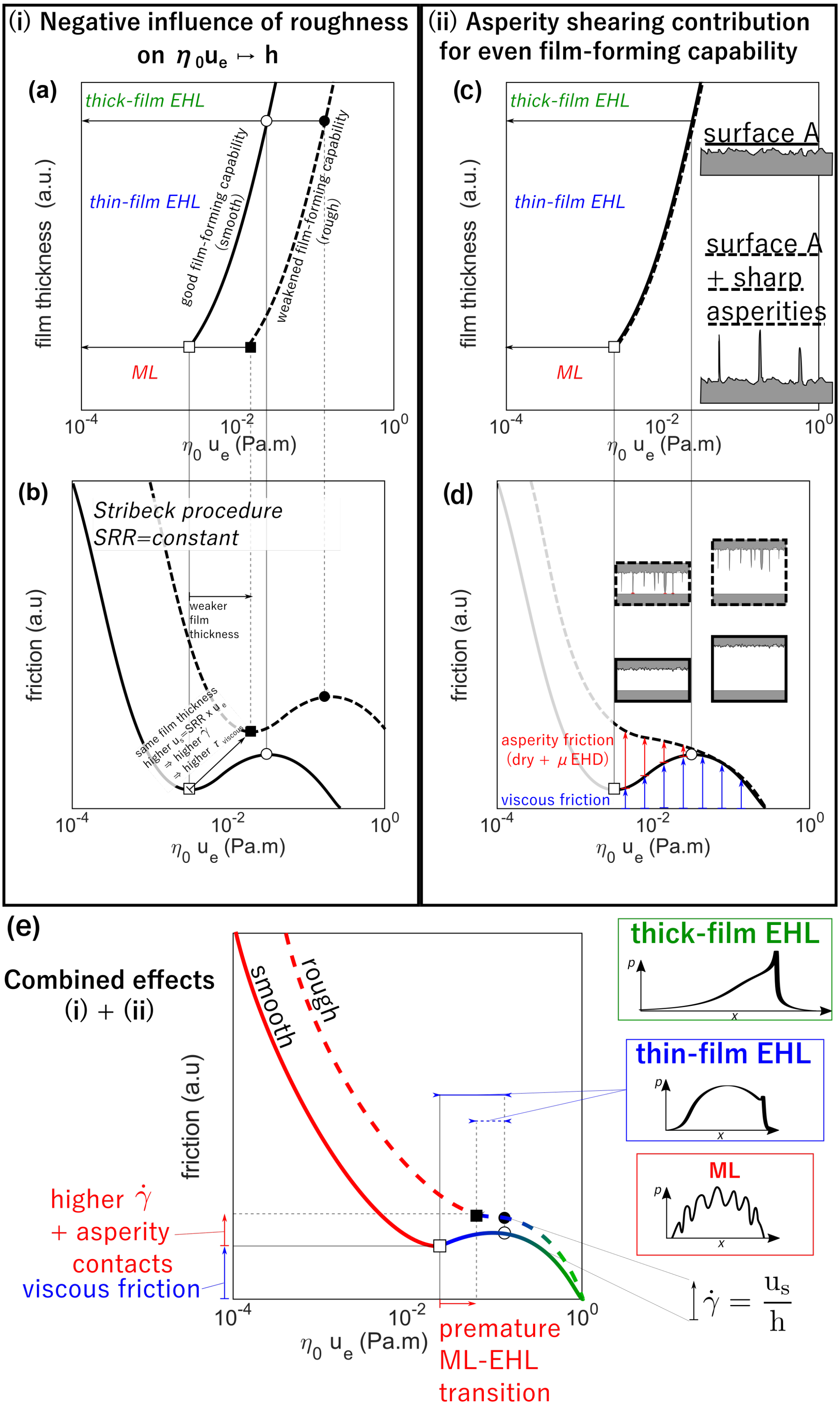

Figure 6.3: (a) : Schematic of the effect of surface roughness on the film thickness with (b) the corresponding evolution of viscous friction in a Stribeck procedure. (c) : Two surfaces are assumed to have the same film-forming capability with one being populated with sharp asperities that cause an additional friction contribution in a Stribeck procedure (d). (e) Schematic of a Stribeck experiment with an ideally smooth contact (solid curve) and with a rough contact with these two effects combined together (dashed curve). The corresponding pressure profiles are also represented schematically presented in the three lubrication regimes on the bottom right part of the figure.

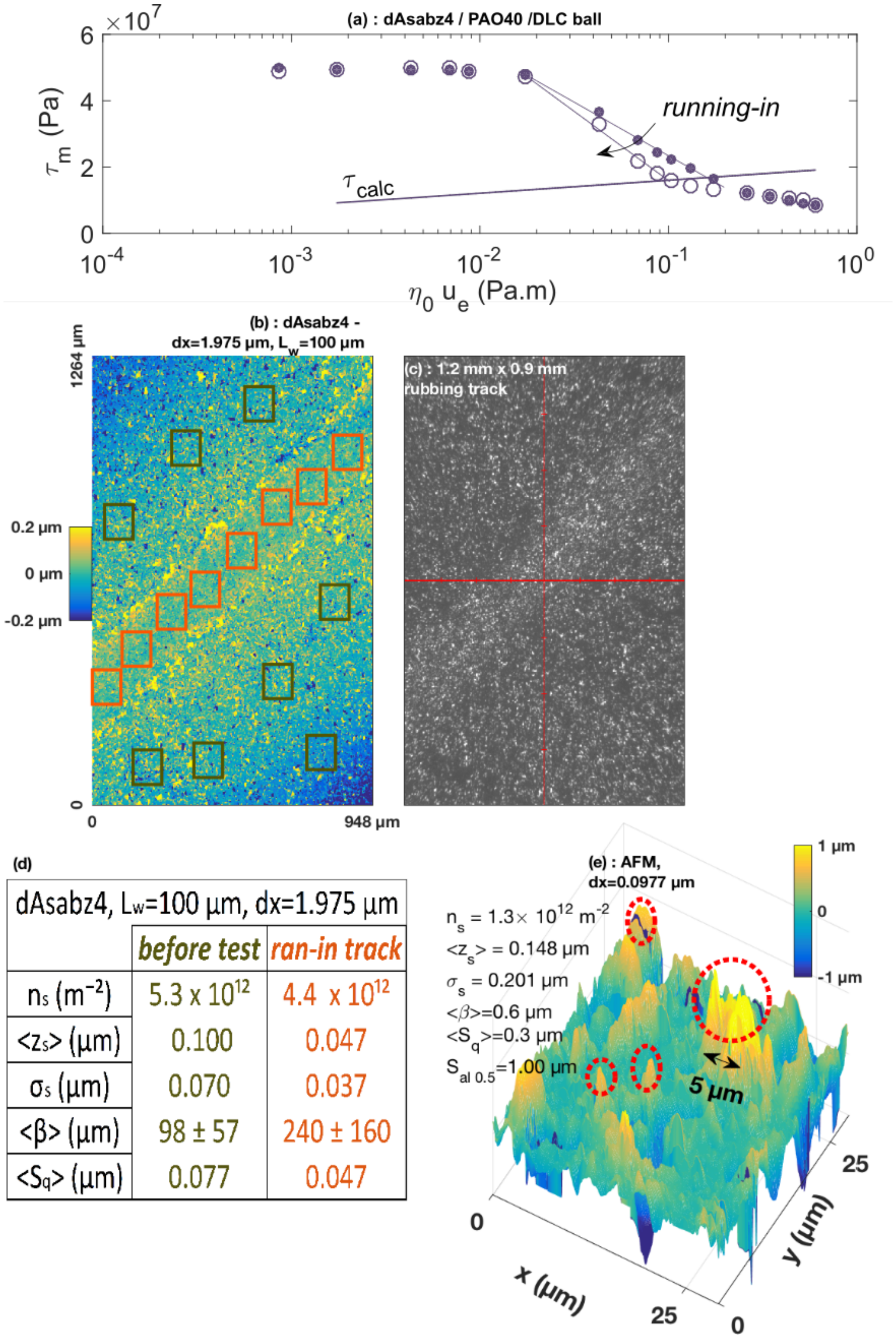

dAsabz4, Lw=100 µm, dx=1.975 µm		
	before test	ran-in track
n_s (m^{-2})	5.3 x 10^{12}	4.4 x 10^{12}
$<z_s>$ (µm)	0.100	0.047
σ_s (µm)	0.070	0.037
$<\beta>$ (µm)	98 ± 57	240 ± 160
$<S_q>$ (µm)	0.077	0.047

Figure 6.4: (a) : Two successive Stribeck tests at 440 MPa with a sandblasted steel disc (*dAsabz4*) against a DLC coated steel ball with PAO40. Each point is the average of a 30 second-long speed step and the experiment total duration was 1 hour. (b) and (c) : Survey ($dx = 1.975$ μm) and photograph of the sandblasted steel (dAsabz4) after rubbing against a smooth DLC-coated ball. (d) : Comparison of the summits and heights parameters outside and inside the ran-in track (grey and red respectively). (e): contact AFM image measured with a smaller sampling interval ($dx = 0.0977$ μm) showing higher height deviations and sharper peaks.

the frontier between thin-film EHL and thick-film EHL remains blurred even after enough runs were performed to remove the sharpest asperities.

The task of fitting correctly the EHD regime with a straight line thus remains uncertain.

6.1.2.4 Friction sub-regimes between ML and EHL

In 1966, Poon and Haines performed sliding-rolling experiments, with the introduction of spin, in mixed and EHD lubrication while measuring the electrical conductivity to evaluate the amount of solid-solid contacts between the surfaces. Their friction versus film thickness curves exhibit two slope ruptures, which allows to spot the EHL regime and two ML regimes (see fig. 6.5.a, from (106)). The electrical measurements allowed to characterize the difference between these two mixed regimes. Significant contact time between the solids was only observed on the far left mixed regime whereas in the *secondary transition region* shown fig. 6.5.a, metal-metal contacts were present but, to the authors, the load remained mainly borne by hydrodynamic action. Furthermore, figure 6.5.a shows that when the sliding-rolling ratio reaches about 1 % ((+), fig. 6.5.a), the EHD regime and the apparent mixed regime between points B and C merge into the same friction evolution. The friction versus film thickness evolution does not allow the spotting of the ML-EHL transition when non negligible sliding is introduced. This work shows that the evolution of friction with $ln(u_e)$ may change with the sliding-rolling ratio and may also be divided into more than two parts:the ML-EHL transition is thus not as abrupt as it is often depicted. Stribeck curves at $p_m = 860$ MPa with PAO40 and two steel surfaces of different roughness are shown fig. 6.5.b. As in the work of (106), the friction evolution exhibits several "sub-regimes" where τ_m evolves more or less linearly with $ln(\eta_0 u_e)$. For the smoothest contact ($dAPMTM$: $S_{qc} = 0.009$ μm), the ML-EHL transition is quite straightforward to spot. For the rougher contact (*dRP80MTM* : $S_{qc} = 0.05$ μm), different slope ruptures appear such that it is impossible to state which one of them corresponds to a *real* transition.

6.1.3 Friction-based definition of ML

Given the above-mentionned uncertainty in spotting the ML-EHL transition thanks to the *evolution* of the friction force versus quantities representing the fluid flow (rolling speed, entrainment product, nominal film thickness, ...), a different approach is conducted to detect the onset of mixed lubrication based on the *value* of friction instead.

For each Stribeck experiment performed with PAO40 and PAO4, the lubricant viscous shear stress is calculated using the Eyring model described with equations (4.32), (4.33), (4.34), (**??**) and the rheological parameters listed in tables 4.2, 4.3. These rheograms are calculated using the mean Hertz pressure p_m, the ambient temperature T_{amb} and the isothermal film thicknesses h_c (eq. 2.15) for the shear rate calculation. This allows one to calculate for each experimental point the ratio R defined as :

$$R \equiv \frac{\tau_m}{\tau_{calc}}(\eta_0, u_e, p_m, T) \tag{6.1}$$

Going from large to low rolling speeds, the onset of mixed lubrication is defined as occuring when friction becomes higher than the viscous friction due to shearing the fluid pressurized at p_m, in thin-film conditions, i.e when :

$$R \geq 1 \Leftrightarrow \text{ML onset} \tag{6.2}$$

Since the roughness may impact the real film thickness, a description based on experimentally accessible parameters seems preferable than the use of calculated film thickness. The entrainment

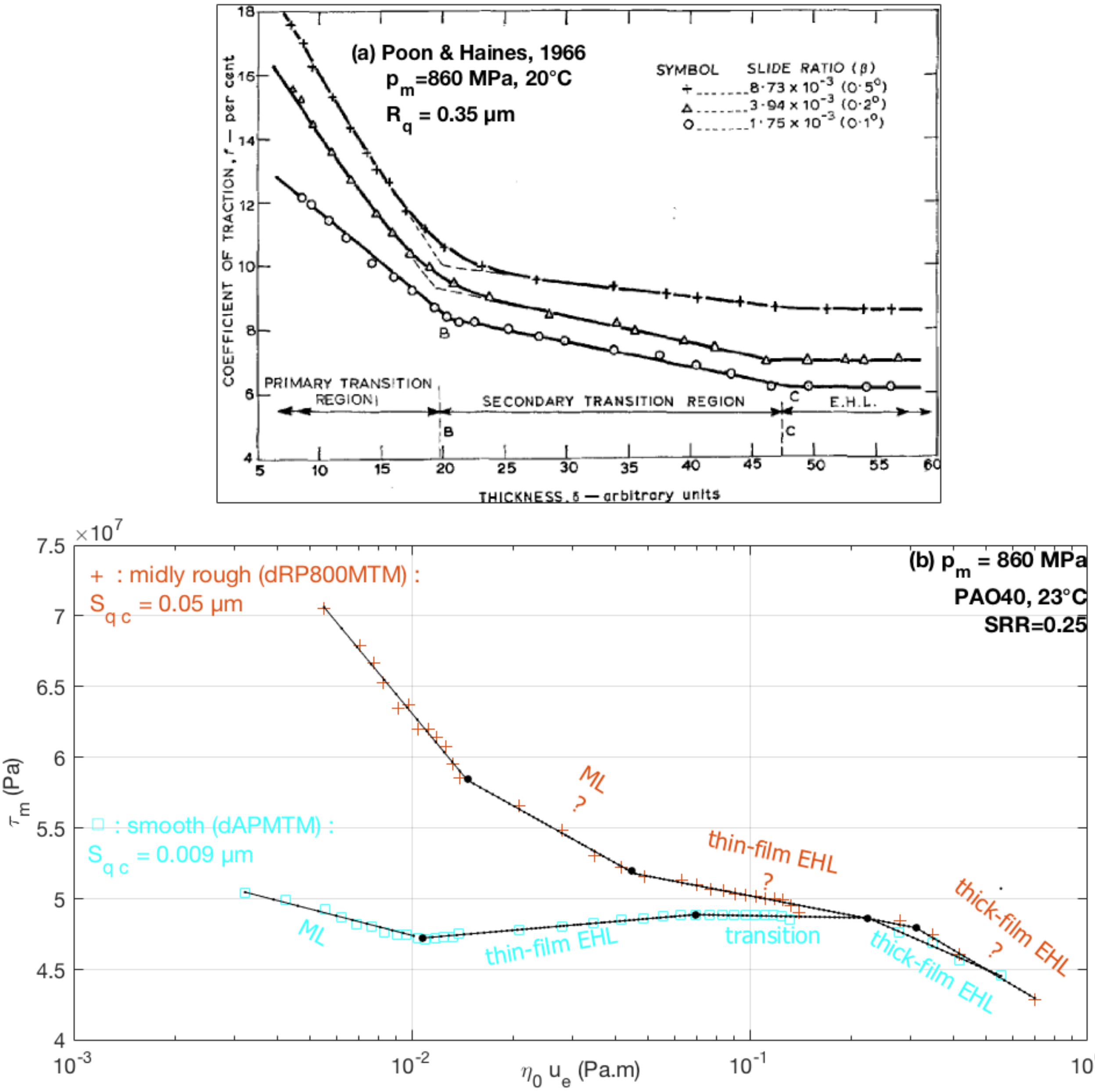

Figure 6.5: (a) : From Poon and Haines (106). (b) : Stribeck tests with PAO40 with two differently rough couple of surfaces.

product $\eta_0 u_e$ is thus used to quantify the ML onset as it is the most influential parameter for the real film thicknesses. It may thereafter be used to calculate nominal transitional film thicknesses to ease the interpretation of the results.

The ML-EHL transition criterion could be set using the reduced traction coefficient introduced by Bair and Winer (10) as : $\frac{\tau_m}{\tau_{max}} > 1$. The issue with such a criterion is that the ML onset would thus be defined as the state where the lubricant shear strength is reached over the whole Hertz area. As it was above-mentionned, the transition from purely viscous friction to ML is continuous. Thus, it is more probable that rough contacts in ML and thin-film EHL be populated at once with several sub-areas with lubricant pressurized at p_m, lubricant pressurized at higher local pressures (micro EHL) and with dry contacts.

The uncertainty for $\eta_0 u_e^{ML-EHL}$ was calculated as follows (see fig. 6.6) : for a given experiment, let ΔR be the uncertainty over R (eq. (6.1)), such that $\tau_{m\ exp} = (1 \pm \Delta R) \times \tau_{m\ calc}$. This uncertainty over the shear stress implies an uncertainty over the transition that depends on the slope of the Stribeck curve at the ML-EHL transition i.e. when $R = 1$: $\Delta(\eta_0 u_e^{ML-EHL}) = \frac{\Delta R}{\left(\frac{d\,R}{d\,(\eta_0 u_e)}\right)}$, evaluated at the intersection between the experimental and the calculated shear stress.

Two sources of uncertainty take part in the determination of the ML-EHL transition : the nominal pressure uncertainty and the shear rates uncertainty due to the negative effect of roughness on film thicknesses. The maximum uncertainty over the Hertz pressure is 10% (see section 3.5.5.1). In the Newtonian, range, $\frac{\Delta\tau_{calc}}{\tau_{calc}} = b_{\eta E}\frac{\Delta p_m}{p_m} \approx 50\%$. Fortunately, all experiments lie in the shear thinning shear rate range, which reduces the impact of pressure on the viscous shear stress. Calculating the Eyring stress while assuming a 10% error on p_m thus leads to an uncertainty of about 15% on the PAO40 and of 20% on the PAO4. Regarding the error on the calculated shear rates, before the contact enters in established ML regime, film thicknesses are typically lowered of 30% with respect to smooth predictions. Again, thanks to the shear thinning behaviour of lubricants, the shear stress is not exactly proportional to $\dot{\gamma}$ and this reduces the error on τ_{calc} to about 20% for the present pressures and lubricants. However, (see section 4.2.4), the shear stress predictions in EHL show more often an error around 10% with respect to the experimental shear stress. For the present investigation, an error of $\Delta R = 10\%$ is thus assumed for the ratio R of eq. (6.1).

Regarding the topographical parameters, it is mentionned in some studies (80), (10), (117) that the cut-off length, to be correlated to friction tests, must be close to the contact length $2\,a_H$ because the surfaces are flattened over the Hertz contact area. Most of the experiments with rough steels were performed with a contact diameter $2a_H = 170\ \mu$m. Unless otherwise specified, the topographical parameters presented in this study are measured using a cut-off length of $L_w = 200\ \mu m$ and with a sampling interval $dx = 3.653\ \mu$m. S_{qc} refers to the RMS composite standard deviation based on the mode of the ball and the disc roughnesses :

$$S_{qc} \equiv \sqrt{Mode(S_{qD})^2 + Mode(S_{qB})^2} \tag{6.3}$$

Finally, in order to make possible the comparison of the present ML-EHL transitions with previous works, the ML-EHL transition is also spotted, when possible, using the classical method (see fig. 6.2), based on the linear extrapolation of the τ_m-vs-$ln(\eta_0\, u_e)$ evolution in the ML and EHL regimes.

6.2 Results on the ML-EHL transition

6.2.1 Sliding speed influence

Figure 6.7 : Stribeck tests at 440 MPa at various slip ratios show the influence of sliding on friction according to the lubrication regime. At entrainment products large enough, the contact is in

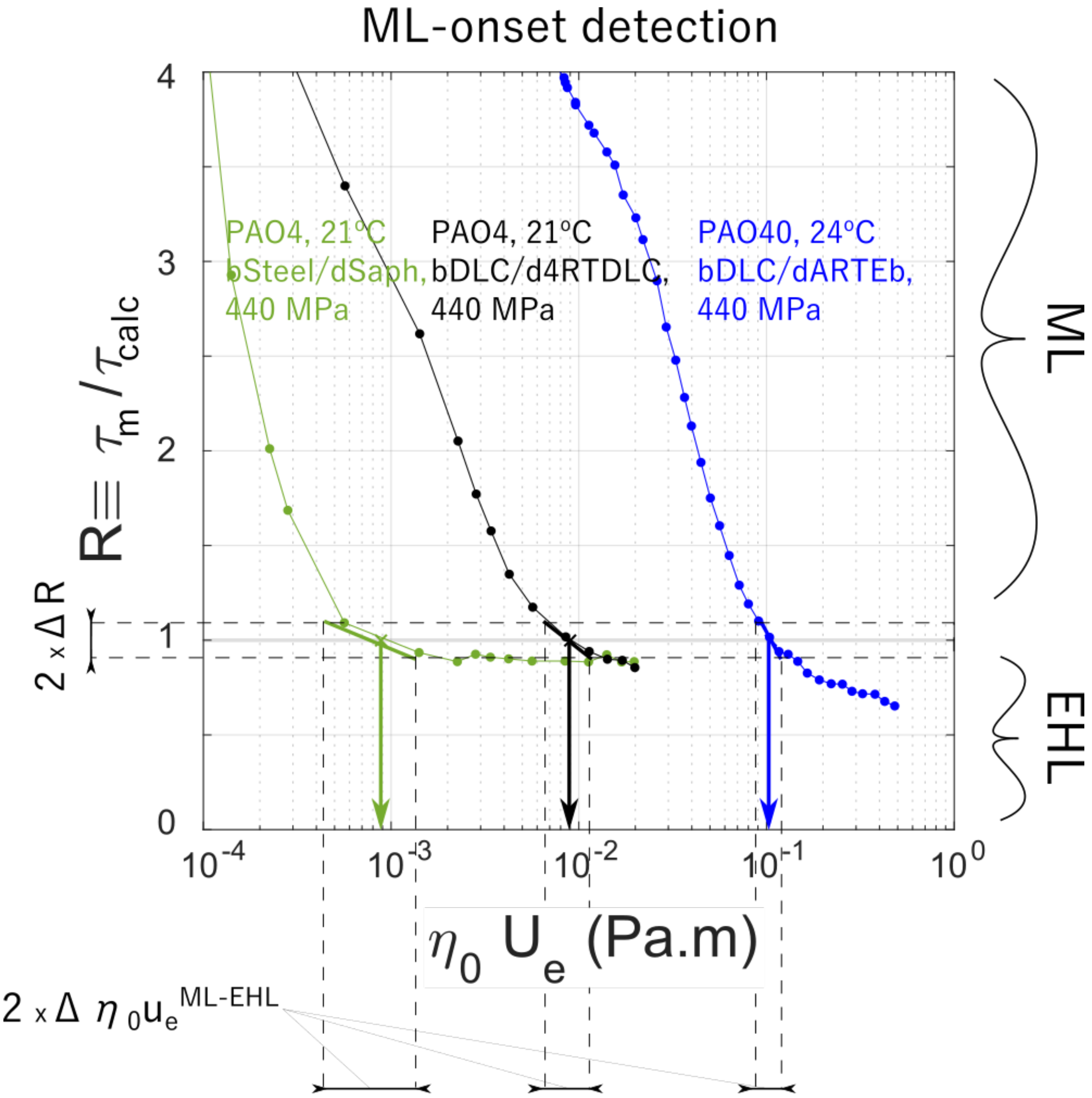

Figure 6.6: Stribeck experiments at $SRR = 0.25$ plotted using the ratio of the experimental shear stress divided by the viscous stress prediction.

full-film EHL and friction increases with SRR because it directly affects the shear rate imposed to the fluid. To this statement, it should be added that during the Stribeck tests conducted with PAO40, $\dot{\gamma}$ stays below $5 \times 10^5 s^{-1}$, and below $5 \times 10^6 s^{-1}$ for those with PAO4. The rheograms presented fig. 4.8, section 4.1, show that at 440 MPa and for this range of pressure and shear rates, the lubricant shear strength is not reached. Similarly, the shear stress is always superior to the fluid Newtonian limiting shear stress $\tau_0(p) = \tau_{00} + a_{\tau_0} \cdot p_m$, which implies a weaker influence of sliding on friction than it would have in the Newtonian shear-regime. All Stribeck experiments of this work lie in the shear-thinning regime, in between the Newtonian and the plastic shear regimes, as it is also confirmed by the shear stress-versus-shear rate plots of Stribeck tests shown in figure 6.8. On these graphs, the lubricant rheology is displayed in solid black line and triangles spot the ML-EHL transition. Crossing the ML regime from EHL to BL with steel/steel and steel-DLC contacts, the influence of sliding on friction progressively vanishes until the BL regime is reached, where the friction is high and independent of both the entrainment speed and the sliding speed. Fig. 6.7 illustrates this decreasing influence of the sliding-rolling ratio as $\eta_0 u_e$ is decreased down to the boundary regime.

Friction-based ML-EHL transition On figures 6.7 and 6.8, the friction-based ML-EHL transition is defined according to equations (6.1) and (6.2) and the values are plotted with full symbols in fig. 6.9.a and 6.9.b, respectively in terms of entrainment product $\eta_0 u_e^{ML-EHL}$ and of transitional nominal film thickness, denoted h_c^{ML-EHL}. For each couple of surfaces, the transitional entrainment products and the associated nominal film thicknesses appear independent of the sliding-rolling ratio. The composite standard deviation $S_{q\,c}$ and the central film thickness allow to calculate transitional lambda ratios :

$$\Lambda^{ML-EHL} \equiv \frac{h_c^{ML-EHL}}{S_{q\,c}} \tag{6.4}$$

Figure 6.9.c shows that the transitional lambda ratios for RMS roughnessess inferior to 0.2 μm cover values between 4 and 15.

6.2.1.1 Classical spotting of the ML-EHL transition

The transitions using the classical slope rupture-based criterion are added to figure 6.9 in empty symbols. The ML onset is then spotted at lambda ratios close to 3 ±1 for the three couples of surfaces where such a spotting was possible.

6.2.2 Pressure influence

Four couples of steel surfaces (*dAPMTM, dRP800MTM, dR0MTM, dRP80MTM*) having a roughness between 0.009 μm and 0.4 μm were used to perform Stribeck tests at $SRR = 0.25$ with PAO40 and with PAO4 at pressures of 315, 440, 500, 750 and 860 MPa. The Hertz diameters for this pressure range lie within [122 ; 334] μm. The cut-off lengths used to calculate the RMS roughness should be adapted to each experiment. However, the relative increases in $Mode(S_{qD})$ between $L_w = 200$ μm and $L_w = 400$ μm are of 31%, 6%, 34% and 10% respectively for the discs denoted *dAPMTM, dRP800MTM, dR0MTM, dRP80MTM.* Accounting for the fact that these height deviations barely change the following results, the same cut-off length $L_w = 200$ μm was used to correlate the ML-EHL transition to roughness.

6.2.2.1 Friction-based ML-EHL transition

The results for the friction-based ML-EHL transition are plotted figure 6.10. The transition from EHD friction to mixed friction occurs at an entrainment product and a nominal film thickness that

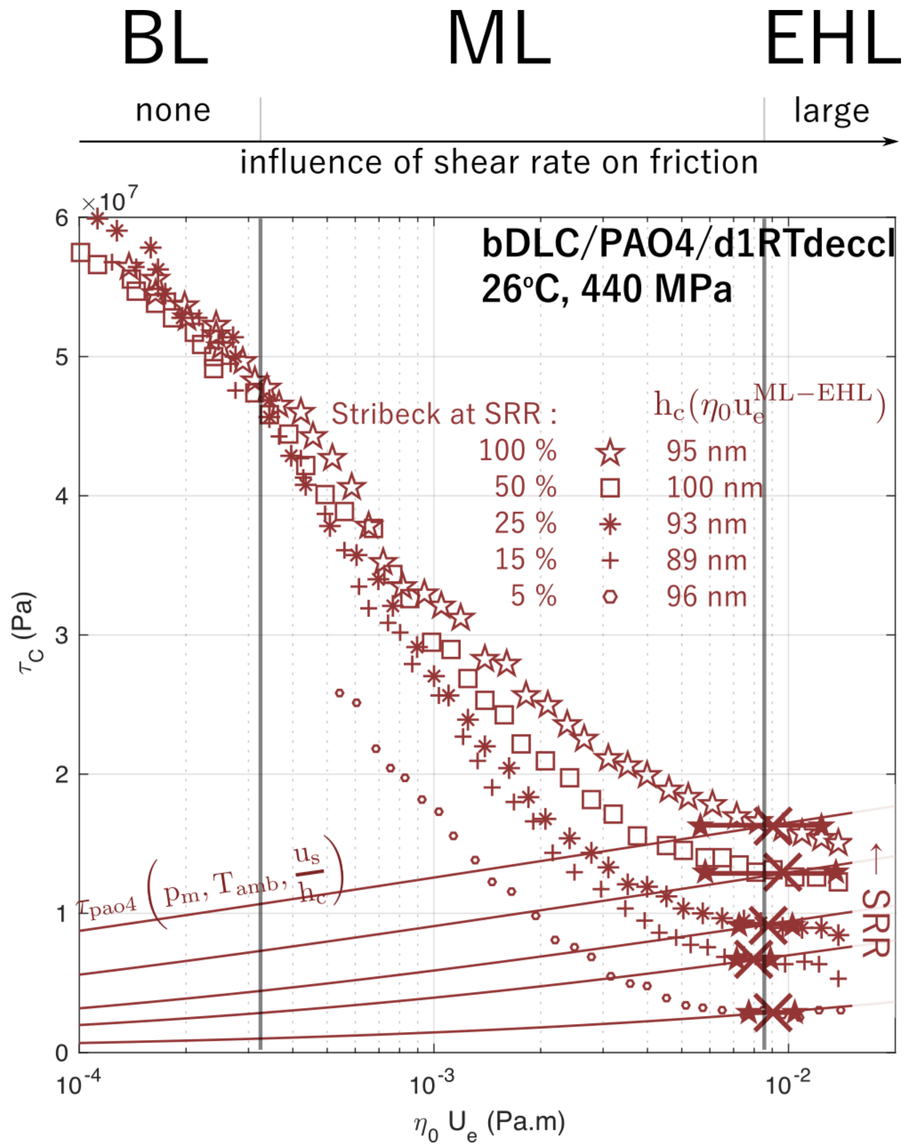

Figure 6.7: Stribeck tests with a DLC-coated ball and a pickled steel (d1RTdeccl : $S_q(L_w = 200\ \mu\text{m}) = 0.016\ \mu\text{m}$) in PAO4, at different sliding-rolling ratios. The ML-EHL transition is spotted at the intersection between the experimental shear stress and the calculated shear stress (solid lines). The horizontal errorbars correspond to the uncertainty over $\eta_0 u_e^{ML-EHL}$.

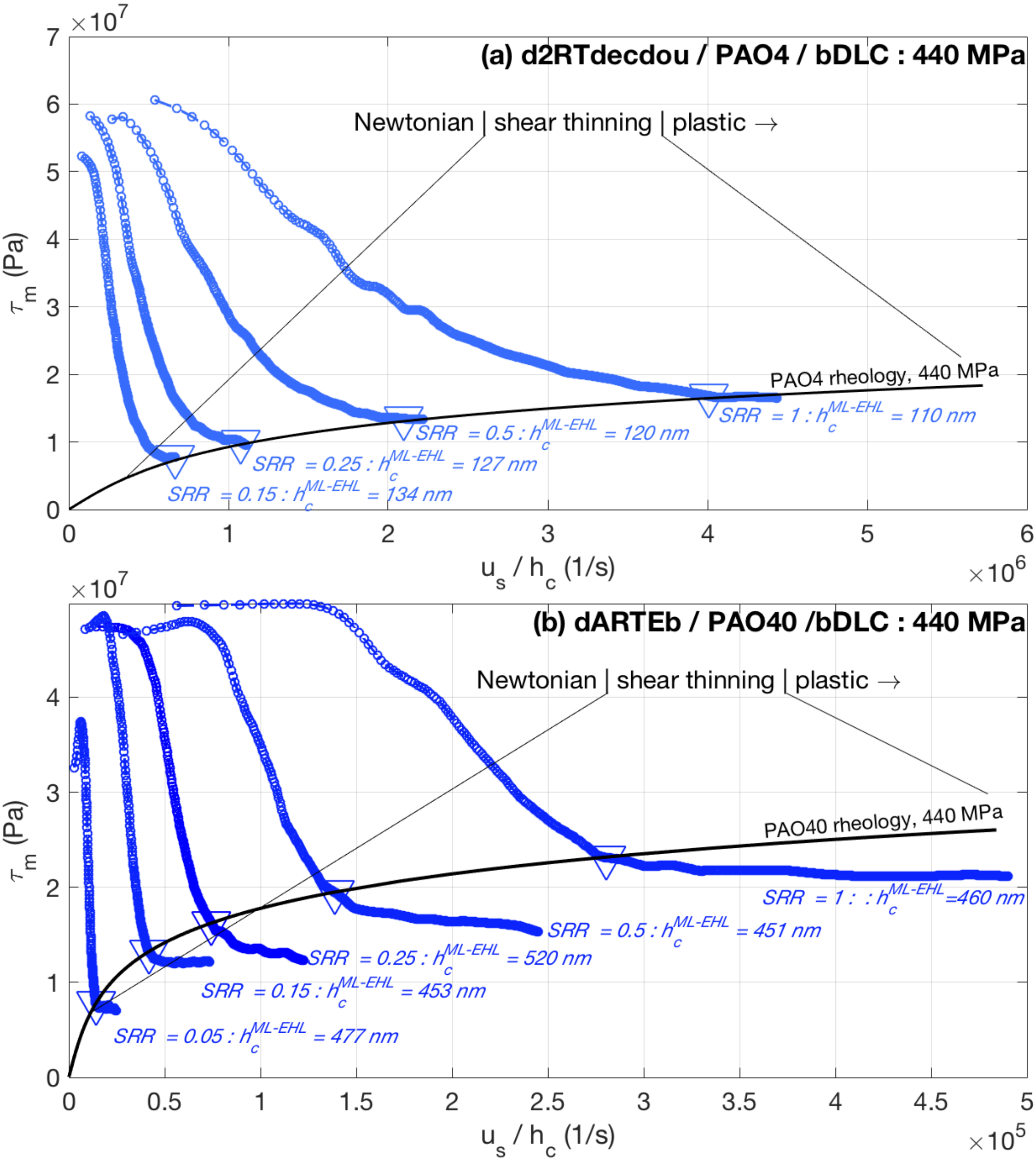

Figure 6.8: Stribeck experiments at 440 MPa at different sliding-rolling ratios. The lubricant thin-film rheology is superimposed in black solid line.

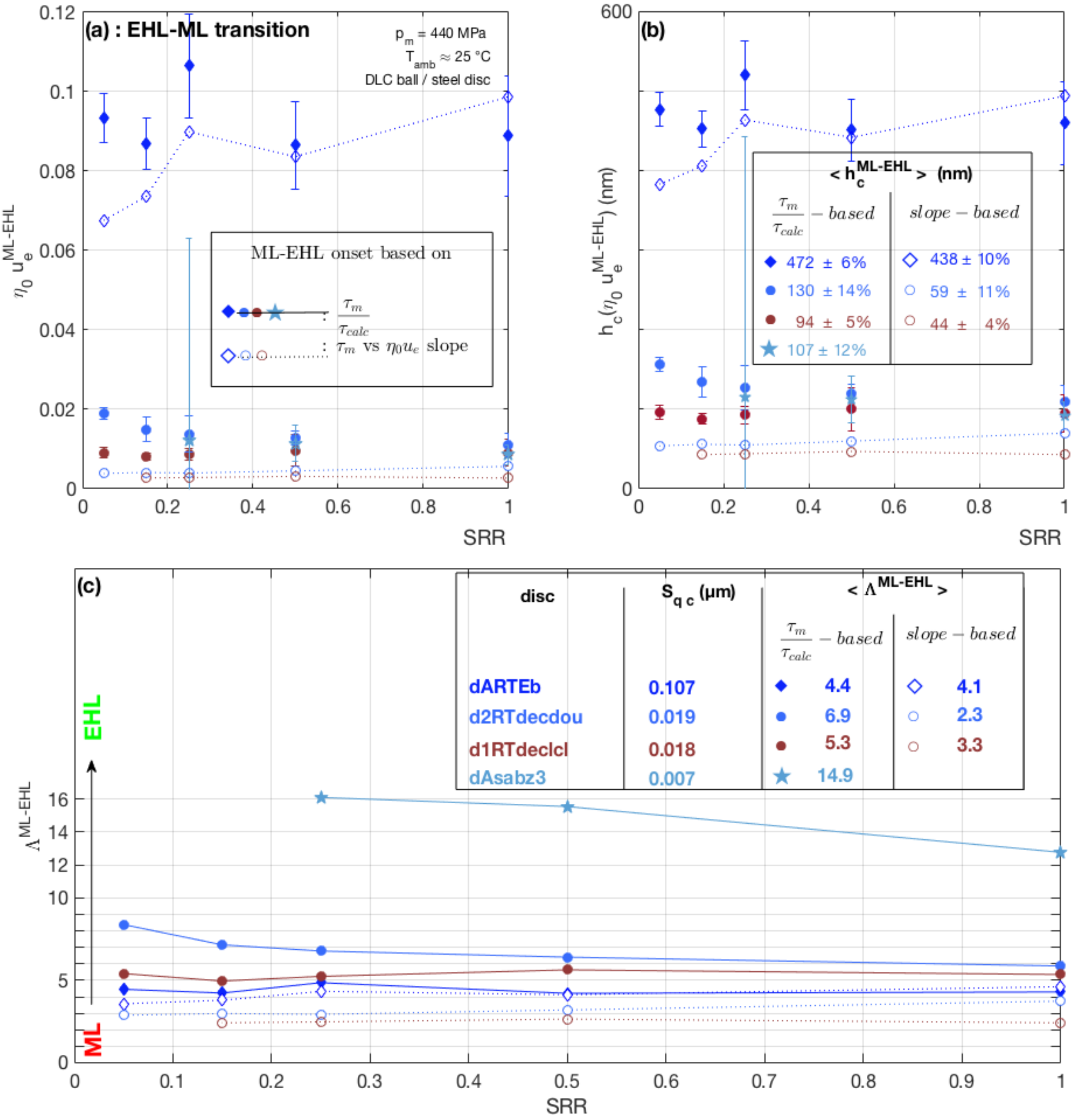

Figure 6.9: Influence of the sliding ratio on the ML-EHL transition. Filled symbols correspond to the friction-based definition of the ML onset while empty symbols correspond to the more classical way of spotting the ML-EHL transition, based on the slope rupture between ML and EHL as represented fig. 6.2. The errorbars are based on a ±10% error over the ratio $\frac{\tau_m}{\tau_{calc}}$. The composite standard deviation, $S_{q\ c}$, are based on measurements using cut-off length $L_w = 200\ \mu$m and a sampling interval $dx = 3.653\ \mu$m. The tables in figures 6.9.b and 6.9.c show the transitional nominal film thickness and lambda ratio, averaged on from $SRR = 0.05$ to $SRR = 1$.

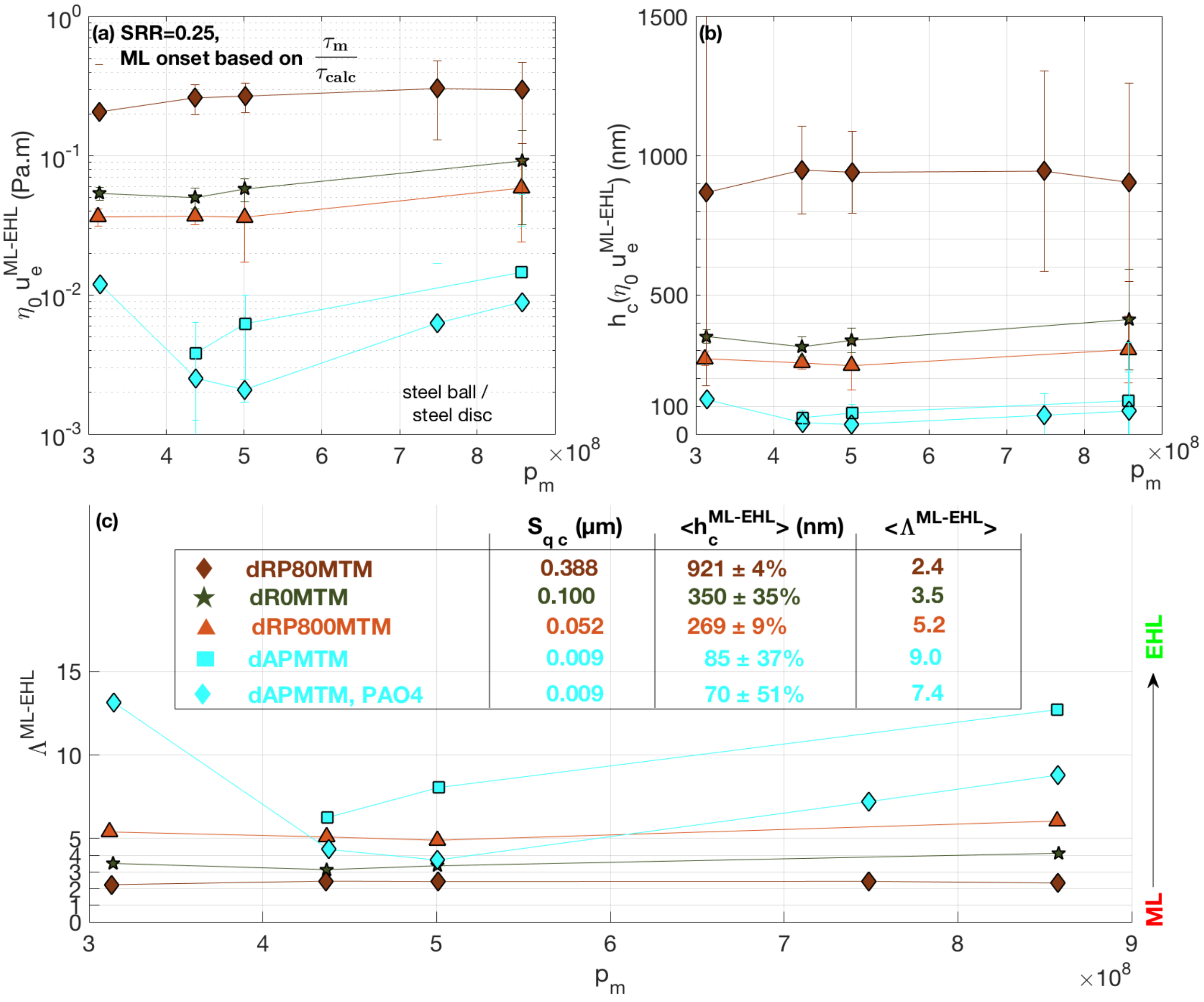

	$S_{q\,c}$ (μm)	$<h_c^{ML-EHL}>$ (nm)	$<\Lambda^{ML-EHL}>$
◆ dRP80MTM	0.388	921 ± 4%	2.4
★ dR0MTM	0.100	350 ± 35%	3.5
▲ dRP800MTM	0.052	269 ± 9%	5.2
■ dAPMTM	0.009	85 ± 37%	9.0
◆ dAPMTM, PAO4	0.009	70 ± 51%	7.4

Figure 6.10: Influence of pressure on the ML-EHL transition based on the friction-based definition of the ML onset. The table on (c) displays the $< h_c^{ML-EHL} >$ and $< \Lambda^{ML-EHL} >$ values, averaged on the whole range of pressure and the surfaces composite roughness measured with a cut-off length $L_w = 200\ \mu$m.

both increase with the surface composite roughness. Figure 6.10.b shows that for a given couple of surfaces, this film thickness does not present any monotonic variation towards pressure and can be considered constant within a 40% error for each couple of surfaces. The transitional lambda ratio takes values between 2 and 10 (see table on graph 6.10.c.), with higher values obtained for smoother surfaces.

6.2.2.2 Classical spotting of the ML-EHL transition

In figure 6.11, the ML-EHL transition is also detected according to the more classical method presented figure 6.2. These results also show that the ML-EHL transition operates at a given film thickness, characteristic of the surfaces and independent of the operating pressure. This nominal film thickness is generally weaker than using the friction-based definition of ML, especially for the smoothest surfaces. As for the previous results concerning the influence of sliding, the transitional lambda ratios lie between 2 and 4 and are hence less dispersed than using the friction-based definition of ML.

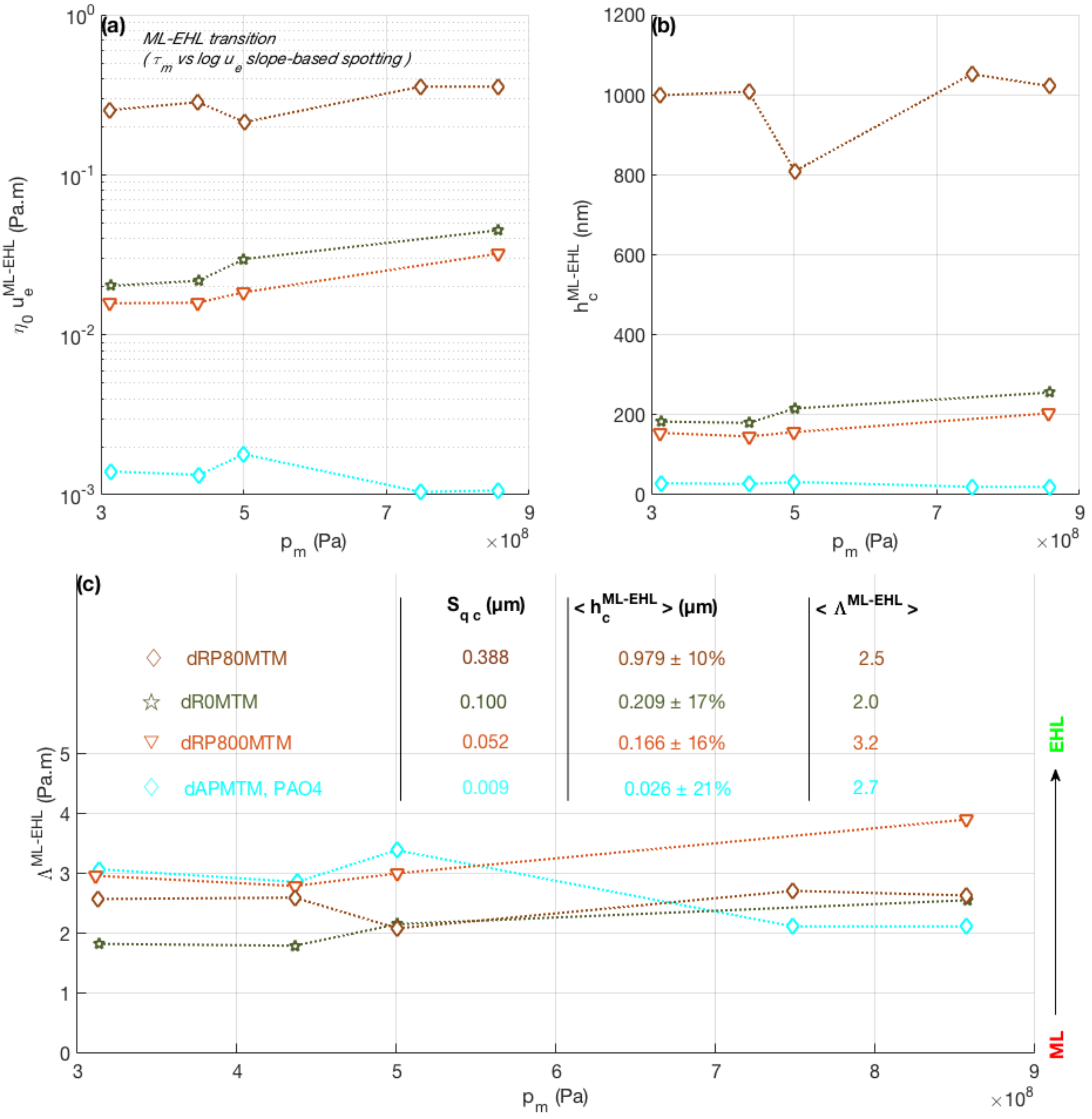

	$S_{q\,c}$ (μm)	$< h_c^{ML-EHL} >$ (μm)	$< \Lambda^{ML-EHL} >$
◇ dRP80MTM	0.388	0.979 ± 10%	2.5
☆ dR0MTM	0.100	0.209 ± 17%	2.0
▽ dRP800MTM	0.052	0.166 ± 16%	3.2
◇ dAPMTM, PAO4	0.009	0.026 ± 21%	2.7

Figure 6.11: ML-EHL transition versus the pressure spotted according to the method presented figure 6.2.

6.2.3 Interpretation of the sliding and pressure influence on the ML-EHL transition

The main difference between the friction-based and the phenomenological criteria is that the latter defines another ML-EHL transition lying in the ML regime, at a point outside of the Stribeck curve and where friction has already started increasing above the EHL friction level (see fig. 6.2). Consequently the transitional entrainment products and film thicknesses are bound to be smaller than using the friction-based criterion. For the smoothest surfaces ($dAPMTM : S_{q\,c} = 0.009\ \mu$m) the friction-based method raises transitional nominal film thicknesses about three times higher than the phenomenological method, while for the roughest surfaces ($S_{q\,c} = 0.388\ \mu$m for dRP80MTM), both methods give the same transition $\eta_0 u_e^{ML-EHL}$. Except for these differences, the same conclusions arise from both ML onset criteria regarding the influence of pressure and sliding.

The results show that for a given couple of rough surfaces, the ML-EHL transition occurs at a nominal film thickness independent of pressure up to 0.9 GPa and of the sliding-rolling ratio up to $SRR = 1$. This film thickness is referred to as the *transitional nominal film thickness* and within the friction-based definition of ML, it describes the smallest nominal film thickness before the bodies roughness start rising the friction above the only viscous shearing contribution.

From the EHD theory with smooth surfaces, the film thickness is determined by the rolling speed. Sliding can have a negative influence on the film thicknesses either by means of inlet heating or by means of inlet thinning, which were respectively shown (section 3.5.5.3) and admitted (section 2.2.3) negligible within the assumption of ideally smooth surfaces. With real surfaces, if inlet heating (or thinning) ceased being negligible at larger SRR, the real film thickness would decrease and this should require a larger nominal film thickness (or entrainment product) to prevent surfaces interactions. Yet h_c^{ML-EHL} remains constant towards the sliding-rolling ratio within a 15% uncertainty, which confirms the unimportance of inlet heating and thinning up to $SRR = 1$, even with rough surfaces like the roughened finished disc ($dARTEb : S_{qc} = 0.107\ \mu$m).

If the ML-EHL transition is assumed to occur at certain nominal film thickness, characteristic of the couple of surfaces, the smooth EHD theory (62) predicts that the transitional entrainment product should scale with pressure as $\eta_0 u_e^{ML-EHL} \propto p_m^{0.3}$ (eq. (2.42)). Schipper (113) used the phenomenological method to detect the ML-EHL transition for Stribeck tests performed at mean Hertz pressures between 100 MPa and 1 GPa. The ML-EHL transition was also observed independent on the sliding speed. Using steel surfaces having a composite centre line average roughness $R_{ac} = 0.025\ \mu$m, measured with a cut-off length of 800 μm, he showed that :

$$\eta_0 u_e^{ML-EHL} \propto p_m^{0.5} \tag{6.5}$$

The difference between a pressure exponent of 0.3 and 0.5 is small, and it is perhaps too optimistic to expect any of the two present ML-EHL spotting methods to answer which one is the truest on less than a pressure decade.

Nevertheless, if the scaling of eq. (6.5) is combined with the smooth EHD theory ($h_c \propto (\eta_0 u_e)^{2/3} \cdot p_m^{-1/5}$) (62), the transitional film thickness should scale with pressure as $h_c^{ML-EHL} \propto p_m^{0.13}$. Between $p_m = 10^8$ Pa and $p_m = 10^9$ Pa, the relative increase in h_c^{ML-EHL} should thus be $\left(\frac{10^9}{10^8}\right)^{0.13} - 1 = 35\%$, which is too small to be distinguished from uncertainties in the present experiments. This picture of h_c^{ML-EHL} increasing with pressure is hence neglected and it is considered that the ML-EHL transition occurs at a constant nominal film thickness, only characteristic of the surfaces composite roughness.

6.2.4 Influence of surface roughness on the ML-EHL transition

In 1988, Schipper measured the ML-EHL transition based on the intercept of the mixed and EHD friction versus $ln(u_e)$ (as on fig. 6.2) on Stribeck tests at $p_m \approx 0.1 - 0.2$ GPa, and $p_m \approx 0.7 - 0.8$ GPa.

Using surfaces having composite centre line average roughnesses ($R_{a\,c}$) in the range [10^{-8} ; 10^{-6}] m, he showed that the ML-EHL transition obeys to :

$$\frac{\eta_0 u_e^{ML-EHL}}{p_m} \propto R_{a\,c}^{1.5} \tag{6.6}$$

Figure 6.12 displays a series of Stribeck tests showing the ML-EHL transition performed at $SRR = 0.25$, $p_m = 440$ MPa, $T_{amb} = 22 \pm 2$°C with PAO4 (empty symbols) and PAO40 (filled symbols). 15 different discs were used against steel balls, with or without DLC-coating.

To compare our results to his, the ML-EHL transition was spotted using the classical slope-based method. The ML-EHL transitions are confronted to his results on graph 6.13 using the same lubrication number as (113) $L' = \frac{2\eta_0 u_e}{p_m}$ at the transition. The composite centre line average roughness was calculated using the same cut-off length[1] $L_w = 800$ μm and added on the horizontal axis. The same approximate scaling is found as that of eq. (6.6). Reminding from eq. (2.15) that $h_c \propto (\eta_0 u_e)^{2/3}$, this is consistent with a nominal film thickness that increases linearly with the centre line average roughness $< S_{a\,c} >$ (in 3D) or $R_{a\,c}$ (in 2D) using a cut-off length $L_w = 800$ μm.

On figure 6.14.a, the Stribeck curves of fig. 6.12 were normalized by the viscous shear stress. The ML-EHL transitions were plotted versus the composite RMS roughness using two different sampling intervals : $dx = 0.099$ μm and $dx = 3.653$ μm on figures 6.12.b and 6.12.c respectively. Both curves yield essentially the same evolution. The measurements using $dx = 3.653$ μm are more reliable because they account for the surface statistics over an area a hundred times larger that those using $dx = 0.099$ μm and because they contain fewer outliers. The following scaling is found, using $dx = 3.653$ μm :

$$\eta_0 u_e^{ML-EHL} = 28.5 \times 10^6 \times S_{q\,c}^{1.2} \tag{6.7}$$

Since $h_c \propto (\eta_0 u_e)^{2/3}$, this scaling implies that the nominal film thickness at the ML onset increases with surface roughness as (see the dashed line on figure 6.14.d.) :

$$h_c^{ML-EHL} = 0.26 \times S_{q\,c}^{0.8} \tag{6.8}$$

The exponent is inferior to 1, which implies a transitional lambda ratio that decreases with roughness as $S_{q\,c}^{-0.2}$. Against the view of a transitional lambda ratio independent of S_{qc}, this means that the transitional nominal film thickness increases less than proportionally with the surface roughness. However, this view especially applies to surfaces having an RMS roughness superior to 0.1 μm. Most of the surfaces used in this work have an RMS roughness inferior to 0.1 μm. For these, the view of a constant transitional lambda ratio may be kept with :

$$\Lambda^{ML-EHL} = \frac{h_c^{ML-EHL}}{S_{q\,c}} \approx 5.5 \tag{6.9}$$

, as it is represented figure 6.14.d with a straight solid line.

---

[1] With a sampling interval $dx = 3.653$ μm and 3D measurements instead of the profilometer measurements used by (113).

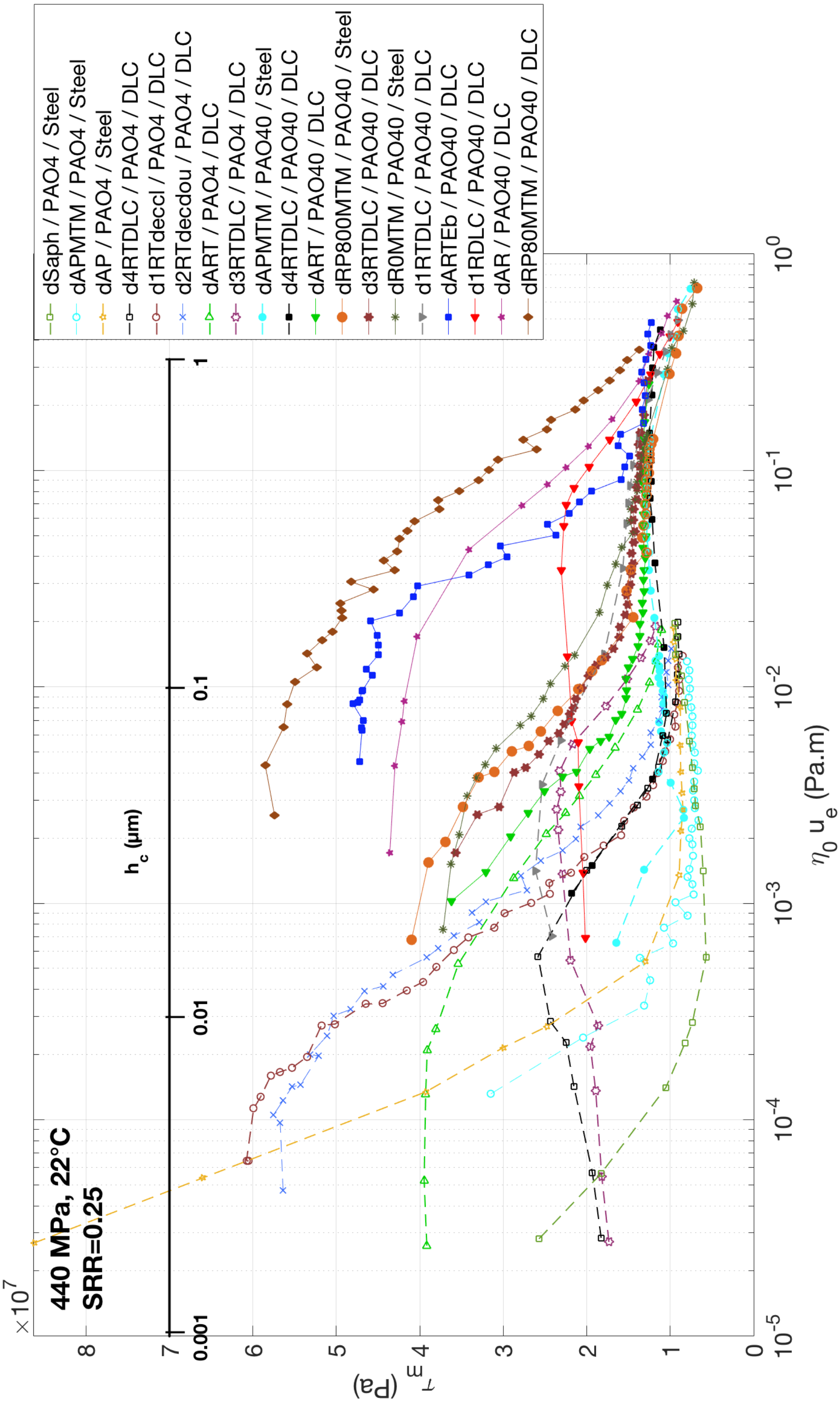

Figure 6.12: Stribeck curves with PAO4 (empty symbols) and PAO40 (filled symbols) at $T_{amb} = 22 \pm 2^\circ$ C, $p_m = 440$ MPa with different surface roughness.

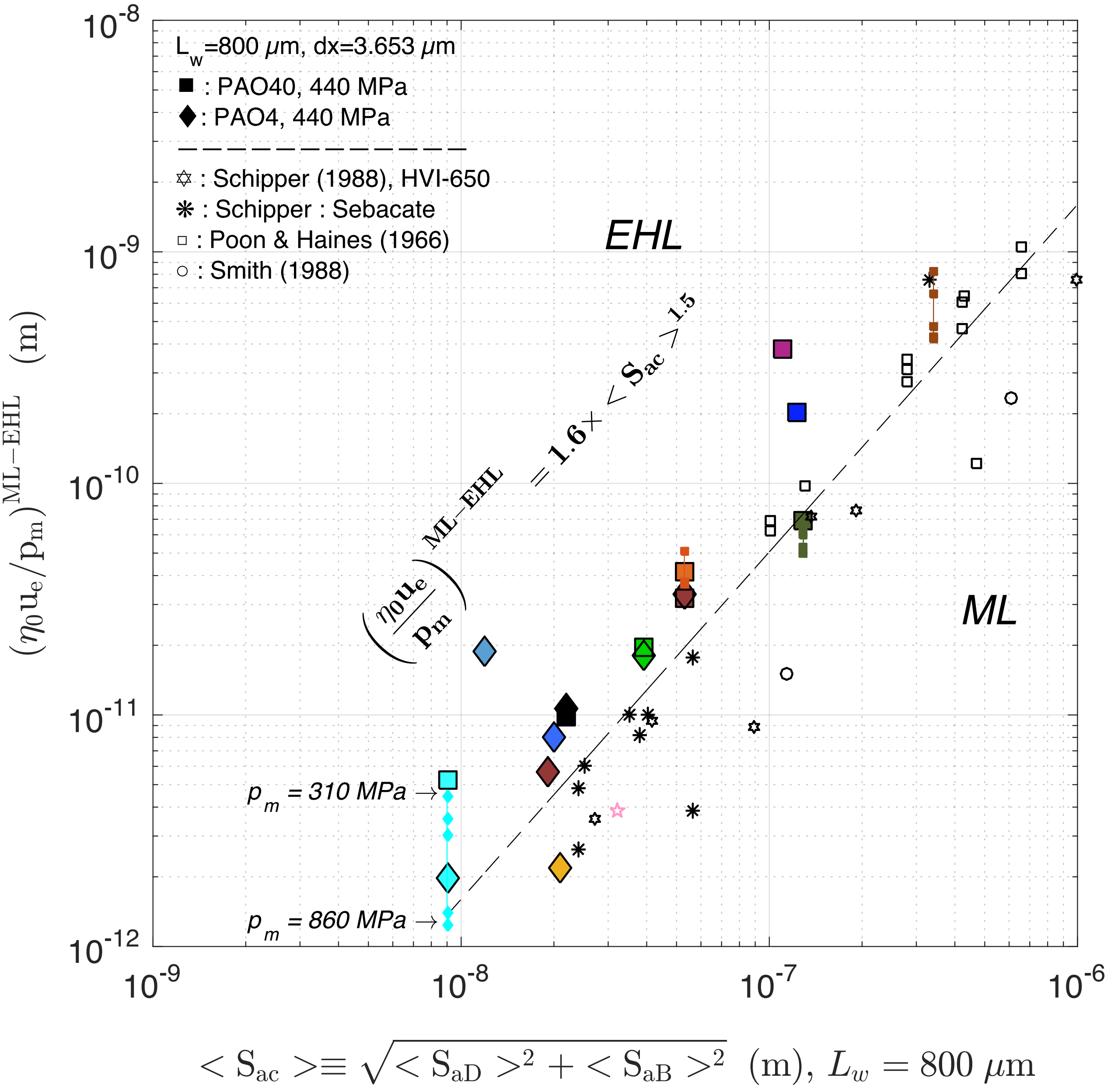

Figure 6.13: Schipper lubrication number, $L' = \frac{2\times\eta_0 u_e}{p_m}$, evaluated at the ML-EHL transition, spotted phenomenologically. Filled diamonds correspond to experiments with PAO4, filled squares correspond to PAO40 experiments. Empty and black symbols are data taken from the litterature (113).

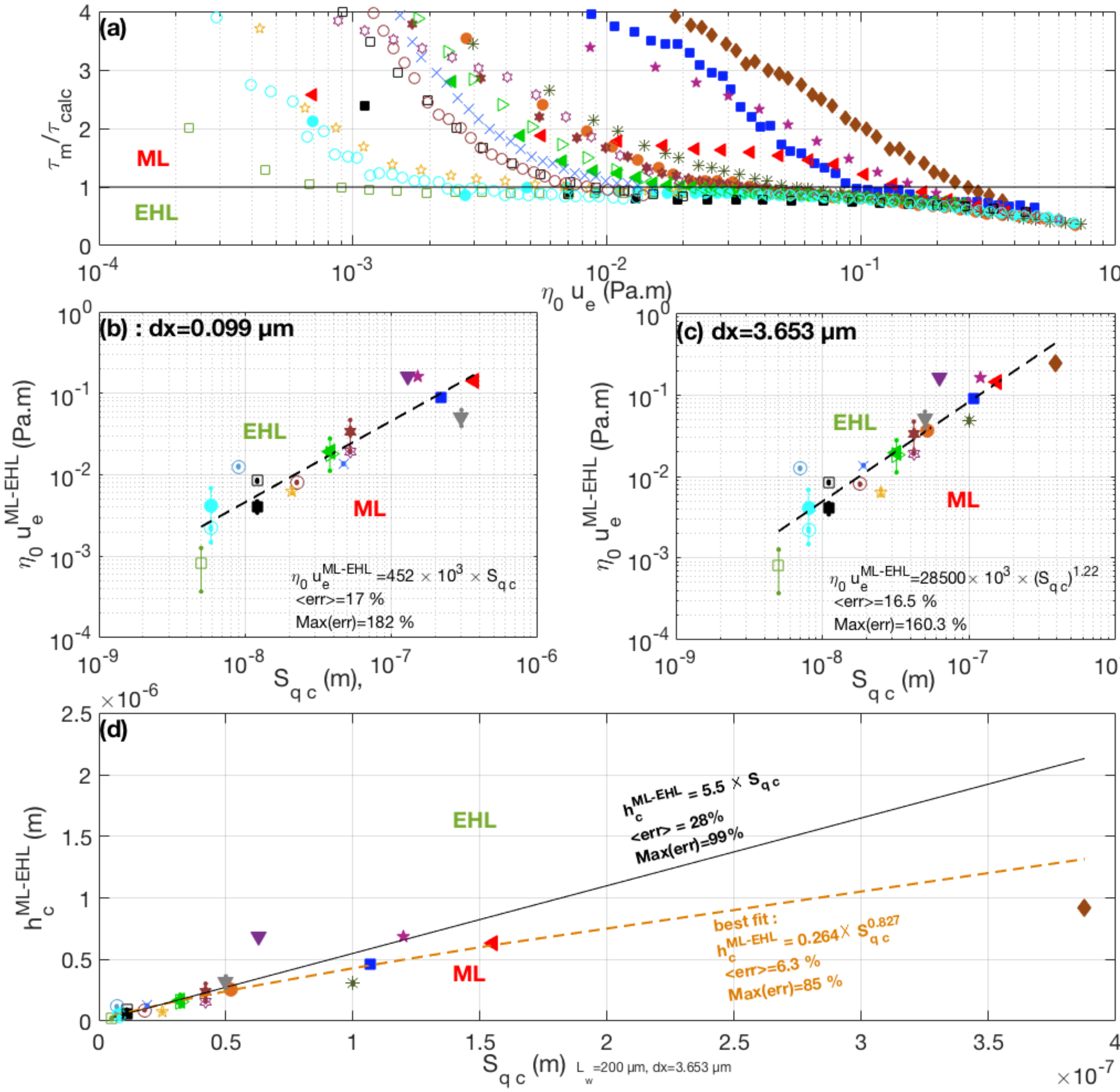

Figure 6.14: Ratio between the experimental and the calculated shear stress **(a)**. Mode of the composite standard deviation $\sqrt{Mode(S_{qD})^2 + Mode(S_{qB})^2}$ measured using $(L_w = 200\ \mu m\ ;\ dx = 3.653\ \mu m)$ versus the transitional entrainment product **(b)** and versus the nominal minimal film thickness **(c)**. An uncertainty of 10% over the ratio $\frac{\tau_m}{\tau_{calc}}$ was assumed to calculate the uncertainty over $\eta_0 u_e^{ML-eHL}$, which corresponds to the vertical errorbars on graph (b).

6.3 Boundary-mixed transition

6.3.1 Spotting of the BL-ML transition

The friction-based method used to spot the ML-EHL transition was implemented in order to compare on the same basis different Stribeck curves. For the roughest surfaces, the friction versus

$ln(u_e)$ show almost no slope variation between ML and EHL, which has made impossible a robust phenomenological spotting of the onset of ML. Regarding the boundary-mixed transition, a phenomenological spotting can be used because all Stribeck curves show clearly a different evolution of friction with the rolling speed in the two regimes. Boundary lubrication occurs when friction reaches a plateau at low entrainment speeds. The mixed friction may be modelled with the following equations (44) :

$$\Theta(x,b) = \frac{1}{2}(tanh(b \cdot x) + 1) \tag{6.10}$$

$$\begin{aligned} \tau_m &= \tau_{BL} \times \Theta\left(ln\left(\frac{c}{\eta_0 u_e}\right), b\right) + \tau_{EHL} \times \Theta\left(ln\left(\frac{\eta_0 u_e}{c}\right), b\right) \\ &= \frac{\tau_{EHL} + \tau_{BL}}{2} + tanh\left[b \cdot ln\left(\frac{\eta_0 u_e}{c}\right)\right] \cdot \left(\frac{\tau_{EHL} - \tau_{BL}}{2}\right) \end{aligned} \tag{6.11}$$

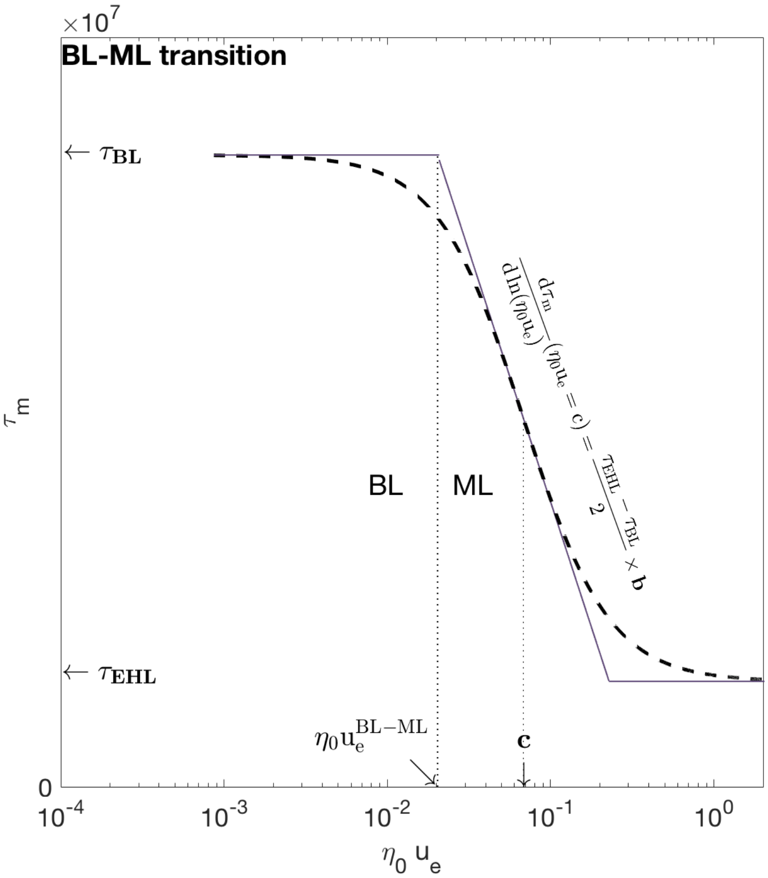

Figure 6.15:

Plot of the fitting model used to fit experimental Stribeck tests and spot the BL-ML transition. Four parameters must be fitted : τ_{BL} (Pa), τ_{EHL} (Pa), b $(\cdot)$ and c (Pa.m). The BL-ML transition corresponds to $\eta_0 u_e^{BL-ML} \equiv c \times e^{-1/b}$.

Eq. (6.11) is simply a sum of the boudary and EHD friction levels, weighted with a smoothed Heaviside function (eq. (6.10)). Four parameters are involved (see fig. 6.15) : the boundary friction level τ_{BL} (Pa), the EHD friction level τ_{EHL} (Pa), the entrainment product located at the middle of the mixed regime c (Pa.m) and a parameter descriptive of the mixed friction steepness b. These are fitted using a least-square criterion. The BL-ML transition is defined by the intersection between the boundary friction level[1] and the tangent[2] in $\eta_0 u_e = c$:

---

[1] $y = \tau_{BL}$

[2] $y = \frac{b}{2}(\tau_{EHL} - \tau_{BL}) \times ln\left(\frac{\eta_0 u_e}{c}\right) + \frac{\tau_{EHL}+\tau_{BL}}{2}$

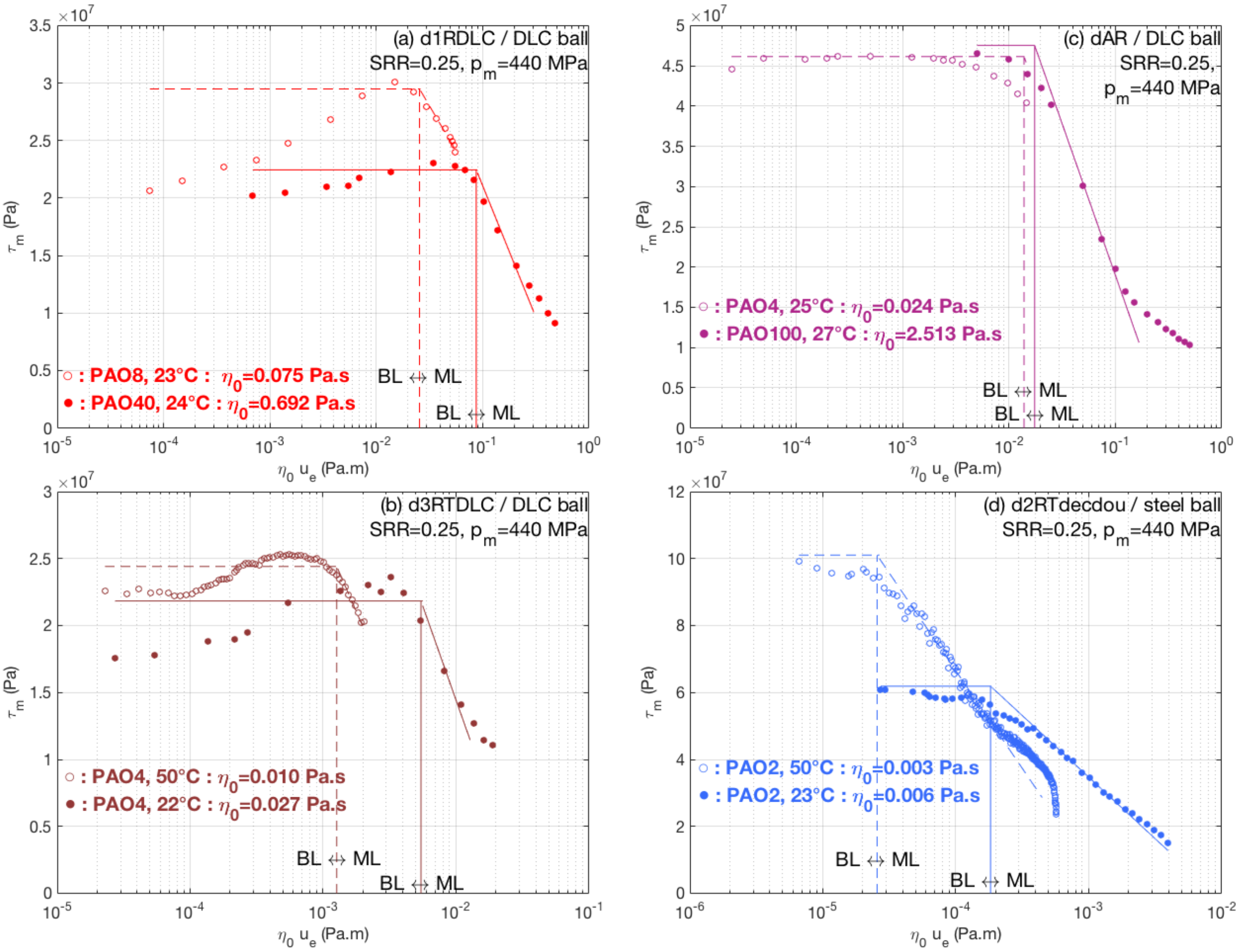

Figure 6.16: Stribeck curves performed with different discs : *d1RDLC* (a), *d3RTDLC* (b), *dAR* (c), *d2RTdecdou* (d). Each graph shows two Stribeck curves obtained with two different lubricants (or ambient temperatures) to show the influence of η_0 on the BL-ML transitional entrainment product.

$$\eta_0 u_e^{BL-ML} \equiv c \cdot e^{-1/b} \tag{6.12}$$

Since for many experiments, the EHD friction is not a plateau as assumed by eq. (6.11), the fitted parameter τ_{EHL} is usually a bad representation of the real EHD friction average level and only permits to reduce the error between the fitting expression and the experimental points near to the ML and BL regimes.

6.3.2 Influence of the inlet viscosity on the BL-ML transition

The BL-ML transition was determined for several steel and DLC-coated steel discs on figure 6.16 using different inlet viscosities. To change the inlet viscosity with a given couple of surfaces, η_0 was lowered either by increasing the temperature at $50°C$ or by using a less viscous PAO among the PAO2, PAO4, PAO8, PAO40 and PAO100. Figure 6.17 shows the transitional entrainment products at the BL-ML transition versus the inlet viscosity for these experiments.

The rectified steel yields the same transition over two order of magnitudes in inlet viscosity. The DLC-DLC contacts and the *d2RTdecdou*-DLC contact show an increase in $\eta_0 u_e^{BL-ML}$ of more than 100% over an order of magnitude in η_0. The entrainment product $\eta_0 \times u_e$ is hence not a perfectly suitable parameter to spot the onset of BL. Yet, no better parameter was found to spot this transition, $\eta_0 u_e^{BL-ML}$ can thus be considered a characteristic of the surfaces within a 70% maximum uncertainty.

6.3.2.1 Influence of surface roughness on the BL-ML transition

Using several steel surfaces, (114) studied the transition between BL and ML and found a proportionality relationship between the transitional entrainment product $\eta_0 u_e^{BL-ML}$ and the composite centre-line average roughness, measured using a cut-off length of 0.8 mm.

$$\eta_0 u_e^{BL-ML} \approx 6.25 \times 10^3 \times R_{ac} \tag{6.13}$$

The BL-ML transition was calculated for several Stribeck tests with DLC-coated balls against different discs, at $p_m = 440$ MPa, $SRR = 0.25$ with PAO4 and PAO40. The transitional lambda ratios at the onset of BL (filled symbols) and at the onset of ML (empty symbols) are plotted versus the composite RMS roughness on fig. 6.18 measured with a sampling interval $dx = 3.653$ μm. The smoothest steel - DLC contacts ($S_{q\,c} \leq 0.04$ μm) and the roughest one ($S_{q\,c} = 0.39$ μm) have their BL-ML transition around $\Lambda^{BL-ML} \sim 10^{-2} - 10^{-1}$. For intermediate roughnesses, the BL-ML transition occurs at $1 \leq \Lambda^{BL-ML} \leq 3$. The trend followed by DLC-DLC contacts and contacts with at least a steel body are different and they must be considered separately.

Figure 6.19.a shows the BL-ML transitional products for DLC-DLC contacts, versus the composite RMS roughness. Interpolating these points with a power law yields :

$$\eta_0 u_e^{BL-ML} = 5.75 \times 10^8 \times S_{qc}^{1.5} \text{ for DLC-DLC contacts} \tag{6.14}$$

The average relative error between the data and the power law fit[1] is of 14%, which allows quite a precise prediction of the BL onset for DLC-DLC contacts.

Figure 6.19.b shows the BL-ML transitions for various Stribeck tests with steel discs against polished balls, with or without DLC coating. A power law fit can approximate the experimental data but with quite a large error of 45%. Surprisingly, the BL-ML transition seems to become independent of the RMS roughness for $S_{qc} \geq 0.1$ μm, whereas smoother contacts follow a power law trend. To account for this saturation, $\eta_0 u_e^{BL-ML}$ is fitted with a power law for low roughnesses and with a plateau for high roughnesses, weighted with the step function of eq. (6.10), yielding :

$$\eta_0 u_e^{BL-ML} = 7.3 \times 10^9 \times S_{q\,c}^{1.77} \times \Theta(S_{qc\,0} - S_{qc}, 10^8) + 1.88 \times 10^{-2} \times \Theta(S_{qc} - S_{qc\,0}, 10^8) \tag{6.15}$$

$$\text{with } S_{qc\,0} = 0.1\ \mu\text{m, for contacts with steel discs}$$

The form of the latter formula is less motivated by physical arguments than by the willing of making easier the reuse of the present results. $S_{qc\,0} = 0.1$ μm determines the boundary between the power law trend and the saturation of $\eta_0 u_e^{BL-ML}$. (113) did not observe such a saturation of the BL-ML transition, certainly because the highest transitional entrainment products measured in his experiments were around a few 10^{-3} Pa.m, whereas in the present work, some surfaces enter in BL an order or magnitude above that. Figure 6.20 displays the BL-ML transitions of the present present experiments along with some of the literature with various fluids, versus the centre line average roughness, which is more often given than other roughness parameters. All contacts with at least a steel body indeed have their BL-ML transition at $\eta_0 u_e \leq 2 \times 10^{-2}$. The black symbols on fig. 6.20 show that it is also true for DLC-DLC contacts, except for the experiments with the DLC-coated rectified disc *d1RDLC*, for which the transitional reaches $\eta_0 u_e^{BL-ML} = 0.06 \pm 0.1$ Pa.m.

---

[1] This error is calculated as $< err >= \left\langle \left| \frac{y_{exp} - y_{fit}}{y_{exp}} \right| \right\rangle$ (i.e. according to eq. (4.37)).

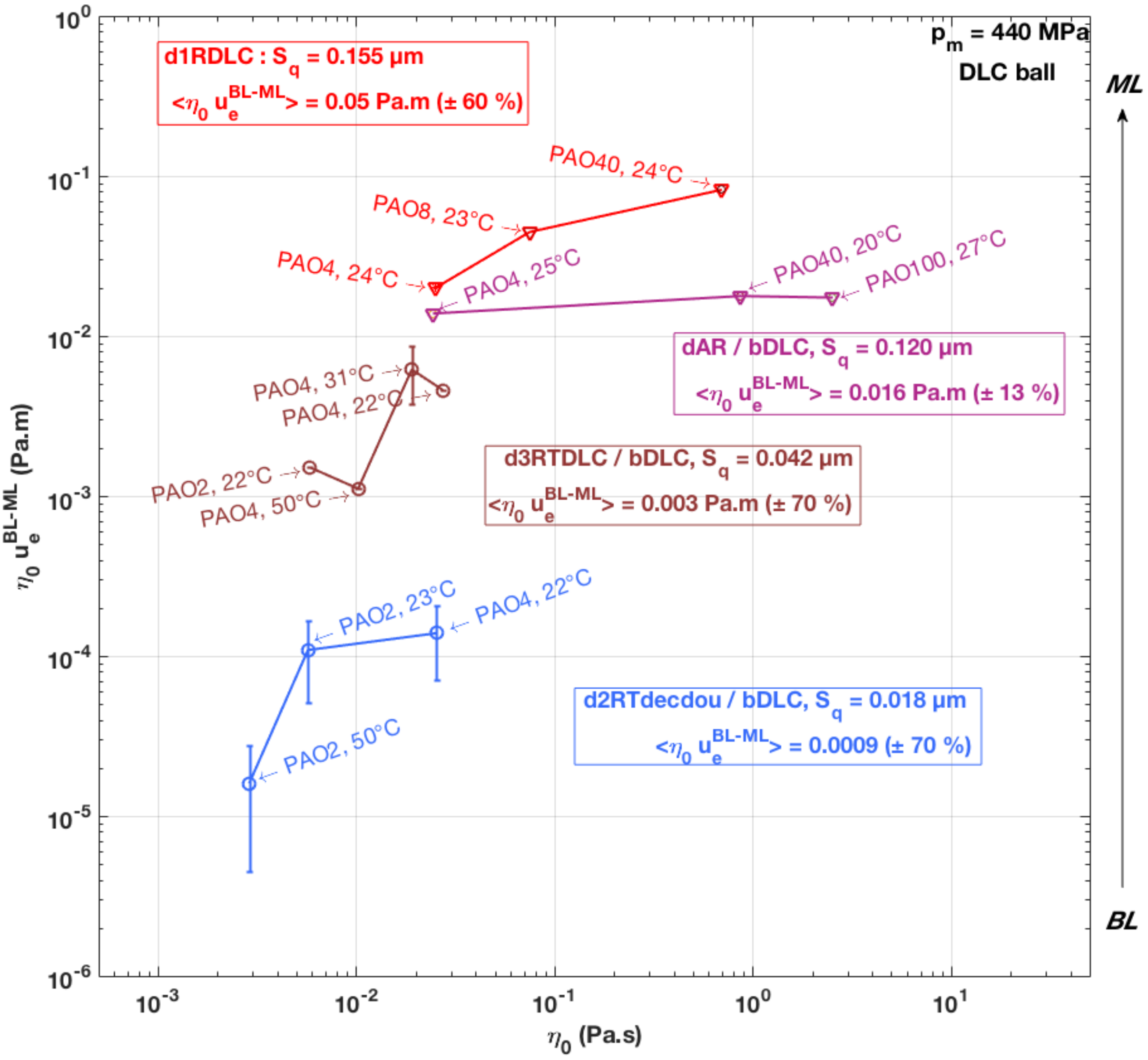

Figure 6.17: Boundary-mixed transition versus the inlet viscosity for various Stribeck tests performed at $p_m = 440$ MPa with various poly-alpha olefins. The errorbars correspond to the standard deviation of $\eta_0 u_e^{BL-ML}$ over different sliding-rolling ratios between 0.05 and 1. Other points correspond to $SRR = 0.25$. For each of the four surfaces, the entrainment product at the BL-ML transition is averaged towards η_0 and displayed in the text boxes, along with relative dispersion expressed in percentage.

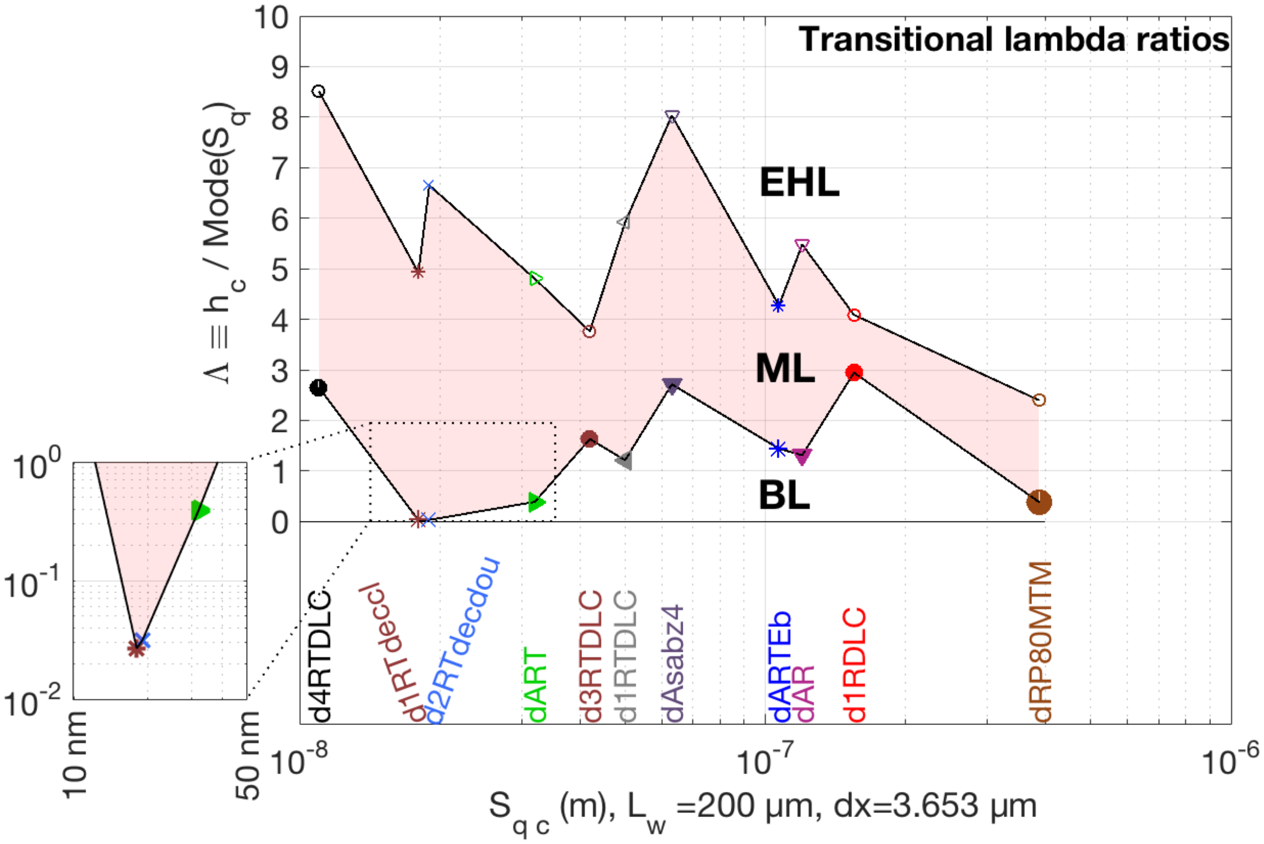

Figure 6.18: Lambda ratio at the ML-EHL and the BL-ML transitions versus the composite RMS roughnesses of different surfaces for Stribeck tests at p_m = 440 MPa, SRR = 0.25 with PAO4 for $S_{q\,c} \leq 0.042$ μm and PAO40 for rougher surfaces.

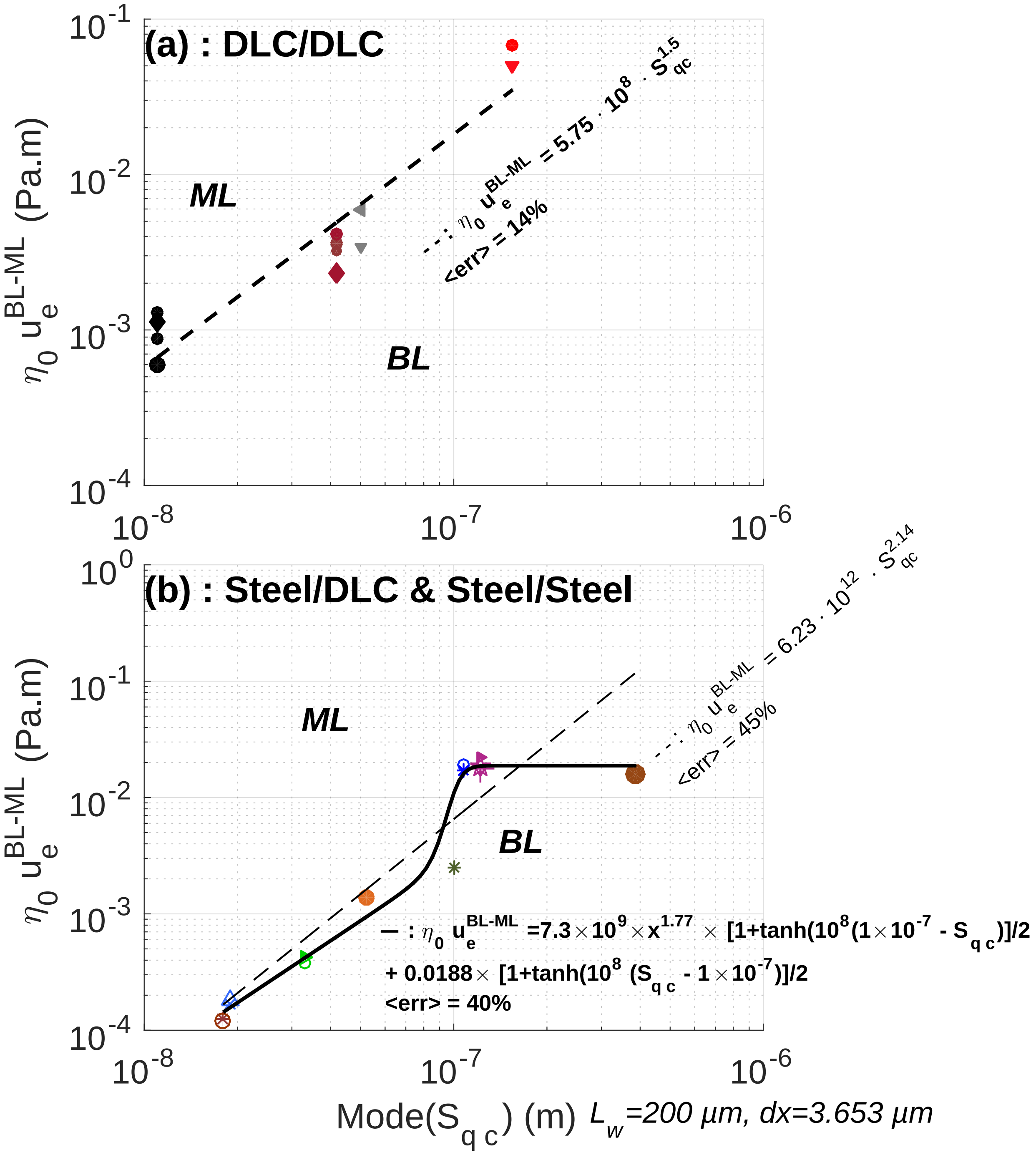

Figure 6.19: BL-ML transitions versus the composite surface RMS roughness for Stribeck tests performed at p_m = 440 MPa, SRR = 0.25 with (a) DLC-DLC contacts and (b) contacts with steel discs against polished steel balls with or without a DLC coating. The displayed errors are the average relative errors of the fit w.r.t. the experimental data (eq. (4.37)). Since the x and y data cover more than one order of magnitude, the error between the logarithms of the data and the fit were also calculated : $< err >_{log} \equiv \left\langle \left| \frac{y_{exp}-y_{fit}}{y_{exp}} \right| \right\rangle$ = 1.2% instead of 14% on (a). $< err >_{log}$= 13% instead of 45% and $< err >_{log}$= 1.1% instead of 40% on (b).

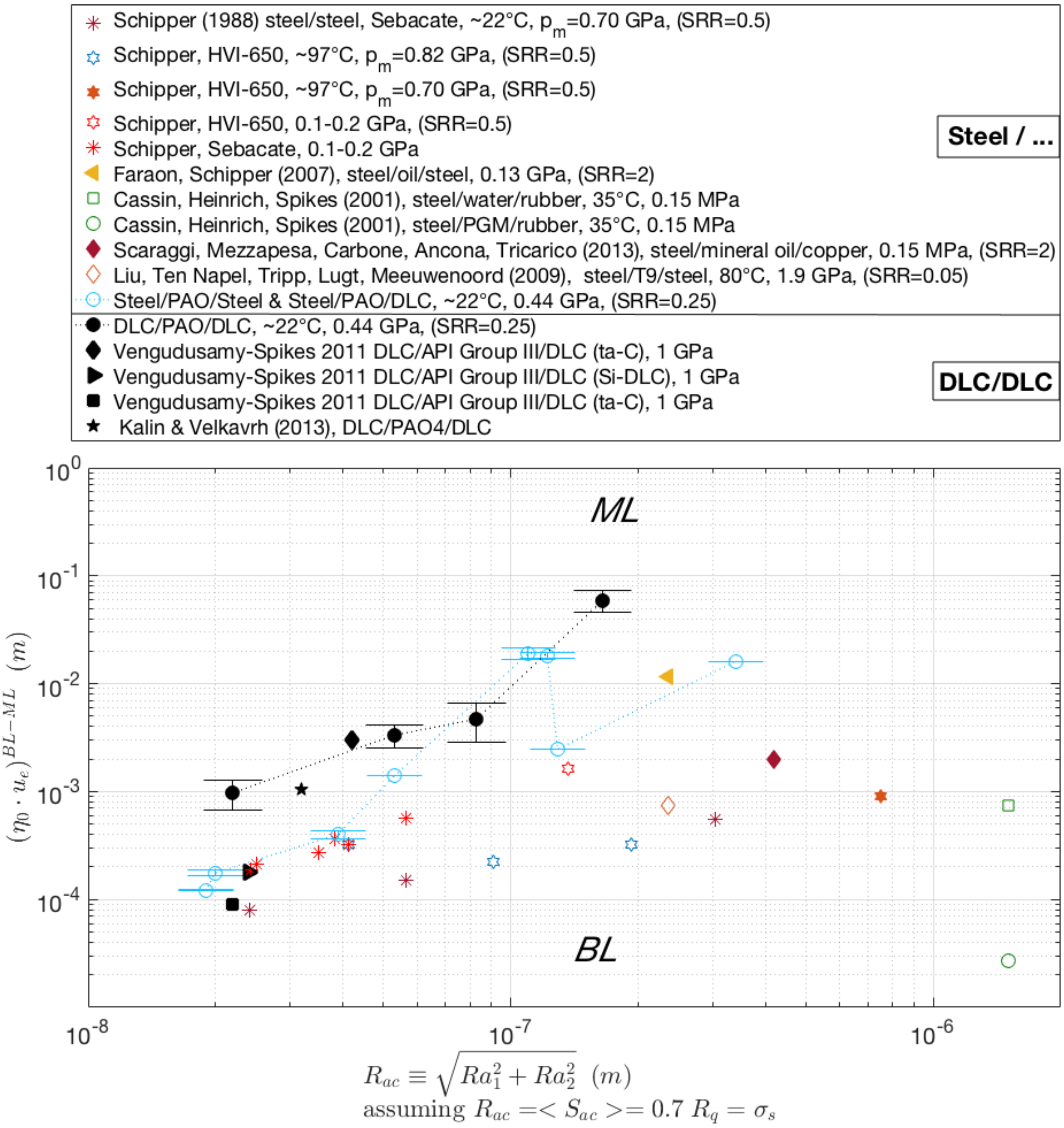

Figure 6.20: BL-ML transition from the literature (113), (49), (25), (112), (81), (129), (74) and the present experiments (dotted lines with errorbars).

The experiments with sapphire, silica and the manually polished steel discs (*dAP*, *d2AP*, *dAPMTM*) did not exhibit any saturation of the mixed friction at the lowest entrainment products $\eta_0 u_e \sim 10^{-5}$ Pa.m, it was thus impossible to state anything about the onset of BL for these surfaces.

6.3.2.2 Nature of asperity contacts in ML with DLC-DLC materials

Asperity interactions can not be avoided in ML and in BL because the fluid film is not thick enough. If the stresses withstood by asperities reach the hardness of one of the two materials, the friction mechanism must involve a contribution of wear. If not, the protuding asperities are elastically deformed either by dry contact against the counter body or by micro EHL.

It was shown that for rough surfaces with at least one of the two bodies made of steel, plastic interactions between the sharpest asperities and the counter surface may occur in thin-film EHL, which has resulted in a decrease of the friction level in ML and in thin-film EHL with time (figures 6.4). If plasticity occurs in EHL, it must occur increasingly close to the BL regime. The boundary friction mechanism with steel surfaces must then involve a contribution of plastically deformed asperities.

DLC-DLC contacts behave differently. Figure 6.21 shows successive Stribeck tests with DLC-coated balls against three different DLC-coated discs : d4RTDLC ($S_q = 0.01$ μm), d3RTDLC ($S_q = 0.042$ μm) and d1RDLC ($S_q = 0.155$ μm). For all DLC-coated discs, the second runs show a friction reduction at lower speeds close to the BL-ML transition, and in the BL regime.

Firstly, the comparison of successive runs does not present any significant friction decrease close to the ML-EHL transition. This means that the asperities do not experience significant removal or plastic deformation in this speed range of the Stribeck curve. Secondly, successive tests with DLC-DLC contacts exhibit a friction drop close to the BL-ML transition which means that asperities were removed or plastically deformed in this speed range. After the test, no wear can be observed with the present topographical apparatuses, but the rubbing tracks present a shiny appearance. A private communication[1] confirmed that the rubbing track enhanced reflectivity is due to the removal of very sharp asperities.

In the ML regime, this friction drop is small or even negligible close to thin-film EHL, which means that asperity removal in the ML regime is scarce and cannot contribute importantly to friction. This interpretation is compatible with the well-known high hardness of DLC coatings that requires high local pressures, which occurs more often in BL than in ML and EHL. Still, whether DLC-DLC asperity contacts in ML are of dry or of micro EHD nature remains unanswered. It should be added that we consider that there is no physical difference between the shearing of a confined nanometric fluid layer (often called a boundary film) and micro-EHL.

From the friction curves fig. 6.21, a slight shift towards lower entrainment products may be observed in time at the BL-ML transition, but the method used to spot this transition does not allow to quantify it reliably because of the peculiar shape of these Stribeck curves (see section 7.2.2). It can be considered that the BL-ML transitional entrainment product with DLC-DLC contacts does not evolve in time.

6.3.3 Influence of pressure and sliding on the BL-ML transition

Figure 6.22.a shows fitted Stribeck curves at the BL-ML transition with three couples of rough surfaces : a pickled AISI-52100 steel (d2RTdecdou), a pickled-DLC-coated AISI 52100 steel (d3RTdecdou) and a roughened M2 steel disc (dRP80MTM). Vertical lines correspond to the spotted BL-ML transitions (eq. (6.12)), black lines correspond to the tanh fits (eq. (6.11)). Below, fig. 6.22.c, the BL-ML transitions are plotted versus the Hertz pressure for different sliding-rolling ratios between 0.05 and 1. Table 6.22.d displays for each surface the transitional entrainment products averaged on all pressures and sliding-rolling ratios along with the corresponding standard deviations. At the first

---

[1] With Christophe Héau, HEF group.

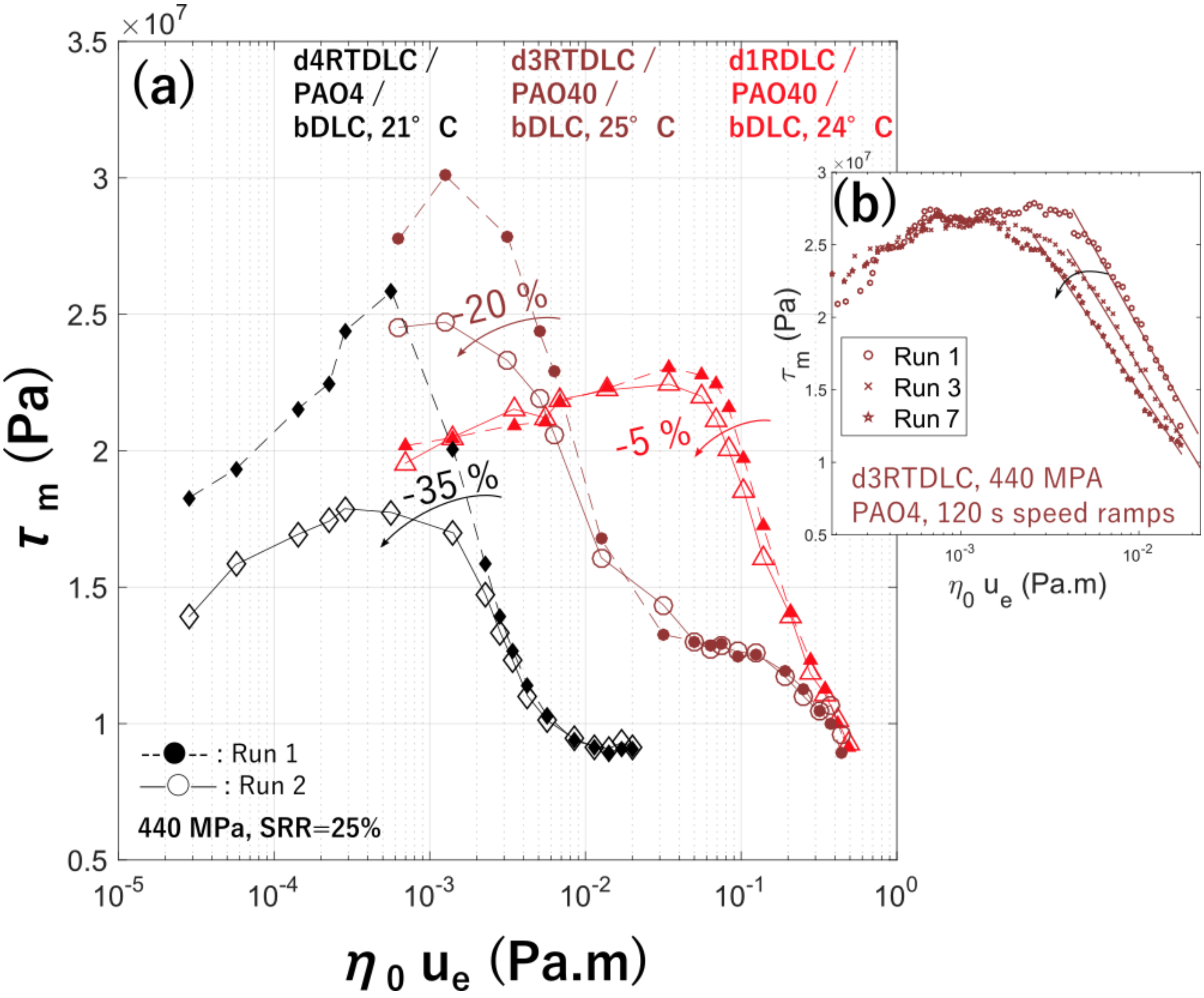

Figure 6.21: Successive Stribeck tests perfomed with two DLC-coated steel surfaces using speed steps (a : about 1 hour-long experiments) and speed ramps (b : 28 minutes-long experiment) that present a friction reduction during the running-in close to the BL-ML transition

order, the BL-ML transitions are independent of pressure and sliding up to a 50% uncertainty on $\eta_0 u_e^{BL-ML}$. This is compatible with the results of Schipper and De Gee (114), who showed that the transitional entrainment product $\eta_0 u_e^{BL-ML}$ does not depend upon the operating pressure.

Differences appear though between DLC-DLC contacts and DLC-steel contacts. On the one hand, the BL-ML transition for contacts involving steel do not present any trend towards the sliding-rolling ratio and have a BL-ML transition slightly shifted towards lower values at increasing pressures, though this trend is not systematically observed. On the other hand, the DLC-DLC contact shows an increase of 55% in $\eta_0 u_e^{BL-ML}$ between $p_m = 315$ MPa and $p_m = 500$ MPa, and an increase of 100% to 300% between sliding ratios of 0.15 and 1 (see fig. 6.22.b).

Increasing the contact pressure and the sliding ratio have in common to yield higher shear stresses in the contact, whether these be of viscous nature (EHD and micro EHD) or related to the amount of dry asperity contacts. The lubricant shear strength is more rapidly reached when the contact Hertz pressure is large and when the sliding rolling ratio is large. The previous observations on DLC-DLC contacts are compatible with a picture where mixed friction is due to the micro EHD friction between asperities and the BL-ML transition is realized when the lubricant shear strength is reached over all micro contacts.

Furthermore, the friction curves in ML at increasingly sliding-rolling ratios appear equally vertically shifted during the whole ML regime with DLC-DLC contacts whereas for steel-DLC contacts and steel-steel contacts (see figures 6.2 and 6.7), this shift, present close to the ML-EHL transition, vanishes close to the BL-ML transition. This peculiar behaviour of DLC-DLC contacts confirms the viscous nature of friction in the ML regime.

This leans towards a micro EHD friction mechanism in ML where the friction is due to the viscous stress between micro EHD contacts between the DLC asperities. As the surface separation is decreased, the pressure on these asperities is sufficiently large so the trapped lubricant layer reaches its tensile strength, yielding a speed-independent friction corresponding to the onset ob BL. Contacts with one or two steel bodies involve plastic deformations in the whole mixed regime. The mixed friction then saturates when the contact area is populated with as many micro contact spots as the surfaces topography allows.

6.4 Synthesis of the results

Rough and smooth surfaces involve the same viscous friction mechanism as long as the film is sufficiently thick to screen the film-thickness weakening caused by the surface roughness. For surfaces characterized in the same conditions, this makes the lamdba ratio a good candidate to estimate the onset of such a film thickness weakening. When the rolling speed is diminished from thick-film EHL to ML, roughness lowers the film thickness progressively compared to a perfectly smooth contact. This results in higher shear rates and more frequent interactions between the opposing surface asperities. Figures 6.23.a and 6.23.b summarize the running-in observations with steel contacts and DLC-DLC contacts.

The onset of ML was defined as the smallest entrainment product where the experimental friction becomes higher than the viscous shear stress, calculated assuming a smooth contact in thin-film conditions and using the fluids rheological parameters measured chapter 4.1. In addition of giving a criterion to answer whether a contact is operating in ML or in EHL, it proposes a simple definition of the onset of ML without presuming the mixed friction mechanism. The ML-EHL thus spotted leads to the same global conclusions as those using a formerly used criterion, namely : the ML-EHL transition occurs when the contact nominal film thickness reaches a value between 2 and 5 times the RMS composite roughness. This transitional film thickness is pressure and sliding independent. This works provides a readily usable formula to predict the transition from EHL to ML according to the lubricant inlet viscosity and the composite RMS roughness measured with a cut-off length close to

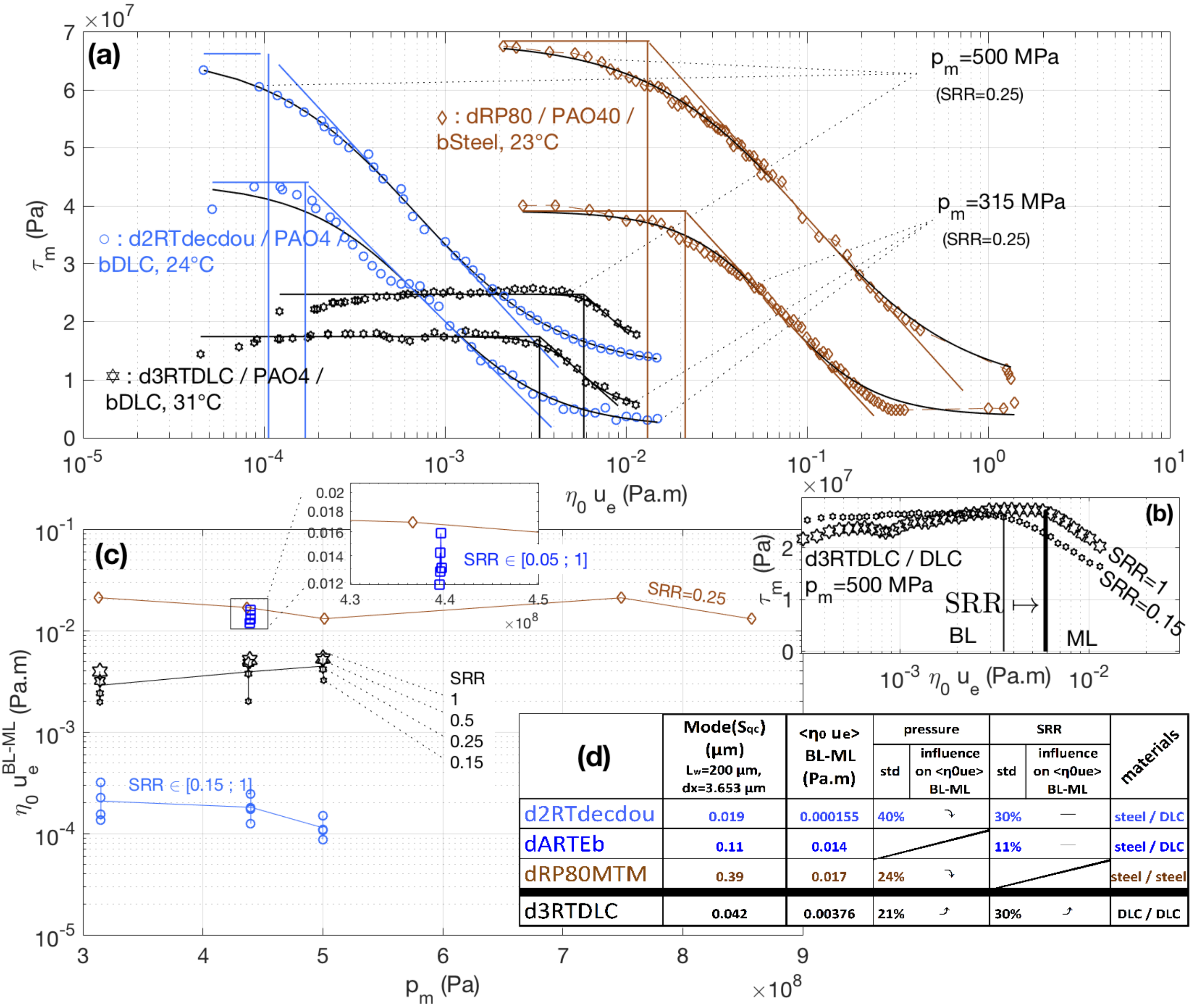

(d)	Mode(S_{qc}) (µm) L_w=200 µm, dx=3.653 µm	<η0 ue> BL-ML (Pa.m)	pressure		SRR		materials
			std	influence on <η0ue> BL-ML	std	influence on <η0ue> BL-ML	
d2RTdecdou	0.019	0.000155	40%	⤵	30%	—	steel / DLC
dARTEb	0.11	0.014			11%	—	steel / DLC
dRP80MTM	0.39	0.017	24%	⤵			steel / steel
d3RTDLC	0.042	0.00376	21%	⤴	30%	⤴	DLC / DLC

Figure 6.22: (a) Spotting of the BL-ML transition the Stribeck tests with three couples of surfaces at $p_m = 315$ MPa and $p_m = 500$ MPa, $SRR = 0.25$. (b) : BL-ML transition versus the operating pressure for different surfaces, at sliding-rolling ratios between 0.15 (smallest symbols) and 1 (largest symbols).

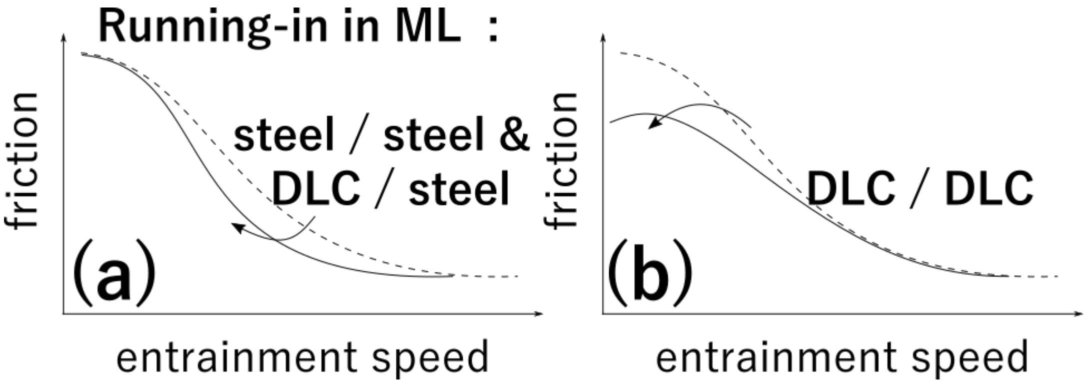

Figure 6.23: (a) : Running-in affecting friction close to EHL. It corresponds to a the removal of the surfaces highest peaks, which shifts the onset of ML to lower entrainment speeds. (b) : running-in that only affects the friction behaviour close to BL, where the friction mechanism is no longer related to an evolution of shear rates as the film forming capability is reduced to zero.

the contact length :

$$\boxed{u_e^{ML-EHL} = \frac{k}{\eta_0} S_{q\,c}^{\;m}} \tag{6.16}$$

in S.I. units, with $k = 28.5 \times 10^6$, $m = 1.2$.

At lower speeds, friction increases until a given speed below which it saturates. This defines phenomenologically the transition from ML to BL. The entrainment product was also used to characterize the BL onset. As the mixed regime is crossed from large to low speeds, the film-forming capability vanishes and $\eta_0 u_e$ is decreasingly related to a film thickness. Contrary to the ML-EHL transition, there is no general relationship between the rolling speed at which the BL onset occurs and the surface roughness.

For steel/steel contacts and steel-DLC contacts, the onset of BL corresponds to a state of equilibrium between lubricated contacts spots and dry contacts that cause a continuous wear of the steel protuding asperities. In the present work, the BL-ML transitional entrainment product increases with S_{qc} in a power law fashion, but it seems to saturate to a constant value close of about 0.02 Pa.m for surfaces rougher than $S_{qc} = 0.1$ μm. Ensuring this would require experiments with surfaces rougher than the present work. Meanwhile, the BL-ML transition with steel bodies may be predicted with the following formula, for $S_{qc} \leq 0.4$ μm :

$$u_e^{BL-ML} = \frac{k''}{2\eta_0} \times S_{q\,c}^{m''} \times tanh(b \cdot (S_{q\,c\,0} - S_{q\,c})) + \frac{k'''}{2\eta_0} \times tanh(b \cdot (S_{q\,c} - S_{q\,c\,0})) \tag{6.17}$$

in, S.I. units, with : $k'' = 7.3 \cdot 10^9$, $m'' = 1.77$, $S_{q\,c\,0} = 0.1$ μm, $b = 10^8$ and $k''' = 1.88 \cdot 10^{-2}$ Pa.m.

For DLC-DLC contacts, the BL-ML transition seems to increase endlessly with the RMS roughness as :

$$u_e^{BL-ML} = \frac{k'}{\eta_0} \times S_{qc}^{m'} \tag{6.18}$$

, in S.I. units, with $k' = 5.75 \times 10^8$ and $m' = 1.5$.

Several remarks about the BL-ML transition with DLC-DLC contacts let suspect that their mixed friction mechanism involves an important part related to micro EHD contacts between asperities, though a better understanding of the friction mechanisms in ML is required.

Chapter 7

Friction in boundary and mixed lubrication with rough surfaces

7.1 Introduction to boundary friction with base oil

7.1.1 Relevance of the Couette and Poiseuille force

Using asymmetrical surfaces in a Stribeck procedure could yield a different friction behaviour according to the sliding speed sign. In HL and EHL, this difference is due to the pressure field assymetry that increases with the rolling speed, which causes the existence of a Poiseuille force acting against the rolling direction. Fig. 7.1 shows that as the entrainment product is reduced from EHL to BL, the shear stress difference between positive and negative sliding (referred to as the Poiseuille force) becomes increasingly small to the average stress (referred to as the Couette force).

The force difference between negative and positive sliding is not always exactly zero in boundary and mixed lubrication but these differences are not repeatable and are probably due to the running-in, the unstationarity of the rubbing track, the out-of-roundness and the vibrations that cause fluctuations of the friction force. Using the Couette shear stress remains appropriate in BL as it is always superior to about 30 times the Poiseuille force. For all Stribeck experiments, the boundary shear stress, denoted $< \tau_{BL} >$, is defined as the Couette shear stress, averaged from the lowest rolling speed to the BL-ML transition.

7.1.2 Influence of pressure on boundary friction

The use of a friction coefficient in EHL is rather inappropriate to characterize friction because the fluid shear stress is not proportional to the pressure, except at large sliding-rolling ratio, when the lubricant strength is reached. On the contrary, in the BL regime : figure 7.2.a shows for different surfaces that the mean shear stress is proportional to the mean pressure. This makes the friction coefficient a more suitable parameter to describe friction in BL.

7.1.3 Influence of the inlet viscosity on boundary friction

Figure 7.2.b displays boundary friction coefficients for two couples of DLC-DLC contacts and one steel-DLC contact, using different PAOs (PAO2, PAO4, PAO8, PAO40, PAO100). Each couple of surfaces has a characteristic friction coefficient irrespective of the inlet viscosity. This confirms that without additives, the boundary friction does not depend on η_0. The *dAR* and *d1RDLC* discs were both rectified and have comparable roughnesses (respectively $S_q = 0.120$ μm and $S_q = 0.155$ μm). However, the *d1RDLC* disc yields a significantly lower friction coefficient than the rectified disc in

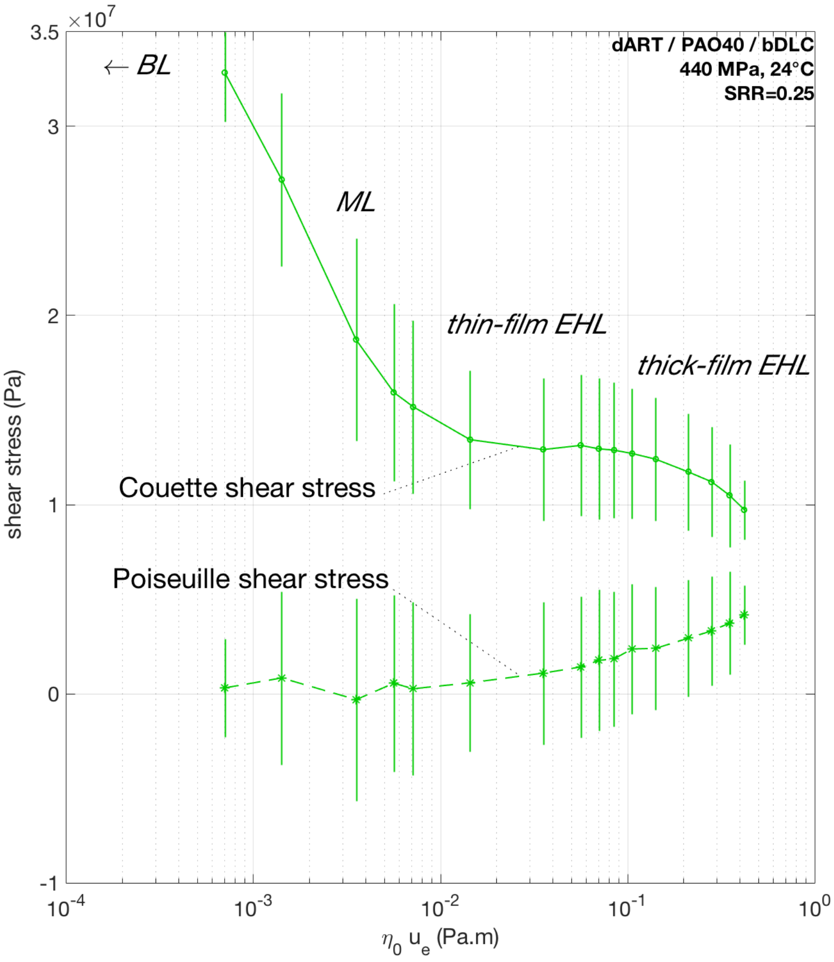

Figure 7.1: Decreasing importance of the Poiseuille force as the entrainment product is reduced from EHL to BL.

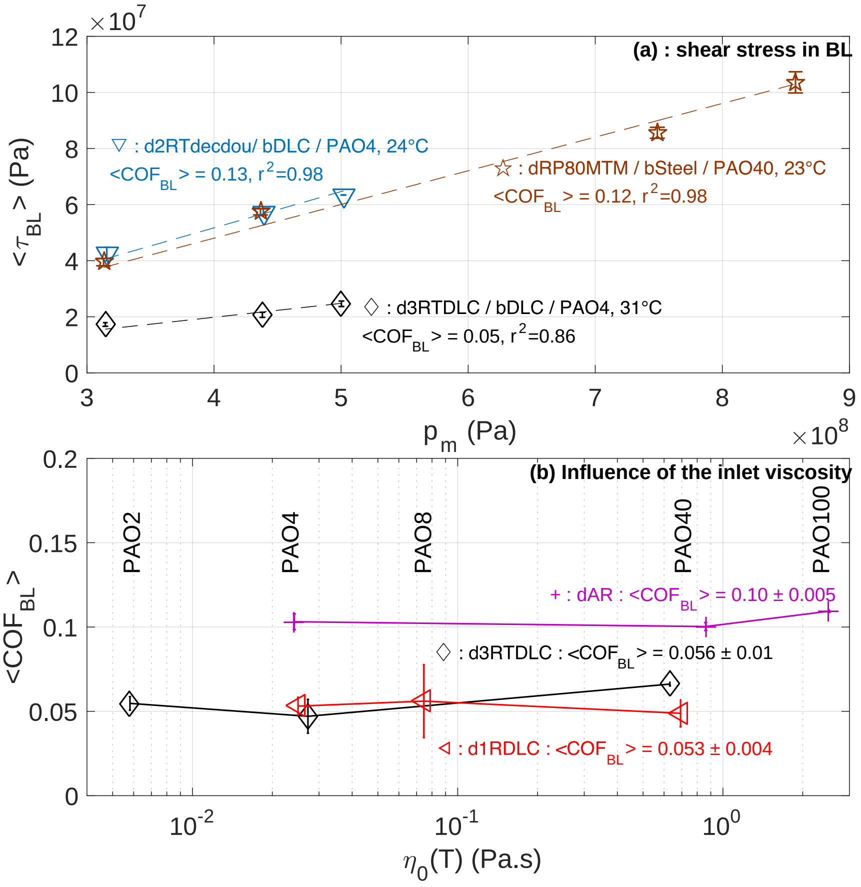

Figure 7.2: (a) : Average shear stress taken during Stribeck curves at $SRR = 0.25\%$ versus the mean Hertz pressure for different contacts with PAOs. (b) : Boundary friction coefficients obtained from Stribeck tests at 440 MPa with DLC-coated balls.

plain steel. Boundary friction thus not only depends on the surface texture but also on the couple of materials used.

It may hence be relevant to classify the rubbing tests in BL first according to the materials used, and thereafter according to their topographical features.

7.2 Mixed and boundary friction for DLC-DLC contacts

For a given couple of DLC-coated surfaces, $< COF_{BL} >$ does not present any monotonous trend with the inlet viscosity varied either with temperature, or by changing of PAO, as it is shown on figures 7.3.a and 7.3.b. These graphs show that between two successive runs, the speed-averaged friction coefficient may be lowered of 0.01 at best, which indicates a removal from protruding asperities and a better conforming of the surfaces.

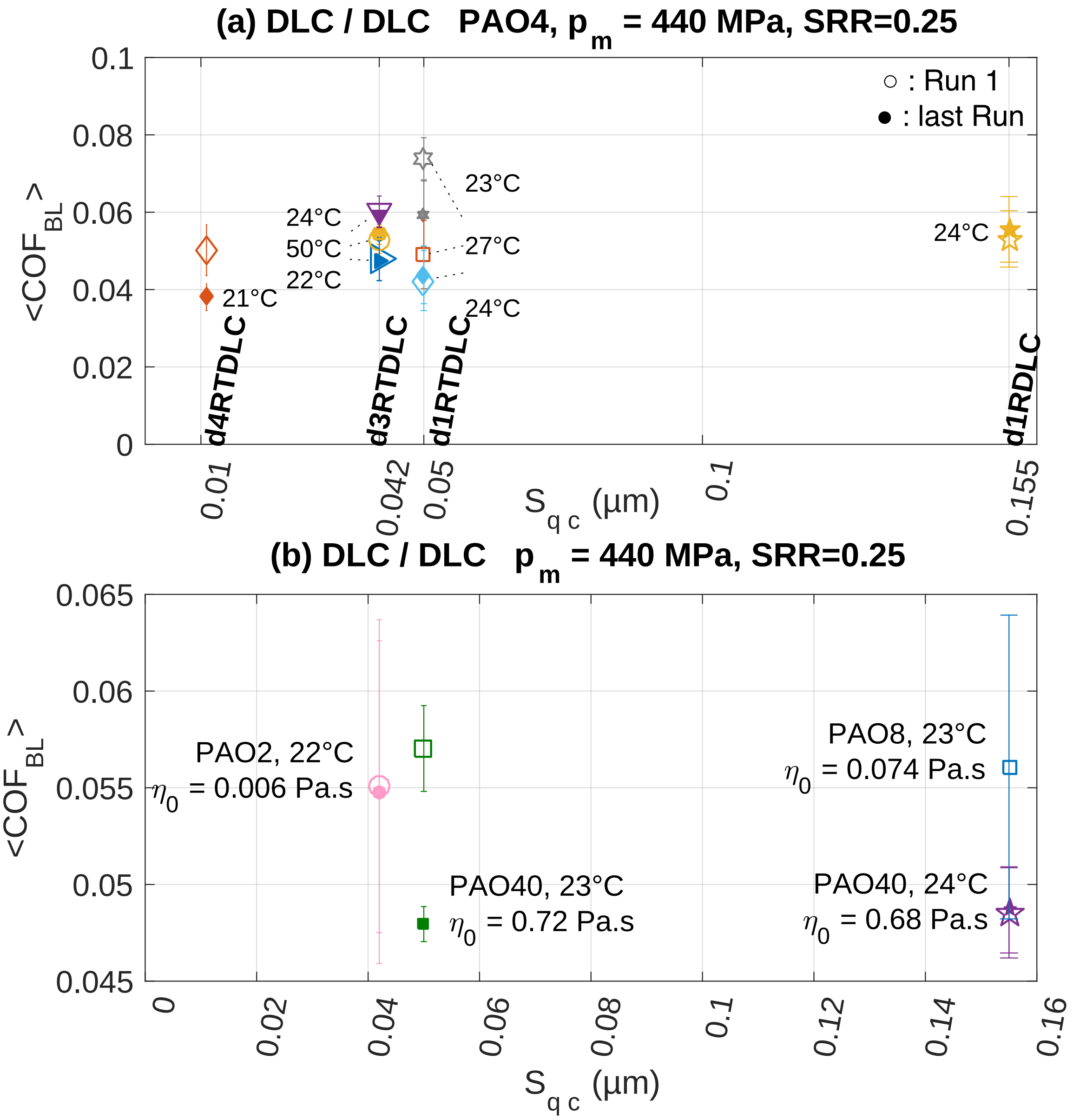

Figure 7.3: Speed-averaged friction coefficient in boundary lubrication versus the standard deviation.

7.2.1 Influence of surface roughness

Figure 7.3.a shows the speed-averaged boundary friction coefficients using PAO4 and four differently rough DLC/DLC contacts, and fig. 7.3.b shows those using other PAOs. Even though

their height deviations are different, the three smoother DLC-coated discs *d4RTDLC*, *d3RTDLC* and *d1RTDLC* have asperity curvature radii of the same order of magnitude, respectively : 3.3 mm, 1.6 mm and 1.3 mm using $dx = 3.653$ μm, and 27 μm, 33 μm and 29 μm using $dx = 0.099$ μm. For the rougher disc *d1RDLC*, this asperity radius is 0.3 mm using $dx = 3.653$ μm and 0.2 μm using $dx = 0.099$ μm. Since the asperities height and curvature are usually recognized as having a large influence on the mixed and boundary friction, it is surprising that these four discs yield about the same boundary friction coefficient :

$$< COF_{BL} >= 0.05 \pm 0.005 \text{ for DLC-DLC contacts in PAOs} \tag{7.1}$$

The boundary friction with DLC-DLC contacts thus seems more or less independent of the surface topographical features.

7.2.2 Influence of kinematics

Figure 7.4.a and 7.4.b show Stribeck tests in the boundary and mixed regimes using respectively speed steps and speed ramps with two DLC-coated bodies. All these Stribeck curves lie in the BL regime and exhibit a visible increase of friction with $\eta_0 u_e$. For these Stribeck tests at $SRR = 0.25$, $p_m = 440$ MPa, the boundary friction increases slowly with the entrainment product with an exponent close to 0.1. The following expression may be used (in S.I. units) as a reasonnable estimate for the friction evolution during Stribeck procedures ($SRR = 0.25$) in the BL regime :

$$COF = (0.035 \pm 0.0005) \times \left(\frac{\eta_0 u_e}{3 \times 10^{-5}} \right)^{0.09 \pm 0.02} \quad \text{for DLC-DLC contacts using PAOs} \tag{7.2}$$

It was suspected that this behaviour towards the entrainment product was somehow related to a different running-in between the lowest and the highest entrainment speeds in BL. Fig. 7.4.a and 7.4.b show that even though friction may be lowered (or increased in some cases) between successive runs, the friction exponent with $\eta_0 u_e$ remains positive, close to 0.1. This discredits a speed-dependent wear mechanism for the observed boundary friction evolution.

This evolution of the friction coefficient with the entrainment product was also observed in the literature. Albertson (1) proposed a boundary friction mechanism attempting to explain the increase of friction with the sliding speed. For this, he assumed that friction gets higher when the surfaces are not fully covered with adsorbed layers of additive molecules. The time required for the adsorption was related to a diffusion time between a lubricant reservoir and the surfaces, and the efficiency of adsorption was governed by the balance between the chemical adsorption time and the time spent by surfaces in the contact. Campen et al. (22) stressed that such a view is unlikely to fully explain the friction dependence towards speed as there is no reservoir of additves from which these could diffuse to the surfaces. Other approaches were proposed (22), based on the concept of thermally activated slip between fluid layers, similar to the Eyring model. However, these become rapidly complex as they input further microscopic parameters (activation volumes, average size and distance between junctions, ...) that are difficult to measure separately without an apparatus specifically designed for it.

The lubricants here used are additive-free PAOs, which are non polar and allow only weak adsorption (physisorption) against surfaces. An explanation based on a rate of chemical adsorption onto the surfaces is thus unlikely to explain the boundary friction dependence towards speed, only observed with base oil and DLC coated surfaces.

In the literature, similar behaviours were observed with DLC-DLC contacts in base oil. Vengudusamy et al. (129), using two DLC-coated steel surfaces (with a ta-C coating, referred to as *DLC*

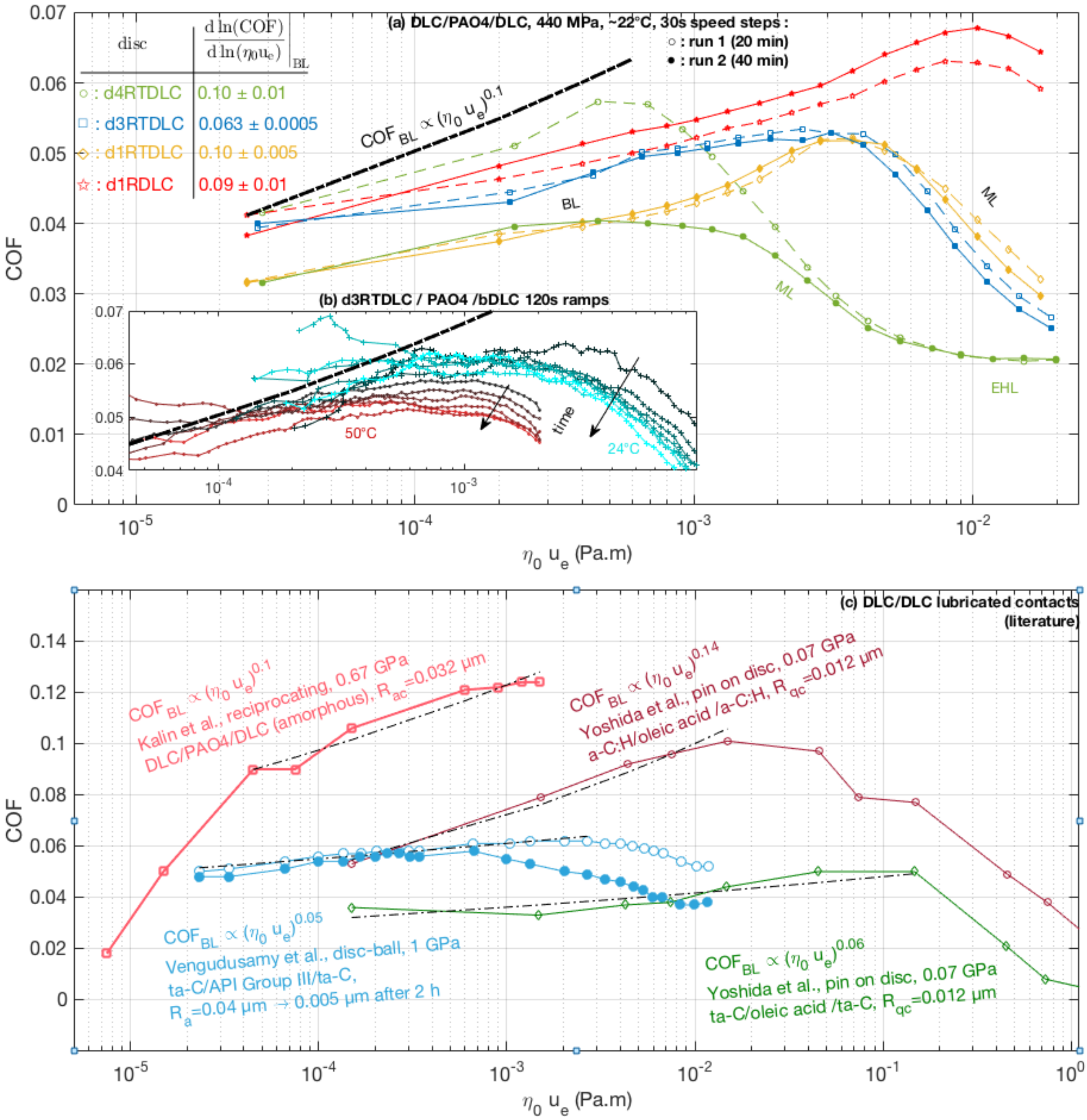

Figure 7.4: Stribeck curves at $SRR = 0.25$ in the boundary regime using speed steps (a) and speed ramps (b) procedures with DLC/DLC contacts. (c) : Experiments from the literature. (a) and (c) : Empty symbols and filled symbols correspond respectively to the first and the last run. Each run was fitted in the boundary regime using a power law : the exponents are displayed in the top left corner of graph (a).

6 in (129)) in a disc-ball tribometer with additive-free base oil, obtained a boundary friction behaviour similar to those observed in the present work (see blue curves on fig. 7.4.c). After two hours rubbing, the centre line average roughness was importantly decreased, which has resulted in a ML regime shifted towards lower entrainment speeds (see filled circles on fig. 7.4.c), without changing the speed-dependence of boundary friction. Yoshida et al. (139) also observed an increase of boundary friction with the entrainment speed (see fig. 7.4) using lubricated pin on disc friction tests with a-C:H (20%-hydrogenated) and ta-C symmetrical DLC-coated surfaces at a moderate pressure of 0.07 GPa. For these two studies, no hypothesis has been provided to explain this peculiar behaviour. Kalin and Velkavrh (74) used several PAOs with non-doped amorphous 30%-hydrogenated DLC-coated steel surfaces in a reciprocating tribometer and found an "inverted" Stribeck curve shape, where the friction decreases as the entrainment speed is reduced from EHL to BL (see reproduced friction curve in pink on fig. 7.4.c). Only a small polishing wear was observed after this experiment. In addition, they measured the friction in a dry DLC-DLC contact at low speeds and obtained a value of 0.01. Since this dry friction coefficient was lower than in all their lubricated conditions, they interpreted the lower friction at low rolling speeds as resulting from the dry DLC-DLC friction properties, assuming the contact becomes increasingly populated with dry contacts at low entrainment speeds. This explanation is dubious for the present contacts as it was reported that a-C:H/a-C:H contacts in atmospheric conditions yield dry friction coefficients around 0.1 to 0.15 (108).

The influence of the sliding-rolling ratio was investigated using two DLC-coated bodies while performing Stribeck tests with PAO4 and the *d3RTDLC* disc at sliding–rolling ratios between 0.05 and 1 at 315, 440 and 500 MPa (see figures 7.5.a, 7.5.b, 7.5.c). The friction evolution in the BL regime was fitted with power laws and the exponents were plotted versus the sliding-rolling ratio on fig. 7.5.d. All exponents are positive, but they take smaller values at sliding-rolling ratios superior to 0.25. Moreover the friction is less speed-dependent at high pressures.

7.2.3 Interpretation of the mixed and boundary friction mechanism with DLC-DLC contacts

In the previous chapter with DLC-DLC contacts, it was concluded that the BL-ML transition occurs at higher entrainment products when :

- The nominal Hertz presssure is increased.
- The sliding-rolling ratio is increased.

Since these factors both contribute in switching the fluid rheology from Newtonian to plastic, it was suspected that the mixed friction with these surfaces was only of viscous nature, i.e. that solid-solid contacts do not contribute to friction. Within this interpretation, the transition from ML to BL corresponds to a state where the fluid confined in micro-EHD contacts becomes plastic, and where the amount of micro-EHD contacts — which increases as $\eta_0 u_e$ is decreased in the ML regime — reaches a maximum. In the present section on DLC-DLC contacts, it was shown that :

- The boundary friction coefficients are independent on the surface roughness.
- The average boundary friction coefficient is approximately 0.05, which is the same friction coefficient in EHD as when the lubricant responds plastically ($\frac{\tau_{max}}{p_m} \approx 0.05$).

The speed averaged friction coefficient of ~ 0.05 agrees with the friction coefficients reviewed by Kalin et al. (73) for non-doped DLC/DLC contacts in PAO. This was attributed to the low chemical interactions between the surfaces and PAOs, which are non-polar, and with the good anti-wear properties of the DLC coatings. It was observed that the use of additives (MoDTC, MoDTC

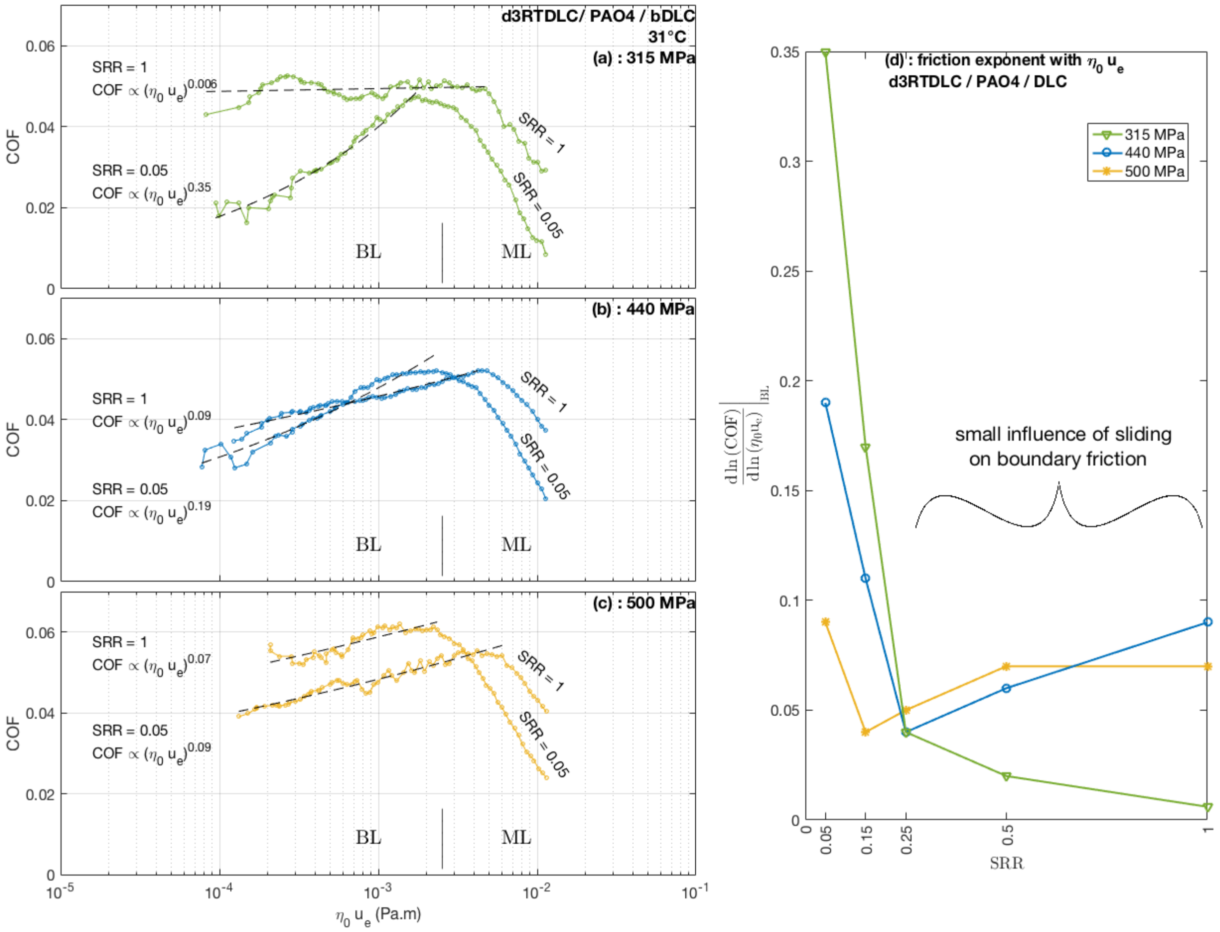

Figure 7.5: (a-c) : Stribeck tests using PAO4 and two DLC coated surfaces in the mixed and boundary lubrication regimes showing the influence of large and low slip ratio on the shape of the Stribeck curve. (d) : Power exponent of the friction coefficient evolution with the entrainment product in the BL regime, for different pressures and sliding-rolling ratios.

+ ZnDDP) generally increases the friction obtained with a-C:H DLC-DLC contacts compared to additive-free PAOs (73), (140). This was interpreted with the lubricant shear strength being increased in the presence of additives (73), which supports the present interpretation about the viscous nature of boundary friction.

Figure 7.6 represent the suspected friction mechanism in the mixed and boundary regimes with DLC-DLC contacts. In thin-film EHL (fig. 7.6.(i).a) the fluid pressure is close to the mean Hertz pressure p_m everywhere in the contact area. From there, reducing the entrainment product lowers the surface separation, which causes micro-EHL entrapment between the highest asperities and the counter surface (fig. 7.6.(i).b). These local pressure increases shift the local fluid rheology towards a plastic behaviour (red curve on fig. 7.6.(iii)). The load balance imposes that the high pressure raised in these micro-EHD spots is counterbalanced with a lower fluid pressure in the valleys, which lowers the viscosity in these areas (green curve on fig. 7.6.(iii)).

Reducing again the surface separation in the mixed regime increases the area covered by micro-EHD contacts until a state where they cover most of the nominal contact area and bear most of the load :

$$\text{Total area covered with } \mu\text{EHD contacts} \approx A_{nom} \text{ (close to the BL-ML transition)}$$

In that state, the load balance between the fluid confined on asperities (at high pressure) and the fluid in the valleys (at low pressure) limits the pressure between the asperities to an average pressure close to p_m (see fig. 7.6.(ii)). In that state (schematized fig. 7.6.(i).c) the amount of asperities bearing the contact by micro-EHL reaches a maximum (either with numerous separate micro-EHD spots or by means of asperity merging between these spots) and decreasing $\eta_0 u_e$ no longer affects the surface separation. This state corresponds to the onset of BL. Once this regime was reached, it was observed that :

- During Stribeck procedures in the BL regime, friction increases linearly with $ln(\eta_0 u_e)$.
- This increase is more important at small than at large sliding-rolling ratios.

At $\eta_0 u_e < \eta_0 u_e^{BL-ML}$ (see fig. 7.6.(i).c), the contact area is populated a nanometric fluid layer that is sufficiently thick to prevent direct solid contacts. The thickness distribution of the fluid layer separating the surfaces is constant towards $\eta_0 u_e$ and since a Stribeck procedure imposes the sliding speed and the entrainment speed to be proportional, reducing u_e leads to reducing the shear rates in the contact such that in some contact spots, the local shear rate $\frac{u_s}{h(x,y)}$ is low enough to make the lubricant quit its purely plastic behaviour and recover a shear rate dependence towards the shear stress. This explains why the boundary friction coefficient decreases when $\eta_0 u_e$ decreases. This statement is illustrated figure 7.7, where Stribeck curves with DLC/DLC contacts at $SRR = 0.25$ are compared to the fluid rheology (in dashed lines) assuming a speed-independent nanometric film thickness and a fluid homogeneously pressurized at p_m. Of course, this view is simplified:in reality, there must exist a distribution of the surface separation, with some asperities more elastically deformed than others and by extension, with a pressure field that is not as smooth as the Hertz pressure field. These strong assumptions certainly explain the divergence between the experimental and the calculated friction evolutions of fig. 7.7.

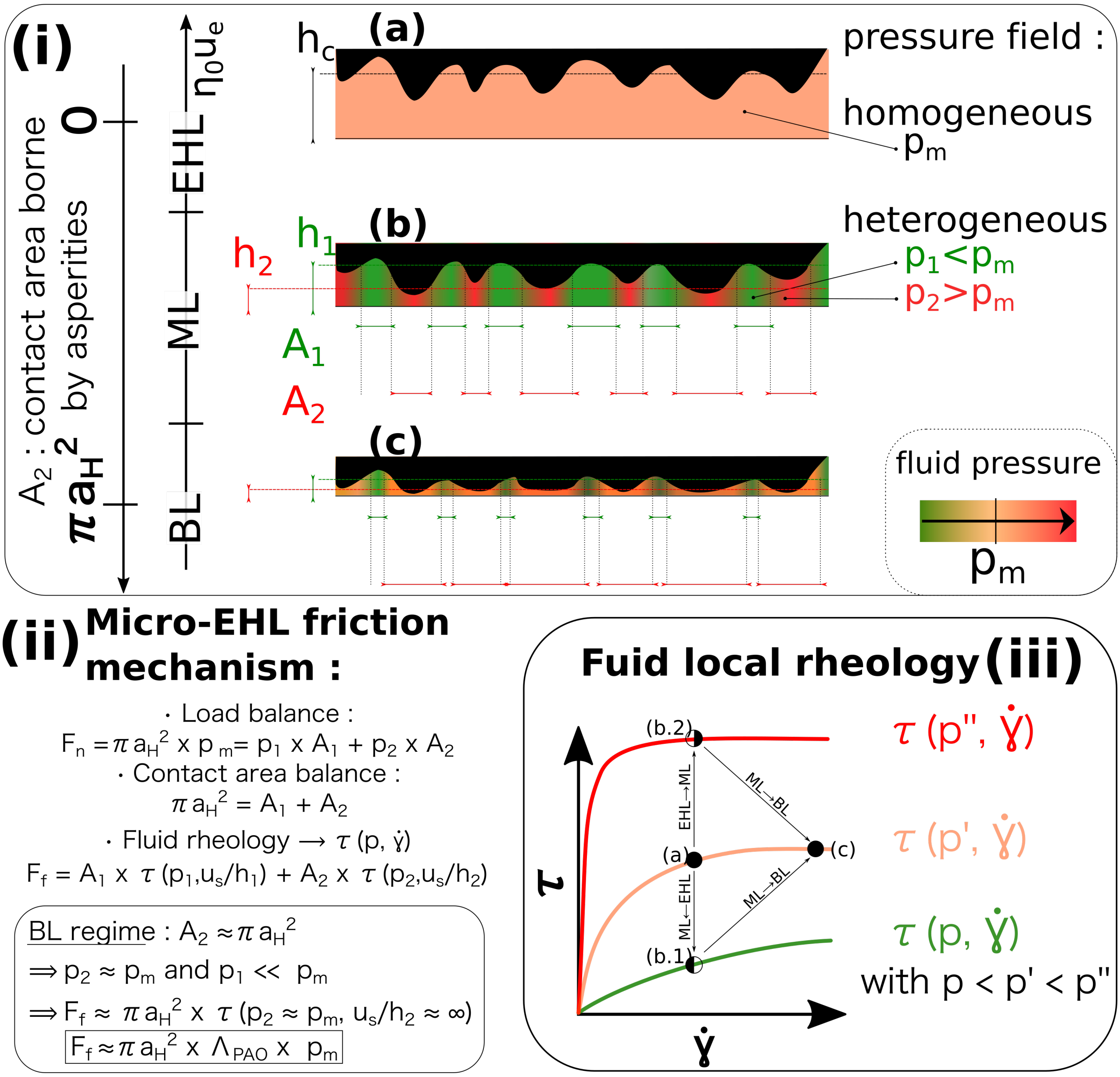

Figure 7.6: Schematic of the asperity interactions assuming a micro EHL friction mechanism. In the mixed and boundary regimes, the contact area separates into areas where the asperities deform elastically (A_2) and increase the local fluid pressure (p_2), and those between the asperities (A_1), where the fluid pressure (p_1) is inferior to the nominal Hertz pressure p_m because of the load balance.

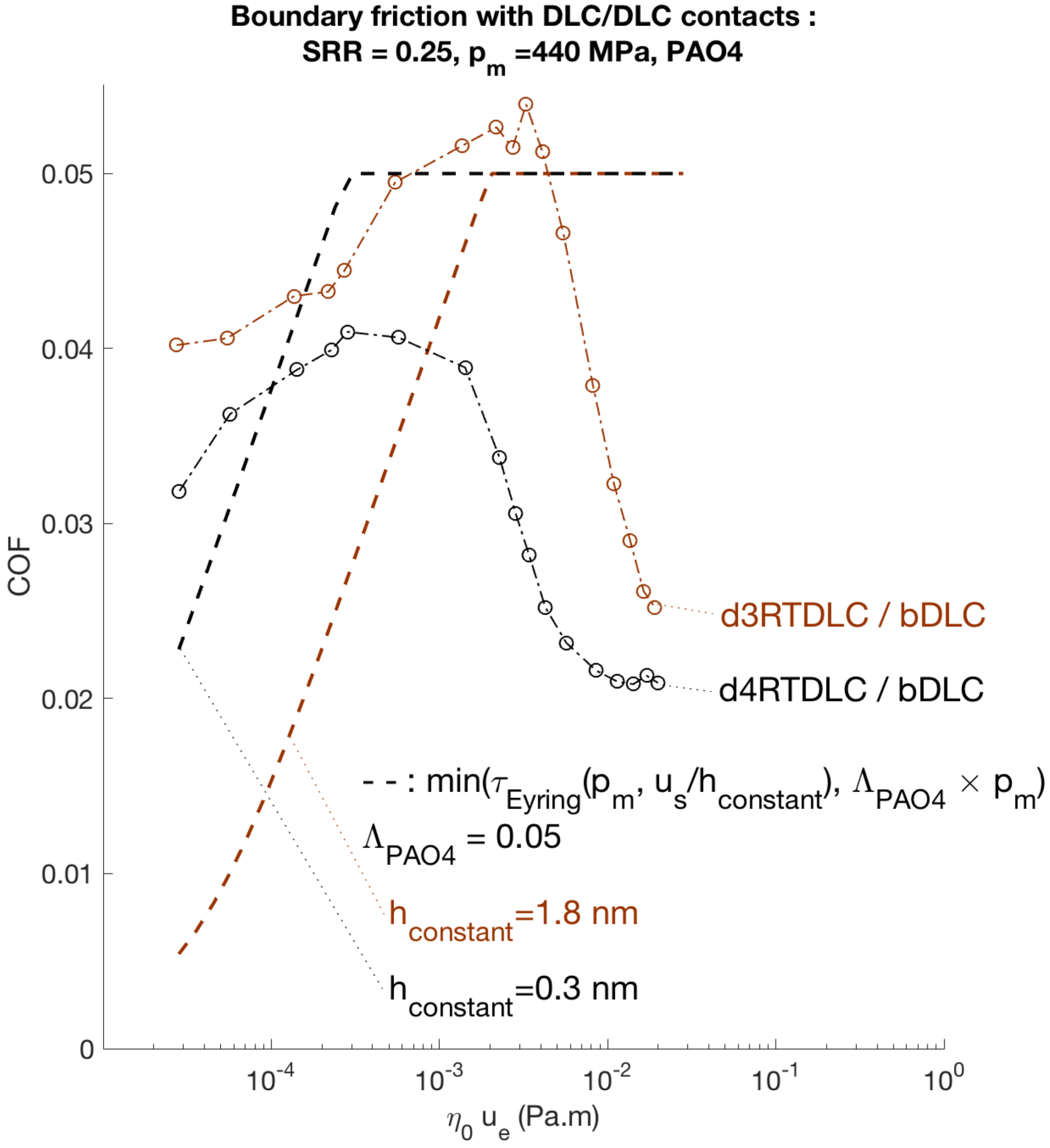

Figure 7.7: Stribeck curves in the BL and ML regimes with DLC/DLC contacts in PAO4 (symbols). The dashed lines represent the fluid rheology at p_m assuming a constant film thickness.

7.3 Mixed friction with nanometrically smooth discs

For some couples of polished surfaces, the boundary lubrication regime — i.e. a saturation of the mixed friction at low entrainment products — could not be reached using Stribeck procedures, as it can be stated from fig. 7.8.a. As $\eta_0 u_e$ is decreased below the ML-EHL transition, friction increases sharply without saturating, such that the friction coefficient may even reach high values superior to 0.1. Since some of these smooth surfaces are transparent, these experiments can help understand the phenomena responsible for the friction being higher in ML than in EHL.

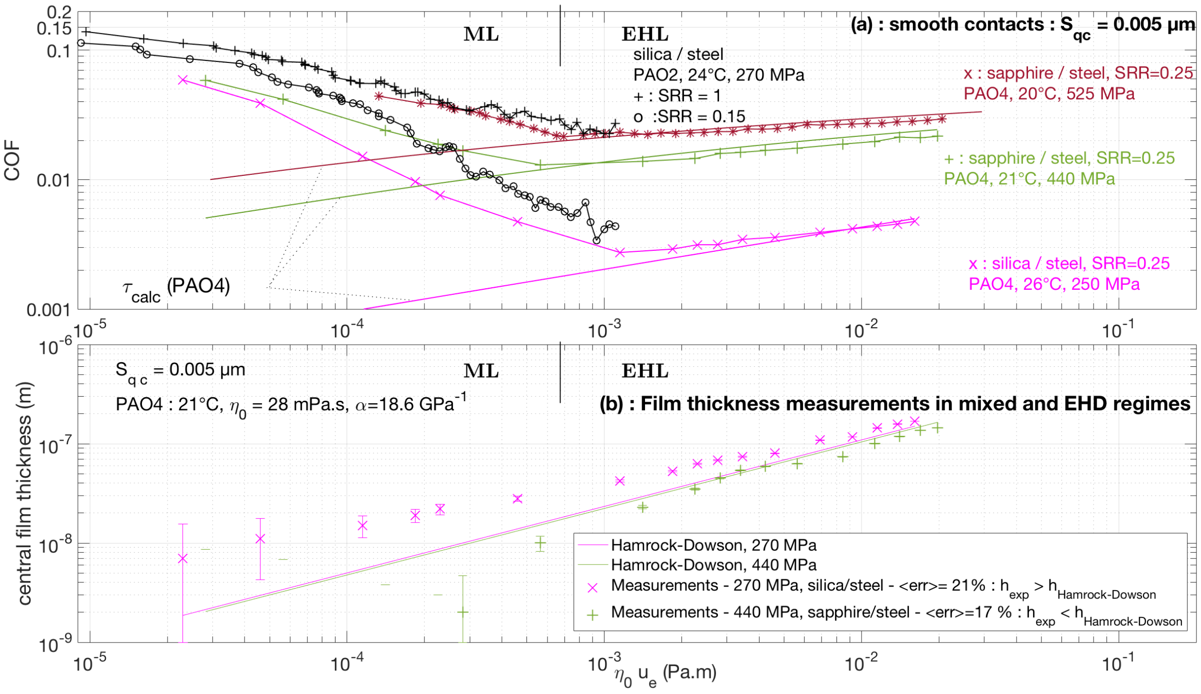

Figure 7.8: (a) Stribeck tests at $SRR = 0.25$ using smooth surfaces. (b) : Film thickness measurements using transparent discs.

7.3.1 In situ film distribution in ML

Hartl et al. (65) measured by interferometry the evolution of the film thickness with the rolling speed, down to 1 nm at 100 MPa for squalane, di-(2-ethylhexyl)phthalate, a mineral oil with and without additives and for hexadecane. For all fluids, the experimental film thickness are compatible with smooth film thickness predictions down to 10 nm, and even below for the hexadecane and the additive-free mineral oil. For other fluids, the film thicknesses were larger than predicted and the measurements were compatible with the presence of an immobile adsorbed layer being between 1 and 3 nm-thick.

Figure 7.8.b shows interferometric film thickness measurements with PAO4 during Stribeck tests with transparent discs. Even though the same fluid was used for the two series of film thickness measurements, they yield different conclusions towards the presence of absence of an adsorbed fluid layer that would not contribute to the fluid flow : with a sapphire disc (at 440 MPa), the film thickness is inferior to the smooth predictions whereas with silica (at 270 MPa), it becomes superior to the smooth prediction. The present film thickness measurements do not allow to conclude about the presence of an adsorbed layer between the solids. Nevertheless, these measurements are compatible with the smooth film thickness formula of (62) within 21 % even in the mixed and EHD lubrication

regimes. The film thickness measurements during traction tests, shown section 4.3.1 (fig. 4.16), also follow the smooth film thickness predictions within 17%. It is thus considered that for such smooth contacts ($S_{qc} = 0.005$ μm) the film thicknesses are not affected by roughness.

Figure 7.9.a shows in situ interferograms obtained during these traction tests on PAO4 at different rolling speeds. Most of these interferograms show quite homogeneous film thickness distributions down to film thicknesses of 6 ± 1 nm, with the infrequent passage of heterogeneities that occupy a small fraction (a few percent) of the contact area. The associated traction experiments, shown fig. 7.9, show that for a given shear rate value, the shear stress increases progressively as the surface separation is reduced.

Purely viscous hypothesis Regarding the nature of the mixed friction mechanism, the small area covered with heterogeneities and the friction dependence towards the sliding speed lean towards a friction mechanism mostly of viscous nature, as for the DLC-DLC contacts. In the present view, the shearing of a thickness formed by the EHD film-forming mechanism and the shearing of an adsorbed fluid layer confined between the solids are both referred to as viscous friction mechanisms. These two mechanisms should be regarded differently only when the chemical affinity between two fluid layers is importantly different from the affinity between the surfaces and the fluid (e.g. for chemically adsorbed films). This is not the case with poly-alpha olefins as they are known to bond weakly with the surfaces (physisorption). Since film thickness measurements agree with the Hamrock and Dowson film-thickness formula, underestimated shear rates can not explain mixed friction being higher than EHD friction. This difference should then be due to pressure increases in the lubricant film which is efficient in increasing the viscosity. Considering the surfaces remain separated with a layer of lubricant molecules, the asperities may deform elastically as the surface separation is decreased, which would locally increase the pressure in the fluid confined between these asperities. It is thus assumed in a first step that the mixed friction is purely viscous and that the fluid viscosity increases locally as the entrainment product is reduced in the ML regime.

To be consistent with this idea, tractions are plotted (fig. 7.9.b) along with the PAO4 Eyring rheology, where the input pressures were adapted to follow the experimental τ_m-vs-$\dot{\gamma}$ evolution. Down to $h_c = 28$ nm, the nominal Hertz pressure, $p_m = 525$ MPa, is sufficient to fit the tractions. At lower film thicknesses, it is required to increase the input viscosity η_E and the Eyring stress τ_0 using higher effective pressures up to $p_{eff} = 760$ MPa for the traction performed at $h_c = 6$ nm. The Stribeck curves plotted figure 7.10.a are similarly interpolated assuming a viscous shear mechanism and adapting the input pressure p_{eff} inside the PAO4 Eyring rheology. These effective pressures are plotted (fig. 7.10.b) versus the lambda ratio for Stribeck tests and the tractions of fig. 7.9.b with transparent discs. Between $\Lambda = 10$ and $\Lambda = 1$ (i.e. film thicknesses from 0.05 μm to 0.005 μm) p_{eff} goes from the nominal Hertz pressure to approximately twice this value. In figure 7.10.c, the effective overpressures ($p_{eff} - p_m$) are plotted versus the nominal film thickness for the Stribeck tests shown fig. 7.10.a and for the tractions shown 7.9.b. These curves follow the same trend whatever the materials or the nominal Hertz pressures involved.

In light of a Greenwood-Williamson contact modelling, it is interesting to compare these effective overpressures to the average pressure on an asperity. The mean asperity pressure is a function of the separation between the mean asperity height of the rough surface and the ideally smooth surface. Transparent discs are considered perfectly smooth. The steel ball mean summit height is betwen 1 and 2 nm above the ball mean plane. This distance is neglected and the separation is equated to the nominal film thickness h_c. Considering the summit heights are Gaussian, the mean pressure over asperities is then equal to :

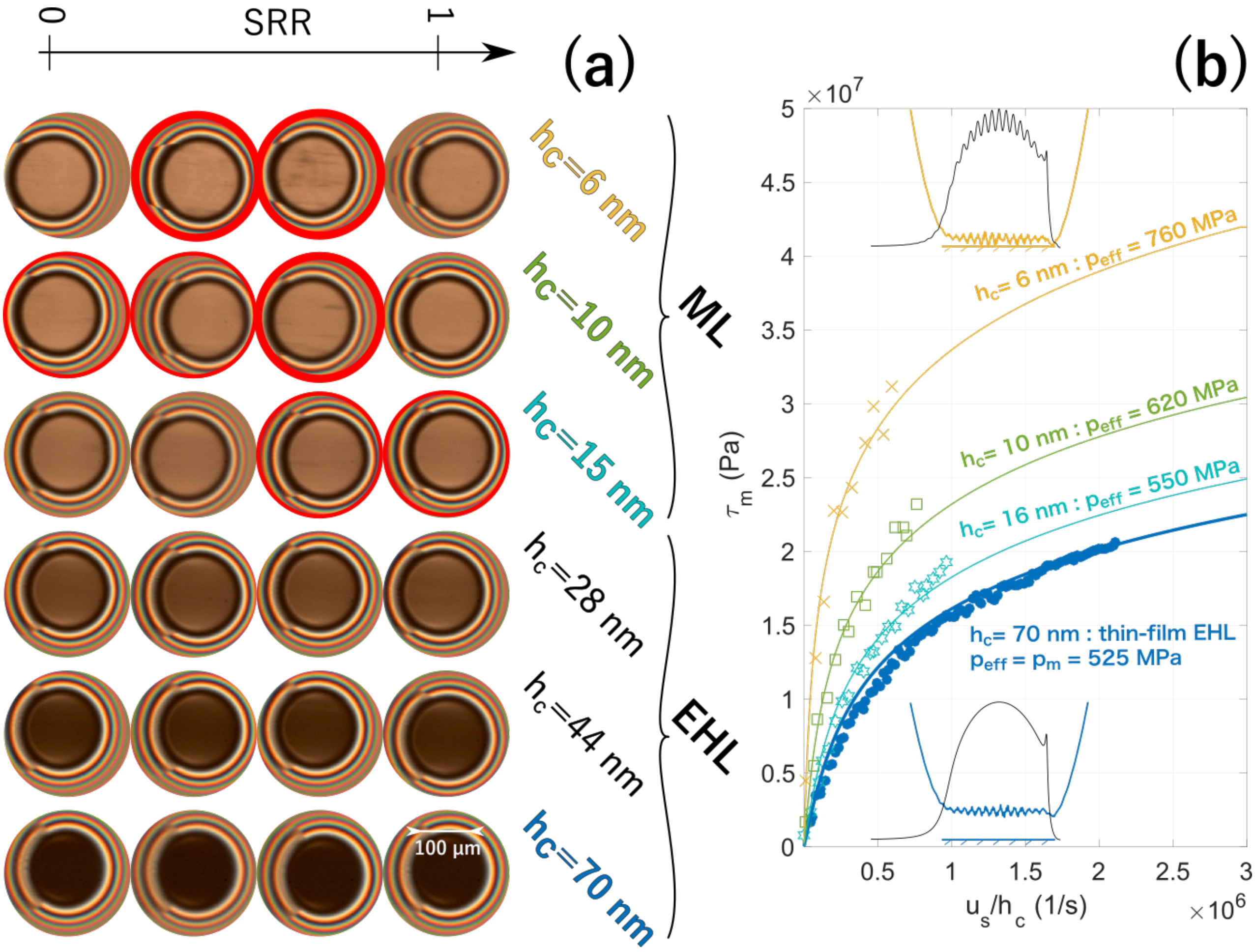

Figure 7.9: In situ contact interferograms taken during tractions on PAO4 at u_e = 0.005, 0.01, 0.02, 0.05, 0.1 and 0.2 m/s showing homogeneous contacts with infrequent heterogeneities on the inteferograms circled in red. (b) : Tractions with sapphire, steel and PAO4 at p_m = 525 MPa. u_e = 0.005, 0.01, 0.02, 0.2 m/s. The filled symbols correspond to thin-film EHL conditions while the empty symbols lie in ML. The solid lines are calculated tractions with different input pressures p_{eff} for the Eyring parameters $\tau_0(p)$ and $\eta_E(p)$.

$$< p_{asp} > = \frac{2\,E'}{3\pi}\sqrt{\frac{\sigma_a}{\beta}}\int_{h_c/\sigma_a}^{\infty} du\, \frac{e^{-\frac{1}{2}u^2}}{\sqrt{2}\,\pi}\left(u-\frac{h_c}{\sigma_a}\right)^{1/2} \tag{7.3}$$

This pressure is calculated using the latter equation and the ball summit curvature radius measured with a sampling interval of 0.099 μm : $Mode(\beta)$ = 35 μm. The asperity pressure is plotted versus the nominal separation on fig. 7.10.c using E' = 305 GPa and E' = 110 GPa (corresponding respectively to the reduced moduli of steel against sapphire and steel against glass) in solid and dashed black lines.

The asperity pressure depends on the reduced modulus E', whereas the inverted effective overpressures do not present any difference between using sapphire or silica against steel. The overpressures are superior to the mean asperity pressures shown fig. 7.10.c, even though the latter were calculated considering the contact reduced modulus (used in eq. (7.3)) unaltered by the presence of a fluid film layer, which is equivalent to considering it as perfectly rigid. Actually, the compressibility of the

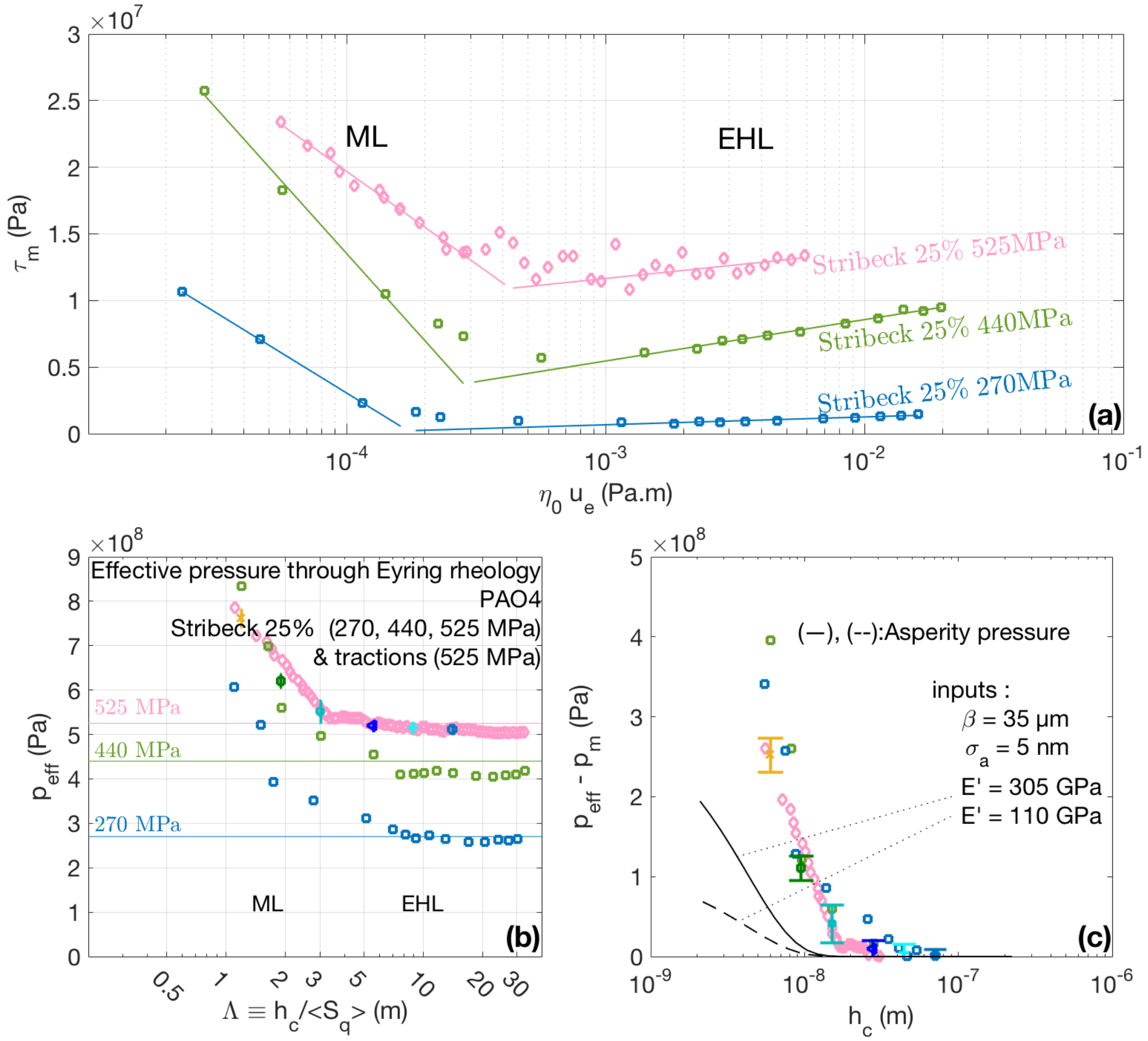

Figure 7.10: (a) : Stribeck tests at $SRR = 0.25\%$ with PAO4 at three Hertz pressures : $p_m = 525$, 440 MPa (steel-sapphire) and 270 MPa (steel-silica). (b) : Effective pressure input in the PAO4 Eyring rheology to equate the experimental shear stress τ_m. (c) : Effective overpressure (symbols) and calculated pressures using equation (7.3) and the steel ball summit topogrographical parameters obtained with a sampling interval of 0.099 μm : $\sigma_s = 5 \times 10^{-9}$ μm, $Mode(\beta) = 35$ μm.

fluid layer should decrease the effective elastic modulus E', which would increase the gap between the effective overpressure and the asperity pressure.

This result discredits the hypothesis of mixed friction being only of viscous nature and leads to consider that solid contacts must occur on the contact area and contribute to a non negligible fraction of the friction in the ML regime. This is consistent with the high friction coefficient of 0.15 obtained with the sapphire/steel contact, whose Stribeck curve is shown fig. 7.8.a. This does not mean that micro-EHL is to be excluded from the mixed friction mechanism.

7.3.2 Feeding mechanism in BL at large sliding-rolling ratio

In order to evaluate whether a boundary friction regime could occur using the smoothest contacts, with polished balls against transparent discs, a different kinematic procedure was applied to a silica/steel contact using the thinnest lubricant (PAO2, $\eta_0 = 0.006$ Pa.s). In these tests, shown fig. 7.11.a, the entrainment speed is reduced from $u_{e\,max} = 0.4$ m/s to zero, while the sliding speed is increased from 0 to $u_s = \pm 2u_{e\,max}$, with linear ramps lasting 30 seconds each.

The ramps where the disc moves faster are displayed in red, those where the ball is faster are shown in blue. In terms of history, going from pure rolling ($SRR = 0$) to pure sliding ($SRR = \pm\infty$) and from pure sliding to pure rolling yield the same friction curves. Though, a repeatable difference is observed according to the sign of the sliding speed : when the smooth silica disc is faster than the steel ball, the friction coefficient presents a peak up to 0.14 in $SRR \approx 30$. In situ interferograms, shown fig. 7.11.b, reveal that from low SRR to $SRR = 18$, the experimental film thickness decreases down to 1 nm, which is the maximum vertical resolution. It is thus possible that solid contacts explain the friction coefficient peaking at 0.14. Yet, at larger sliding-rolling ratios, the film thickness gets slightly higher than the vertical resolution ($h_c = 2$ nm) and the friction coefficient decreases from 0.14 down to about 0.05. This indicates the reformation of a protective fluid layer between the surfaces.

Since the entrainment product is nominally zero, the presence of this protective layer must be due to a different mechanism than that predicted by the EHD theory. The most plausible explanation is that in pure sliding, the contact is supplied with lubricant brought out of the surface valleys. The friction peak observed when the smooth silica is faster would then correspond to a transient state between the two lubricating mechanisms, where neither the classical EHD film-forming mechanism nor the amount of lubricant brought by the surfaces valleys would be sufficient to prevent solid contact spots.

The speed ramps where the ball is faster than the silica disc (in blue, fig. 7.11.a) do not present any friction peak, which indicates that at the end of the EHD film-forming regime, there is always enough lubricant brought by the second supply mechanism. Given the silica disc RMS roughness ($S_q \leq 1$ nm), it can be considered that most of the reservoirs are on the ball ($S_q = 4$ nm). On the one hand, the [rougher] ball motion supplies the contact with lubricant reservoirs. On the other hand, the [smoother] silica disc motion only spreads the available fluid on the rubbing track. As a consequence, when the rougher surface (the ball, here) is faster than the smoother one (the silica disc, here), the contact is more unlikely to lack of lubricant, which explains qualitatively that in the former case, the contact does not dry-up and friction remains low, with a friction coefficient compatible with the lubricant shear strength.

To question this presumed oil supply mechanism, the same kinematic is used using this time a ball smoother than the counter disc (DLC-coated steel surfaces). The friction tests are shown fig. 7.11.c. These experiments indeed exhibit a friction peak of $COF \approx 0.08$ when the smoother surface is the fastest, and no peak when the rougher one is the fastest, which agrees with the presumed valley-induced feeding mechanism. The smaller amplitude of the friction peak is certainly due to both surfaces being rough enough ($S_q = 7$ nm for the DLC-coated ball and $S_q = 16$ nm for the *d4RTDLC* disc) to provide lubricant reservoirs in the contact.

3 minute-long speed steps were performed in pure sliding ($u_e = 0$, $u_{ball} = -u_{disc}$) at different sliding speeds with the two couples of surfaces. The time-averaged friction coefficients are displayed fig. 7.11.d. During these steps, the friction coefficient remains quite stable, as it is shown with the friction standard deviation plotted with errorbars, and has an average value of :

$$COF = 0.054 \pm 0.003 \text{ at } u_e = 0 \pm 10^{-4} \text{ m/s with PAO2} \tag{7.4}$$

During these speed steps, the occurrence of solid contact must hence be rare, and the valley supply mechanism holds during the whole speed steps at zero entrainment product. The value of the friction coefficient at zero entrainement and $SRR > 10$ are close to those obtained when the lubricant shear strength is reached (see section 4.1.3.1) : between 0.05 and 0.08.

To conclude about the mixed friction mechanism with nanometrically smooth contacts, when a Stribeck procedure at $SRR \leq 0.25$ is used, it is not possible to reach a boundary regime — in the sense of a saturation of the friction towards low $\eta_0 u_e$ — because the lubricant flow is too low to feed the contact with an EHD film-forming mechanism. The friction coefficient at $\eta_0 u_e < 10^{-4}$ Pa.m thus takes values superior to 0.1 because of solid contact spots that take place because of the lack of lubricant in the contact area. Nevertheless, the contact can be supplied with lubricant thanks to the fluid contained in the valleys of the roughest body. Solid contacts can thus be prevented provided this body moves fast enough, which requires a sliding-rolling ratio superior to 100. Surprisingly, a large sliding-rolling ratio thus has a beneficial effect on the friction force because it promotes this valley-supply mechanism that prevents solid contact spots.

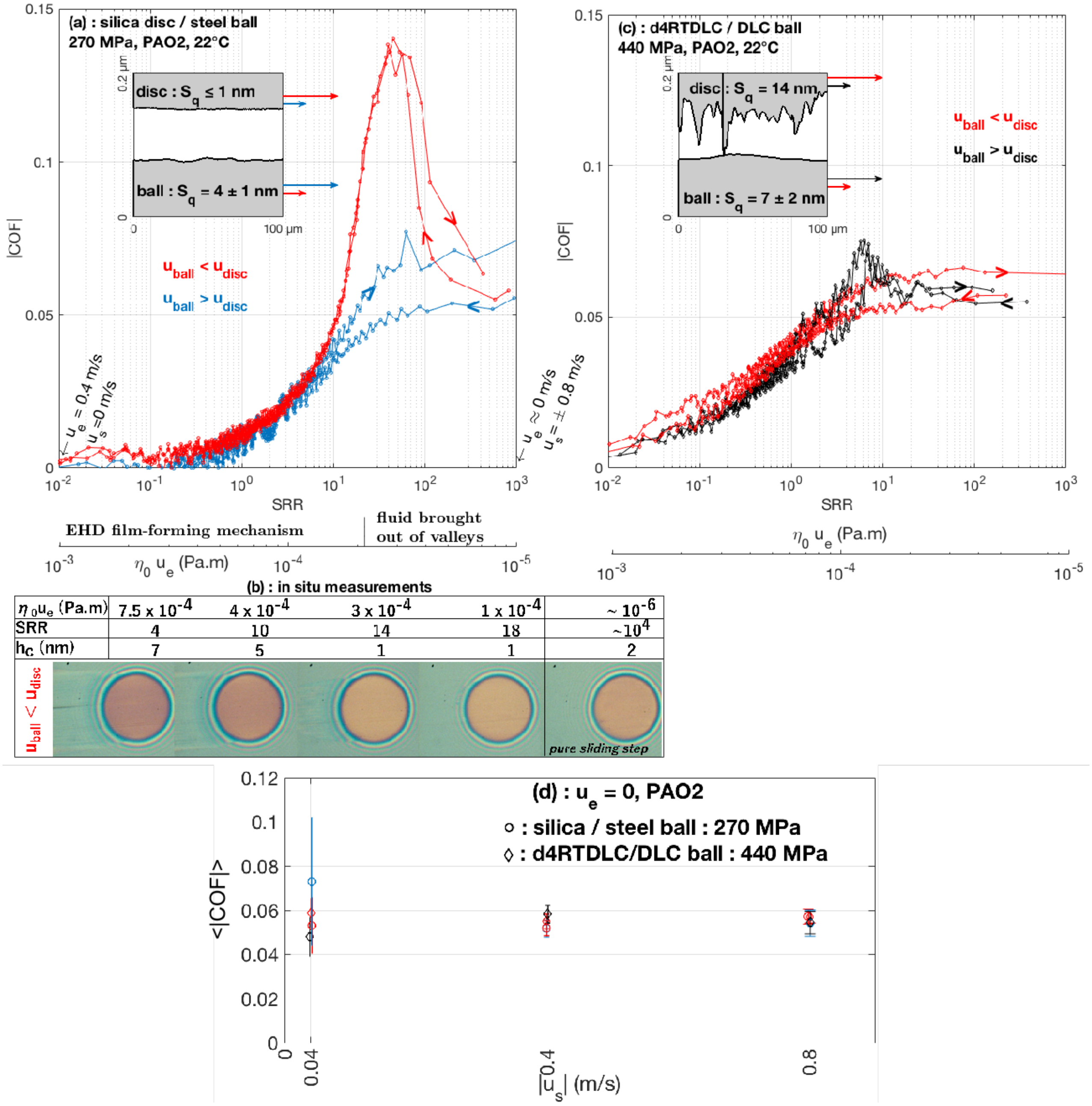

$\eta_0 u_e$ (Pa.m)	7.5×10^{-4}	4×10^{-4}	3×10^{-4}	1×10^{-4}	~ 10^{-6}
SRR	4	10	14	18	~10^4
h_c (nm)	7	5	1	1	2
$u_{ball} < u_{disc}$					

Figure 7.11: Friction evolution using speed ramps from pure sliding ($SRR = \pm\infty$) to pure rolling ($SRR = 0$) with (a) silica against steel and (c) DLC coated surfaces. (d) Friction coefficient averaged during speed steps at different sliding speeds where the entrainment speed is imposed to zero. (b) : In situ interferograms in the silica/steel contact showing the film thickness distribution and the central film thickness measured experimentally.

7.4 Mixed and boundary friction with rough steel surfaces

In the previous section, it was first shown that the mixed friction with smooth contacts must induce a contribution from solid contacts between the solids for the present moderate sliding-rolling ratios ($SRR \leq 1$).

Figure 7.12.a displays the Stribeck tests with rougher steel discs rubbed against polished balls (either made of steel or coated with DLC). From left to right, the surface roughness increases. On figures 7.12.b, 7.12.c, the maximum boundary friction coefficient is plotted versus the summit standard deviation and their curvature, measured using $dx = 0.099$ μm. Two trends arise from these graphs. When the surfaces are rough enough ($S_{qc} > 0.03$ μm), the contacts reach the boundary regime, with boundary friction coefficients between 0.09 and 0.14. For these contacts, the larger the height deviations, the higher the friction coefficient. These friction coefficients being higher than the fluid shear strength ($\tau_{max} \sim 0.05 \times p_m$), solid contacts might occur between the solids. After the tests, a rubbing track on the steel disc can be distinguished from the eye, certainly because of worn — or plastically deformed — asperities that change the surface reflectivity. However, this wear is too small to be quantified on a topographical survey because it is impossible to distinguish the asperities that were modified from those that remained unchanged. The boundary friction mechanism seems to be firstly related to the amount of wear and plastic contacts between asperities, as it is shown fig 7.12.c with the trend followed by colored points : the sharper the asperity tip, the higher the boundary friction.

The grey Stribeck curves of fig. 7.12.a correspond to smoother steel/steel and steel/DLC contacts (*dAP*, *d1RTdeccl*, *d2Tdecdou* : $S_{qc} \leq 0.025$ μm). The maximum friction coefficient with these contacts is generally higher than with rough contacts, even though they have lower summit heights and blunt asperities, which lowers the probability of plastic indentations. However, as it is illustrated with the profiles of fig. 7.12.d, when dry contacts occur between two surfaces, polished surfaces yield wider dry contact areas than with surfaces populated with sharp asperities. Alike the contacts with nanometrically smooth transparent discs against polished balls of fig. 7.11.a, when the entrainment product becomes too low to separate the surfaces by hydrodynamic action, the lubricant available in the contact is spread over the Hertz area. Then, the surfaces conform over wide solid contact areas, raising generally friction coefficients superior to 0.1 and possible adhesive contact spots.

7.5 Modelling Stribeck curves

To sum up, EHL friction may be calculated using the rheological formulas obtained section 4.1 (eq. (4.41)). The friction in the BL regime follows a Coulomb friction law, whether the underlying mechanism be the plastic shearing of a boundary fluid layer (DLC/DLC contacts), or an equilibrium between dry contacts and viscous shearing (steel/DLC, steel/steel).

To conclude this chapter, the mixed bearing model developped by Johnson et al. (72) was used to calculate Stribeck curves a priori. The topographical inputs of this model are : the number of asperities per unit surface (n_a), their curvature radius (β), their standard height deviation (σ_a) and the composite RMS roughness (σ_c).

The load borne by the asperities and the area they cover, in the Greenwood-Williamson model, are recalled here :

$$F_{n\,a} = \frac{2}{3} E' A_{nom} \times (n_a\, \beta\, \sigma_a) \sqrt{\frac{\sigma_a}{\beta}} \boldsymbol{F_{3/2}} \left(\frac{d_e}{\sigma_a}\right) \tag{7.5}$$

$$A_a = A_{nom} \times \pi\, (n_a\, \beta\, \sigma_a) \boldsymbol{F_1} \left(\frac{d_e}{\sigma_a}\right) \tag{7.6}$$

$$\tag{7.7}$$

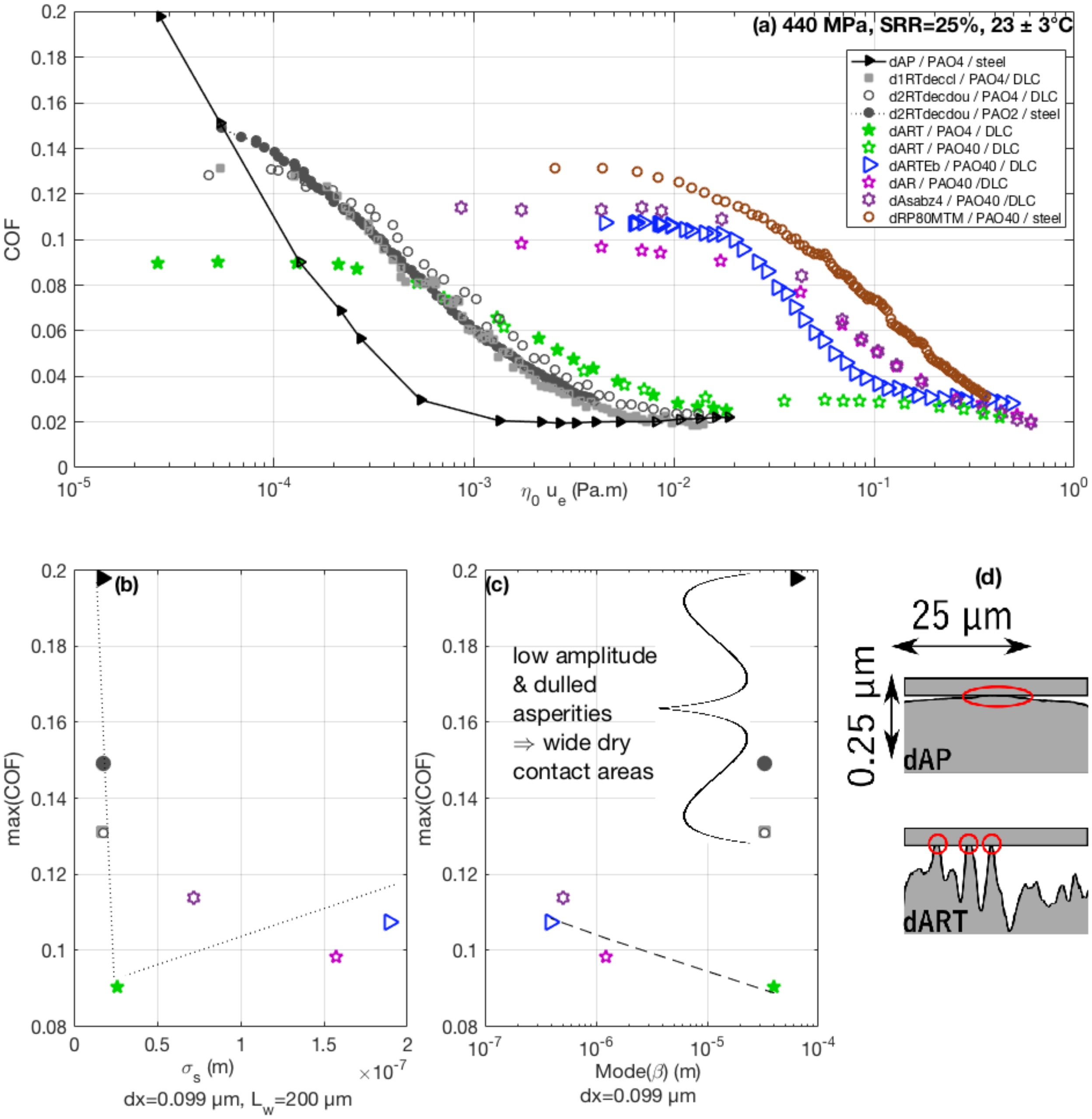

Figure 7.12: (a) Stribeck curves with steel/steel and steel/DLC contacts for various roughnesses. Maximum friction coefficient versus the summit standard deviation (b) and versus the summit curvature (c) measured using $dx = 0.099$ μm. (d) : Surface profiles showing that high and sharp asperities prevent large dry contact areas.

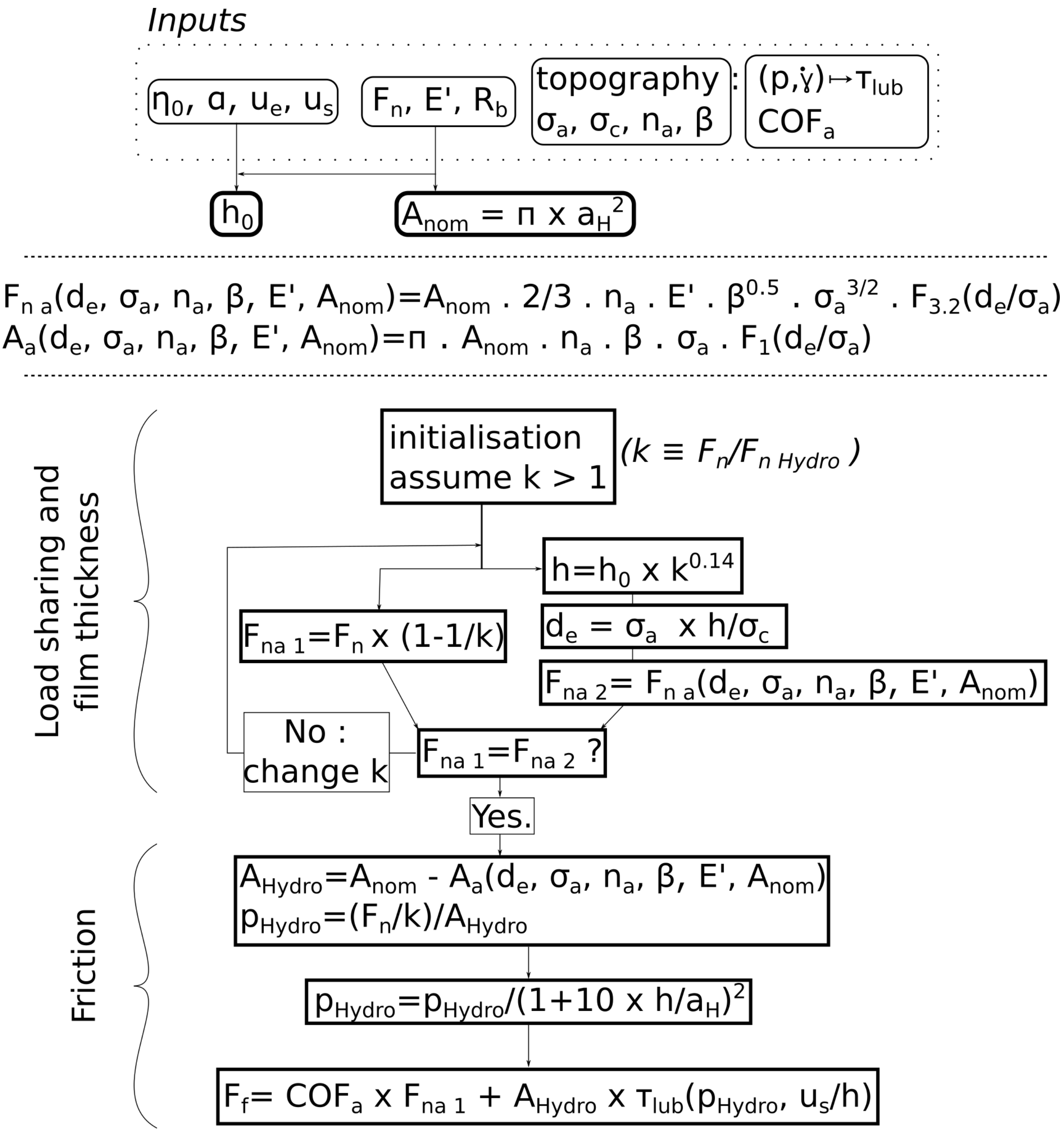

Figure 7.13: Numerical procedure used to calculate Stribeck curves with rough surfaces.

where $\boldsymbol{F_p}$ is defined as :

$$\boldsymbol{F_p}(x) \equiv \int_x^\infty du\,(u-x)^p \frac{e^{-\frac{1}{2}u^2}}{\sqrt{2\pi}} \tag{7.8}$$

The numerical procedure is summarized fig. 7.13. For each set of experimental parameters, a classical Newton scheme is used to calculate the ratio between the input load and the load borne by the fluid : $k \equiv \frac{F_n}{F_{n\ Hydro}}$. On the one hand, the load balance imposes that the sum of the hydrodynamic load and the asperity load be equal to the input load F_n. On the other hand, the asperity load is calculated within the Greenwood-Williamson rough contact modelling. The film thickness is given by the Hamrock-Dowson formula with the replacements $E' \rightarrow E'/k$ and $F_n \rightarrow F_n/k$ (see section 2.3.3) :

$$h \equiv h_c(\eta_0, \alpha, R_b, u_e, E'/k, F_n/k) = h_c(\eta_0, \alpha, R_b, u_e, E', F_n) \times k^{0.14} = h_0 \times k^{0.14} \tag{7.9}$$

Then, the input separation d_e, present in equations (7.5) and (7.6), is calculated using the aproximation proposed by (72) :

$$\frac{d_e}{\sigma_a} = \frac{h}{\sigma_c} \tag{7.10}$$

This allows to calculate a second expression for the asperity load with eq. (7.5). A classical Newton procedure is used to find the value of k allowing to equate these two calculated asperity load within 10^{-12} N. Then, the area borne by the fluid is imposed to conserve the total contact area equal to the nominal Hertz area, which allows to calculate the fluid pressure. Finally, the fluid pressure is multiplied by $\frac{1}{\left(1+10\times\frac{h}{a_H}\right)^2}$ to account for the EHD pressure field widening that becomes significant at large film thicknesses (see section 4.3.2.2). The total friction force is finally calculated assuming a Coulomb friction law for the asperities, combined with the PAO4 and PAO40 rheological equations obtained chapter 4.1 for the friction arising from the hydrodynamic loading.

The product $n_a \times \beta \times \sigma_a$ is often assumed equal to 0.05 (72), (51), (85). According to our topographical measurements, $n_s \times Mode(\beta) \times \sigma_s$ is generally around 0.09 (±12%) or 0.2 (±83%) using respectively sampling intervals equal to 3.653 and 0.099 μm. The ratio $\sqrt{\frac{\sigma_s}{\beta}}$ is generally of the order a few 10^{-3} using $dx = 3.653$ μm, and between 10 and 60 times higher using a sampling interval of $dx = 0.099$ μm. As a consequence, the asperity load (eq. (7.5)), calculated with topographical parameters measured with $dx = 3.653$ μm, take values between 20 and 600 times lower than with the smaller sampling interval, and do not allow to increase the asperity load $F_{n\,a}$ enough to reproduce a higher friction at low entrainment products. Because of undersampling, the summit properties measured using $dx = 3.653$ μm represent fake asperities and it seems that using a sampling interval of 0.099 μm is sufficient to observe true asperities.

Figure 7.14.a shows the calculated Stribeck along with the Coulomb and viscous friction contribution. When the lambda ratio becomes close to 1, the asperities start bearing a fraction of the total load (see fig. 7.14.b and 7.14.c). At decreasing lambda ratios, the film thickness h almost stops decreasing with decreasing $\eta_0 u_e$ because the lower lubricant flow is compensated by a lower load to be withstood by the fluid.

With smooth surfaces ($S_{qc} \leq 0.3$ μm) the error can be large compared to the experimental points, as it is exemplified fig. 7.15.a for the dAP disc. For this Stribeck test, an asperity friction coefficient of 0.22 was taken since this value was reported in the literature for steel/steel contacts in the BL regime with base oil (128). Instead of using the experimentally measured parameters ($\sigma_a = \sigma_s$, $\sigma_c = S_{q\,c}$),

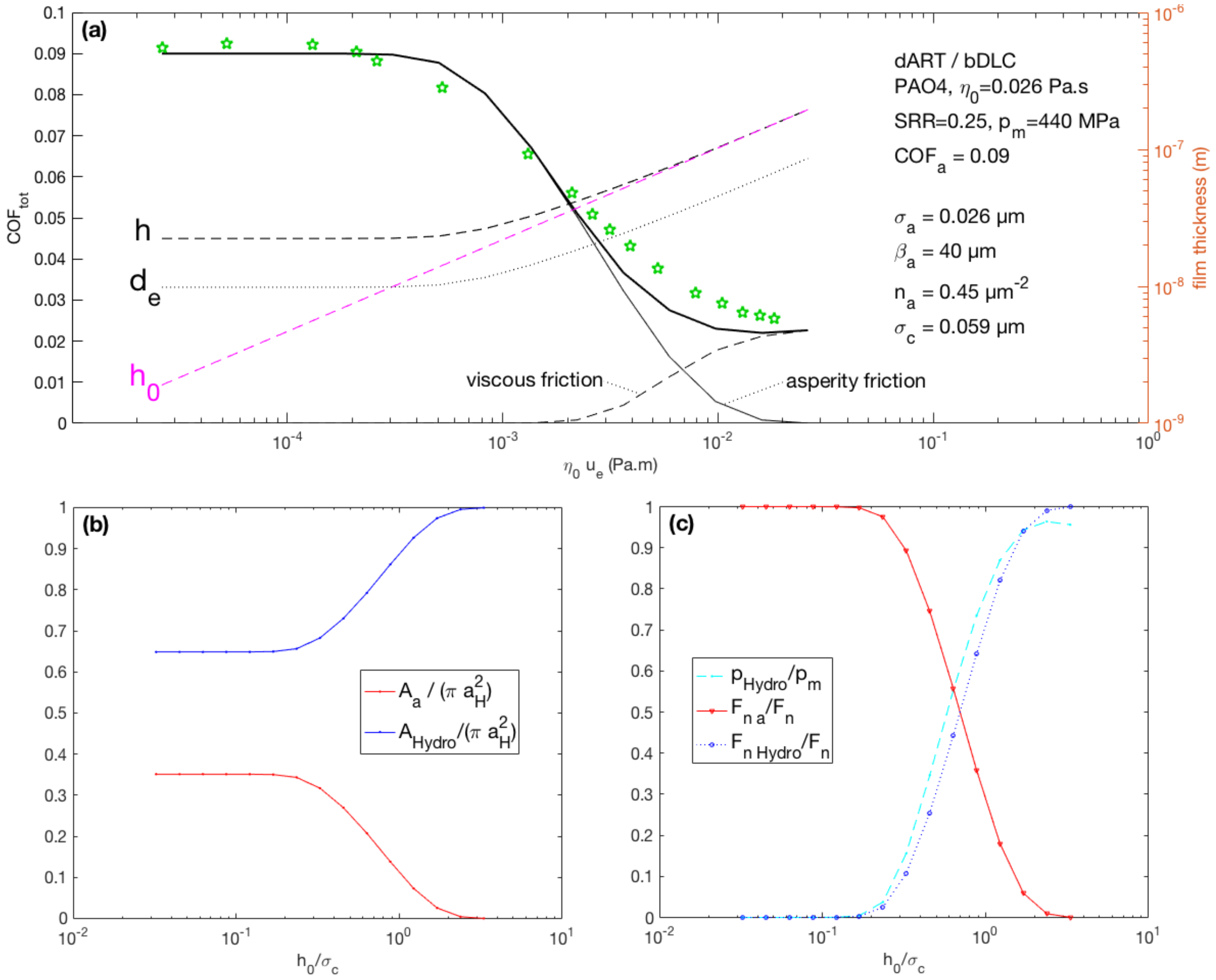

Figure 7.14: (a) : Left axis : calculated Stribeck curve using topographical parameters measured with a sampling interval $dx = 0.099\ \mu$m for a finished steel against a DLC coated ball in PAO4. Right axis : Nominal film thickness h_0, calculated film thickness $h = h_0 \times \left(\frac{F_n}{F_{n\ Hydro}}\right)^{0.14}$ and separation between the smooth surface and the asperity mean plane d_e within the frame of the Greenwood-Williamson model. (b) Fraction of the nominal area borne by the fluid (A_{Hydro}) and by the asperities A_a versus the lambda ratio. (c) : Fraction of the total load borne by the fluid ($F_{n\ Hydro}$) and by the asperities ($F_{n\ a}$) versus the lambda ratio. The ratio of the fluid pressure to the nominal Hertz pressure is plotted in dashed cyan dashed line.

the experimental evolution of friction is better captured by adjusting the parameters σ_a and σ_c (see fig. 7.15.b) towards lower values. An important step of this model is the constitutive equation that relates the film thickness h and the distance d_e between the smooth surface and the mean asperity height within the Greenwood-Williamson modelling. Figure 9.17 shows the evolution of $\frac{d_e}{\sigma_a}$ with $\frac{h}{\sigma_c}$ considering the approximate (eq. (9.21)) and exact (eq. (9.21)) relationships proposed by (72). Surprisingly, the exact relationship yielded a less accurate prediction of the experimental data than the approximate one (eq. (2.37)). Nevertheless, it is believed that the model could reproduce the experimental evolution of friction for such smooth contacts with a smart modification of the $\frac{d_e}{\sigma_a}$ vs $\frac{h}{\sigma_c}$ relationship.

Other calculated Stribeck curves are shown fig. 7.16.a (steel/DLC contacts) and fig. 7.16.b (DLC/DLC contacts). The agreement with experimental points is better for finished and rectified

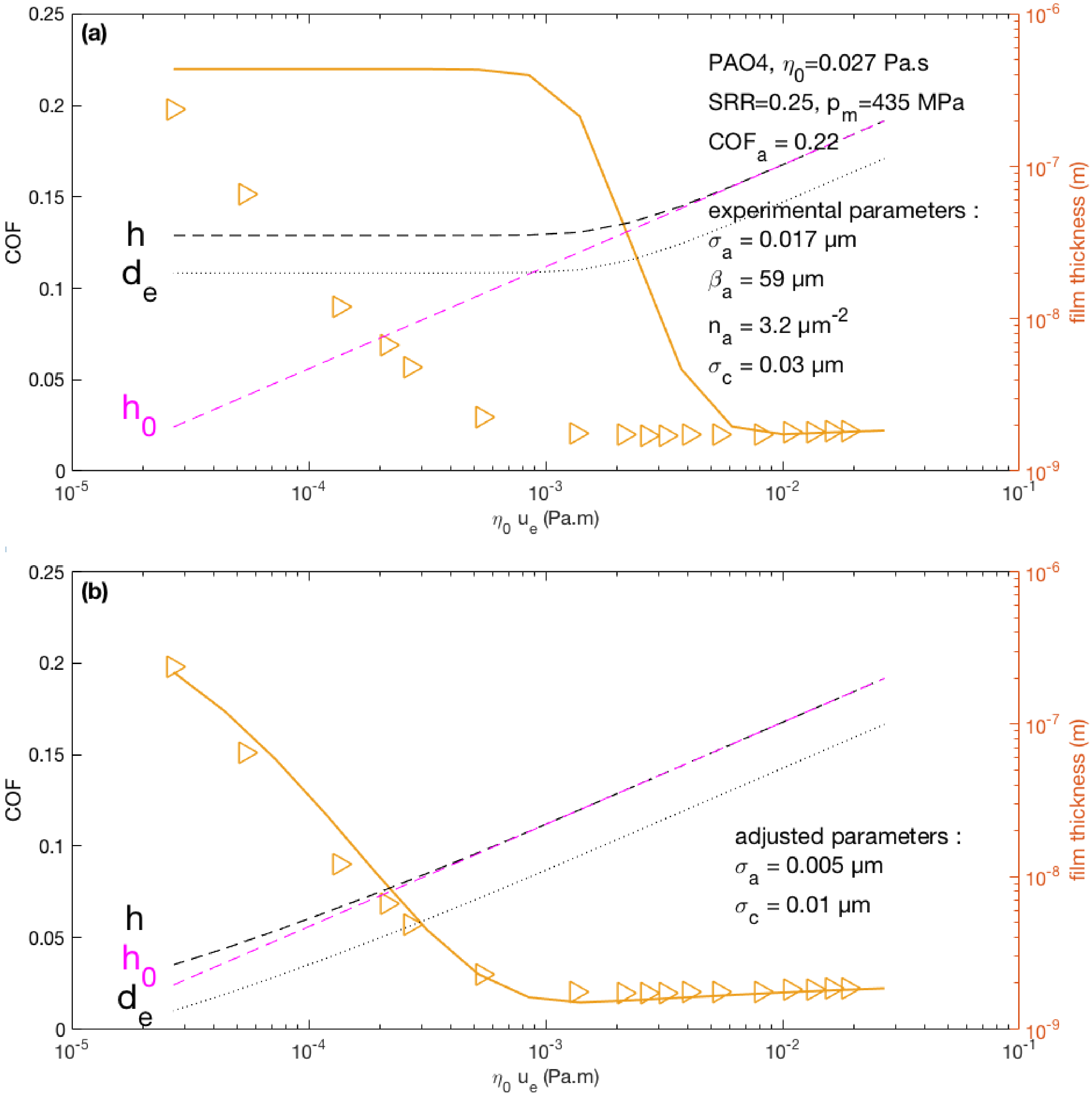

Figure 7.15: Comparison between calculated and experimental Stribeck curve for a polished steel disc (dAP) in PAO4 at $SRR0.25$, $p_m = 440MPa$ using the summit ($\sigma_a = \sigma_s$, $n_a = n_s$, $Mode(\beta)$) and height ($\sigma_c = S_{q\,c}$) parameters measured using $dx = 0.099$ μm (a) and with adjusted parameters σ_c and σ_a (b).

surfaces than for pickled and polished ones, especially from the top part of the mixed regime to the boundary regime. These calculated Stribeck curves allow us to predict the BL-ML transition provided the summits parameters (n_s, β, σ_s), the composite RMS roughness (S_{qc}), the fluid rheology $(p,\ \dot{\gamma}) \mapsto \tau_{lub}(p, \dot{\gamma})$ and the boundary friction coefficient be measured beforehand. The BL-ML transitional entrainment product $\eta_0 u_e^{BL-ML}$ on the calculated Stribeck curves reproduces the experimental transition with an error inferior to 20% for most contacts rougher than $S_{qc} = 0.03\ \mu$m.

In the ML regime close to the ML-EHL transition, friction is generally underestimated for two reasons. The first one is that h is bound to remain superior to the nominal film thickness, whereas in reality, surface roughness lowers the real film thickness, which yields underestimated shear rates. The second one is that in thin-film EHL, rough contacts often induce a partial asperity friction that was not accounted for here.

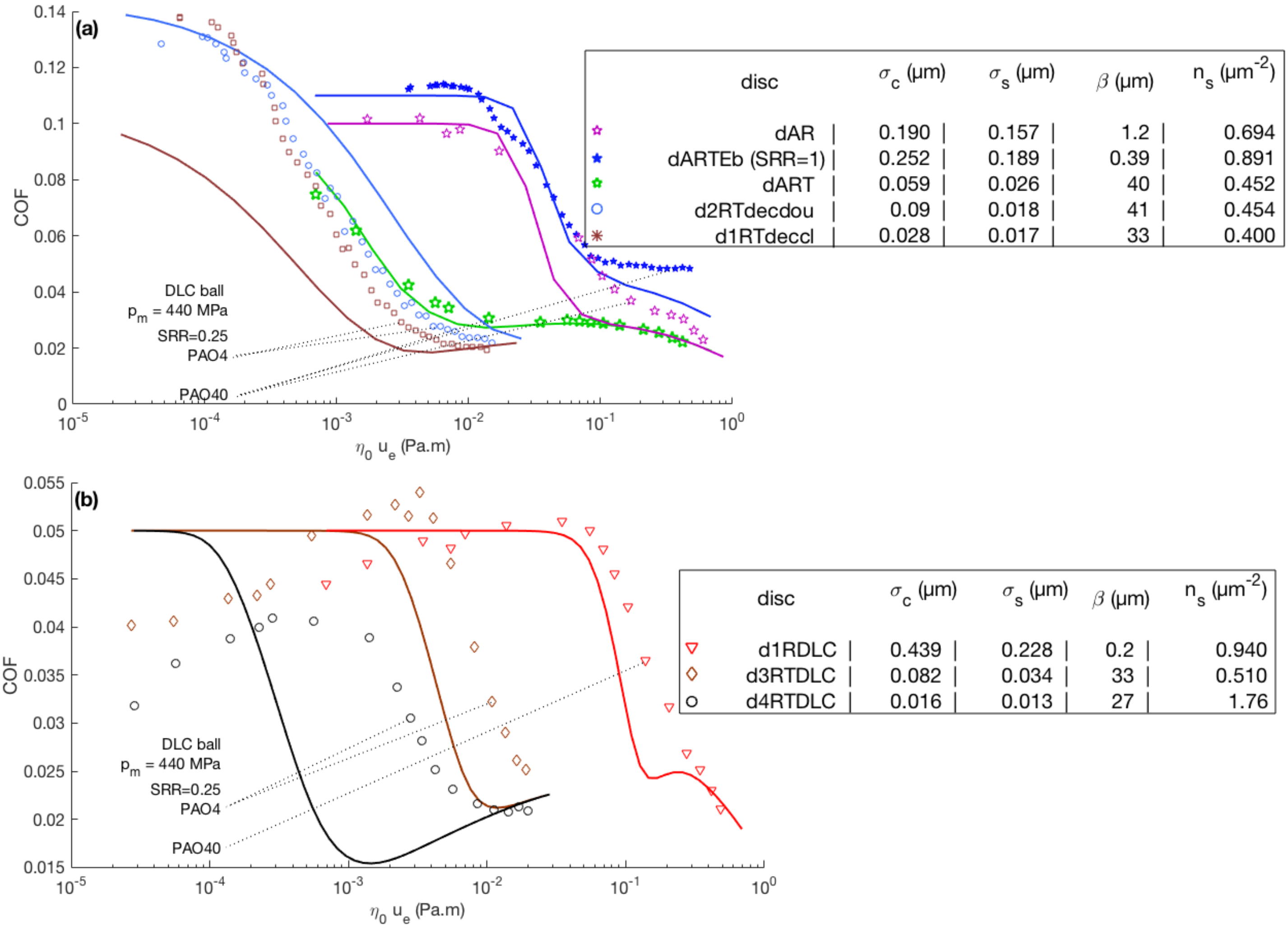

Figure 7.16: Calculated Stribeck curves using topographical parameters measured with a sampling interval of $dx = 0.099\ \mu$m and asperity friction coefficients equal to the friction coefficients measured in the boundary regime for each set of Stribeck test.

7.6 Conclusion

Using the mixed bearing model developped by (72) allows to understand the onset of BL. From ML to BL, the entrainment product has a decreasing influence on the film thickness because part of the load becomes borne by the asperities, whether by direct contact or by the shearing of base oil confined between the asperities. This causes the existence of minimum surface separation and hence, of a maximum asperity load at zero entrainment product. Thankfully, the friction between solids and the shearing of a nanometric layer both follow Coulomb laws, which explains why the Coulomb behaviour of boundary friction is always observed irrespective of the true underlying mechanism.

The boundary and mixed friction with DLC/DLC contacts seems to be mostly attributable to the lubricant. The wear with these contacts is very low and their boundary friction increases with the sliding speed, with is compatible with a viscous shearing of lubricant between the surfaces, with a friction coefficient close to 0.05. Yet, this friction increase is rather small because most of the pressurized lubricant between the surfaces has a thickness between a few Angstroms and 2 nm, which shifts the lubricant towards its plastic regime over most of the contact area.

Using very smooth contacts can be detrimental in the ML regime because wide solid-solid contact spots may exist. At low entrainment product the lubricant feeding mechanism becomes governed by the presence of valleys on at least one of the two bodies. However, it is required that this body moves fast to provide enough lubricant to avoid dry contacts on large spots. Thus, large sliding-rolling ratios may have a beneficial effect on friction if the roughest body is the fastest.

Finished and rougher surfaces are sufficiently populated in valleys to prevent wide dry contact spots. They are also more populated in sharp asperities than polished surfaces, and their friction in the ML regime contains a large contribution from the plastic deformations of protruding asperities. For this range of surfaces, the rougher the surfaces, the more important is the wear. The friction coefficient may thus vary between 0.09 for curvature radii around 30-50 μm and 0.14 for curvature radii close to 1 μm. This remains well inferior to the maximum friction coefficient obtained with polished steel/steel contacts, which may reach 0.22, certainly because of adhesion between the surfaces.

Regarding surface topography, the asperity properties have a crucial influence on the pressure increases. Defining the asperities as summits, i.e. three-dimensional local maximas on a survey, the asperity properties are drastically different between low ($\sim 0.1\ \mu m$) and large ($\sim 4\ \mu m$) sampling intervals because of undersampling. Even though the asperity curvature radius should increase, and groups of asperities could merge into a single rounder one as the surface separation is lowered, the Greenwood-Williamson contact modelling yields a realistic asperity load versus entrainment product considering the summit properties extracted from ex-situ topographical surveys with a sampling interval of 0.099 μm.

Chapter 8

Conclusions

8.1 Summary

8.1.1 Friction in lubricated contacts

The Stribeck curve was used as an experimental tool allowing to study contacts with various roughnesses in the three lubrication regimes that are EHL, ML and BL. The EHL friction level is primarily determined by the fluid rheology. It is generally not sufficient to know the fluid low-shear viscosity because in EHL, most fluids are sheared beyond their Newtonian regime and become shear thinning.

The rheology was measured on two fluids (PAO4 and PAO40) using traction tests in thin-film EHL ($h_c \leq 0.2$ μm) to ensure isothermal conditions, homogeneous shear rates, and a pressure distribution close to the dry Hertz pressure distribution. The evolution of the contact mean shear stress with the shear rates was fitted according to a pressure and temperature dependent Eyring law. These rheograms permitted the quantitative prediction of the friction force in fully lubricated conditions for various loads, surface speeds and operating temperatures.

When the film thickness gets higher than about 0.2 μm, the shear stress becomes easily overestimated by these predictions and even decreases with the entrainment product. At large entrainment products, in a Stribeck procedure, the film thickness and the shear rates are high:since both these factors increase the energy dissipation, the friction decrease has often been attributed to shear heating that lowers the fuid viscosity (76). However, using the flash temperature theory and the lubricant temperature rise formulas provided by (24) does not allow to explain quantitatively the observed friction drop. It has thus been explained by the pressure field that widens towards the inlet and diverges from the Hertz pressure profile at large surface separations. Using a self-consistent approach, a thickness-dependent corrective factor was derived to lower the input pressure used in a viscous shear stress prediction and this allowed to reproduce perfectly the experimental friction with thick films.

Below a certain entrainment product, the counter surface asperities interact and cause a higher friction than in EHL, which defines the onset of ML. The ML-EHL transition was defined as the entrainment product $\eta_0 u_e^{ML-EHL}$ corresponding to the intersection between the viscous stress prediction and the experimental friction. This friction-based ML-EHL transition criterion has proved especially useful for surfaces rougher than 0.1 μm:for these surfaces, the mixed regime, thin-film and thick-film EHD regimes are not delimited with slope ruptures on a Stribeck curve, which is the classical methodology to detect the ML-EHL transition. Beyond these specific differences, both criteria yield the same conclusions:the ML-EHL transition occurs at a nominal film thickness, characteristic of the composite roughness and constant towards the contact pressure and the sliding introduced between the surfaces, as long as inlet thinning and heating remain negligible. The lambda ratio, evaluated at the ML-EHL transition is roughly equal to 5.5. Considering more precisely the data, this lambda ratio takes higher values for smooth contacts than for rough ones, and decreases with the composite roughness as $\frac{h_c^{ML-EHL}}{S_{qc}} \approx 0.26 \times S_{qc}^{-0.2}$. Equivalently, the ML-EHL transitional entrainment product increases with the RMS roughness as $\eta_0 u_e^{ML-EHL} = 28.5 \times 10^6 \times S_{qc}^{1.2}$.

The transition from ML to BL was similarly studied versus the roughness, and the entrainment product was also used to characterize the onset of the BL regime for each couple of surfaces. Using the mixed bearing model of (72), the balance between the load borne by asperities and that borne by hydrodynamic action leads to the existence of a minimum surface separation that depends on the surface RMS roughness, summit density, summit curvature radius and summit RMS height deviations. The onset of BL occurs when this minimum surface separation is reached. Contrary to the ML-EHL transition, $\eta_0 u_e^{BL-ML}$ does not follow the same trend with respect to roughness between different materials. DLC-DLC contacts generally enter in BL at a larger entrainment product than contacts with at least one steel body :

- For DLC/DLC contacts, the strong material hardness allows a negligible contribution from wear in all lubrication regimes, such that the boundary friction is independent of the surface features. In the ML regime, decreasing $\eta_0 u_e$ increases the amount of local pressure rise between the asperities, until the minimum surface separation is reached. The present work allows to predict the transitional entrainment product with eq. (6.18). All DLC-DLC contacts rub with a boundary shear stress close to the fluid strength (at the operating mean pressure), which is the most striking argument leaning towards a friction mechanism due to the shearing of a nanometric fluid layer between the surfaces. Even though the EHD film forming capability becomes zero at the BL-ML transition, the contact becomes supplied in lubricant by the surface valleys that play the role of reservoirs.

- For contacts with one or two steel bodies, the BL-ML transitional entrainment product follows a power law for roughnesses inferior to $S_{qc\,0} \approx 0.1\mu$m and the experiments performed with the roughest surfaces show that the BL-ML transition seems to saturate around an entraiment product close to 0.02 Pa.m. These two features were summarized into eq. (6.17). Regarding the value of the boundary friction coefficient, two trends arise according to the surface roughness.

  Surfaces with a RMS roughness superior to $S_{qc} = 0.025$ μm have a boundary friction coefficient that increases with the surface roughness from 0.09 to 0.14. The higher friction coefficient obtained for rougher contacts is due to their asperities being generally higher, sharper and more numerous than for low S_{qc}. The boundary shear stress being higher than the fluid strength, it is expected that most of the asperity contacts do not remain protected by a fluid layer. The rubbing tracks indeed exhibited traces of wear that confirmed the occurrence of solid-solid contact.

  For surfaces smoother than 0.025 μm, the boundary friction coefficient increases with decreasing S_{qc}. The wide smooth areas permit the existence of wide solid contact spots. These surfaces have blunter asperities, which reduces the probability of plastic indentations and hence, of wear, but also have shallow valleys that limit the efficiency of valley feeding mechanism, necessary to prevent wide dry contacts at low entrainment products, in the ML regime.

With the present study of the transitions between lubrication regimes, summarized fig. 8.1.a, the single knownledge of the RMS roughness is sufficient to predict these transitions in terms of entrainment product. Furthermore, if the boundary and EHL friction levels are known a priori, the evolution of the Stribeck curve in the ML regime can be roughly approximated using the tanh expression of eq. (6.11), first introduced by (44), as shown fig. 8.2. The mixed-bearing model of (72), combined with the fluid rheology and an asperity friction coefficient (see fig. 7.13) allows better quantitative friction predictions, especially in the mixed and boundary lubrication regimes.

In addition to the friction levels, this model requires the measurement of the summit density n_s, curvature radius β, RMS deviation σ_s and the composite RMS height deviation S_{qc}. The dependence of these parameters with the cut-off length, the sampling interval and their non stationarity required a metrological study of surface roughness.

8.1.2 Surface roughness

Real surfaces, shaped with a machining process, are multiscale in that they contain patterns of various dimensions in the $x - y$ plane. The RMS roughness S_q is very variable from an area to another and its relative dispersion $\frac{std(S_q)}{<S_q>}$ decreases linearly with the logarithm of the cut-off length. For the purpose of correlating the RMS roughness to friction experiments, the scales larger than the Hertz length were removed from the contact because of the surface elastic flattening. This the cut-off lengths under interest lied in the range $L_w = 2\ a_H \in [100\ ;\ 350]\ \mu$m. Yet, the variability of S_q for this range of scales remained betwen 20% and 50%. This variability can be due to outliers as well as true height deviations. To get around it, the most frequent value of S_q was used to characterize surface roughness, on the basis of surveys large enough (1 cm^2) to cover all their features. Other surface parameters such as the autocorrelation length or the summit curvature radius revealed also highly variable from an area to another, and this procedure helped capturing stationary surface parameters.

Because of undersampling, the RMS roughness may be underestimated if the sampling interval is not inferior to the surface smallest patterns. Using a small sampling interval implies a small error due to undersampling. However, a small sampling interval generally implies a small probing area because the number of bins contained in the survey becomes rapidly too large to be processed with a common PC. Beyond the computer memory performance, such measurements are often difficult to perform because of other technical problems such as thermal drift (in particular for lengthy AFM and profilometric measurements) or the geometry of the measurement apparatus.

Given the non stationarity of surfaces, it is recommended to rely first on least magnified surveys to evaluate height parameters such as S_q or S_a because of the wider area (in m^2) covered with the current technological restraints of topographical apparatuses. High-resolution surveys allow to identify sharper patterns and are less likely to be perturbated by undersampling, which makes them more suited to the hybrid parameters (S_{al}, summit properties, slopes, ...) evaluation. The recommended procedure to measure height deviation paramaters (RMS roughness, centre line average roughness, ...) and hybrid parameters (curvature, slopes, ...) is schematized figure 8.3.

A major reason why the simple planar detrending operation was used instead of a Fourier high-pass filter is that generally, these filters affect the shape of surface patterns like summits. Nevertheless, for height deviation parameters, the Gaussian filter gave approximately the same response as the planar detrending for most of the surfaces presently used.

8.2 Prospects

- If the Hertz pressure field is a good approximation in thin-film conditions, this approximation becomes dubious when the surface separation becomes greater than, say, a tenth of the Hertz radius. Regarding the pressure correction proposed in paragraph 4.3.2.2 (eq. (4.42)), it would be interesting to conduct a numerical study of EHD pressure profiles solving the Reynolds equation for surface separations superior in the range $0.1\ -\ 10\ \mu$m. Though this was already done by many people, these results are only shown graphically in the literature. The lack of ready-to-use analytical formulas for those pressure fields has led the majority of experimental works to use the Hertz analogy. With analytical expressions of these pressure fields, it would

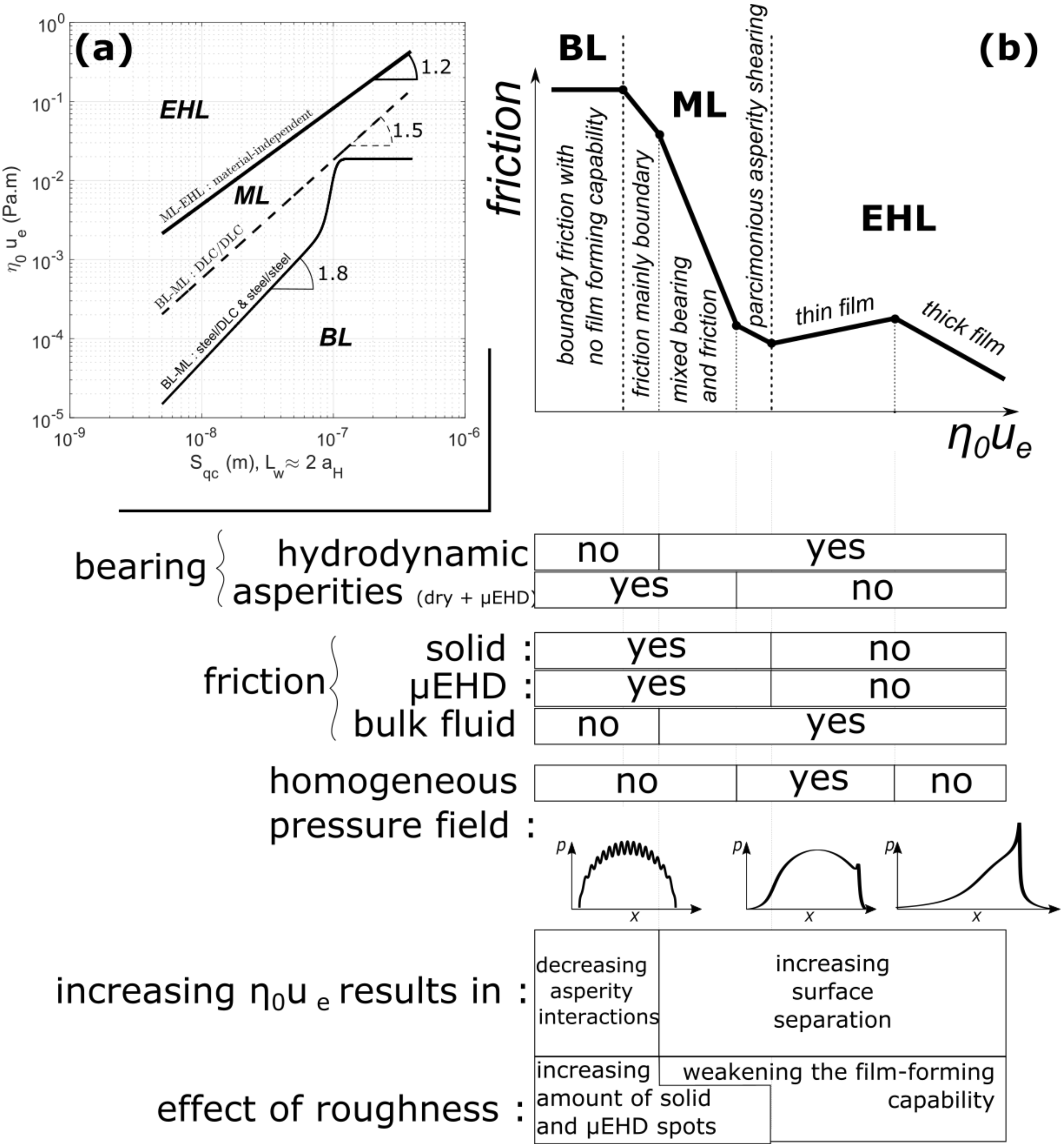

Figure 8.1: (a) Transitions between the lubrication regimes versus the contact composite roughness. (b) Schematic of a Stribeck curve with the events occurring in each lubrication regime.

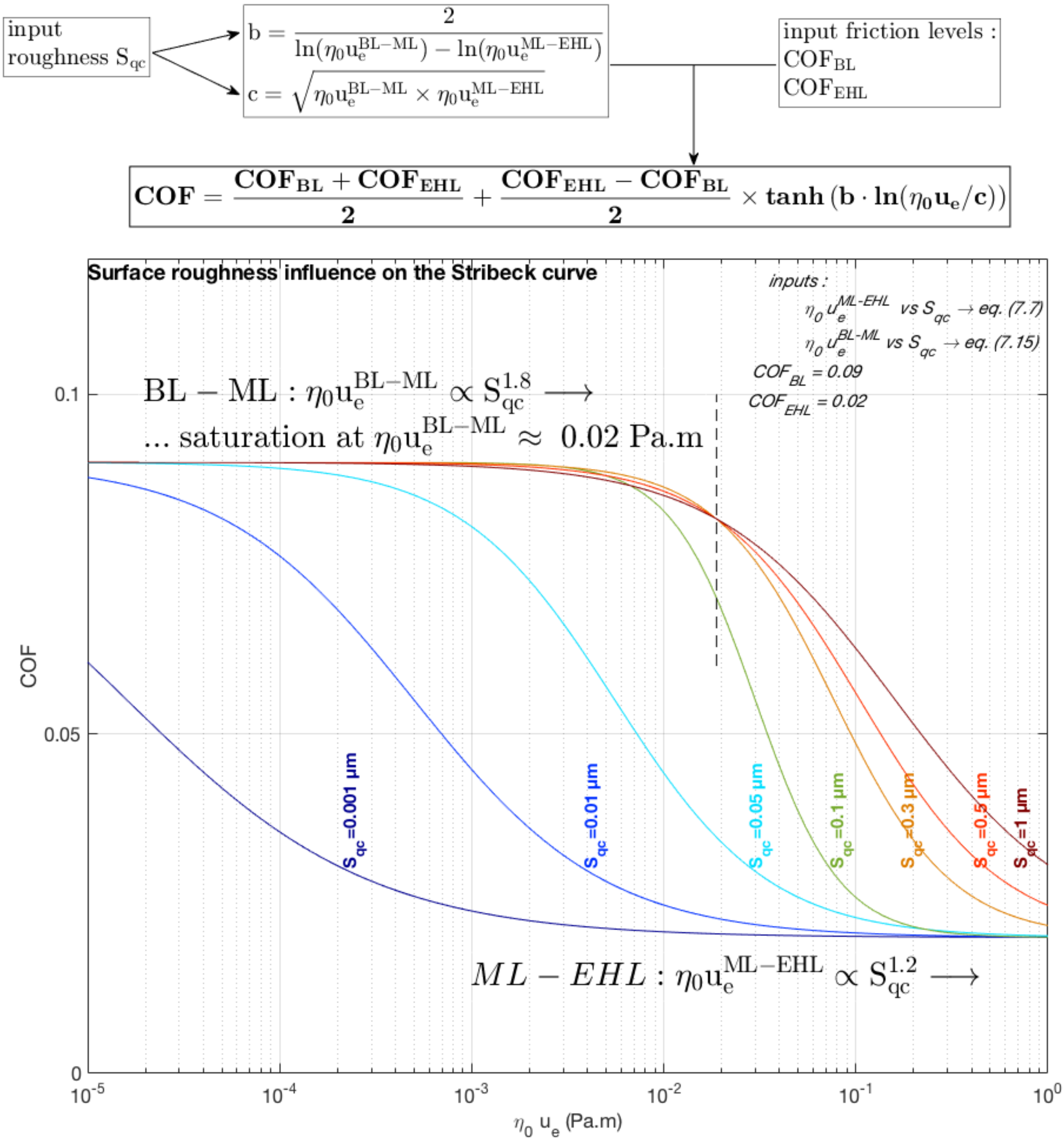
input roughness S_{qc}
$b = \frac{2}{\ln(\eta_0 u_e^{BL-ML}) - \ln(\eta_0 u_e^{ML-EHL})}$
$c = \sqrt{\eta_0 u_e^{BL-ML} \times \eta_0 u_e^{ML-EHL}}$
input friction levels : COF_{BL} COF_{EHL}
$\mathbf{COF = \frac{COF_{BL} + COF_{EHL}}{2} + \frac{COF_{EHL} - COF_{BL}}{2} \times tanh\,(b \cdot ln(\eta_0 u_e / c))}$
Surface roughness influence on the Stribeck curve
inputs :
$\eta_0 u_e^{ML\text{-}EHL}$ vs $S_{qc} \rightarrow$ eq. (7.7)
$\eta_0 u_e^{BL\text{-}ML}$ vs $S_{qc} \rightarrow$ eq. (7.15)
$COF_{BL} = 0.09$
$COF_{EHL} = 0.02$
$\mathrm{BL - ML} : \eta_0 u_e^{BL-ML} \propto S_{qc}^{1.8} \longrightarrow$
... saturation at $\eta_0 u_e^{BL-ML} \approx$ 0.02 Pa.m
$ML - EHL : \eta_0 u_e^{ML-EHL} \propto S_{qc}^{1.2} \longrightarrow$
S_{qc}=0.001 µm
S_{qc}=0.01 µm
S_{qc}=0.05 µm
S_{qc}=0.1 µm
S_{qc}=0.3 µm
S_{qc}=0.5 µm
S_{qc}=1 µm
COF
0.1
0.05
0
10^{-5}
10^{-4}
10^{-3}
10^{-2}
10^{-1}
10^{0}
η_0 u_e (Pa.m)

Figure 8.2

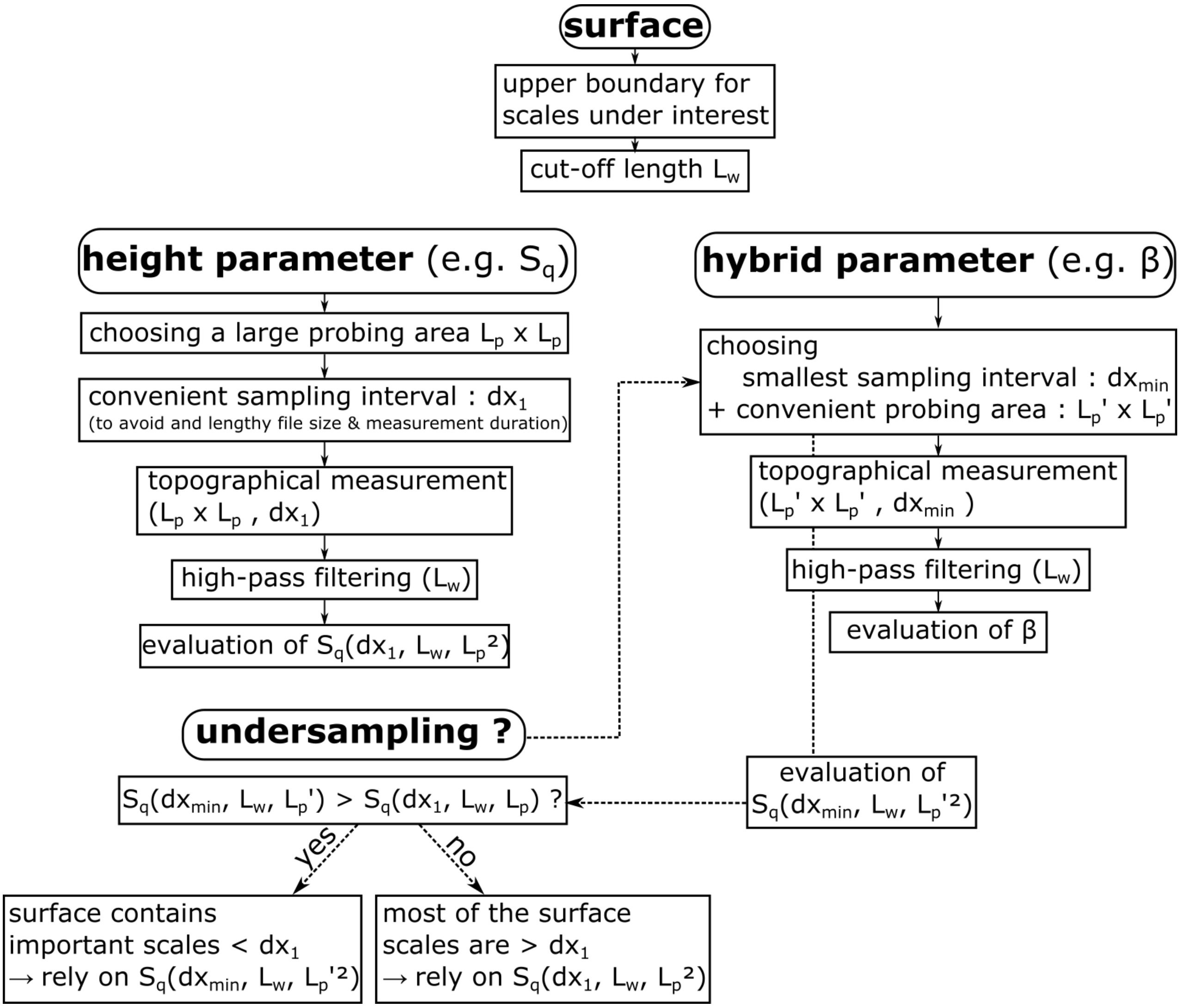

Figure 8.3: Recommended experimental procedure to measure a surface height parameters (S_a, S_q, σ_s, ...), hybrid ones (β, n_s, S_{dq}, ...) and to evaluate whether the sampling interval is suited to the surface regarding the problem of undersampling.

become easy to integrate rheological models in the real contact area and to obtain quantitative predictions of the friction force, even at large surface separations.

- The mixed load bearing model of (72) predicts that roughness generates thicker films than in smooth contacts because part of the load is borne by the asperities. If this is suited to mixed lubrication, it misses the fact that in EHL, roughness lowers the real film thickness compared to the smooth case. Without a realistic film thickness weakening prediction, the only ready-to-use formulas are those obtained in ideally smooth contacts, and the description of rough surface lubrication will always be bound to use indirect approaches based on the smooth EHD theory. Interferometry seems to be the most direct way to measure film thicknesses in situ. This method requires that one of the two bodies be transparent and coated with a semi reflective layer, which is generally easily destructed at the first contacts against a non polished surface. Nevertheless, some authors (118) obtained promising results that should motivate for further experimental studies of film thicknesses with rough contacts.

- Most of the present surfaces were machined with real-life industrial processes and contain a continuous spectrum of scales such that the contributions of different scales on the film thickness cannot be considered separately. Different cheap techniques already exist to generate a random texture (sandblasting, shot blasting, ...). Starting with highly smooth surfaces, these techniques permit to obtain random surfaces with a narrow range of scales governed by the grain size. The measurement of the film thickness in EHD contacts with such surfaces would permit to measure the lower boundary for the scales able to affect the film thickness and the friction mechanism in mixed and boundary lubrication. Such an information would allow to specify the smallest scales that should be filtered out of a topographical survey with the purposes of predicting a rough contact film-forming capability and of identifying the surface patterns that contribute to friction in the ML and BL regimes.

- No additives were used in the present study whereas the lubricants used in real engines are formulated. It is expected that the present results about the ML-EHL transition hold true even with formulated lubricants because this transition is determined by the surface roughness and the lubricant bulk properties (namely α and η_0) that determine the EHD film-forming capability. However, the BL-ML transition was shown to be related to the friction mechanism induced by the lubricant rheology, the material hardness and the surface features — when the materials strength is too low to prevent wear. With molecules that adsorb chemically onto the surfaces, the friction mechanism in ML and BL will be governed by the rheology of the adsorbed layer and by its ability to prevent wear between the asperities. In tribological tests with formulated lubricants, the equilibrium between wear and chemical adsorption leads to the formation of what is referred to as a tribofilm. The chemical composition of these tribofilms requires ex-situ analyses (SEM, IR spectroscopy, ...), such that it is difficult to tell which surface patterns have first contributed to their formation during the tests. This is why it would be of great interest to perform in-situ observations of their formation with surfaces whose texture is not as multi-scale as the present surfaces.

Chapter 9

Annexes

9.1 Flash temperature theory

9.1.1 Slow source

9.1.1.1 Electrical analogy :

The simplest case is that of a slowly moving — or immobile – body, where steady conduction establish almost instantly as it passes through the heat source (see scheme on fig. 4.5). The heat conduction in the bulk medium is analogous to the Ohm law that governs the electrical current between two surfaces separated with a given resistance and having different electrical potentials. The smallness of the contact area makes the bulk medium act as a constriction for the heat flow inside the body. In the medium of thermal conductivity K_s, the thermal resistance between two concentric hemispheric surfaces (see fig. 4.5.a) of radii r and $r+dr$ is $dR = \frac{dr}{\frac{1}{2}K_s\, 4\pi r^2}$. This infinitesimal resistance must then be integrated between the hemispheres of radii $r = a$ and $r \to \infty$, which gives the total[1] *constriction resistance* between the contact area and the medium. For a circular source of radius a, assuming the contact area isothermal, the temperature difference ΔT between the contact area and the medium is (66) :

$$\Delta T = \frac{q_s\, \pi a}{2K_s} = \frac{Q}{2aK_s} \tag{9.1}$$

9.1.1.2 General flash temperature theory

More generally, the homogeneous heat equation, verified by temperature in each of the bulk media initially at zero temperature, reads :

$$\frac{1}{D_s}\frac{\partial T}{\partial t}(\mathbf{x},t) - \vec{\nabla}\cdot\vec{\nabla}T(\mathbf{x},t) = 0 \tag{9.2}$$

, where D_s is the thermal diffusivity. For an instantaneous volumetric source of heat δq_v located at $\mathbf{x}' = (x', y', z')$ and only active at $t = t'$ (Dirac), the solution of equation (9.2) is (24, p.353) :

$$T(\mathbf{x},t) = \int_0^\infty dt' \int_{-\infty}^\infty d^n x'\; \mathcal{G}_3(\mathbf{x}-\mathbf{x}', t-t')\; \delta q(\mathbf{x}', t') \tag{9.3}$$

$$\text{, where }\; \mathcal{G}_n(\mathbf{x},t) = \frac{1}{\rho_s\, c_s\, (2\sqrt{\pi D_s t})^n} e^{-\frac{\mathbf{x}^2}{4D_s t}} \tag{9.4}$$

---

[1] with the replacement $\pi a \to 2a$ according to (66, p.4)

$\mathcal{G}_n$ is the general Green function, solution of the heat equation (eq. (9.4)) in dimension n (3).

Jaeger (70) calculated analytically and numerically the solutions using the Green's function given eq. (9.4) for lineic ($n = 1$), rectangular and circular ($n = 2$) heating source. These results were extended in particular by (5), Crook, (50), (54). Jaeger considered the transient heat equation (eq. (9.2)) and obtained in particular the solution for a slowly moving circular source of extent πa^2 :

$$\boxed{\Delta T_{flash\ slow} = \frac{q_s\, a}{K} = \frac{Q}{\pi\, a\, K}} \qquad \text{(slow circular source)} \tag{9.5}$$

This results is the same temperature rise formula as that obtained using the constriction resistance concept (eq. (9.1)) up to a $\frac{\pi}{2}$ multiplicative factor.

9.1.2 Fast source

For a fast moving source, the conduction depends on the surface speeds. During a time interval Δt, heat is generated in the fluid at a rate $Q = F_f \cdot u_s$. Hence, during their passage in the contact, the lubricant and the surfaces receive a dissipated energy $Q \cdot \Delta t$. A given point on the surface will meet the contact during a time

$$t_{s\,transit} = 2\, a/U \tag{9.6}$$

With $U \in [10^{-3}\,;\, 1]$ m/s, $t_{s\,transit}$ ranges in $[10^{-4}\,;\, 10^{-1}]$ s. For comparison, over a surface revolution the time spent by the moving surface out of the contact area is hundreds times longer because the contact length is of the order 10^{-4} m while the rubbing tracks are centimetric. The contact can then be visualized as a transient heat source for the moving bodies. Jaeger introduced a Peclet-like number for the moving bodies :

$$J \equiv \frac{a\, U}{D_s} \tag{9.7}$$

, where a, U, and D_s are the contact half-length, the surface speed and thermal diffusivity respectively. Assuming an infinite time elapsed so the transient thermal problem reached a steady state, Jaeger provided the following maximum[1] temperature rise formula for a fast square source of half length a, while solving eq. (9.2) in 2 dimensions :

$$\boxed{\Delta T_{flash\ fast} = 2\sqrt{\frac{2}{\pi}}\, \frac{q_s\, a}{K}\, J^{-1/2}} \qquad \text{(fast square source)} \tag{9.8}$$

The result does not change importantly with a circular source of equal radius (5), (54).

9.1.3 Intermediate surface speeds

According to (70) and (5), the source motion can be considered slow for $J < 0.1$ and the fast source solution (eq. (9.8)) is only valid for $J > 10$ (70), (5), (54). Our conditions ($10^{-2} < J < 10^{0}$) are hence in between the two asymptotical cases, and require the numerical integration of eq. (9.2) for each separate condition that depend on the surface materials, speeds and Q. Alternately, Greenwood (54) proposed a way to interpolate the intermediate cases solved numerically by (70) with the following rule :

---

[1] In the spatial sense.

$$\frac{1}{\Delta T^2_{0.1<J<10}} = \frac{1}{\Delta T^2_{fast}} + \frac{1}{\Delta T^2_{slow}} \tag{9.9}$$

This allows to obtain maximum and average flash temperature rises close to those obtained by Jaeger for $J = [0.1; 10]$. Combining equations (9.5) and (9.8) with the latter rule leads to the following maximum temperature rise formula for a circular source, assuming a source of heat Q homogeneous over the contact area (54) :

$$\boxed{\Delta T_{flash\ max} = \frac{\pi\, a_H\, q_s}{K_s}\frac{0.508}{\sqrt{J+2.546}}} = \frac{Q}{a_H K_s}\frac{0.508}{\sqrt{J+2.546}} \quad \text{for moderate speeds} \tag{9.10}$$

9.2 Equivalent line contact parameters and effective inlet temperature

Equivalence between cylinder-plane and ball-plane The majority of inlet thinning studies were made in line contact, which is not the configuration in our experiments, the underlying physics between point and line EHD contacts are very similar[1]. This allowed equivalences be made between line and point contacts (98).

Some thermal factors $\frac{h^{1D}_{therm}}{h^{1D}_{isoth}}$ were expressed (see section 2.2.4) in the litterature as function of the number $L_h = \frac{\eta_0 u_e^2 \beta_l}{K_l}$. Yet, these corrective factors were obtained for line contacts, where the influence of the u_e, α, p_m, R_x, E' parameters on the central film thickness is different from the point contact. The central film thickness in a line contact is (101) :

$$h_c^{1D} = K_1 \cdot R_x^{0.308} \cdot (\eta_0 u_e^{1D})^{0.692} \cdot \alpha^{0.47} \cdot E'^{0.11} \cdot p_{m\,1D}^{-0.332} \tag{9.11}$$

, with $K_1 = 2.922 \cdot \left(\frac{\pi}{32}\right)^{+0.166}$. Using the following expression for the entrainment speed in the line contact formula (eq. (9.11)) gives the point contact formula of (62) (eq. (2.15)) :

$$u_{e\,1D} = \left(\frac{K_2}{K_1}\right)^{1.45} \cdot R_x^{0.032} \cdot \eta_0^{-0.032} \cdot \alpha^{0.087} \cdot E'^{-0.071} \cdot p_m^{0.189} \cdot u_e^{0.968} \tag{9.12}$$

, with $K_2 = 2.69 \cdot (1 - 0.61e^{-0.73\times 1.03}) \cdot \left(\frac{4}{9\pi^3}\right)^{0.067}$. Regarding shear heating, the quantity on the basis of which the two configurations should be regarded equally is the film thickness. To apply the thermal corrective factors $\frac{h^{1D}_{therm}}{h^{1D}_{isoth}}$ to point contacts, L_h is thus calculated as $L_h = \frac{\eta_0 u^2_{e\,1D}(-\partial_T ln\eta_0)}{K_l}$, where $u_{e\,1D}$ is given by eq. (9.12).

Effective inlet temperature To calculate the effective inlet temperature yielded by a thermal correction factor $\frac{h^{1D}_{therm}}{h^{1D}_{isoth}}$, the effective inlet temperature $T_{eff\ inlet}$ is defined by the relationship :

$$h_c^{1D}(\eta_0(T_{eff\ inlet})) = \frac{h^{1D}_{therm}}{h^{1D}_{isoth}} \times h_c^{1D}(\eta_0(T_{amb})) \tag{9.13}$$

---

[1] The macro-shape of the surfaces is sufficient to predicted accurately film thicknesses, at least for smooth surfaces ($S_q \lesssim 20$ nm)

Inverting this relationship using eq. (9.11) and the Vogel temperature-viscosity relationship (eq. (3.3)) gives :

$$\boxed{T_{eff\ inlet} = C + \frac{1}{\frac{1}{T_{amb}-C} + \frac{ln\left(\frac{h^{1D}_{therm}}{h^{1D}_{isoth}}\right)}{0.692\,B}}} \tag{9.14}$$

, with B, C the lubricant Vogel parameters and T_{amb} the room temperature.

9.3 Reynolds equation : derivation

(α) : Let us write the equilibrium of normal and tangential stresses acting over an elementary volume of fluid into a stationary EHD contact :

$$\partial_i p = \partial_z \vec{\tau_i} \cdot \vec{n}_i \text{ , i=x, y.} \tag{9.15}$$

If the fluid is Newtonian, its rheology imposes a shear stress constitutive equation writen $\vec{\tau_i} = \eta \partial_z \vec{u}_i$. Let us nottice that even if the fluid is not Newtonian, one can still use this relationship using the concept of effective viscosity, i.e. where η is a function of $\partial_j u_i$.

$$\partial_i p = \partial_z(\eta \partial_z u_i) \tag{9.16}$$

Integrating twice the previous relationship between $z = 0$ and $z = h$ yields the following velocity field, where the fluid is assumed to stick to the solid bodies in $z = 0$ and $z = h$ and under the hyoptheses of laminar thin fluid film such that $\partial_x, \partial_y u_i << \partial_z u_i$:

$$u_i = \left(\frac{z^2 - zh}{2\eta}\right) \partial_i p + (u_{i\ h} - u_{i\ b})\frac{z}{h} + u_{i\ b} \tag{9.17}$$

The fluid flows per unit [orthogonal] contact width $q_i = \int_0^h u_i dz$, can then be calculated :

$$q_i = -\frac{h^3}{12\eta}\partial_i p + h\frac{(u_{i\ b} + u_{i\ h})}{2} \tag{9.18}$$

(β) : The mass balance equation is :

$$\partial_x q_x + \partial_y q_y + u_{z\ h} - u_{z\ b} = 0 \tag{9.19}$$

Inserting equation 9.18 into (9.19) leads to the stationnary Reynolds equation :

$$\vec{\nabla}_{(x;y)} \cdot \left(-\frac{h^3}{12\eta}\vec{\nabla}_{(x;y)} p + \vec{u}_{e(x;y)} h\right) + u_{z\ h} - u_{z\ b} = 0 \tag{9.20}$$

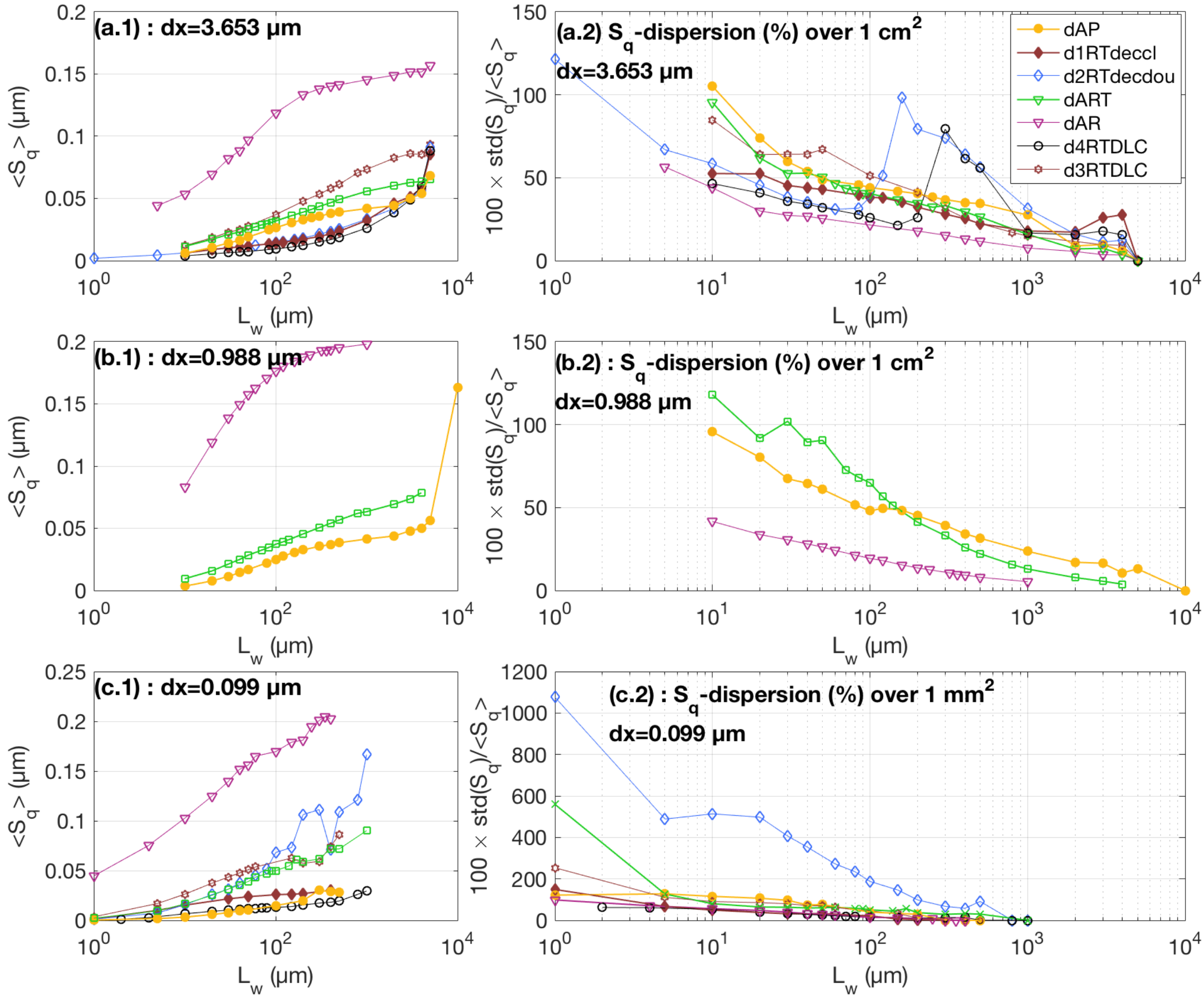

Figure 9.1: Evolution of the mean RMS roughness (removing the 5% least probable local values of S_q for each cut-off length) versus the cut-off length using local planar detrending with different sampling intervals (a.1, b.1, c.1). The relative dispersion of $< S_q >$ is plotted on graphs a.2, b.2, c.2.

9.4 Surface roughness

9.4.1 Roughness variability

9.4.2 Spectral density

Hybrid parameters such as the curvature depend highly on the sampling interval because these parameters involve partial derivatives along the x and y directions. It was sometimes advised to rely on the surface Fourier transform to calculate hybrid parameters (93). Figure 9.2 shows the variability in azimut-averaged power spectral density between two areas of the same surfaces. The relative error between these PSD is routinely of 30% to 100%. Consequently, the calculation of surface statistical moments based on the evaluated Fourier transforms (or on the autocorrelation function, its Fourier transform) are bound to vary importantly with the probing zone. Furthermore, most surfaces are not isotropic, which leads to reject the use of azimut averaged spectra, and to presume on each survey the *relevant* surface orientation. For instance $S_{al\,0.5}$, which corresponds to the fastest memory decay direction, was collected on centimetric surveys and still showed fluctuations of 20% to 50% its mean for the cut-off lengths under interest. The non stationarity of random surfaces spectra prevents the

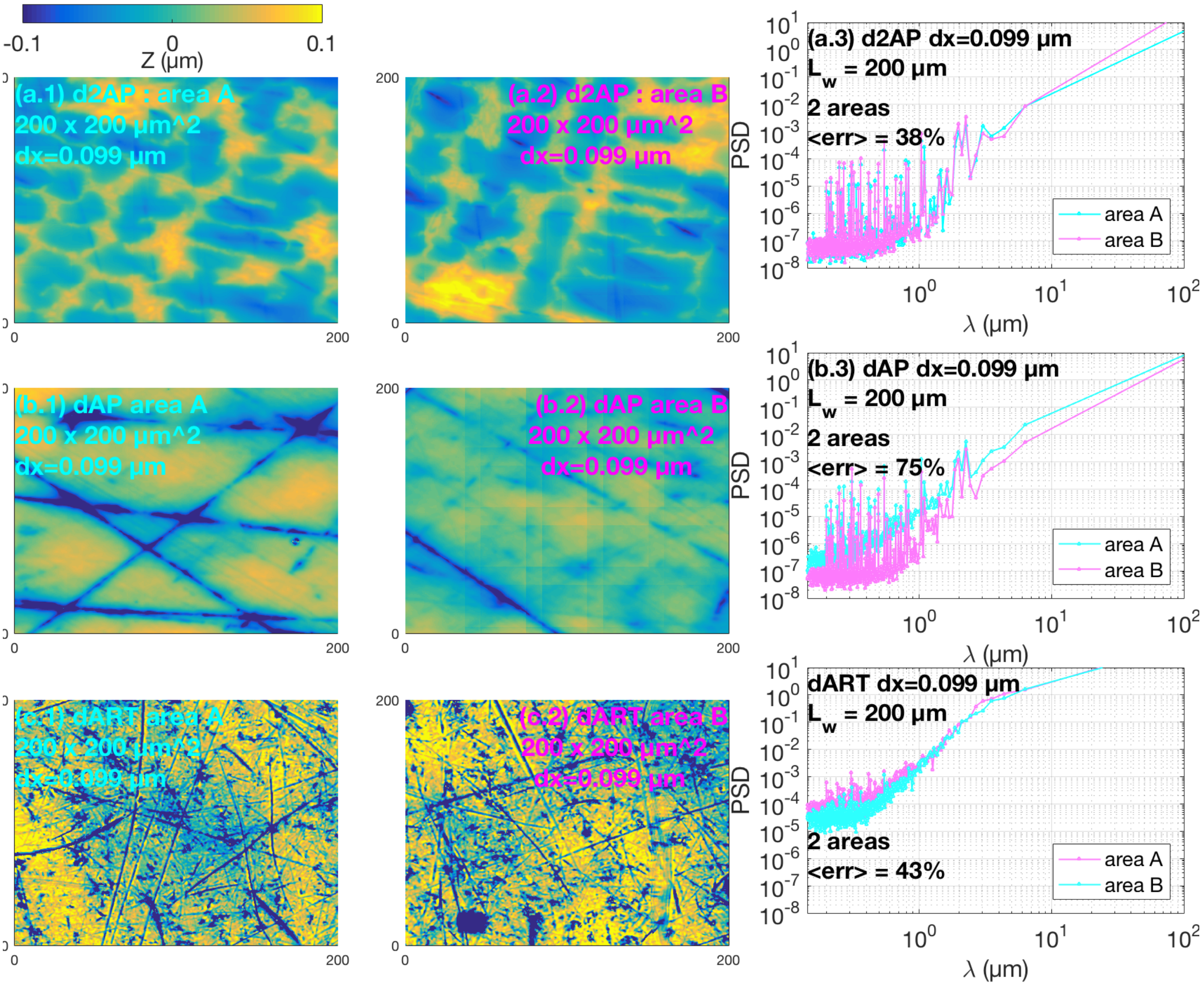

Figure 9.2: Two raw surveys of a manually polished disc (*d2AP*) (a.1, a.2), of an other one (*dAP*) (b.1, b.2) and of a finished steel disc (*dART*) (c.1, c.2), measured with a sampling interval of $dx = 0.099$ μm. The 2D Power spectral density were calulated for each survey, and averaged on all angles in the Fourier space, yielding the 2D PSD on figures a.3, b.3 and c.3.

concrete use of their PSD or of their ACF for the purpose of characterizing their scale distribution.

9.4.3 Surface topography and sampling interval

9.4.4 Other surface parameters

Figures 9.15 to 9.16 show more surface parameters such as the RMS deviations $\sqrt{<(z-<z>)^2>}$ among the ensembles of negative ($std(z)$, $z < 0$) and positive ($std(z)$, $z > 0$) heights, the skewness, the kurtosis (or flatness) and the texture aspect ratio ($S_{tr0.5}$). These parameters were extracted from surveys measured using $dx = 3.653$ μm and a probing area equal to 2.6 mm^2 for each disc. The black lines correspond to the mode of the parameters, whereas the colored errorbars correspond to averages ± the standard error of the parameters over the survey.

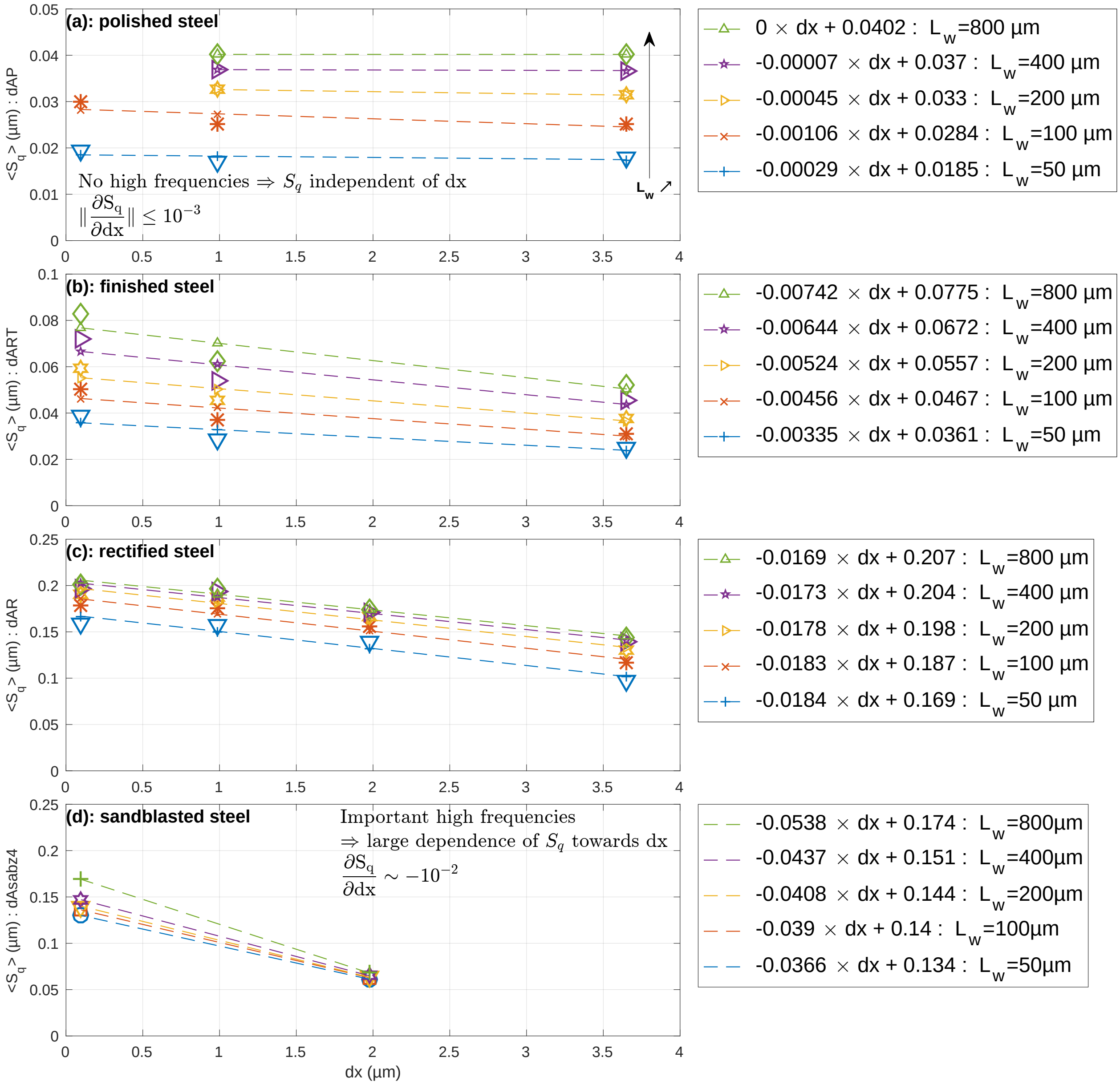

Figure 9.3: Evolution of the mean standard deviation with the sampling interval for different discs.

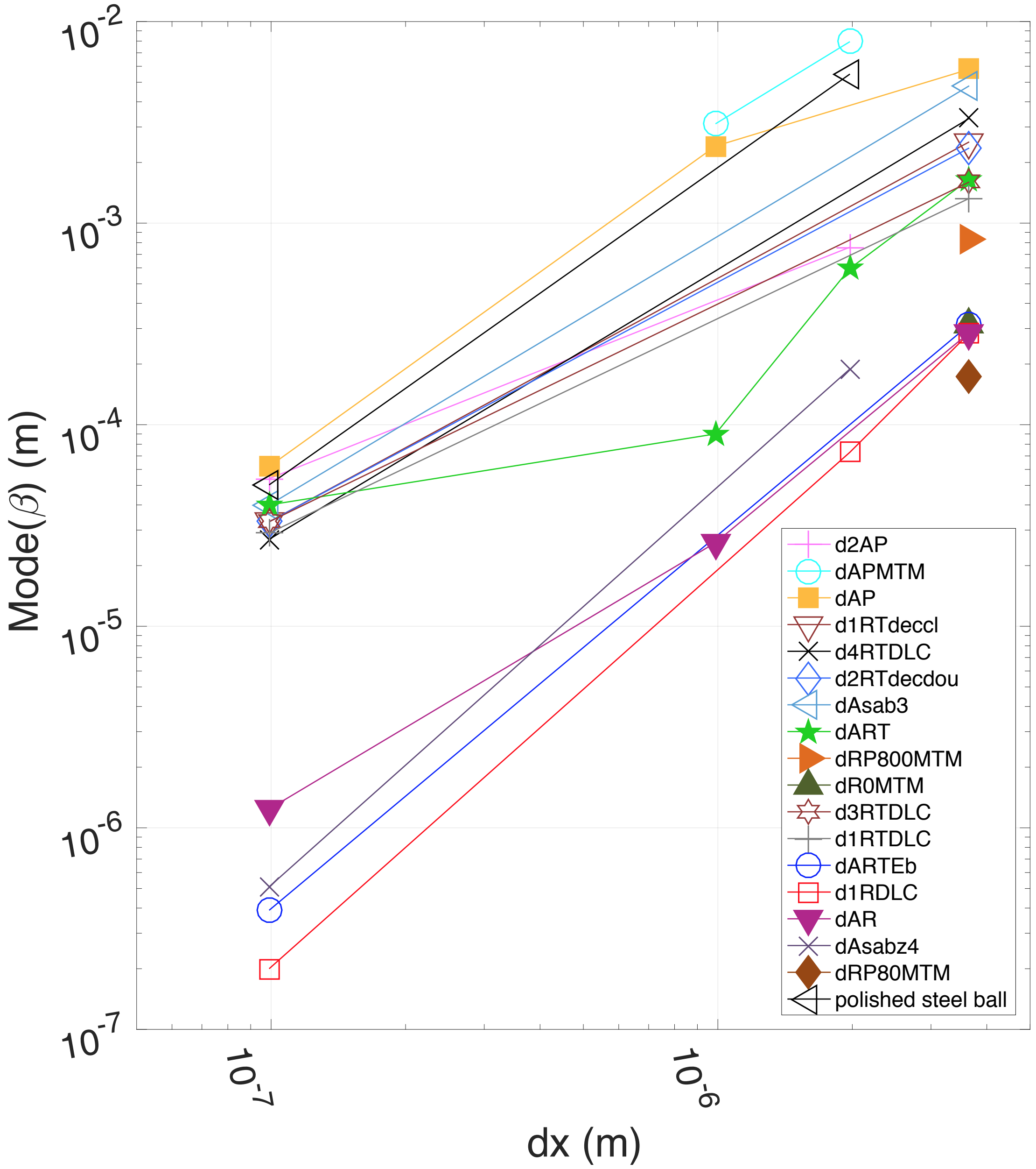

Figure 9.4: Influence of the sampling interval on the asperity curvature radius.

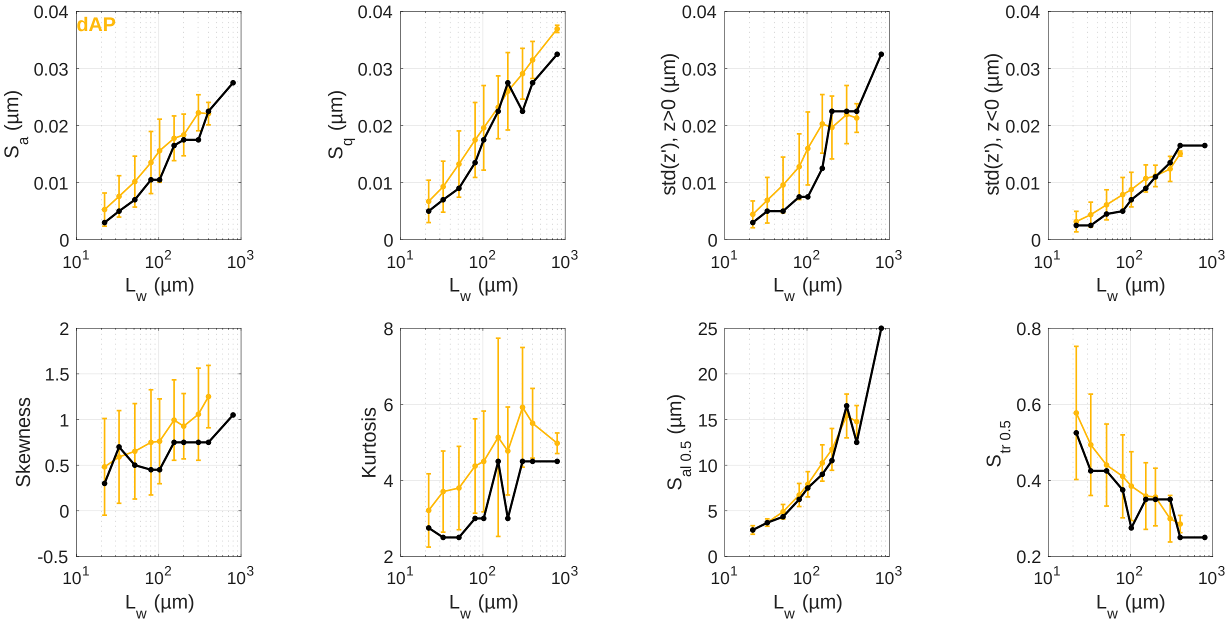

Figure 9.5: For the dAP disc : evolution of topographical parameters with the cut-off length, based on a probing area of 2.6 mm^2 and a sampling interval of 3.653 μm. Colored curves show the mean, the errorbars represent the standard deviation. Black curves represent the mode.

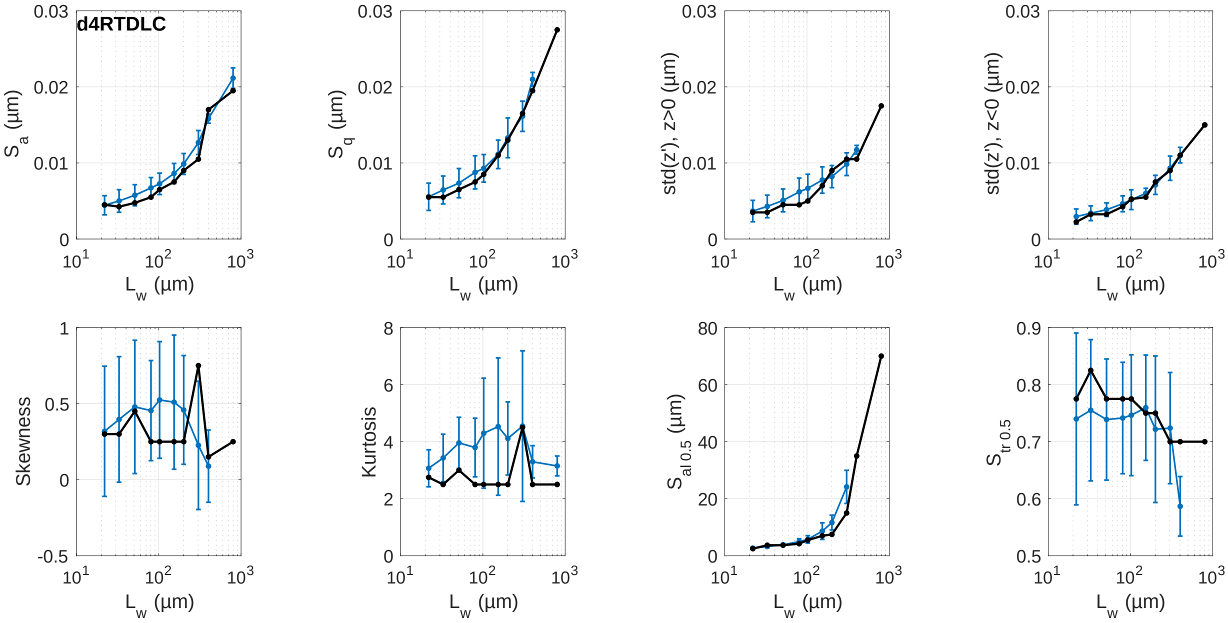

Figure 9.6: For the d4RTDLC disc : evolution of topographical parameters with the cut-off length, based on a probing area of 2.6 mm^2 and a sampling interval of 3.653 μm. Colored curves show the mean, the errorbars represent the standard deviation. Black curves represent the mode.

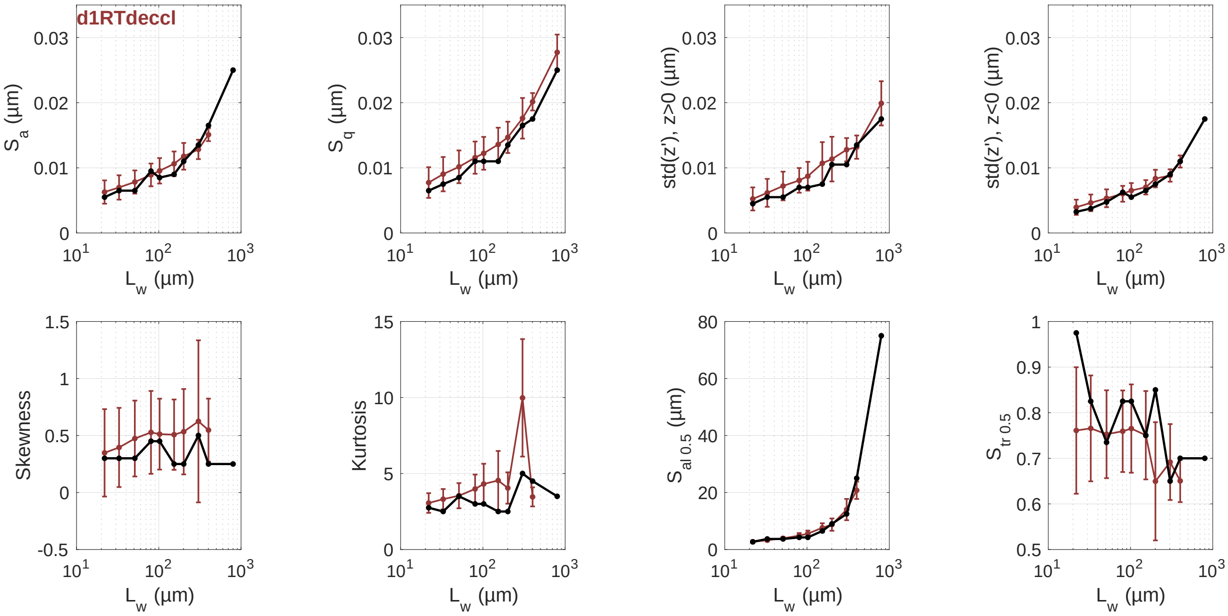

Figure 9.7: For the d1RTdeccl disc : evolution of topographical parameters with the cut-off length, based on a probing area of 2.6 mm^2 and a sampling interval of 3.653 μm. Colored curves show the mean, the errorbars represent the standard deviation. Black curves represent the mode.

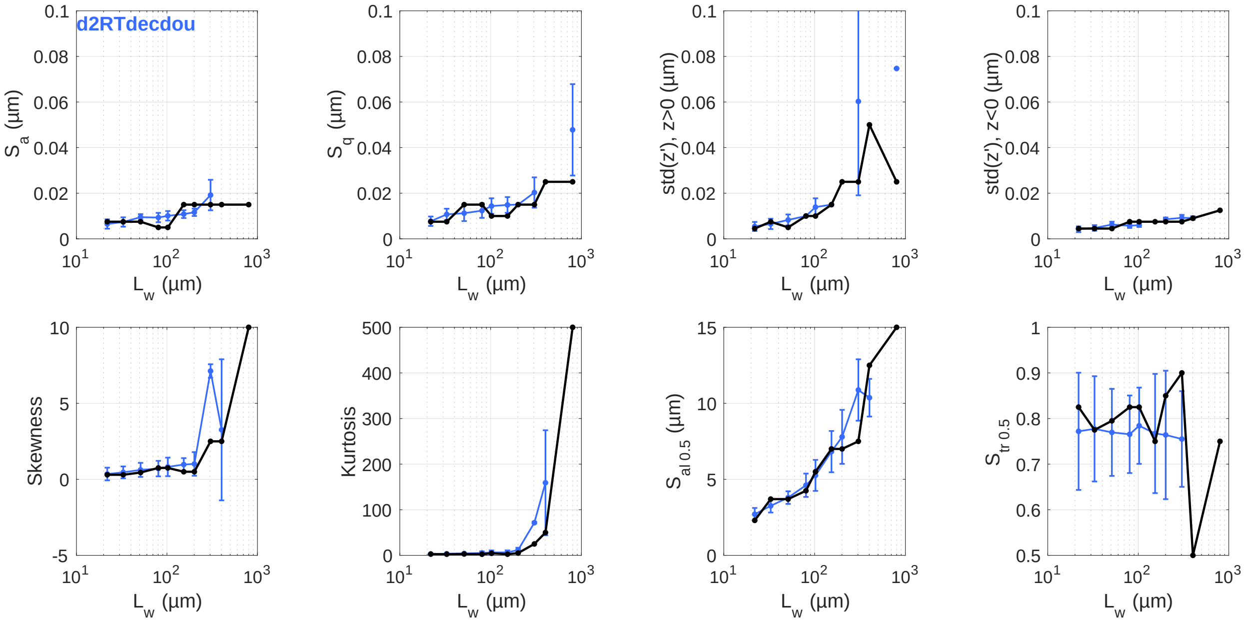

Figure 9.8: For the d2RTdecdou disc : evolution of topographical parameters with the cut-off length, based on a probing area of 2.6 mm^2 and a sampling interval of 3.653 μm. Colored curves show the mean, the errorbars represent the standard deviation. Black curves represent the mode.

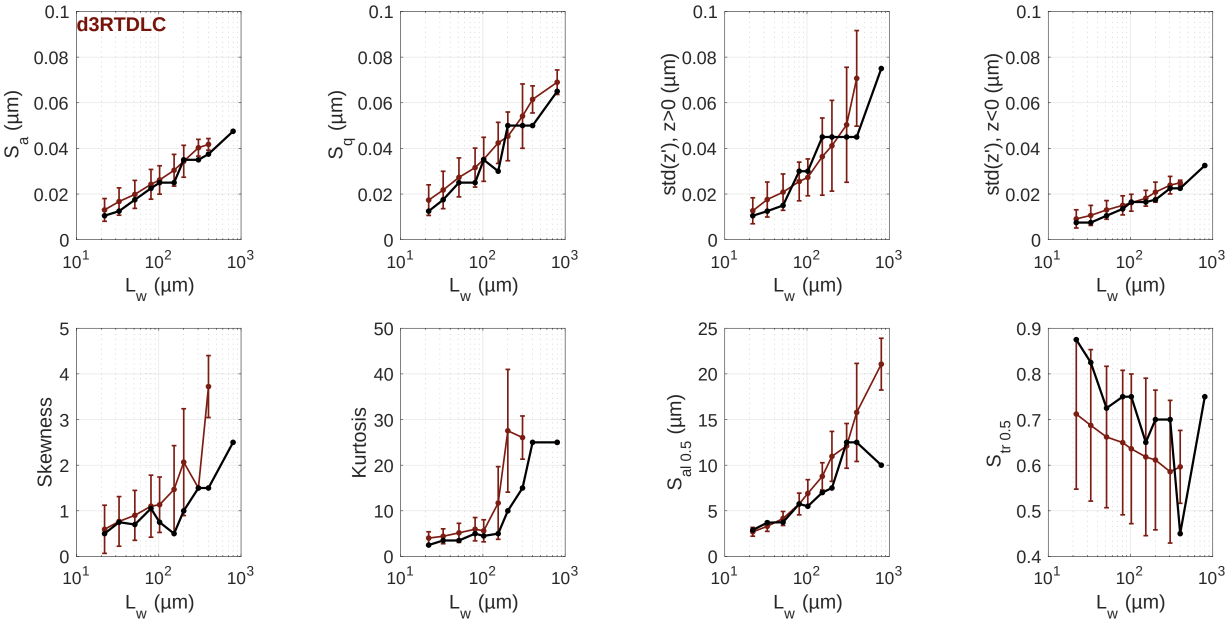

Figure 9.9: For the d3RTDLC disc : evolution of topographical parameters with the cut-off length, based on a probing area of 2.6 mm^2 and a sampling interval of 3.653 μm. Colored curves show the mean, the errorbars represent the standard deviation. Black curves represent the mode.

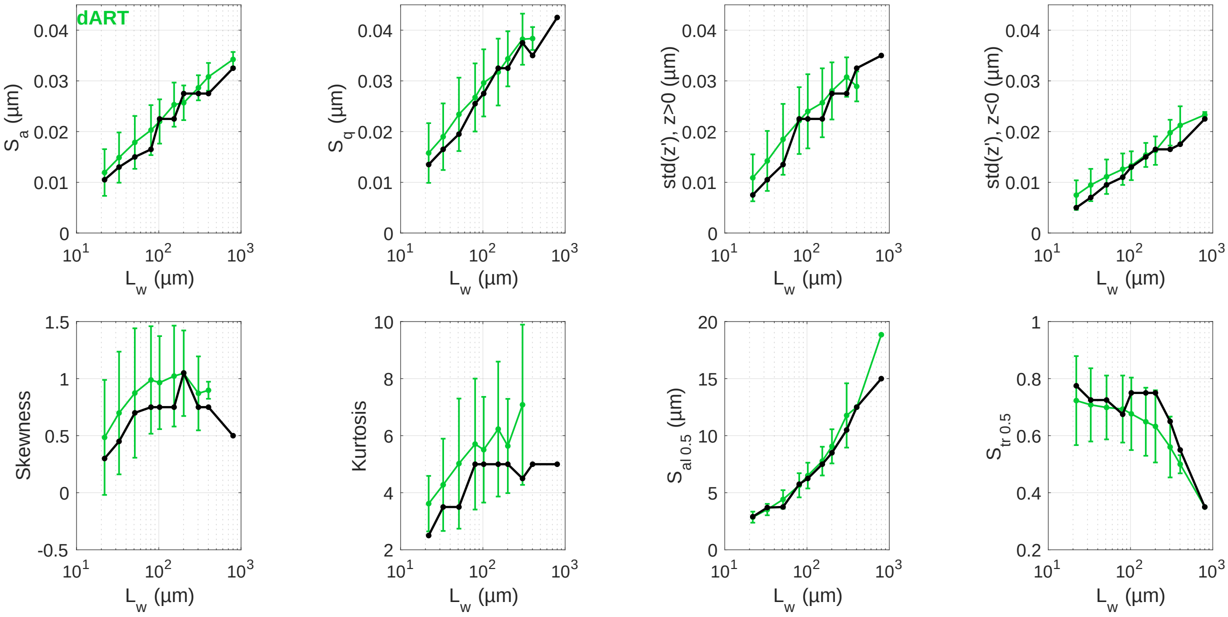

Figure 9.10: For the dART disc : evolution of topographical parameters with the cut-off length, based on a probing area of 2.6 mm^2 and a sampling interval of 3.653 μm. Colored curves show the mean, the errorbars represent the standard deviation. Black curves represent the mode.

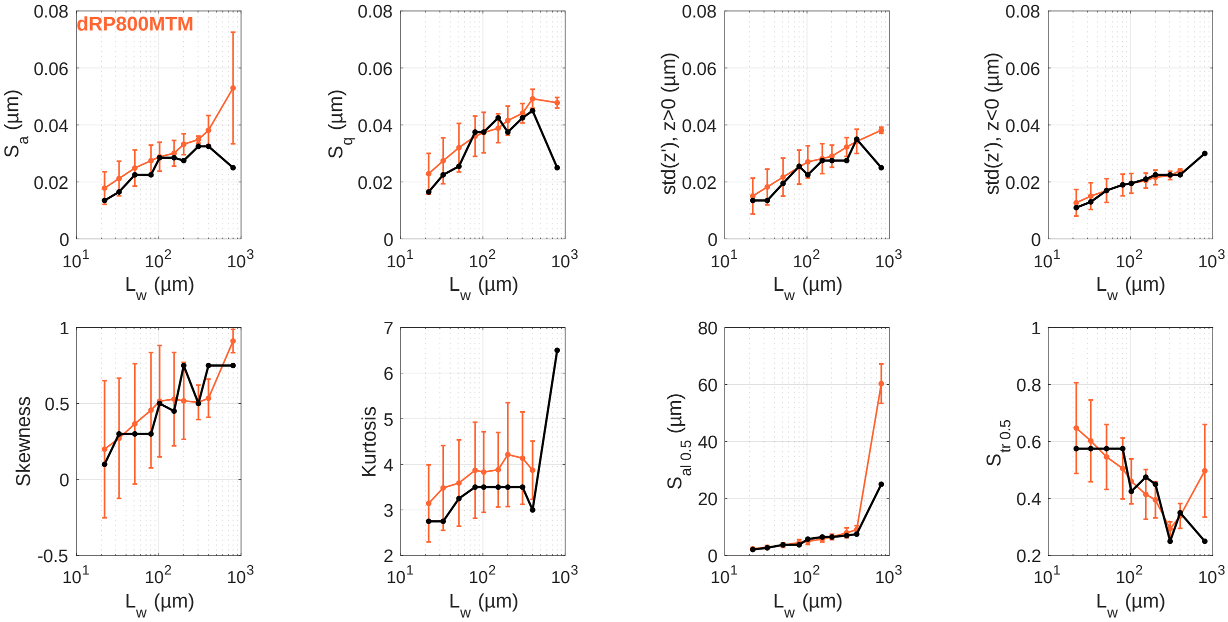

Figure 9.11: For the dRP800MTM disc : evolution of topographical parameters with the cut-off length, based on a probing area of 2.6 mm^2 and a sampling interval of 3.653 μm. Colored curves show the mean, the errorbars represent the standard deviation. Black curves represent the mode.

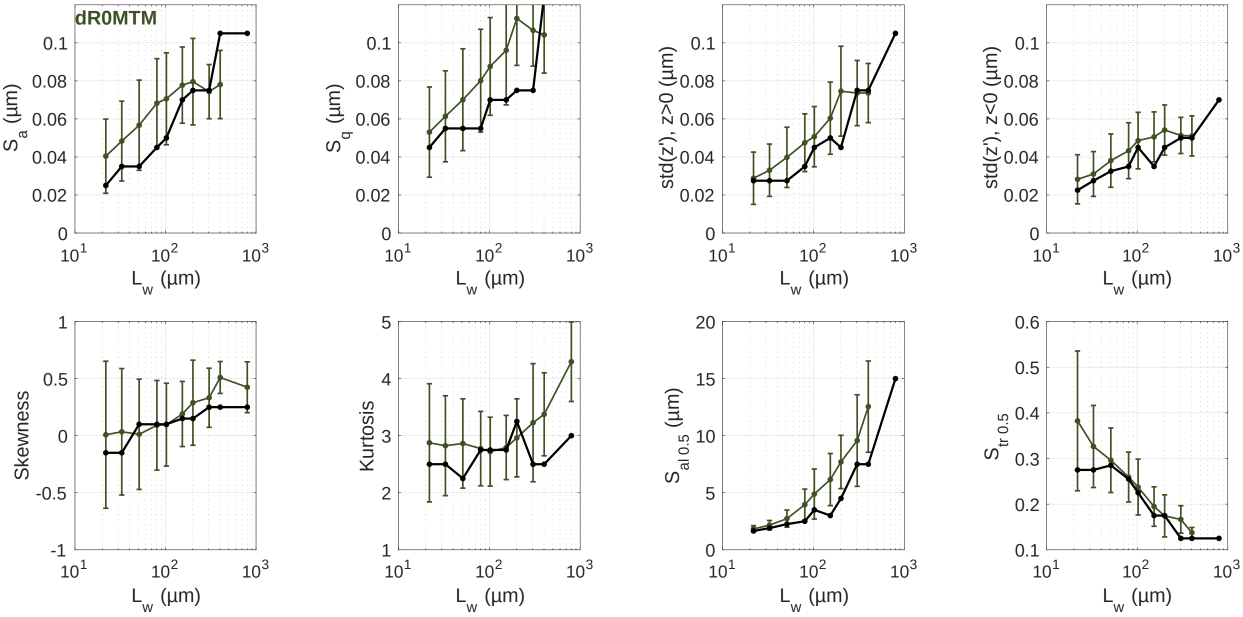

Figure 9.12: For the dR0MTM disc : evolution of topographical parameters with the cut-off length, based on a probing area of 2.6 mm^2 and a sampling interval of 3.653 μm. Colored curves show the mean, the errorbars represent the standard deviation. Black curves represent the mode.

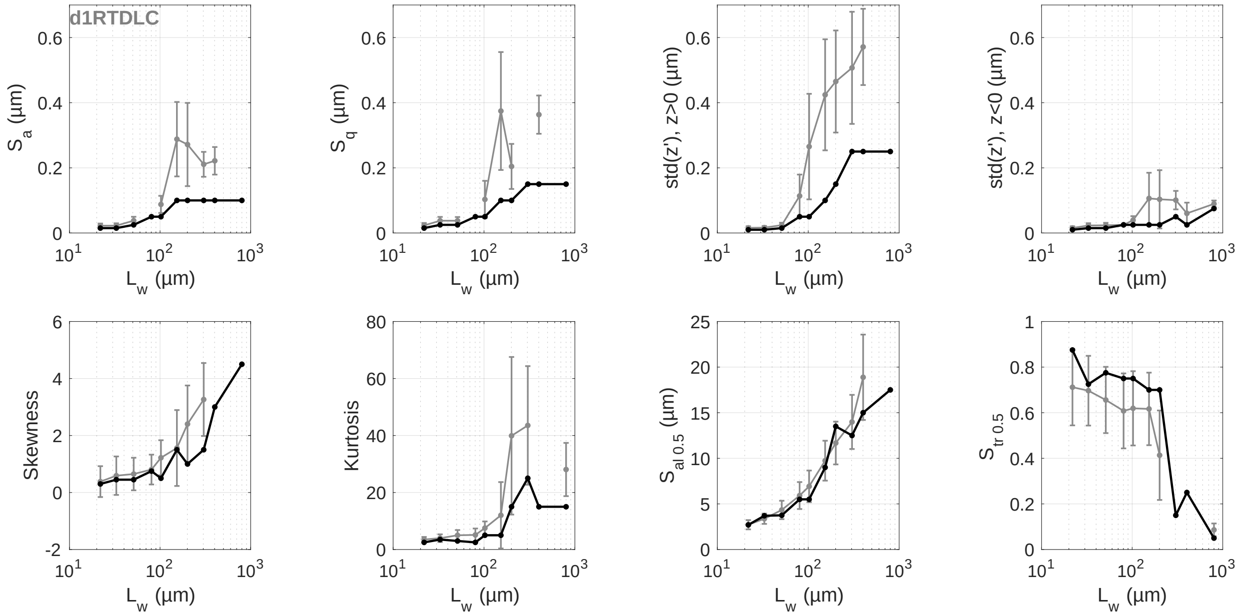

Figure 9.13: For the d1RTDLC disc : evolution of topographical parameters with the cut-off length, based on a probing area of 2.6 mm^2 and a sampling interval of 3.653 μm. Colored curves show the mean, the errorbars represent the standard deviation. Black curves represent the mode.

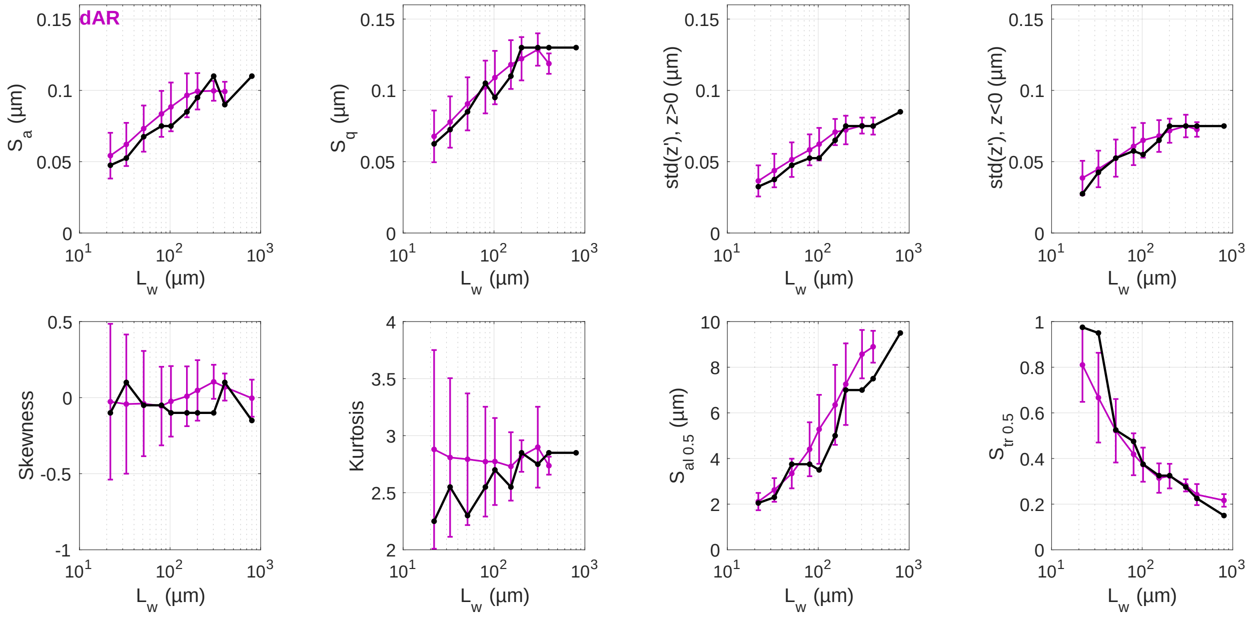

Figure 9.14: For the dAR disc : evolution of topographical parameters with the cut-off length, based on a probing area of 2.6 mm^2 and a sampling interval of 3.653 μm. Colored curves show the mean, the errorbars represent the standard deviation. Black curves represent the mode.

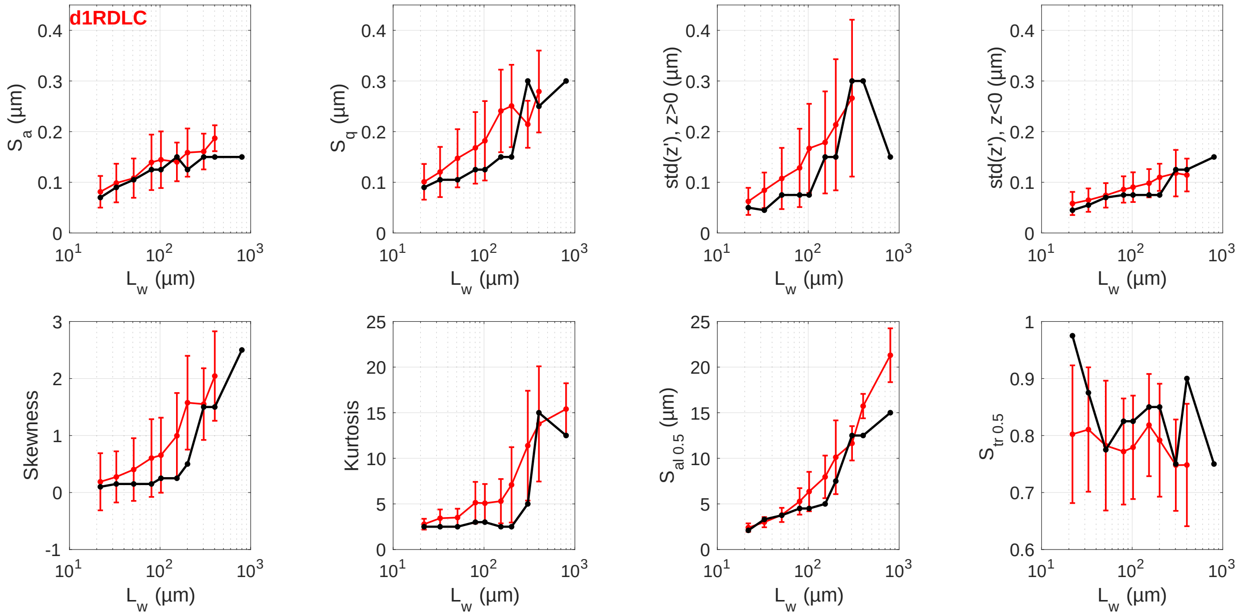

Figure 9.15: For the d1RDLC disc : evolution of topographical parameters with the cut-off length, based on a probing area of 2.6 mm^2 and a sampling interval of 3.653 μm. Colored curves show the mean, the errorbars represent the standard deviation. Black curves represent the mode.

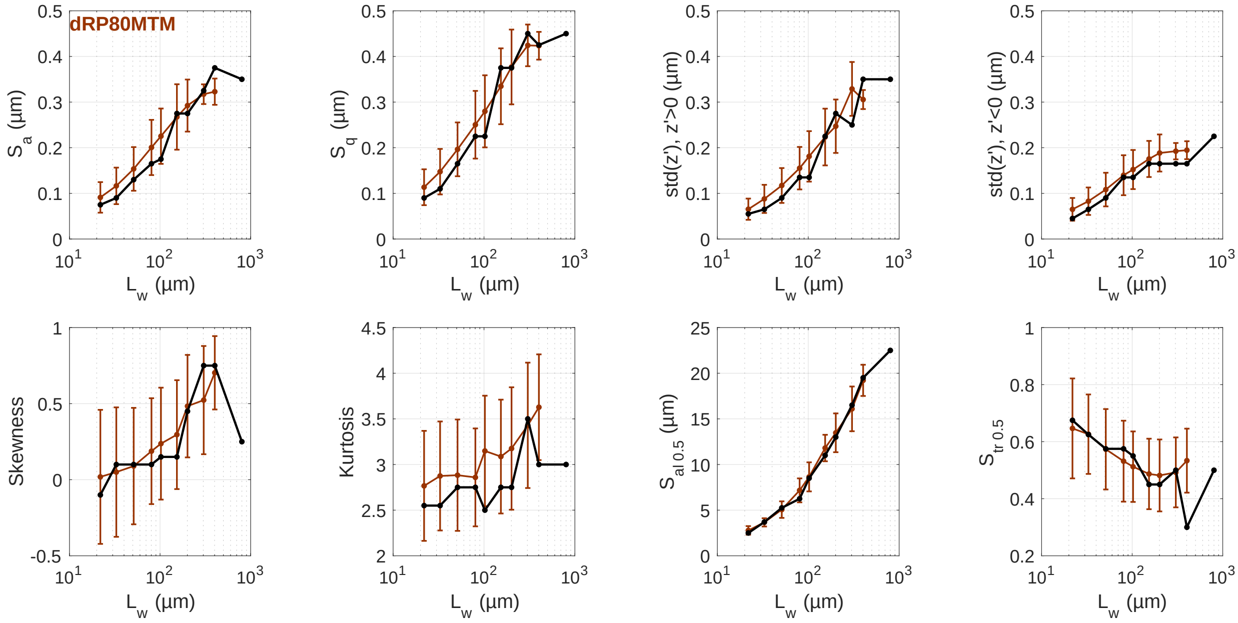

Figure 9.16: For the dRP80MTM disc : evolution of topographical parameters with the cut-off length, based on a probing area of 2.6 mm^2 and a sampling interval of 3.653 μm. Colored curves show the mean, the errorbars represent the standard deviation. Black curves represent the mode.

9.5 Relationship between the film thickness and the surface separation with the (72) model.

To relate the fraction of load borne by the asperities to the film thickness, Johnson et al. combined experimental observations from surface metrologists (in particular from Whitehouse and Archard) to the film thickness defined by the volume conservation, Johnson et al. proposed :

$$\frac{d_e}{\sigma_p} = 1.4\frac{s}{\sigma_c} - 0.9 \tag{9.21}$$

$$\text{and } \frac{h}{\sigma_c} = \frac{s}{\sigma_c} + \int_{s/\sigma_c}^{\infty} du \left(u - \frac{s}{\sigma_c}\right) \frac{e^{-\frac{1}{2}u^2}}{\sqrt{2\pi}} \tag{9.22}$$

Since this formulation requires a numerical integration, they used the simplified equation (2.37) recalled here :

$$\frac{d_e}{\sigma_a} = \frac{h}{\sigma_c} \tag{9.23}$$

Both the exact and approximate relationships are plotted on fig. 9.17 respectively in solid and dashed line.

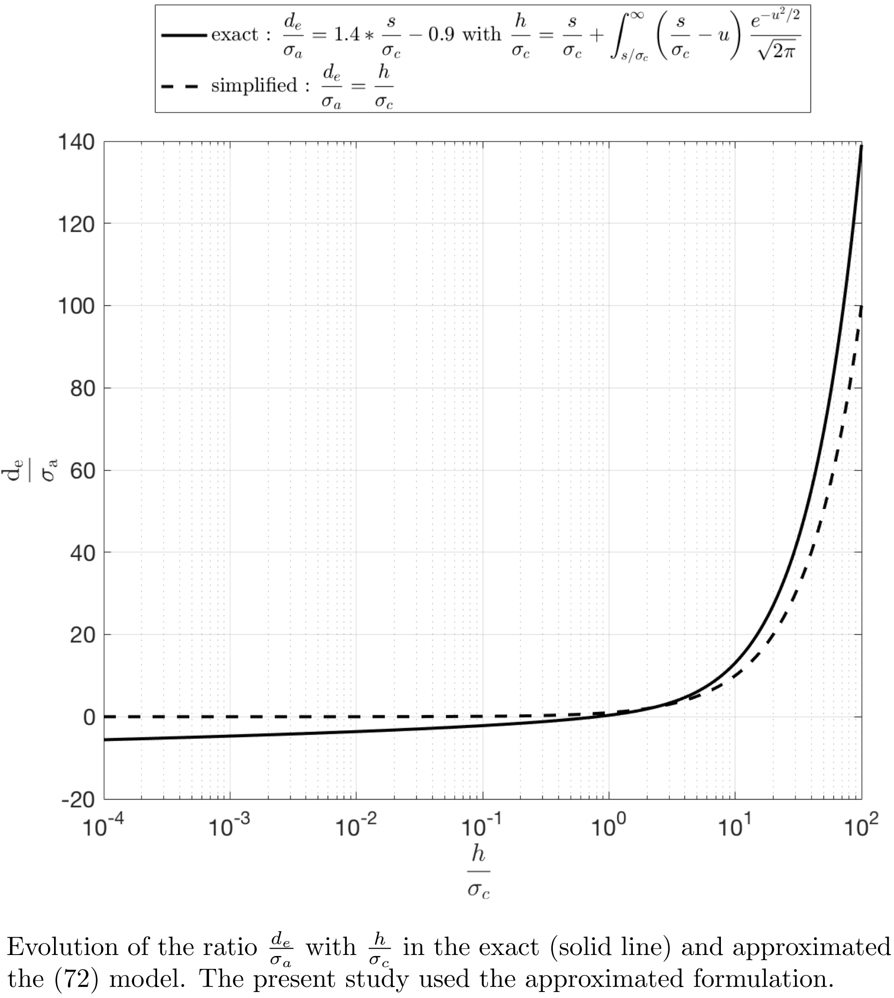

Figure 9.17: Evolution of the ratio $\frac{d_e}{\sigma_a}$ with $\frac{h}{\sigma_c}$ in the exact (solid line) and approximated (dashed line) formulation of the (72) model. The present study used the approximated formulation.

9.6 Pressure-dependent pressure viscosity coefficient

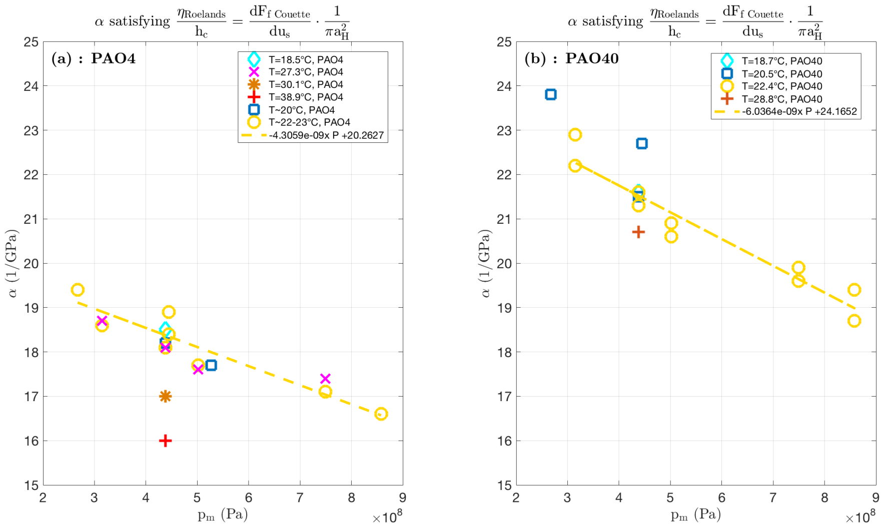

Figure 9.18: Pressure-viscosity coefficients obtained while fitting the initial slope of $F_{f\ Couette}$ with u_s during various traction experiments on PAO4 (a) and PAO40 (b). The lubricant was then assumed Newtonian and the Roelands isothermal relationship (eq. (2.4)) was assumed valid to describe the lubricants low-shear viscosity and the (62) formula (eq. (2.15)) was used to convert the sliding speed into shear rates.

Bibliography

(1) C. E Albertson. The mechanism of anti-squawk additive behavior in automatic transmission fluids. ASLE Transactions, 6(4): 300–315, 1963. 145

(2) H. Allmaier, C. Priestner, D.E. Sander, and F. Reich. Friction in automotive engines. Tribology in engineering, pages 149–84, 2013. 1

(3) W. Appel and E. Kowalski. Mathematics for physics and physicists. Princeton University Press, 2007. 176

(4) Walter Appel. Probabilités pour les non probabilistes. Princeton University Press, 2015. 93

(5) J.F. Archard. The temperature of rubbing surfaces. Wear, 2(6): 438 – 455, 1959. 57, 176

(6) S. Bair. The shear rheology of thin compressed liquid films. Proceedings of the Institution of Mechanical Engineers, Part J: Journal of Engineering Tribology, 216(1):1–17, 2002. doi: 10.1243/1350650021543834. 52

(7) S. Bair. Complete isothermal solution for the viscous regime of concentrated contact traction. Applied Mechanics and Engineering, 7(3):719–728, 2002. 52

(8) S. Bair. Shear thinning correction for rolling/sliding elastohydrodynamic film thickness. Proceedings of the Institution of Mechanical Engineers, Part J: Journal of Engineering Tribology, 219(1):69–74, 2005. 11, 54

(9) S. Bair and W. O. Winer. A rheological model for elastohydrodynamic contacts based on primary laboratory data. Journal of Lubrication Technology, 101(3):258–264, 07 1979. 52

(10) S. Bair and W. O. Winer. Regimes of traction in concentrated contact lubrication. Journal of Lubrication Technology, 104(3): 382–386, 07 1982. 16, 22, 23, 115

(11) S. Bair and W. O. Winer. The high pressure high shear stress rheology of liquid lubricants. Journal of Tribology, 114(1):1–9, 01 1992. 52

(12) S. Bair, P. Vergne, and M. Querry. A unified shear-thinning treatment of both film thickness and traction in EHD. ArXiv e-prints, April 2007. 66

(13) Scott Bair. Normal stress difference in liquid lubricants sheared under high pressure. Rheologica Acta, 35(1):13–23, 1996. 52

(14) Scott Bair. Elastohydrodynamic film forming with shear thinning liquids. Journal of Tribology, 120(2):173–178, 04 1998. 11

(15) Scott Bair. The nature of the logarithmic traction gradient. Tribology international, 35(9):591–597, 2002. 55

(16) Scott Bair and Clare McCabe. A study of mechanical shear bands in liquids at high pressure. Tribology international, 37(10):783–789, 2004. 52

(17) Scott S Bair. High pressure rheology for quantitative elastohydrodynamics, volume 54. Elsevier, 2007. 52, 53, 66

(18) JC Bell. Lubrication of rolling surfaces by a ree-eyring fluid. ASLE Transactions, 5(1):160–171, 1962. 11

(19) L. Bobach, D. Bartel, R. Beilicke, J. Mayer, K. Michaelis, K. Stahl, S. Bachmann, J. Schnagl, and H. Ziegele. Reduction in ehl friction by a dlc coating. Tribology Letters, 60(1):17, 2015. 58

(20) AW Bush, RD Gibson, and TR Thomas. The elastic contact of a rough surface. Wear, 35(1):87–111, 1975. 19

(21) H.-J. Butt and M. Kappl. Surface and interfacial forces. John Wiley & Sons, 2009. 107

(22) S. Campen, J. Green, G. Lamb, D. Atkinson, and H. Spikes. On the increase in boundary friction with sliding speed. Tribology letters, 48(2):237–248, 2012. 145

(23) P. Cann, E. Ioannides, B. Jacobson, and A.A. Lubrecht. The lambda ratio - a critical reexamination. WEAR, 175:177–188, 1994. 9, 16

(24) H. S. Carslaw and J. C. Jaeger. Conduction of heat in solids. 1959. 57, 167, 175

(25) G. Cassin, E. Heinrich, and H.A. Spikes. The influence of surface roughness on the lubrication properties of adsorbing and non-adsorbing biopolymers. Tribology Letters, 11(2):95–102, 2001. 134

(26) L. Chang. On the shear bands and shear localizations in elastohydrodynamic lubrication films. Journal of Tribology, 127(1): 245–247, 02 2005. 52

(27) A. D. Chapkov, C. H. Venner, and A. A. Lubrecht. Roughness amplitude reduction under non-newtonian ehd lubrication conditions. Journal of Tribology, 128(4):753–760, 06 2006. 18

(28) H. S. Cheng. A refined solution to the thermal-elastohydrodynamic lubrication of rolling and sliding cylinders. ASLE Transactions, 8(4):397–410, 1965. 11, 12

(29) J.H. Choo, R.P. Glovnea, A.K. Forrest, and H.A. Spikes. A low friction bearing based on liquid slip at the wall. Journal of Tribology, 129(3):611–620, 2007. 7

(30) H. Christensen. Stochastic models for hydrodynamic lubrication of rough surfaces. Proceedings of the Institution of Mechanical Engineers, 184:1013–1026, 1969. 16, 19

(31) M. Ciavarella, V. Delfine, and G. Demelio. A “revitalized”greenwood and williamson model of elastic contact between fractal surfaces. Journal of the Mechanics and Physics of Solids, 54(12):2569–2591, 12 2006. 19

(32) T.F. Conry, S. Wang, and C. Cusano. Thermal analysis of elastohydrodynamic lubrication of line contacts using the ree-eyring fluid model. Journal of tribology, 113(2):232–242, 1991. 14

(33) AW Crook. The lubrication of rollers iii. a theoretical discussion of friction and the temperatures in the oil film. Philosophical Transactions of the Royal Society of London A: Mathematical, Physical and Engineering Sciences, 254(1040):237–258, 1961. 56, 176

(34) M. M. Cross. Rheology of non-Newtonian fluids: A new flow equation for pseudoplastic systems. Journal of Colloid Science, 20(5):417–437, June 1965. 53

(35) A. de Kraker, R.A.J. van Ostayen, and D.J. Rixen. Development of a texture averaged reynolds equation. Tribology International, 43(11):2100 – 2109, 2010. 17

(36) J. M. Dealy. Weissenberg and deborah numberstheir definition and use. Rheol. Bull, 79(2):14–18, 2010. 54

(37) M. Diew, A. Ernesto, J. Cayer-Barrioz, and D. Mazuyer. Stribeck and traction curves under moderate contact pressure: From friction to interfacial rheology. Tribology Letters, 57(1):8, 2015. 66

(38) M. B. Diew. Contribution à la compréhension des mécanismes d’action des additifs modificateurs de frottement et du couplage additif/surface dans tous les régimes de lubrification. PhD thesis, Ecully, Ecole centrale de Lyon, 2013. 1

(39) D. Dowson and G. R. Higginson. Elasto-hydrodynamic lubrication: the fundamentals of roller and gear lubrication, volume 23. 1966. 22

(40) D. Dowson and G.R. Higginson. New roller bearing lubrication formula. Engineering (London), 192(4972):158–159, 1961. 12

(41) D. Dowson, G.R. Higginson, and A.V. Whitaker. Elasto-hydrodynamic lubrication: a survey of isothermal solutions. Journal of Mechanical Engineering Science, 4(2):121–126, 1962. 19

(42) D. Dowson, G. R. Higginson, J. F. Archard, and A.W. Crook. Elasto-hydrodynamic lubrication. Oxford : Pergamon Press, 1977. 18

(43) L. Dufrancatel Veiller. Etude du gonflement des polymères et de son incidence sur la précision dimensionnelle des profilés extrudés. Application aux polyuréthannes thermoplastiques. PhD thesis, 1998. 54

(44) W. C. Emmens. Tribology of flat contacts and its application in deep drawing. PhD thesis, 1997. 128, 168

(45) C. R. Evans. Measurement and mapping of the rheological properties of elastohydrodynamic lubricants. Theses, University of Cambridge, November 1983. 9, 22, 50, 52, 54, 63, 66

(46) C. R. Evans and K. L. Johnson. Regimes of traction in elastohydrodynamic lubrication. Proceedings of the Institution of Mechanical Engineers, Part C: Journal of Mechanical Engineering Science, 200(5):313–324, 1986. 23

(47) C R Evans and K L Johnson. The influence of surface roughness on elastohydrodynamic traction. Proceedings of the Institution of Mechanical Engineers, Part C: Journal of Mechanical Engineering Science, 201(2):145–150, 1987. 16, 22, 72

(48) H. Eyring. Viscosity, plasticity, and diffusion as examples of absolute reaction rates. The Journal of Chemical Physics, 4(4): 283–291, 1936. 52

(49) I. C. Faraon and D. J. Schipper. Stribeck curve for starved line contacts. Journal of Tribology, 129(1):181–187, 10 2006. 21, 134

(50) H.A. Francis. Interfacial temperature distribution within a sliding hertzian contact. ASLE Transactions, 14(1):41–54, 1971. 176

(51) E. R. M. Gelinck and D. J. Schipper. Calculation of stribeck curves for line contacts. Tribology International, 33(3–4):175–181, 4 2000. 21, 162

(52) J. A. Greenwood. A unified theory of surface roughness. Proceedings of the Royal Society of London. A. Mathematical and Physical Sciences, 393(1804):133–157, 1984. 26, 27, 96

(53) J. A. Greenwood and J. J. Kauzlarich. Inlet shear heating in elastohydrodynamic lubrication. Journal of Lubrication Technology, 95(4):417–423, 10 1973. 9, 12, 13, 47

(54) J.A. Greenwood. An interpolation formula for flash temperatures. Wear, 150(1):153 – 158, 1991. 58, 60, 176, 177

(55) J.A. Greenwood and Williamson J.B.P. Contact of nominally flat surfaces. Proceedings of the royal society, 295(1442):300–319, 1966. 18, 19

(56) J.A. Greenwood and J.J. Wu. Surface roughness and contact: An apology. Meccanica, 36(6):617–630, 2001. 26

(57) Raynald Guilbault. A simplified thermal analysis of elastohydrodynamic contacts. Journal of Tribology, 135(2):021502–021502, 02 2013. 13, 47

(58) P.K. Gupta, H.S. Cheng, D. Zhu, N.H. Forster, and J.B. Schrand. Viscoelastic effects in mil-l-7808-type lubricant, part i: Analytical formulation. Tribology transactions, 35(2):269–274, 1992. 14, 47, 53

(59) W. Habchi and P. Vergne. On the compressive heating/cooling mechanism in thermal elastohydrodynamic lubricated contacts. Tribology International, 88:143 – 152, 2015. 12

(60) W. Habchi, D. Eyheramendy, S. Bair, P. Vergne, and G. Morales-Espejel. Thermal elastohydrodynamic lubrication of point contacts using a newtonian/generalized newtonian lubricant. Tribology Letters, 30(1):41–52, 2008. 11, 12

(61) W. Habchi, S. Bair, and P. Vergne. On friction regimes in quantitative elastohydrodynamics. Tribology International, 58:107 – 117, 2013. 54

(62) B. J. Hamrock and D. Dowson. Isothermal elastohydrodynamic lubrication of point contacts: Part iii—fully flooded results. Journal of Lubrication Technology, 99(2):264–275, 04 1977. 8, 47, 66, 78, 81, 123, 152, 153, 177, 190

(63) B. J. Hamrock, S. R. Schmid, and B. O. Jacobson. Fundamentals of fluid film lubrication, 2nd ed. 2004. 6, 107

(64) S. R. Harp and R. F. Salant. An average flow model of rough surface lubrication with inter-asperity cavitation. Journal of Tribology, 123(1):134–143, 2001. 17

(65) M.J.I.P.M.R. Hartl, I. Krupka, R. Poliscuk, M. Liska, J. Molimard, M. Querry, and P. Vergne. Thin film colorimetric interferometry. Tribology Transactions, 44(2):270–276, 2001. 152

(66) Ragnar Holm. Electric Contacts. 1967. 175

(67) K. Holmberg, P. Andersson, and A. Erdemir. Global energy consumption due to friction in passenger cars. Tribology International, 47:221–234, 2012. 1

(68) B. Jacobson and E. Hoglund. Experimental investigation of the shear strength of lubricants subjected to high pressure and temperature. Journal of tribology, 108:571, 1986. 52

(69) Bo O Jacobson. Rheology and elastohydrodynamic lubrication, volume 19. Elsevier, 1991. 63

(70) J.C. Jaeger. Moving sources of heat and the temperature at sliding contacts. Journal and Proceedings of the Royal Society of New South Wales, 76:203–224, 1942. 58, 59, 60, 176, 177

(71) K. L. Johnson and J. L. Tevaarwerk. Shear behaviour of elastohydrodynamic oil films. Proceedings of the Royal Society of London A: Mathematical, Physical and Engineering Sciences, 356(1685): 215–236, 1977. 11, 52, 53, 54, 63

(72) K.L. Johnson, J.A. Greenwood, and S.Y. Poon. A simple theory of asperity contact in elastohydro-dynamic lubrication. Wear, 19 (1):91 – 108, 1972. x, 19, 20, 21, 70, 159, 162, 163, 166, 168, 173, 189

(73) M Kalin, I Velkavrh, J Vižintin, and L Ožbolt. Review of boundary lubrication mechanisms of dlc coatings used in mechanical applications. Meccanica, 43(6):623–637, 2008. 147, 149

(74) Mitjan Kalin and Igor Velkavrh. Non-conventional inverse-stribeck-curve behaviour and other characteristics of dlc coatings in all lubrication regimes. Wear, 297(1):911–918, 2013. 134, 147

(75) I Krupka, P Svoboda, and M Hartl. Effect of surface topography on mixed lubrication film formation during start up under rolling/sliding conditions. Tribology International, 43(5):1035–1042, 2010. 107

(76) A. LaFountain, G.J. Johnston, and H.A. Spikes. Elastohydrodynamic friction behavior of polyalphaolefin blends. In T.H.C. Childs G. Dalmaz Y. Berthier L. Flamand J.-M. Georges D. Dowson, C.M. Taylor and A.A. Lubrecht, editors, Tribology for Energy ConservationProceedings of the 24th Leeds-Lyon Symposium on Tribology, volume 34 of Tribology Series, pages 465 – 475. Elsevier, 1998. 14, 63, 81, 167

(77) R Larsson and O Andersson. Lubricant thermal conductivity and heat capacity under high pressure. Proceedings of the Institution of Mechanical Engineers, Part J: Journal of Engineering Tribology, 214(4):337–342, 2000. 58, 59

(78) R. Larsson, P.O. Larsson, E. Eriksson, M. Sjöberg, and E. Höglund. Lubricant properties for input to hydrodynamic and elastohydrodynamic lubrication analyses. Proceedings of the Institution of Mechanical Engineers, Part J: Journal of Engineering Tribology, 214(1):17–27, 2000. 58, 59

(79) R.K. Leach. Characterisation of areal surface texture. Springer, 2013. 84, 86, 102

(80) R. H. Leaver, R. S. Sayles, and T. R. Thomas. Mixed lubrication and surface topography of rolling contacts. Proceedings of the Institution of Mechanical Engineers, 188(1):461–469, 1974. 28, 29, 87, 115

(81) Q. Liu, W. T. Napel, J. H. Tripp, P. M. Lugt, and R. Meeuwenoord. Friction in highly loaded mixed lubricated point contacts. Tribology Transactions, 52(3):360–369, 2009. 134

(82) Qiang Liu. Friction in mixed and elastohydrodynamic lubricated contacts including thermal effects. University of Twente, 2002. 21

(83) M. S. Longuet-Higgins. Statistical properties of an isotropic random surface. Philosophical Transactions of the Royal Society of London A: Mathematical, Physical and Engineering Sciences, 250(975):157–174, 1957. 28

(84) J Lord and R Larsson. Effects of slide-roll ratio and lubricant properties on elastohydrodynamic lubrication film thickness and traction. Proceedings of the Institution of Mechanical Engineers, Part J: Journal of Engineering Tribology, 215(3):301–308, 2001. 14

(85) X. Lu, M. M. Khonsari, and E. R. Gelinck. The stribeck curve: experimental results and theoretical prediction. Journal of tribology, 128(4):789–794, 2006. 162

(86) A. A. Lubrecht, D. Graille, C. H. Venner, and J. A. Greenwood. Waviness amplitude reduction in ehl line contacts under rolling-sliding. Journal of Tribology, 120(4):705–709, 10 1998. 18

(87) A.A. Lubrecht, W. E. Ten Napel, and R. Bosma. The influence of longitudinal and transverse roughness on the elastohydrodynamic lubrication of circular contacts. Journal of Tribology, 1988. 18

(88) David M Maietta and L Chang. An asperity microcontact model incorporating the transition from elastic deformation to fully plastic flow. Journal of Tribology, pages 86–93, 2000. 19, 22

(89) B. N. Markov and A. V. Shulepov. Two-dimensional filters for images of surface roughness. Measurement Techniques, 58(8): 835–838, 2015. 84

(90) Giuseppe Marrucci and Gianni Astarita. Significance of the deborah number in steady flows. Meccanica, 2(3):141–143, 1967. 54

(91) M. Masjedi and M.M. Khonsari. On the effect of surface roughness in point-contact ehl: Formulas for film thickness and asperity load. Tribology International, 82, Part A:228 – 244, 2015. 21, 22

(92) H. Moalic, J. A. Fitzpatrick, and A. A. Torrance. The correlation of the characteristics of rough surfaces with their friction coefficients. Proceedings of the Institution of Mechanical Engineers, Part C: Journal of Mechanical Engineering Science, 201(5):321–329, 1987. 28

(93) H Moalic, JA Fitzpatrick, and AA Torrance. A spectral approach to the analysis of rough surfaces. Journal of tribology, 111(2): 359–363, 1989. 179

(94) Balasubramanian Muralikrishnan and Jayaraman Raja. Computational surface and roundness metrology. Springer Science & Business Media, 2008. 84

(95) L. E. Murch and W. R. D. Wilson. A thermal elastohydrodynamic inlet zone analysis. Journal of Lubrication Technology, 97 (2):212–216, 04 1975. 13

(96) Y. Nagata. EHD phenomena in grease lubricated contacts. PhD thesis, University of Sussex, 2011. 52, 63

(97) P. R. Nayak. Random process model of rough surfaces. Journal of Lubrication Technology, 93(3):398–407, 07 1971. 26, 27, 99, 101

(98) G. Nijenbanning, C.H. Venner, and H. Moes. Film thickness in elastohydrodynamically lubricated elliptic contacts. Wear, 176 (2):217 – 229, 1994. 8, 18, 73, 77, 177

(99) M. Novak and D. Sharma. Comparing 3d optical microscopy techniques for metrology applications - application note 503. URL `https://www.bruker.com/fileadmin/user_upload/8-PDF-Docs/SurfaceAnalysis/3D-OpticalMicroscopy/ApplicationNotes/AN503-RevB0-Comparing_3D_Optical_Microscopy_Techniques_for_Metrology_Applications-AppNote.pdf`. 97

(100) J. M. Palacios. Elastohydrodynamic films in mixed lubrication: an experimental investigation. Wear, 89(3):303–312, 1983. 107

(101) Ping Pan and B. J. Hamrock. Simple formulas for performance parameters used in elastohydrodynamically lubricated line contacts. Journal of Tribology, 111(2):246–251, 04 1989. 177

(102) N. Patir and H. S. Cheng. An average flow model for determining effects of three-dimensional roughness on partial hydrodynamic lubrication. Journal of Lubrication Technology, 100:12–17, 1978. 16, 17

(103) Y. Peiran and W. Shizhu. A generalized reynolds equation for non-newtonian thermal elastohydrodynamic lubrication. Journal of Tribology, 112(4):631–636, 10 1990. 11, 12

(104) B. N. J. Persson. Theory of rubber friction and contact mechanics. The Journal of Chemical Physics, 115(8):3840–3861, 2001. 30

(105) R. J. Poole. An experimental study of grease in elastohydrodynamic lubrication. Rheology Bulletin, pages 32–39, 2012. 54

(106) S. Y. Poon and D. J. Haines. Third paper: Frictional behaviour of lubricated rolling-contact elements. Proceedings of the Institution of Mechanical Engineers, 181(1):363–389, 1966. 107, 113, 114

(107) T. Reddyhoff, H. A. Spikes, and A. V. Olver. Compression heating and cooling in elastohydrodynamic contacts. Tribology letters, 36(1):69–80, 2009. 12, 13

(108) J. Robertson. Diamond-like amorphous carbon. Materials Science and Engineering: R: Reports, 37(4):129–281, 2002. 147

(109) C. J. A. Roelands. Correlational aspects of the viscosity-temperature-pressure relationship of lubricating oils. PhD thesis, Technische Hogeschool te Delft, 1966. 7, 11

(110) F. Sadeghi and W. D.Jr. McClung. Formulas used in thermal elastohydrodynamic lubrication. Tribology Transactions, 34(4): 588–596, 1991. 12

(111) R. S. Sayles and T. R. Thomas. Surface topography as a nonstationary random process. Nature, 271(5644):431–434, 02 1978. 28, 88, 93

(112) M. Scaraggi, F. P. Mezzapesa, G. Carbone, A. Ancona, and L. Tricarico. Friction properties of lubricated laser-microtextured-surfaces: An experimental study from boundary-to hydrodynamic-lubrication. Tribology Letters, pages 117–125, 2013. 134

(113) D. J. Schipper. Transitions in the lubrication of concentrated contacts. PhD thesis, 1988. 22, 23, 24, 25, 50, 52, 54, 109, 123, 124, 126, 130, 134

(114) D. J. Schipper and A. W. J. De Gee. Lubrication modes and the irg transition diagram. Lubrication Science, 8(1):27–35, 1995. 22, 24, 130, 137

(115) J. Schmit. Surface measurement 101 non-contact 3d optical metrology. URL `https://www.bruker.com/fileadmin/user_upload/8-PDF-Docs/SurfaceAnalysis/3D-OpticalMicroscopy/Webinars/Surface_Metrology_101.pdf`. 38

(116) I. L. Singer and H. Pollock. Fundamentals of friction: macroscopic and microscopic processes, volume 220. Springer Science & Business Media, 2012. 107

(117) M. Smeeth and H. A. Spikes. The influence of slide/roll ratio on the film thickness of an ehd contact operating within the mixed lubrication regime. Tribology Series, 31:695–703, 1996. 14, 87, 115

(118) P. Sperka, I. Krupka, and M. Hartl. Experimental study of real roughness attenuation in concentrated contacts. Tribology International, 43(10):1893 – 1901, 2010. 173

(119) H. A. Spikes. Mixed lubrication an overview. Lubrication Science, 9(3):221–253, 1997. 6, 16

(120) H. A. Spikes. Sixty years of ehl. Lubrication Science, 18(4): 265–291, 2006. 52

(121) H. A. Spikes and Z. Jie. History, origins and prediction of elastohydrodynamic friction. Tribology Letters, 56(1):1–25, 2014. 9, 11, 14, 52, 82

(122) G. Stachowiak and A. W. Batchelor. Engineering tribology. Butterworth-Heinemann, 2013. 25, 56

(123) K. Stout, P. Sullivan, W. Dong, E. Mainsah, N. Luo, T. Mathia, and H. Zahouani. Development of methods for the characterisation of roughness in three dimensions. 2000. 84, 102

(124) D. Tabor. The role of surface and intermolecular forces in thin film lubrication. 7:651 – 682, 1981. 52, 54

(125) T. R. Thomas. Characterization of surface roughness. Precision Engineering, 3(2):97–104, 1981. 30

(126) T. R. Thomas. Rough surfaces. World Scientific, 1998. 84

(127) T. R; Thomas and G. Charlton. Variation of roughness parameters on some typical manufactured surfaces. Precision Engineering, 3(2):91–96, 1981. 28, 30, 31, 86, 87, 88

(128) B. Vengudusamy, J. H. Green, G. D. Lamb, and H. A. Spikes. Tribological properties of tribofilms formed from zddp in dlc/dlc and dlc/steel contacts. Tribology International, 44(2):165–174, 2011. 162

(129) B. Vengudusamy, R. A. Mufti, G. D. Lamb, J. H. Green, and H. A. Spikes. Friction properties of dlc/dlc contacts in base oil. Tribology International, 44(78):922 – 932, 2011. 134, 145, 147

(130) C.H. Venner and A.A. Lubrecht. Numerical simulation of waviness in a circular ehl contact under rolling/sliding. Elsevier Tribology Series, 30:259–272, 1995. 18

(131) Cornelis H Venner and AA Lubrecht. Amplitude reduction of non-isotropic harmonic patterns in circular ehl contacts, under pure rolling. Tribology Series, 36:151–162, 1999. 18

(132) P. Vyas. Effects of Stochastic (Random) Surface Roughness on Hydrodynamic Lubrication of Deterministic Asperity. Master's thesis, University of Kentucky, 2005. 18

(133) J. Wang, C.H. Venner, and T. Lubrecht. Amplitude reduction in EHL line contacts under rolling sliding conditions. Tribology International, 44(12):1997–2001, 2011. 18

(134) Q Jane Wang and Yip-Wah Chung. Encyclopedia of tribology: With 3650 Figures and 493 Tables. Springer, 2013. 107

(135) David J. Whitehouse. Handbook of Surface and Nanometrology. 2003. 84, 97

(136) David John Whitehouse and JF Archard. The properties of random surfaces of significance in their contact. In Proceedings of the Royal Society of London A: Mathematical, Physical and Engineering Sciences, volume 316, pages 97–121. The Royal Society, 1970. 26, 27

(137) W. R. D. Wilson and S. Sheu. Effect of inlet shear heating due to sliding on elastohydrodynamic film thickness. Journal of Lubrication Technology, 105(2):187–188, 04 1983. 13, 14

(138) W. R. D. Wilson and C. J. Wong. Analysis of the lubricant film formation process in plane strain forging. Journal of Lubrication Technology, 96(4):605–610, 1974. 13

(139) K Yoshida, M Kano, and M Masuko. Effect of polar groups in lubricants on sliding speed dependent friction coefficients of dlc coatings. Tribology-Materials, Surfaces & Interfaces, 9(1):54–61, 2015. 147

(140) R. Zahid, M. B. H. Hassan, M. Varman, R. A. Mufti, M. A. Kalam, N. W. B. M. Zulkifli, and M. Gulzar. A review on effects of lubricant formulations on tribological performance and boundary lubrication mechanisms of non-doped dlc/dlc contacts. Critical Reviews in Solid State and Materials Sciences, pages 1–28, 2016. 149

dernière page de la thèse

AUTORISATION DE SOUTENANCE

Vu les dispositions de l'arrêté du 25 mai 2016,

Vu la demande des directeurs de thèse

Messieurs J. CAYER-BARRIOZ et D. MAZUYER

et les rapports de

M. D.J. SCHIPPER
Professeur - University of Twente - Department of Mechancs of Solids, Surfaces and Systemes - Drienerlolaan 5 - 7522 NB Enschede - Pays-Bas

et de

M. N. BRUNETIERE
Chargé de recherche HDR - Institut Pprime - UPR 3346 Dépt. Génie Mécanique et Systèmes Complexes CNRS - Université de Poitiers - ENSMA SP2MI - Téléport 2 - bd Pierre et Marie Curie - BP 30179 - 86962 Futuroscope Chasseneuil cedex

Monsieur BONAVENTURE Julien, Paul

est autorisé à soutenir une thèse pour l'obtention du grade de **DOCTEUR**

Ecole doctorale MECANIQUE, ENERGETIQUE, GENIE CIVIL ET ACOUSTIQUE

Fait à Ecully, le 11 octobre 2017

P/Le directeur de l'E.C.L.
La directrice des Etudes

Service Scolarité

M-A. GALLAND

Résumé

La plupart des sytèmes mécaniques contiennent des contacts lubrifiés (articulations, roulements, ...) qui sont soumis à des efforts importants. Dans ce travail expérimental, on s'intéresse à l'influence de la rugosité sur la friction dans les régimes de lubrification élastohydrodynamique (EHD), mixte, et limite dans des conditions représentatives des contacts dans un moteur de voiture. Les surfaces utilisées dans ce travail sont principalement des aciers usinés industriellement, revêtus ou non de Diamond-Like Carbon (DLC).

La force de friction dans les régimes mixte et limite étant bien plus importante qu'en régime EHD, il est important de pouvoir prédire les transitions d'un régime à l'autre. Le problème est que la rugosité affecte significativement les vitesses de transition entre ces régimes, de telle manière qu'il est difficile de prédire le régime de fonctionnement d'un couple donné de surfaces. Les travaux expérimentaux s'attardant sur ce problème sont rares, et les tentatives théoriques d'inclure l'effet de rugosités aléatoires reposent sur des paramètres difficiles à mesurer à cause de leur grande dépendance vis-à-vis des conditions de filtrage, d'échantillonnage, et de leur non-stationnarité. À partir de nombreuses mesures topograhiques (interférométrie et AFM), une méthode assurant la représentativité des paramètres statistiques de rugosité est donc d'abord mise en oeuvre pour caractériser des surfaces dont la rugosité va du nanomètre au micron. Des expériences de Stribeck sont ensuite menées avec ces surfaces afin de corréler leur signature morphologique à leur comportement en friction.

La rhéologie sous pression de lubrifiants (poly-α oléfines) est mesurée dans un contact lisse en fonction de la pression et de la température, ce qui permet de prédire quantitativement la friction en régime élastohydrodynamique pour tout couple de surfaces, mais aussi de définir un critère non phénoménologique d'entrée en régime de lubrification mixte. À haute vitesse d'entrainement, la contrainte visqueuse décroît avec le taux de cisaillement ce qui est traditionnellement attribué à un échauffement du lubrifiant. On montre que les effets thermiques ne peuvent expliquer une telle chute et on l'explique par l'étalement du profil de pression dans le convergent, phénomène significatif quand l'épaisseur de lubrifiant devient de l'ordre d'un dixième de la taille du contact.

Les résultats montrent que le produit de la viscosité dans le convergent avec la vitesse d'entrainement à la transition mixte-EHD suit une loi de puissance super-linéaire avec la rugosité, tous matériaux confondus, ce qui permet de prédire cette transition en fonction de la rugosité. La transition entre régimes mixte et limite est plus complexe et laisse apparaître un comportement clairement différent entre les contacts DLC/DLC et les contacts mettant en jeu au moins une surface d'acier. Pour les contacts DLC/DLC, la friction en régime limite correspond au cisaillement plastique du lubrifiant, ce qui explique que la rugosité n'affecte pas le frottement limite de ces contacts. Le frottement des contacts acier/acier et acier/DLC est plus important et présente deux évolutions monotones avec la rugosité composite du contact, que nous interprétons grâce à des expériences tribologiques à haut taux de glissement.

Finalement, un modèle de portance mixte basé sur la théorie de Greenwood-Williamson est mis en oeuvre et permet de reproduire avec une précision honorable les courbes de Stribeck obtenues expérimentalement. En particulier, ce modèle permet de déterminer les conditions d'échantillonnage optimales pour déterminer les propriétés des aspérités.

Mots-Clés : Friction, Lubrification Elastohydrodynamique, Mixte et Limite, Courbe de Stribeck, Rugosité Aléatoire, Caractérisation Multi-Échelle de Surface.

Abstract

Most mechanical systems include lubricated contacts submitted to important strengths. The present work deals with the influence of surface roughness on friction in the elastohydrodynamic (EHD), mixed and boundary lubrication regimes, with operating conditions that are typically those found in an internal combustion engine. Most of the surfaces used in the experiments are machined steel, with or with a Diamond-Like Carbon (DLC) coating.

Given the friction in boundary and mixed lubrication being higher than in EHD lubrication, it is crucial to predict the transitions between these regimes. These strongly depend on surface roughness. There are very few experimental works that deal with this issue, and the theoretical attempts to include the influence of random surface roughness are based on roughness parameters that are difficult to measure because of their dependence towards the sampling conditions and their non-stationarity. Based on numerous topographical surveys (using interferometry and AFM), a method is implemented to ensure the representativeness of roughness statistical parameters in order to characterize a range of surface roughnesses within the interval [0.001 ; 1] μm. Then, these surfaces are rubbed against each other using Stribeck procedures in order to correlate their morphology to their friction behaviour.

The high-pressure rheology of poly-α olefins is measured in smooth contacts with respect to the pressure and the temperature. This not only allows to quantify the friction force for any contact operating in EHD lubrication, but also to set a criterion to spot the onset of mixed lubrication. At high entrainment speed, the viscous shear stress vanishes, which is often attributed to shear heating. It is shown that thermal effects can not explain such a drop of friction for our own experiments. However, the widening of the pressure profile — which becomes significant when the film thickness becomes comparable to a tenth the contact length — is more likely to explain this behaviour.

Our results show that the product of the inlet viscosity with the entrainment speed, spotted at the mixed-EHD transition, follows a super linear power law with the RMS roughness, whatever the materials involved, which allows to predict whether a contact operate in mixed lubrication or not. The transition from mixed to boundary lubrication reveals material and roughness-dependent with a clearly different behaviour between DLC/DLC contacts and contacts involving at least one steel body. Regarding the DLC/DLC contacts, the boundary friction is due to the plastic shearing of the lubricant, which explains why surface roughness has no influence on boundary friction for these contacts. With Steel/DLC and steel/steel contacts, the boundary friction presents two monotonous trends versus the composite RMS roughness.

Eventually, a mixed bearing model based on the Greenwood-Willimason assumptions was implemented and allowed to reproduce quite closely the experimentally obtained Stribeck curves. This implementation indicates in particular the sampling conditions that are optimal to capture relevant asperity parameters.

Keywords: Friction, Elastohydrodynamic, Mixed and Boundary Lubrication, Stribeck Curve, Random Roughness, Multi-Scale Surface Characterization.